UNIVERSITY OF SOUTHAMPTON

FACULTY OF NATURAL AND ENVIRONMENTAL SCIENCES

Ocean and Earth Science

Volume 1 of 1

Fluid flow in an active orogenic mountain belt;
the Southern Alps, New Zealand

by

James Paul Coussens

Thesis for the degree of Doctor of Philosophy

February 2018

UNIVERSITY OF SOUTHAMPTON

ABSTRACT

FACULTY OF NATURAL AND ENVIRONMENTAL SCIENCES

Ocean and Earth Science

Thesis for the degree of Doctor of Philosophy

FLUID FLOW IN AN ACTIVE OROGENIC MOUNTAIN BELT;

THE SOUTHERN ALPS, NEW ZEALAND

James Paul Coussens

Groundwater can influence processes in mountain belts and associated fault zones through heat and mass transfer and the influence of fluid pressure on deformation. Modelling at a range of scales, utilising new data from the DFDP-2B borehole, is employed to investigate groundwater and heat flow in the Southern Alps mountain belt, New Zealand, which experiences active, rapid uplift on the plate-bounding Alpine Fault. Models indicate bulk permeability of the brittle crust in the orogen in the range 10^{-16} m^2 to 10^{-13} m^2. Estimated permeability for basement rocks obtained using DFDP-2B data (10^{-16} m^2) falls at the lower end of this range. Models of the region's heavy rainfall, highly elevated water tables, and extensive seeps, indicate that >20 % of precipitation may infiltrate into the groundwater system. The majority of infiltrating water penetrates to <500 m below ground level. DFDP-2B temperature data indicates Darcy velocities of ~10^{-9} $m{\cdot}s^{-1}$. These are sufficiently high that groundwater transports significant amounts of heat, more than three times that transported by rock advection at DFDP-2B. High heat fluxes of ~720 $mW{\cdot}m^{-2}$ result from the advection of heat from ridges perpendicular to the Alpine Fault into the intervening valleys by groundwater flow. High bulk permeabilities and less significant permeability reductions with depth increase shallow temperatures beneath valleys relative to ridges and decrease temperatures at the base of the groundwater system in regional models. Groundwater convergence produces steep increases in hydraulic head with depth beneath valleys, with DFDP-2B data indicating >60 m head at 818 m depth. However, thermal decreases in water density restrict increases in head to the near-surface (~1 km below sea level). Thermal buoyancy provides the major driving contribution to vertical flow in parts of the groundwater system and thermally decreased water viscosity may facilitate penetration of greater fluxes of meteoric water to the brittle-ductile transition in the Southern Alps than in settings with lower geothermal gradients.

Table of Contents

List of Tables

Chapter 6

List of Figures

Chapter 1

Chapter 2

Chapter 3

Chapter 4

Chapter 5

Chapter 6

List of Accompanying Materials

Appendix A:

Sutherland, R., Townend, J., Toy, V., Upton, P., Coussens, J., Allen, M., Baratin, L.-M., Barth, N., Becroft, L., Boese, C., Boles, A., Boulton, C., Broderick, N.G.R., Janku-Capova, L., Carpenter, B.M., Célérier, B., Chamberlain, C., Cooper, A., Coutts, A., Cox, S., Craw, L., Doan, M.-L., Eccles, J., Faulkner, D., Grieve, J., Grochowski, J., Gulley, A., Hartog, A., Howarth, J., Jacobs, K., Jeppson, T., Kato, N., Keys, S., Kirilova, M., Kometani, Y., Langridge, R., Lin, W., Little, T., Lukacs, A., Mallyon, D., Mariani, E., Massiot, C., Mathewson, L., Melosh, B., Menzies, C., Moore, J., Morales, L., Morgan, C., Mori, H., Niemeijer, A., Nishikawa, O., Prior, D., Sauer, K., Savage, M., Schleicher, A., Schmitt, D.R., Shigematsu, N., Taylor-Offord, S., Teagle, D., Tobin, H., Valdez, R., Weaver, K., Wiersberg, T., Williams, J., Woodman, N., Zimmer, M., 2017. Extreme hydrothermal conditions at an active plate-bounding fault. Nature 546, 137–140. doi:10.1038/nature22355

Appendix B:

Hydraulic dataset collected during periodic measurements at the DFDP-2B borehole (including data file and index file describing data fields), provided on accompanying DVD.

DECLARATION OF AUTHORSHIP

I, James Paul Coussens, declare that this thesis and the work presented in it are my own and has been generated by me as the result of my own original research.

Fluid flow in an active orogenic mountain belt; the Southern Alps, New Zealand

I confirm that:

1. This work was done wholly or mainly while in candidature for a research degree at this University;
2. Where any part of this thesis has previously been submitted for a degree or any other qualification at this University or any other institution, this has been clearly stated;
3. Where I have consulted the published work of others, this is always clearly attributed;
4. Where I have quoted from the work of others, the source is always given. With the exception of such quotations, this thesis is entirely my own work;
5. I have acknowledged all main sources of help;
6. Where the thesis is based on work done by myself jointly with others, I have made clear exactly what was done by others and what I have contributed myself;
7. Parts of this work have been published as:

Sutherland, R., Townend, J., Toy, V., Upton, P., Coussens, J., Allen, M., Baratin, L.-M., Barth, N., Becroft, L., Boese, C., Boles, A., Boulton, C., Broderick, N.G.R., Janku-Capova, L., Carpenter, B.M., Célérier, B., Chamberlain, C., Cooper, A., Coutts, A., Cox, S., Craw, L., Doan, M.-L., Eccles, J., Faulkner, D., Grieve, J., Grochowski, J., Gulley, A., Hartog, A., Howarth, J., Jacobs, K., Jeppson, T., Kato, N., Keys, S., Kirilova, M., Kometani, Y., Langridge, R., Lin, W., Little, T., Lukacs, A., Mallyon, D., Mariani, E., Massiot, C., Mathewson, L., Melosh, B., Menzies, C., Moore, J., Morales, L., Morgan, C., Mori, H., Niemeijer, A., Nishikawa, O., Prior, D., Sauer, K., Savage, M., Schleicher, A., Schmitt, D.R., Shigematsu, N., Taylor-Offord, S., Teagle, D., Tobin, H., Valdez, R., Weaver, K., Wiersberg, T., Williams, J., Woodman, N., Zimmer, M., 2017. Extreme hydrothermal conditions at an active plate-bounding fault. Nature 546, 137–140. doi:10.1038/nature22355

Signed: .....

Date: .....

Acknowledgements

I would like to thank my supervisors Damon Teagle, Nicholas Woodman, Catriona Menzies, Phaedra Upton and Simon Cox for their advice, support and supervision throughout my PhD. Damon, thank you for being a constant source of inspirational ideas. Thank you for your support throughout my PhD, even when I nearly got stuck in San Francisco. Nick, thank you for providing so much advice through my PhD and always being available for a chat. I am extremely grateful for all your time spent helping me to improve my work, as well as providing much moral support. Catriona, I am thankful to you for all of your good advice, helping me to navigate the challenges of doing a PhD and sharing the good times and the challenges (including drastic shortages of good quality tea and my introduction sandfly bites) of my time in New Zealand – I raise a can of Irn Bru to you! Thank you Phaedra for all your modelling advice and for giving me my first glimpse of the Alpine Fault in an outcrop. Thank you Simon for imparting a great deal of knowledge about groundwater in the Southern Alps- I particularly appreciated your explanations of the passing landscape and geology on our drive across the Southern Alps. You have all been fantastic supervisors and I am extremely grateful for your constructive feedback on the numerous drafts that have eventually resulted in this thesis.

I would also like to thank all members of the DFDP-2 team. It has been a pleasure to work and get soaked by the West Coast rain alongside you. I learned a lot and had great fun doing so. In particular, I would like to thank Rupert Sutherland for the guidance that he provided while we were on site at DFDP-2B and in subsequent discussions. Rupert, your undying enthusiasm throughout the DFDP-2 project was a great encouragement. I would also like to thank the other Principal Investigators John Townend and Virgina Toy, with whom I have also enjoyed working. Other members of the DFDP-2 team to whom I extend particular thanks are Lucie Janku-Capova, Mai-Linh Doan, Cécile Massiot and Bernard Célérier. Your knowledge regarding the DFDP-2B wireline dataset has been valuable and I enjoyed eating pancakes with you in Grenoble very much! Lucie, it was a pleasure working with you while in Whataroa to make sure that the borehole did not overflow!

I am grateful to Carolyn Boulton, Daniel Faulkner, Elizabetta Mariani and Michael Allen. Meetings between the Liverpool and Southampton Alpine Fault research groups have been valuable and helped me to learn more about the mechanics of the fault. Carolyn, I am particularly grateful to you for taking time to discuss some of the finer points of fault mechanics with me and for introducing me to wiffle ball. I am very grateful to Dave Craw, who has provided advice and feedback on drafts. Thank you Dave, I have enjoyed our discussions immensely. My thanks also go

to John Barker, who has provided valuable advice regarding analytical solutions and feedback on a number of drafts. A spreadsheet created by John Barker was also used for calculating values for the Theis well function in this thesis and other spreadsheet models created by John Barker were utilised in the preparations for DFDP-2. John, I am very grateful for you for your time and for allowing the use of your spreadsheets. My thanks also go to Robert Langridge for providing advice regarding the position of the Alpine Fault.

A great deal of thanks go to my family and friends, including those not named individually here. Mum, Dad, Gran and Thomas, thank you for all that you have done to help me throughout my PhD. Grandad, Grandad and Nanny, you helped make me who I am today.

Above all my thanks go to Maya Coussens, my wife and to God. Maya has been an essential support throughout, helping me to keep pressing on and also proof reading for me. Maya, your love and kindness has been vital to me throughout this PhD. I thank God, who has been so gracious to me in every way and without whose strength this work would not have been possible.

Nomenclature

Roman Symbols

Symbol	Definition	Dimension
A	Initial upward displacement of mud level from steady state during a slug test	L
a	Model temperature gradient	ΘL^{-1}
B	Slug test mud level decay constant	T^{-1}
b	Buoyancy body force per unit mass	LT^{-2}
C	Volumetric heat capacity	$ML^{-1}T^{-2}\Theta^{-1}$
C_1	Constant of integration used in Dupuit water table models	L
C_2	Constant of integration used in Dupuit water table models	L^2
C_3	Constant of integration used in Dupuit water table models	L
C_4	Constant of integration used in Dupuit water table models	L^2
C_e	Effective volumetric heat capacity of the fluid-rock medium	$ML^{-1}T^{-2}\Theta^{-1}$
C_f	Volumetric heat capacity of the fluid phase	$ML^{-1}T^{-2}\Theta^{-1}$
C_s	Volumetric heat capacity of the solid (rock) phase	$ML^{-1}T^{-2}\Theta^{-1}$
C_τ	Cohesion	$ML^{-1}T^{-2}$
D	Borehole vertical depth	L
D_d	Hydrodynamic dispersion coefficient for a fluid-rock medium (solute transport)†	L^2T^{-1}
D_e	Effective molecular diffusivity of the fluid (solute transport)†	L^2T^{-1}
D_h	Distance of section division of a Dupuit water table model	L
D_m	Mechanical dispersion coefficient of the fluid-rock medium (solute transport)†	L^2T^{-1}
d	Length of borehole open interval	L
F_n	Heat flux parameter in the nth model section	ML^2T^{-2}
f	Heat flux parameter	ML^2T^{-2}
f_n	Heat flux parameter in the nth model section	ML^2T^{-2}

Symbol (cont.)	Definition (cont.)	Dimension (cont.)
G_n	Change in heat flux parameter f_n between model section n and model section $(n-1)$	ML^2T^{-2}
g	Acceleration due to gravity	LT^{-2}
H_0	Borehole steady state hydraulic head	L
h	Hydraulic head	L
h_0	Fixed head at model surface	L
h_1	Fixed head at start of a Dupuit water table model	L
h_2	Fixed head at end of a Dupuit water table model	L
$\boldsymbol{K}$	Hydraulic conductivity tensor	LT^{-1}
K	Hydraulic conductivity†	LT^{-1}
K_1	Isotropic hydraulic conductivity of section 1 of a Dupuit water table model	LT^{-1}
K_2	Isotropic hydraulic conductivity of section 2 of a Dupuit water table model	LT^{-1}
K_n	Hydraulic conductivity normal to foliation	LT^{-1}
K_p	Hydraulic conductivity parallel to foliation	LT^{-1}
$\boldsymbol{k}$	Permeability tensor	L^2
k	Permeability†	L^2
k_b	Isotropic permeability assigned to model basement rocks	L^2
k_{bh}	Isotropic permeability assigned to model borehole	L^2
k_c	Isotropic permeability assigned to model borehole casing	L^2
k_n	Permeability normal to foliation	L^2
k_p	Permeability parallel to foliation	L^2
k_s	Isotropic permeability assigned to model sediments	L^2
k_z	Permeability along the vertical axis	L^2
L	Length scale for heat/solute transport	L
L_h	Length of a Dupuit water table model	L
l	Model section length	L

Symbol (cont.)	Definition (cont.)	Dimension (cont.)
M	Borehole drilling mud level	L
M_0	Borehole steady state drilling mud level	L
M_b	Earthquake body wave magnitude	-
M_L	Earthquake local magnitude	-
M_w	Earthquake moment magnitude	-
$\widehat{\boldsymbol{n}}$	Unit vector in the z direction	-
P	Péclet number (heat transport)	-
P_f	Péclet number for rate of heat advection rate by fluid phase only relative to conduction in both fluid and solid (rock) phases (where both fluid and rock advection are considered)	-
P_n	Péclet number (heat transport) in the nth model section	-
P_γ	Péclet number (solute transport)	-
p	Fluid pressure	$ML^{-1}T^{-2}$
p_h	Hydrostatic pressure	$ML^{-1}T^{-2}$
p_r	Reduced pressure	$ML^{-1}T^{-2}$
$\boldsymbol{Q_{adv}}$	Advective heat flux vector	MT^{-3}
$\boldsymbol{Q_{adv}^*}$	Advective heat flux vector applied to simulate rock advection	MT^{-3}
Q	Heat flux along the axis of fluid/heat flow for single dimensional problems	MT^{-3}
Q_n	One-dimensional heat flux in the nth model section	MT^{-3}
$Q_{a,n}$	Absolute one-dimensional heat flux in the nth model section	MT^{-3}
$Q_{s,n}$	One-dimensional heat flux in the nth model section relative to surface temperature	MT^{-3}
Q_T	Rate of internal heat generation per unit volume	$ML^{-1}T^{-3}$
Q_γ	Rate of internal generation of the chemical species per unit volume	$ML^{-3}T^{-1}$
Q_w	Rate of heat extraction from a borehole (well) per unit length	MT^{-2}

Symbol (cont.)	Definition (cont.)	Dimension (cont.)
$\boldsymbol{q}$	Darcy velocity vector	LT^{-1}
$\boldsymbol{q}_0$	Darcy velocity vector prior to modification for simulation of thermal effects of rock advection and to heat flow simulation	LT^{-1}
$\boldsymbol{q}_1$	Darcy velocity vector following modification for simulation of thermal effects of rock advection, prior to heat flow simulation	LT^{-1}
$\boldsymbol{q}_2$	Darcy velocity vector prior to second modification for simulation of thermal effects of rock advection, following heat flow simulation	LT^{-1}
$\boldsymbol{q}_3$	Darcy velocity vector following second modification for simulation of rock advection and heat flow simulation	LT^{-1}
$\boldsymbol{q}^*$	Darcy velocity vector applied for simulation of rock advection	LT^{-1}
q	Darcy velocity along the axis of fluid/heat flow for single dimensional problems	LT^{-1}
q_n	One-dimensional Darcy velocity in the nth model section	LT^{-1}
q_z	Vertical Darcy velocity	LT^{-1}
R_e	Effective radius of water table drawdown	L
R^2	Coefficient of determination	-
r	Reduced pressure driven component of vertical flow	LT^{-2}
r_c	Borehole (well) casing radius	L
r_w	Borehole (well) radius	L
S	Rate of internal heat generation per unit volume	$ML^{-1}T^{-3}$
S_γ	Rate of internal generation of a transported chemical species per unit volume	$ML^{-3}T^{-1}$
SG_d	Specific gravity of drilling mud	-
SD	Standard deviation	N/A
T	Temperature	Θ
T_0	Initial temperature formation temperature, prior to drilling	Θ
T_a	Model ambient surface temperature	Θ

Symbol (cont.)	Definition (cont.)	Dimension (cont.)
T_b	Model basal temperature	Θ
T_n	Temperature in the nth model section	Θ
T_w	Temperature at borehole (well)-formation interface	Θ
t	Time	T
t_μ	Time for 1 U.S. quart of drilling mud to drain through a march funnel	T
$\boldsymbol{v}$	Average linear velocity vector of the fluid phase	LT^{-1}
$\boldsymbol{v_s}$	Average linear velocity vector of solid (rock) and fluid phases in the z direction	LT^{-1}
v_e	Effective vertical average linear velocity in vertical direction	LT^{-1}
$v_{e,n}$	Effective vertical average linear velocity in the nth model section	LT^{-1}
v_f	Vertical average linear velocity of fluid phase relative to solid rock phase in vertical direction	LT^{-1}
v_u	Average linear uplift velocity of solid (rock) and fluid phases in the vertical direction	LT^{-1}
W	Theis (1935) well function	N/A
w	Surface infiltration rate	LT^{-1}
w_1	Surface infiltration rate in section 1 of a Dupuit water table model	LT^{-1}
w_2	Surface infiltration rate in section 2 of a Dupuit water table model	LT^{-1}
x	Distance from the fixed hydraulic head starting point of a Dupuit water table model	L
y	Borehole fluid level relative to its unperturbed level at time t	L
y_i	Change in borehole fluid level relative to its unperturbed level at the initiation of a slug test	L

Symbol (cont.)	Definition (cont.)	Dimension (cont.)
z	Vertical coordinate (elevation or depth) with origin and orientation defined within each chapter	L
z_0	Depth of top of model section	L
z_a	Model surface elevation	L
z_b	Model basal elevation	L
z_l	Depth of base of model section	L
$z_{l,n}$	Depth of base of the nth model section	L
z_{km}	Depth in km	L

†Along the axis of fluid/heat flow for one-dimensional problems, isotropic value for multi-dimensional problems.

Greek Symbols

Symbol	Definition	Dimension
β	Coefficient of thermal expansion	Θ^{-1}
γ	Concentration	ML^{-3}
Δ	Denotes the difference in values for a parameter (e.g. Δf_n represents the difference in f_n between the nth and $(n-1)$th model sections)	N/A
δ	Denotes the uncertainty associated with a parameter (e.g. δH_0 represents the uncertainty associated with H_0)	N/A
κ	Thermal diffusivity†	L^2T^{-1}
κ_d	Thermal dispersion coefficient of the fluid-rock medium†	L^2T^{-1}
κ_e	Effective thermal diffusivity of the fluid-rock medium†	L^2T^{-1}
κ_f	Thermal diffusivity of the fluid phase†	L^2T^{-1}
κ_s	Thermal diffusivity of the solid (rock) phase†	L^2T^{-1}
κ_m	Mechanical thermal dispersion coefficient for a fluid-rock medium †	L^2T^{-1}
$\boldsymbol{\Lambda_e}$	Effective thermal conductivity tensor of the fluid-rock medium	$MLT^{-3}\Theta^{-1}$

Symbol (cont.)	Definition (cont.)	Dimension (cont.)
$\boldsymbol{\Lambda_f}$	Thermal conductivity tensor of the fluid phase	$MLT^{-3}\Theta^{-1}$
$\boldsymbol{\Lambda_s}$	Thermal conductivity tensor of the solid (rock) phase	$MLT^{-3}\Theta^{-1}$
Λ	Thermal conductivity†	$MLT^{-3}\Theta^{-1}$
Λ_e	Effective thermal conductivity of the fluid-rock medium†	$MLT^{-3}\Theta^{-1}$
Λ_f	Thermal conductivity of the fluid phase†	$MLT^{-3}\Theta^{-1}$
Λ_s	Thermal conductivity of the solid (rock) phase†	$MLT^{-3}\Theta^{-1}$
μ	Fluid viscosity	$ML^{-1}T^{-1}$
μ_0	Reference fluid viscosity under specified conditions	$ML^{-1}T^{-1}$
μ_d	Drilling mud viscosity	$ML^{-1}T^{-1}$
μ_τ	Coefficient of friction	-
ρ	Fluid density	ML^{-3}
ρ_0	Reference fluid density under specified conditions	ML^{-3}
ρ_a	Fluid density under ambient surface temperature and pressure	ML^{-3}
ρ_d	Drilling mud density	ML^{-3}
ρ_m	Mean fluid density in the domain of fluid flow	ML^{-3}
ρ_w	Reference density for water	ML^{-3}
ς	Dimensionless depth	-
ς_n	Dimensionless depth in the nth model section	-
σ	Standard deviation in fitted steady state mud level	L
σ_n	Normal stress	$ML^{-1}T^{-2}$
τ	Shear stress	$ML^{-1}T^{-2}$
φ	Porosity	-

†Along the axis of fluid/heat flow for one-dimensional problems, isotropic value for multi-dimensional problems.

Chapter 1:

Introduction

1.1 Rationale

Orogenic mountain belts are major topographic features of Earth's surface today and the geology of many regions reflects orogenic processes of the past (Fig. 1.1). They are sites where rocks may undergo significant modification, through deformation (Holdsworth and Strachan, 1991; Imber et al., 2001; Schmid et al., 2008; Sibson et al., 1979), metamorphism (England and Thompson, 1984; Searle et al., 2003; Thompson and England, 1984; Vance et al., 1998), mineralisation (Groves et al., 1998; Koons and Craw, 1991; Pitcairn et al., 2006, 2014) and melting (Harris and Massey, 1994; Owens and Zandt, 1997; Searle et al., 2010). Rocks from depth are exhumed and eroded, with new strata formed from the sediment produced (Beaumont, 1981; DeCelles and Giles, 1996; Yin, 2006). The uplift of mountain belts has the potential to influence climate, both locally and globally (Cox and Sutherland, 2007; Koons, 1989; Molnar et al., 1993; Zhisheng et al., 2001). Orogenic mountain belts contain major fault zones, many of which generate large magnitude earthquakes when they fail (Avouac et al., 2015; Kao and Chen, 2000; Sutherland et al., 2007).

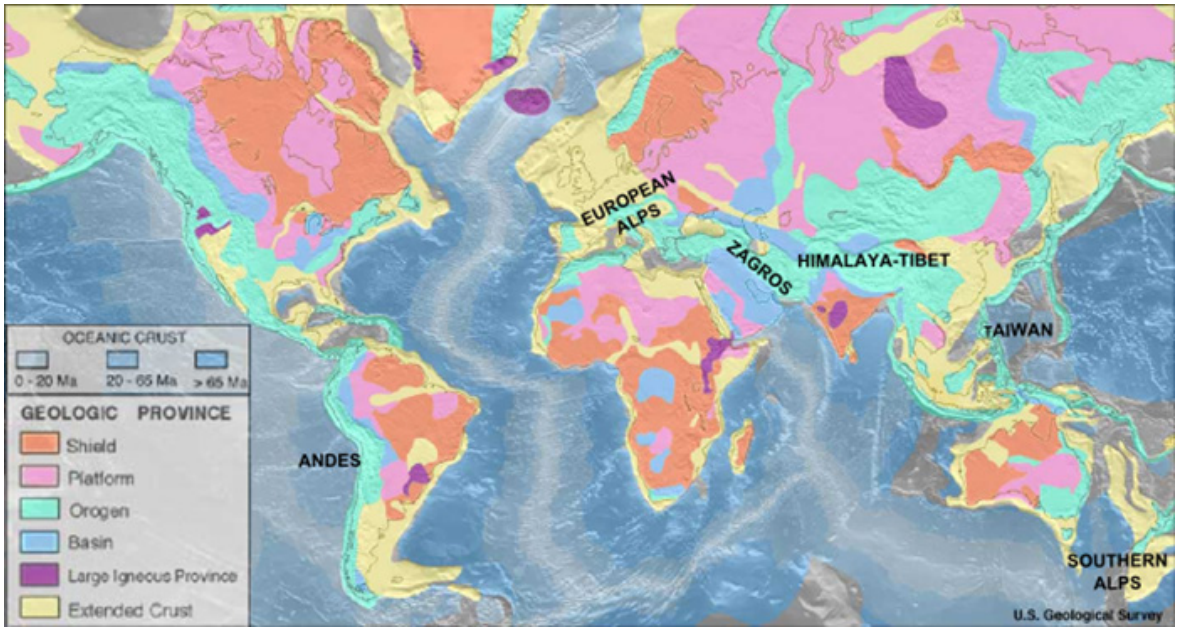

Figure 1.1 Map of orogenic and other geologic provinces forming the continental crust of Earth today, with major active orogenic mountain belts labelled. Adapted from (U.S. Geological Survey, 2017).

An understanding of orogenic processes is therefore key to understanding present day tectonic processes as well as interpreting much of the geological record. Fluid flow has the potential to significantly influence thermal, geochemical and deformational processes, including seismicity along major fault zones (see sections 1.2.4 and 1.2.5). In this thesis, the role of groundwater circulation in an active orogenic mountain belt, the Southern Alps, is investigated.

1.2 Groundwater flow and its geological significance

1.2.1 Fluid flow in porous media

For the purposes of the study of fluid flow, rocks are commonly considered as porous media. A porous medium consists of a solid matrix, found within every representative elementary volume of the medium, and at least one non-solid phase, such as water, present within an interconnected void space, with relatively narrow openings and a relatively high surface area per unit volume of the medium (Bear, 1972). Porosity (φ) is the volume fraction void space of a porous medium. Possible voids include pores between grains and fractures. Some void spaces may be isolated, not forming part of a network that facilitates fluid flow. Effective porosity is defined as the volume fraction of interconnected void space (Bear, 1972). Fluid flow in a porous medium is described by Darcy's Law:

$$\boldsymbol{q} = -\frac{\boldsymbol{k}}{\mu} \cdot (\nabla p + \rho g \hat{\boldsymbol{n}}) \tag{1.1}$$

Where $\boldsymbol{q}$ is the Darcy velocity vector, $\boldsymbol{k}$ is the permeability tensor, μ is the dynamic viscosity of the water, p is the fluid pressure, ρ is the density of the water, g is the acceleration due to gravity, $\hat{\boldsymbol{n}}$ is a unit vector oriented vertically upward. Darcy velocity is the product of average linear velocity, $\boldsymbol{v}$ and porosity φ:

$$\boldsymbol{q} = \varphi \boldsymbol{v} \tag{1.2}$$

Darcian flow is commonly assumed for rocks of the upper crust. In tectonically active regions, deformation can also create interconnected pore networks in the middle to lower crust and where this is the case flow is also likely to remain Darcian (Manning and Ingebritsen, 1999).

Fluid flow may be driven by fluid pressure differences in a system with constant fluid density. It may also be driven by buoyancy, resulting from density differences. Terms associated with these two driving forces may be separated in Darcy's Law by considering reduced pressure, p_r, the difference between hydrostatic pressure, p_h, and total fluid pressure, p, based on mean groundwater density in the domain of fluid flow, ρ_m (Phillips, 2009). In this case:

$$p_r = p - p_h \tag{1.3}$$

$$\boldsymbol{q} = -\frac{\boldsymbol{k}\rho_m}{\mu} \cdot \left(\frac{\nabla p_r}{\rho_m} + b\hat{\boldsymbol{n}}\right) \tag{1.4}$$

$$b = \left(\frac{\rho - \rho_m}{\rho_m}\right) g \tag{1.5}$$

Where b is buoyancy, a body force per unit mass.

Pressure differentials that can drive fluid flow arise in nature as a result of topographic relief (Hubbert, 1940), which allows for different elevations of water table at different locations, resulting in variation in fluid pressures at a reference depth (Fig. 1.2). Complex patterns of groundwater flow can arise as a result of topography even if rocks are isotropic and homogeneous (Tóth, 1962, 1963).

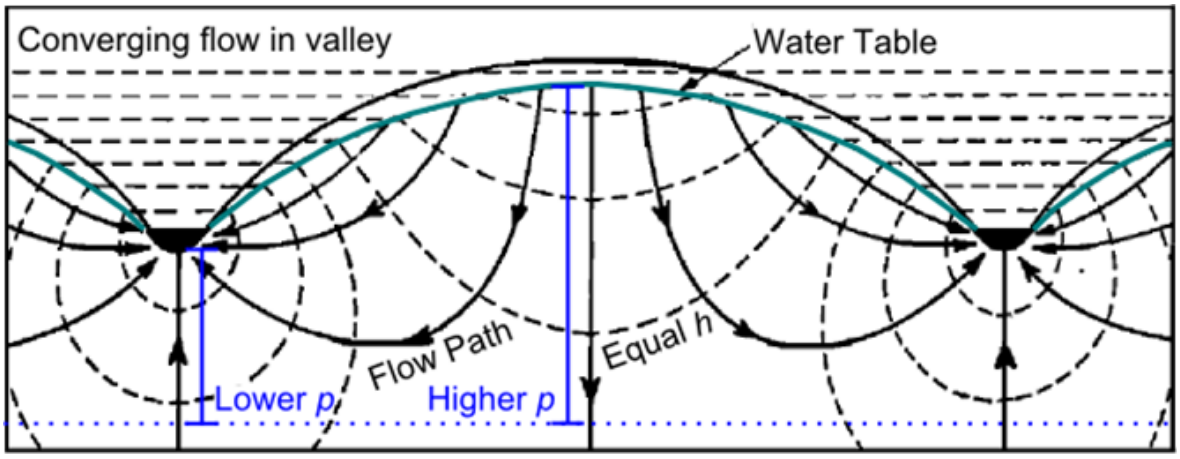

Figure 1.2 A simple two dimensional topography driven flow regime, in which lateral pressure differentials arise from of differing water table elevation, which results in convergence of flow into valleys. Solid lines with arrows show flow paths and dashed lines indicate equal hydraulic head, h (Eq. 1.6). Adapted from Tóth (1962), after Hubbert (1940).

Fluid pressure gradients can also arise through stress related changes in the porosity such as in compaction or contraction and dilation (Brace et al., 1966; Connolly and Podladchikov, 2004; Deming, 1994; Sibson, 1996; Zhang et al., 1994). Tectonic dilatancy has been invoked as a mechanism for downward penetration of fluids into the ductile deformational regime (McCaig, 1988; Upton et al., 1995). Density variations that may drive or modify flow can arise as a result of spatial variations in temperature or in the amount of dissolved chemical species within water (Diersch and Kolditz, 2002).

As water density is a function of temperature, pressure and solute concentration, and water viscosity is a function of temperature and solute concentration, it can be convenient to consider a

reference density, ρ_0 and viscosity μ_0 under specified conditions, such as surface temperature and atmospheric pressure, with negligible solute. Fluid pressure is commonly represented in terms of a hydraulic head, h, the elevation of hydrostatic column of water of density, ρ_0 that the pressure would support:

$$h = \frac{p}{\rho_0 g} + z \tag{1.6}$$

Where z is the elevation relative to a reference datum, such as sea level.

Darcy's Law may be expressed in terms of hydraulic head and hydraulic conductivity, K, a parameter that describes both the permeability and the properties of the fluid flowing. In this case it takes the form:

$$\boldsymbol{q} = -\boldsymbol{K}\frac{\mu_0}{\mu} \cdot \left[\nabla h + \left(\frac{\rho - \rho_0}{\rho_0}\right)\hat{\boldsymbol{n}}\right] \tag{1.7}$$

$$\boldsymbol{K} = \frac{\boldsymbol{k}\rho_0 g}{\mu_0} \tag{1.8}$$

Where $\boldsymbol{K}$ is defined as the hydraulic conductivity tensor.

Where fluid properties can be assumed to be homogeneous Eq. 1.7 simplifies to:

$$\boldsymbol{q} = -\boldsymbol{K} \cdot \nabla h \tag{1.9}$$

1.2.2 Fluid pressure and rheological regimes

Observations from boreholes with depths of up 12.2 km show fluid pressures that vary about hydrostatic pressure in the brittle crust (Townend and Zoback 2000 and references therin). In contrast, experimental phase equilibria, the presence of veins formed through tensile fracture and predicted increases in water volume with temperature suggest that deeper in the lithosphere, during metamorphism, pore fluid pressures are near-lithostatic (Etheridge et al., 1983; Fyfe et al., 1978; Norris and Henley, 1976; Yardley, 2009). The transition between these two fluid pressure regimes occurs near to the brittle-ductile transition zone (Coombs, 1993; Manning and Ingebritsen, 1999), a region across which significant changes in rock strength and rheological behaviour occur (Fig. 1.3).

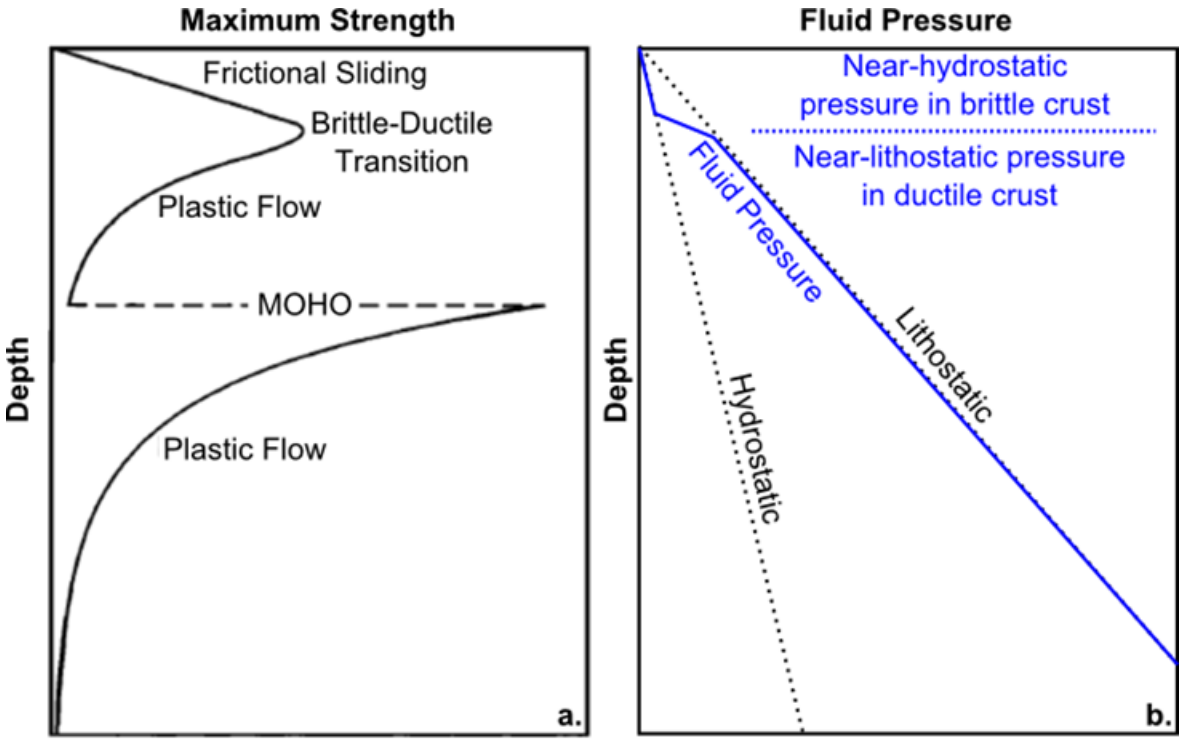

Figure 1.3 Illustration of typical strength and fluid pressure profiles inferred for continental lithosphere and the transition from near-hydrostatic fluid pressures observed in boreholes to near-lithostatic conditions, which are common during metamorphism. This transition is inferred to correspond to the onset of plastic (ductile) deformation. Adapted from Kohlstedt et al. (1995).

The Mohr-Coulomb failure criterion for frictional sliding and brittle failure is:

$$\tau = C_\tau + \mu_\tau(\sigma_n - p) \tag{1.10}$$

Where τ is the critical shear stress for failure (shear strength, i.e. the shear stress under which for brittle failure occurs), C_τ is cohesion, μ_τ is the coefficient of friction, σ_n is the confining stress and p is the pore fluid pressure. Byerlee (1968; 1978) related the following empirical forms of Eq. 1.10 to strength in the brittle crust:

$$\tau = 0.85\sigma_n \qquad \begin{matrix}\sigma_n < 200\ MPa \\ Depth < {\sim}8\ km\end{matrix} \tag{1.11}$$

$$\tau = 0.5 + 0.6\sigma_n \qquad \begin{matrix}200\ MPa < \sigma_n < 2000\ MPa \\ {\sim}8\ km < Depth < {\sim}80\ km\end{matrix} \tag{1.12}$$

In situ stress measurements indicate that these equations describe the stress state of the upper brittle crust well (Townend and Zoback, 2000). Thus, as normal stress increases with depth, the shear strength according to this relation increases. Shear strength with respect to plastic deformation mechanisms decreases with depth as a function of temperature, eventually becoming lower than the shear strength with respect to Mohr-Coulomb failure, at which point there is a transition from brittle to ductile deformation (Brace and Kohlstedt, 1980). As the onset

of ductile deformation occurs at different temperatures in different minerals, crustal rheological regime does not change at a discrete depth, but rather the change occurs across a brittle-ductile transition zone (Kohlstedt et al., 1995). The result of the different relationships of brittle and ductile deformation to temperature and pressure is that crustal strength increases up to the brittle-ductile transition zone (Fig. 1.3), below which it decreases rapidly (Kohlstedt et al., 1995; Sibson, 1983). In weaker ductile rocks, porosity collapses around fluid in pores, increasing fluid pressure to near lithostatic pressure (Ague, 2003).

1.2.3 Permeability

Permeability (k) is a measure of the ability of a porous material to allow fluids to pass through it (Bear, 1972) and a key parameter for controlling fluid flow rates (Manning and Ingebritsen, 1999). The permeability of natural systems can vary by numerous orders of magnitude (Bear, 1972; Clauser, 1992; Manning and Ingebritsen, 1999). Methods of permeability estimation differ in the scale over which they sample. Laboratory estimates of permeability, which may be obtained by pumping fluid through a sample (e.g. Carpenter et al. 2014) generally investigate samples with length scales <1 m (Clauser, 1992; Manning and Ingebritsen, 1999). Permeability may be estimated at length scales of one to hundreds of meters through testing in boreholes, using methods such as slug tests (e.g. Bouwer and Rice 1976; Hvorslev 1951), pumping tests (e.g. Theis, 1935; Thiem, 1906), packer tests (e.g. Houlsby, 1976) and tracer tests (e.g. Garabedian and Leblanc, 1991; Hess et al., 1992; Leblanc et al., 1991). Methods that estimate permeability over length scales of hundreds of meters to tens of kilometres include modelling of groundwater discharge data (e.g. Saar and Manga 2004), studies of microseismicity (e.g. Shapiro et al. 2015), and modelling geothermal data (e.g. Manning and Ingebritsen 1999 and references therein). Time-integrated fluid fluxes can be calculated based on metamorphic mineral assemblages (Bickle, 1992; Dipple and Ferry, 1992). These fluxes can be used to estimate regional-scale permeability in flow regimes involved in metamorphism and mineralisation and which occur at depths in the crust too deep for direct observations (Manning and Ingebritsen 1999 and references therein).

Compilations of permeability estimates show a relationship between the scale of measurement and the values obtained, which are reduced with decreasing scale of measurement (e.g. Brace 1984; Brace and Kohlstedt 1980; Clauser 1992). This is because, where the scale of sampling is small, the investigated volume may not be representative of the medium (Bear, 1972; Clauser, 1992). For example, laboratory tests are normally carried out on mechanically sound rocks, lacking fractures that may act as important pathways for flow (Manning and Ingebritsen, 1999). Measurements at scales above ~100 m do not show a clear scale dependence (Clauser, 1992). It

has been argued that the permeability is not scale dependent if suitable efforts are made to ensure that the sampled volume is representative (Ingebritsen and Manning, 1999).

Manning and Ingebritsen (1999) compiled permeability data based on geothermal and metamorphic studies, on which basis they proposed a permeability-depth relationship of:

$$\log k = -14 - 3.2 \log z_{km} \tag{1.13}$$

Where z_{km} is depth in kilometres. Subsequent studies of permeability variation with depth over large length scales based on in situ measurements and seismicity (Achtziger-Zupančič et al., 2017; Ingebritsen and Manning, 2010; Saar and Manga, 2004; Stober and Bucher, 2015, 2007; Townend and Zoback, 2000) and on laboratory experiments investigating crustal-scale permeability (Shmonov et al., 2003) are compatible with this relationship. The relation in Eq. 1.13 gives a rapid decrease in permeability with depth above ~12.5 km, with near constant permeability below. An assumption of a constant permeability of $10^{-18.3}$ m^2 below this depth gives an equally good fit to compiled permeability data (Fig. 1.4) (Ingebritsen and Manning, 2002). The depth interval over which the transition to near constant permeability takes place corresponds approximately to the depth of the brittle-ductile transition, although this varies between different geological settings (Ingebritsen and Manning, 2002; Manning and Ingebritsen, 1999).

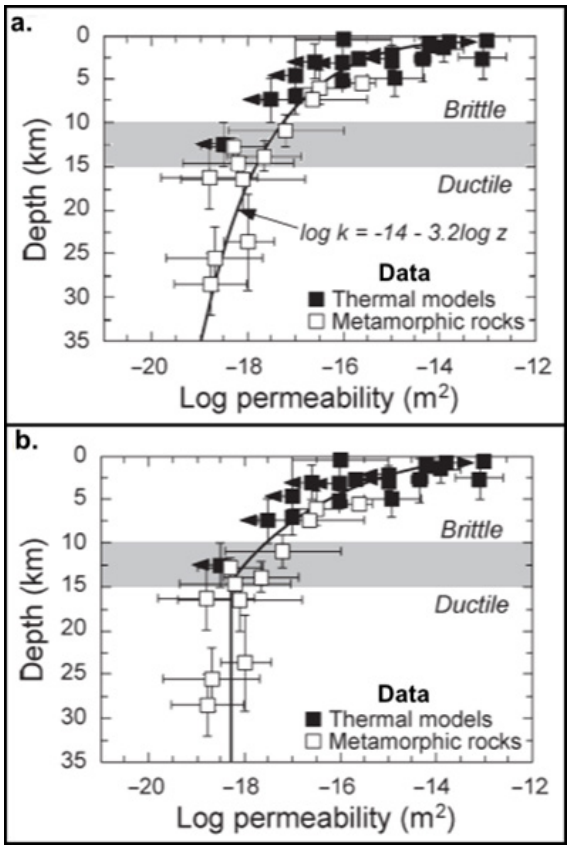

Figure 1.4 a. The permeability-depth relation of Manning and Ingebritsen (1999). b. A similar relationship assuming constant permeability of $10^{-18.3}$ m^2 below 12.5 km depth (Ingebritsen and Manning, 2002). Adapted from (Ingebritsen and Manning, 2010).

The permeability-depth relation of Manning and Ingebritsen (1999) represents a spatial and temporal average and is based on a dataset that purposefully omits data from fault and shear zones (Ingebritsen and Manning, 2010). Permeability in crustal rocks varies significantly from these averages as a result of differing rock type (Domenico and Schwartz, 1990; Freeze and Cherry, 1979). Permeability differences between rock types are greatest in the near-surface (Manning and Ingebritsen, 1999). The highest permeabilities in sediments and sedimentary rocks are associated with gravels and karst limestones, with permeability generally decreasing in rocks where finer clasts or grains are present (Fig. 1.5). Amongst igneous and metamorphic rocks, basalts commonly have the highest permeabilities and the degree of fracturing has an important influence (Fig. 1.5).

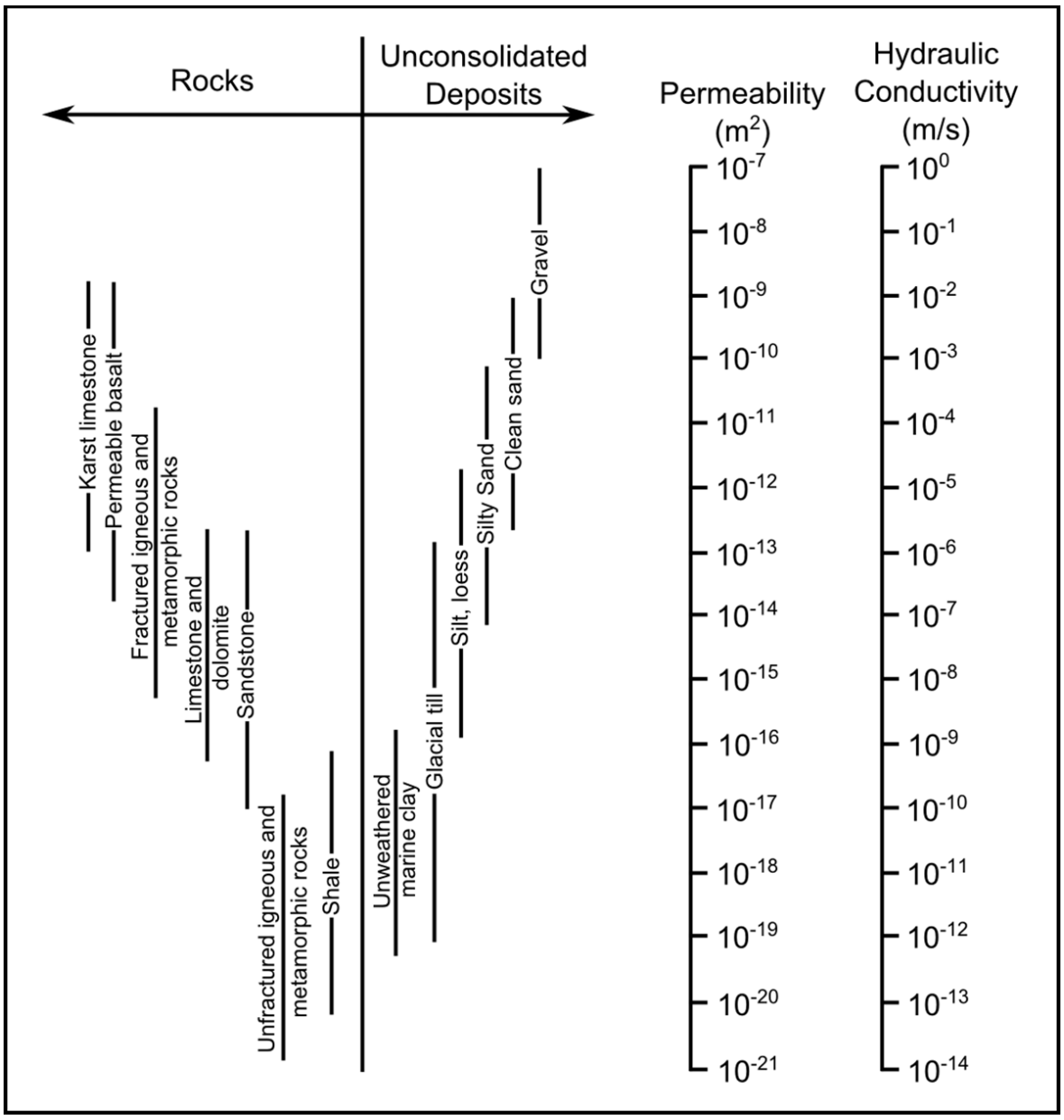

Figure 1.5 Typical permeability, k and hydraulic conductivity, K ranges for a selection of rock types and sediments. Adapted from Freeze and Cherry (1979).

Measured permeability values and modelling of geothermal data in mountain belts suggest that stress state can have a significant influence on permeability (Morin, 2002; Upton and Sutherland, 2014). Stress fields vary with topographic relief, which is commonly of the order of kilometres in orogenic mountain belts. Valleys act to concentrate far-field compressional tectonic stress in these regions, while it is reduced and may be reversed at ridges (Savage and Swolfs, 1986; Savage et al., 1985). These stress variations can affect permeability by influencing the proximity to failure of rocks and the orientation of structures along which failure occurs (Koons and Kirby, 2007; Miller and Dunne, 1996).

Permeabilities in fault and shear zones are typically higher than those away from them (Ingebritsen and Manning, 2010). High permeabilities in some fault zones may play an important role in facilitating fluid circulation in the brittle crust and maintaining near-hydrostatic fluid pressures (Townend and Zoback, 2000). However, fault zone architectures suggest that as well as acting as conduits for fluid flow, faults may also act as barriers to fluid flow or combined conduit-barrier systems (Fig. 1.6) (Caine et al., 1996).

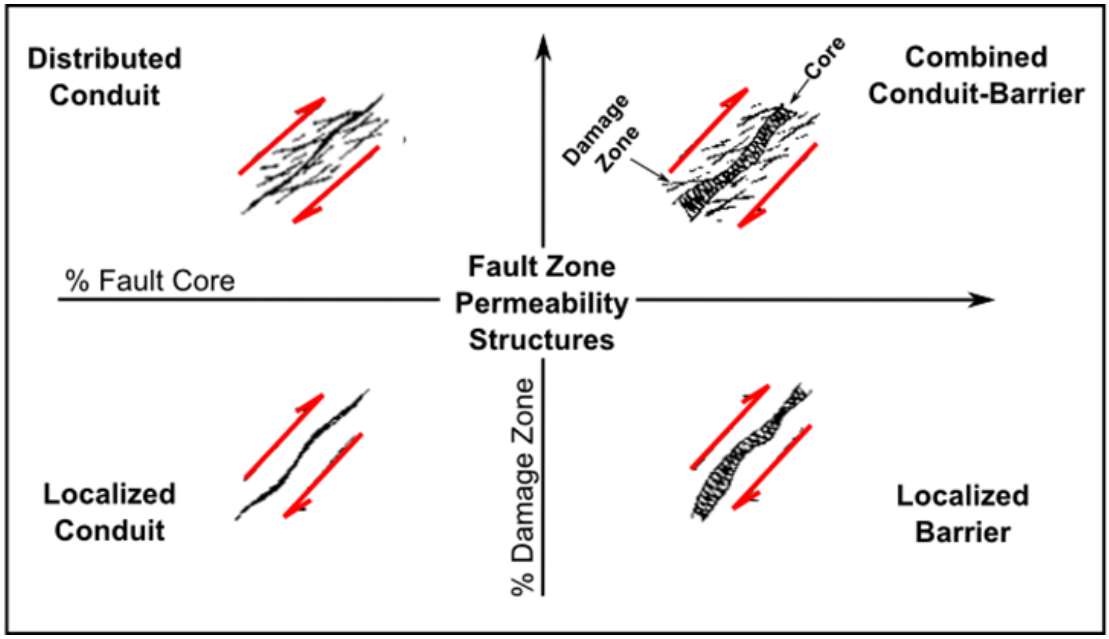

Figure 1.6 Illustrations of possible fault zone permeability architectures, with increasing fault core material acting to reduce permeability and fault damage acting to increase it. Adapted from Caine et al. (1996).

Fault zones are typically divided into a high strain fault core, which accommodates the majority of displacement and a fractured damage zone, where strain is lower (Bense et al., 2013; Caine et al., 1996; Faulkner et al., 2010). It has been hypothesised that fault cores, which are commonly dominated by gouge and fault breccia, have low permeabilities as a result of secondary mineral formation and grain size reduction, whereas damage zones have increased permeability above

that of their original protolith, as a result of fracturing (Caine et al., 1996). This is supported by studies of fault rocks both in situ and in laboratory tests (e.g. Balsamo and Storti, 2010; Doan et al., 2006; Lockner et al., 2009; Micarelli et al., 2006). Fault zone permeability structures can be significantly more complex where fault rocks have differing protoliths, as this can result in significant permeability contrasts superimposed on the fault core-damage zone architecture (Wibberley and Shimamoto, 2003). In damage zones, microfracture densities typically decrease exponentially with distance from a fault, meaning that the highest damage zone permeabilities are typically closest to the fault (Mitchell and Faulkner, 2009, 2012). Simulations of faulting in laboratory studies have also reproduced a low permeability fault core and high permeability damage zone fault architecture (Evans et al., 1997). The relative extents of the fault core and damage zones, as well as the degree of permeability anisotropy within these zones control the influence that a fault has on fluid flow (Caine et al., 1996; Lopez and Smith, 1996).

Temporal variations in permeability may result from changes in stress state (e.g. Germanovich and Lowell, 1992; Manga et al., 2012; Upton and Sutherland, 2014), from permeability generation by fracturing and from permeability reduction as a result of secondary mineral formation or compaction (Aydin and Johnson, 1978; Ingebritsen and Manning, 2010; Rojstaczer et al., 2008; Sibson, 1996). These temporal changes may be particularly significant in fault zones, where permeability reduction associated with fluid flow has the potential to increase fluid pressures and induce fault failure, with the resulting damage returning permeability to higher values (Sibson, 1990). Episodes of permeability generation through fracturing may be important in allowing release of lithostatically pressured fluids from the ductile crust into the brittle crust. Norris and Henley (1976) demonstrated how fluids in rocks that are being uplifted may increase in volume along part of their p-T exhumation path (Fig. 1.7), resulting in elevated permeability as a result of hydrofracturing, which can facilitate flow into the hydrostatically pressured regime above.

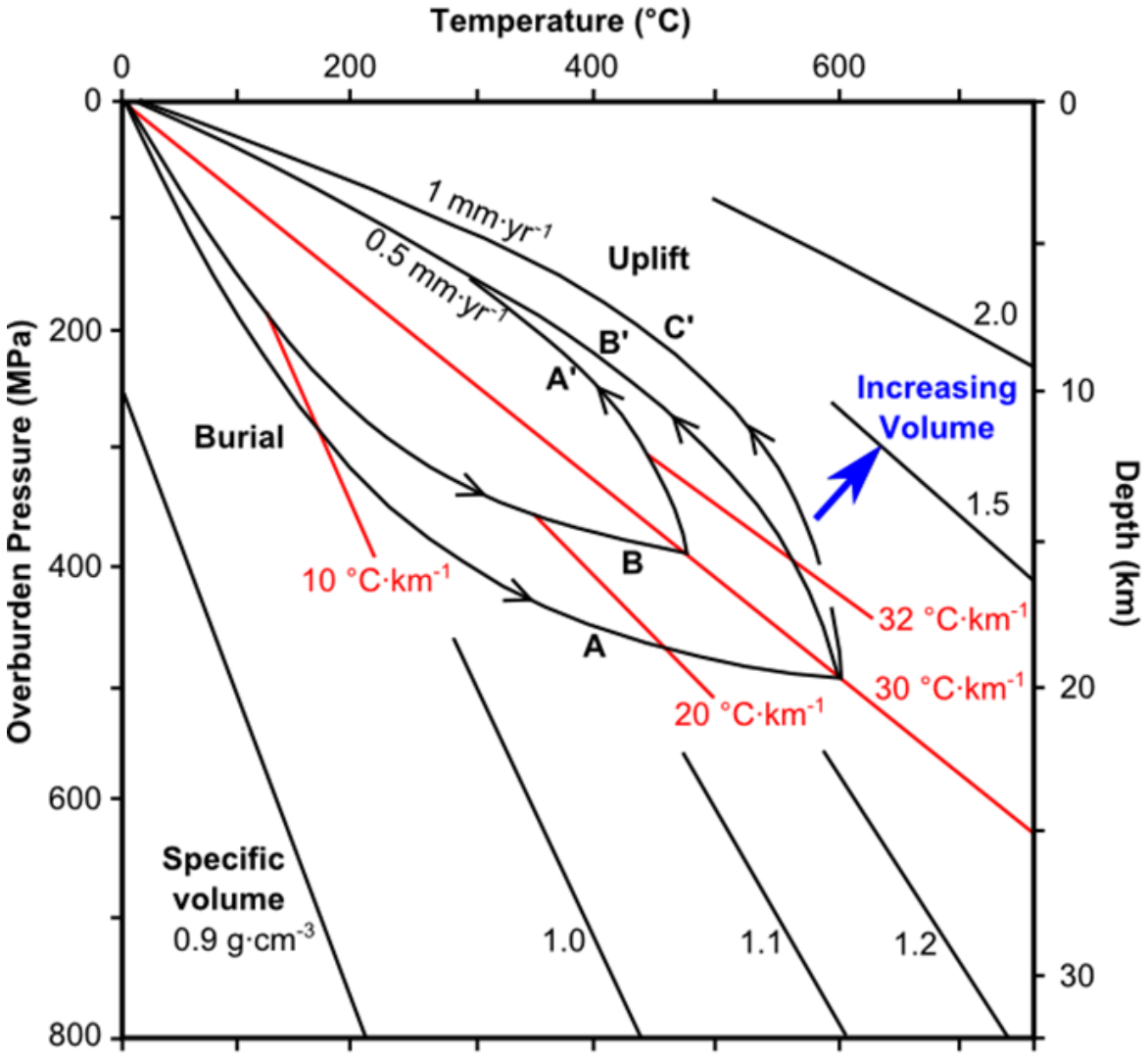

Figure 1.7 Model p-T paths for burial to 16 km and 20 km depth, followed by uplift at 0.5 mm·yr^{-1} (A and B) and 1 mm·yr^{-1} (C). These trajectories result in increasing specific volume of water along sections of the uplift path, which could result in hydrofracture, thus increasing permeability. Adapted from Norris and Henley (1976).

1.2.4 The role of water in heat and mass transfer

The role of water in heat and mass transfer is of major significance for geological processes. Heat and mass transfer in a stationary porous medium may occur through fluid advection, in which the movement of a fluid also transports its heat and solute content, through diffusional processes resulting from random thermal movement at molecular or ionic level (heat conduction and molecular diffusion) and through mechanical dispersion- the spreading of heat or solute as a result of mixing during fluid advection due to inhomogeneity at a microscopic level (Allaby, 2008; Bear, 1972; Freeze and Cherry, 1979; Phillips, 2009). Mechanical dispersion does not occur in the absence of fluid flow, in contrast to diffusional processes, which do (Bear, 1972).

The transport of heat by fluid flow relative to a fixed homogeneous and isotropic porous rock phase in one dimension, z, is described by the energy balance equation (Phillips, 2009):

$$C_e \frac{\partial T}{\partial t} + C_f q \frac{\partial T}{\partial z} - C_e \kappa_d \frac{\partial^2 T}{\partial z^2} = Q_T \tag{1.14}$$

$$\kappa_d = (\kappa_e + \kappa_m) \tag{1.15}$$

Where C_e is the effective volumetric heat capacity of the bulk fluid-rock medium, C_f is the volumetric heat capacity of the fluid, T is temperature, t is time, q is the Darcy velocity in the z direction and Q_T is rate of internal heat generation per unit volume, for example as a result of radioactive decay. The thermal dispersion coefficient for the fluid-rock medium, κ_d, combines κ_e, the effective thermal diffusivity for the fluid-rock medium (which describes heat conduction) and κ_m, the mechanical thermal dispersion coefficient for the fluid-rock medium (which describes mechanical dispersion).

Transport of species dissolved in the fluid phase can also be described by a similar equation (Phillips, 2009):

$$\varphi \frac{\partial \gamma}{\partial t} + q \frac{\partial \gamma}{\partial z} - D_d \frac{\partial^2 \gamma}{\partial z^2} = Q_\gamma \tag{1.16}$$

$$D_d = (D_e + D_m) \tag{1.17}$$

Where γ is the mass concentration of the dissolved species and Q_γ is rate of internal generation of the chemical species per unit volume, for example as a result of chemical reactions. The hydrodynamic dispersion coefficient for the fluid-rock medium, D_d, combines D_e, the effective molecular diffusivity for the fluid (which describes molecular diffusion) and D_m, the mechanical dispersion coefficient for the fluid-rock medium (which describes mechanical dispersion).

D_m varies as a function of q, resulting in the dependence of D_d on flow rate (Fetter, 1999). Although mechanical dispersion may provide some contribution to κ_d, is far less significant than in solute transport, due to the high values of κ_e compared to D_e for transport by water though a rock medium (Bear, 1972), although exact quantification of this contribution is difficult, as field-scale studies are sparse (Rau et al. 2014). Both linear (e.g. Bear 1972) and square (e.g. Rau et al. 2012) relationships between q and κ_m have been proposed and values for dispersivity coefficients in these relationships, as well as their potential scale dependence are not well constrained (Anderson, 2005; Rau et al., 2014).

The Péclet number gives the ratio of the rate of advective transport to the rate of diffusive transport (Bear, 1972). In the case of (1.14) and (1.16), Péclet numbers are:

$$P_T = \frac{C_f L q}{C_e \kappa_e} \tag{1.18}$$

$$P_\gamma = \frac{Lq_z}{D_e} \tag{1.19}$$

Where P_T is the thermal Péclet number, P_γ is the Peclet number for solute transport and L is the length scale for transport. Because diffusive coefficients for heat transport are larger than those for solute transport, Péclet number becomes large and advection dominates transport at lower Darcy velocities for solute transport than for heat transport (Fig. 1.8) (Bickle and McKenzie, 1987). As Péclet number is proportional to length scale, greater transport distances are associated with increasingly significant advective transport.

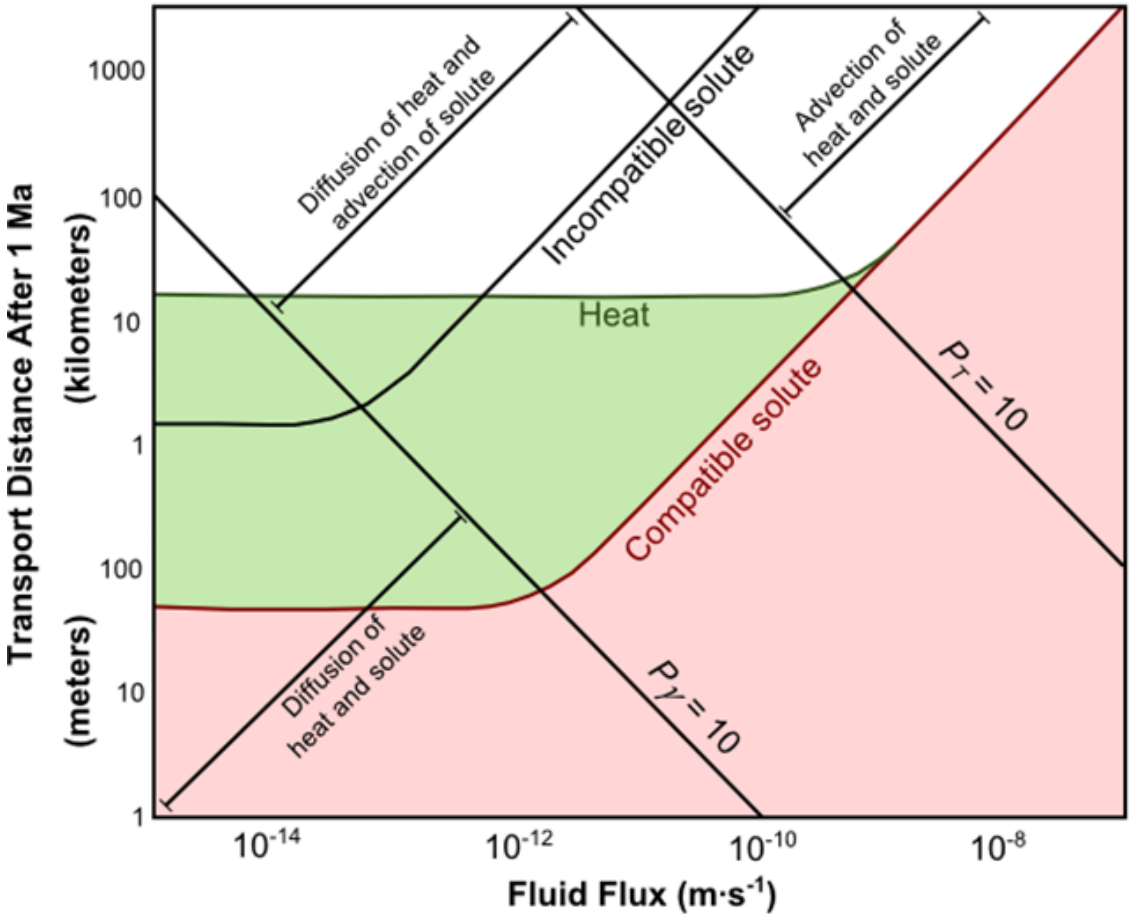

Figure 1.8 Model transport distances for heat and solute (compatible and incompatible) after 1 Ma. Fluid flow dominates mass transport ($P_\gamma \geq 10$) at lower Darcy velocities than for heat flow. Adapted from Bickle and McKenzie (1987).

The rapid advective transport of mass by fluid flow relative to diffusive transport facilitates chemical transfer on regional scales, producing infiltration metasomatism, in which bulk rock compositions are altered (Bickle and McKenzie, 1987; Ferry and Dipple, 1991; Putnis and Austrheim, 2010). This includes the generation of ore deposits through the concentration of metals (Craw et al., 2002; Groves et al., 1998). However, fluids can also play important roles in isochemical metamorphism, in which transport distances are significantly smaller, by reducing

chemical reaction activation energies by ~10 orders of magnitude (Putnis and Austrheim, 2010). In addition to transporting other chemical species, water is also a reactant and product of metamorphic reactions, with water generally released during prograde metamorphism and reacting with rocks on retrograde paths to form hydrous minerals (Yardley, 2009). Evidence from a range of studies of metamorphism and metasomatism indicates significant infiltration of water in ancient orogens in order to produce observed mineral assemblages and compositions (Ague, 2003; Ferry, 1994; Ferry et al., 2013), textures (e.g. John et al. 2008), zoning (e.g. Yardley et al. 1991), isotope ratios (e.g. Zheng et al. 2003) and ore deposits (Goldfarb et al., 2001).

Although heat flow in continental lithosphere is largely dominated by conduction (Stein, 1995), thermal data from many borehole studies indicate a significant role for heat advection by groundwater in some regions (e.g. Brott et al. 1981; Lachenbruch et al. 1976, Van Orstrand 1934). In the Himalaya-Tibet orogen, thermochronometric age distributions, along with elevated surface heat fluxes and steepened shallow geothermal gradients associated with hot springs, suggest significant heat advection and modification of local geothermal structure by groundwater circulation (Derry et al., 2009; Shankar et al., 1991; Whipp and Ehlers, 2007). Examples of high heat fluxes associated with fluid flow have also been indicated by studies of other present day mountainous regions such as the European Alps and the Grand Mesa, USA (Dzikowski et al., 2016; Lazear, 2006). Numerical models for mountainous topography indicate that permeability is a key control in determining whether thermal structure in mountain belts is perturbed by groundwater flow (Forster and Smith, 1989) but knowledge of crustal permeability structures remains poor. Evidence of perturbation of thermal structure also exists in rocks from ancient orogenic belts. Short durations of peak metamorphism in Barrovian rocks of north-east Scotland are inconsistent with the longer timescales predicted by thermal orogenic models (e.g. Thompson and England 1984) and are interpreted as resulting from pulses of heat advection by fluid flow (Ague and Baxter, 2007). Similar timing of peak metamorphism across metamorphic grades in the Wepwaug Schist in Connecticut is also interpreted as resulting from the redistribution of heat by fluid flow (Lancaster et al., 2008). Therefore, there is abundant evidence for fluid flow having an impact on both mass and heat transfer in orogenic belts.

1.2.5 The role of water in deformation

As evident in the Mohr-Coulomb failure criterion (Eq. 1.10), a key role of fluids in brittle failure is to reduce effective confining stress through increasing pore fluid pressure, p, which consequently decreases the critical shear stress for failure (shear strength, τ). Fluids may influence temperature-dependent ductile deformation by advecting heat and by aiding mass transfer (Kohlstedt et al., 1995). Therefore fluids have considerable influence on crustal strength profiles,

with the presence of significant amounts of fluids having the effect of shallowing the depth of onset of ductile processes and weakening rocks at depth (Yardley, 2009).

At individual faults in an orogenic belt, the role of fluids in brittle failure on faults with the potential to generate earthquakes is of particular interest. As changes in fluid pressure modify fault frictional strength, they may influence whether a fault is weak enough to fail and therefore when failure occurs (Hubbert and Rubey, 1959). Fluid facilitated mineral precipitation may result in porosity and permeability reduction, resulting in local elevation of pore fluid pressures and promoting failure in fault zones (Blanpied et al., 1992; Byerlee, 1993; Sibson, 1992). In altering the mineralogy and temperature of fault rocks, fluid flow will also modify the frictional properties of the fault rocks themselves, which are dependent on both temperature and composition (Kohlstedt et al., 1995). The coefficient of friction of fault rocks influences not only whether a fault is weak enough to fail, but also how it fails. For a fault to slip seismically, producing earthquakes, rather than creeping aseismically, the materials of the fault zone must be *velocity weakening*, meaning that fault strength must decrease with increased fault slip velocity (Scholz, 1998). Whether a fault is velocity weakening or not is thought to be largely dependent on changes in fault friction with increased fault velocity (Segall and Rice, 2006). Velocity weakening behaviour in geological material only occurs over a limited temperature range, with stable slip at low temperatures and above ~300 °C, the approximate temperature at which ductile deformation of quartz commences in quartzofeldspathic rocks (Scholz, 1998). Although the influence of mineralogy on velocity weakening behaviour is complex, with different mineral phases showing differing behaviour depending on slip rate, phyllosilicate minerals tend to be associated with velocity strengthening behaviour and may therefore promote stable creep (Faulkner et al., 2003, 2010). The response of fault strength to slip can also be influenced by changes in pore fluid pressure as the fault moves (Segall and Rice, 2006). Thermal pressurisation, in which frictional heating and expansion of fluids during fault movement reduces the effective confining pressure on the fault as it moves, may contribute to velocity weakening behaviour (Blanpied et al., 1992; Sibson, 1973; Wibberley and Shimamoto, 2005). Thus, fluids may influence not only if and when a fault fails, but also its behaviour during failure through the transport of heat and mass and changes in pore fluid pressures.

1.3 Geological setting of the Southern Alps of New Zealand

1.3.1 Regional tectonic setting

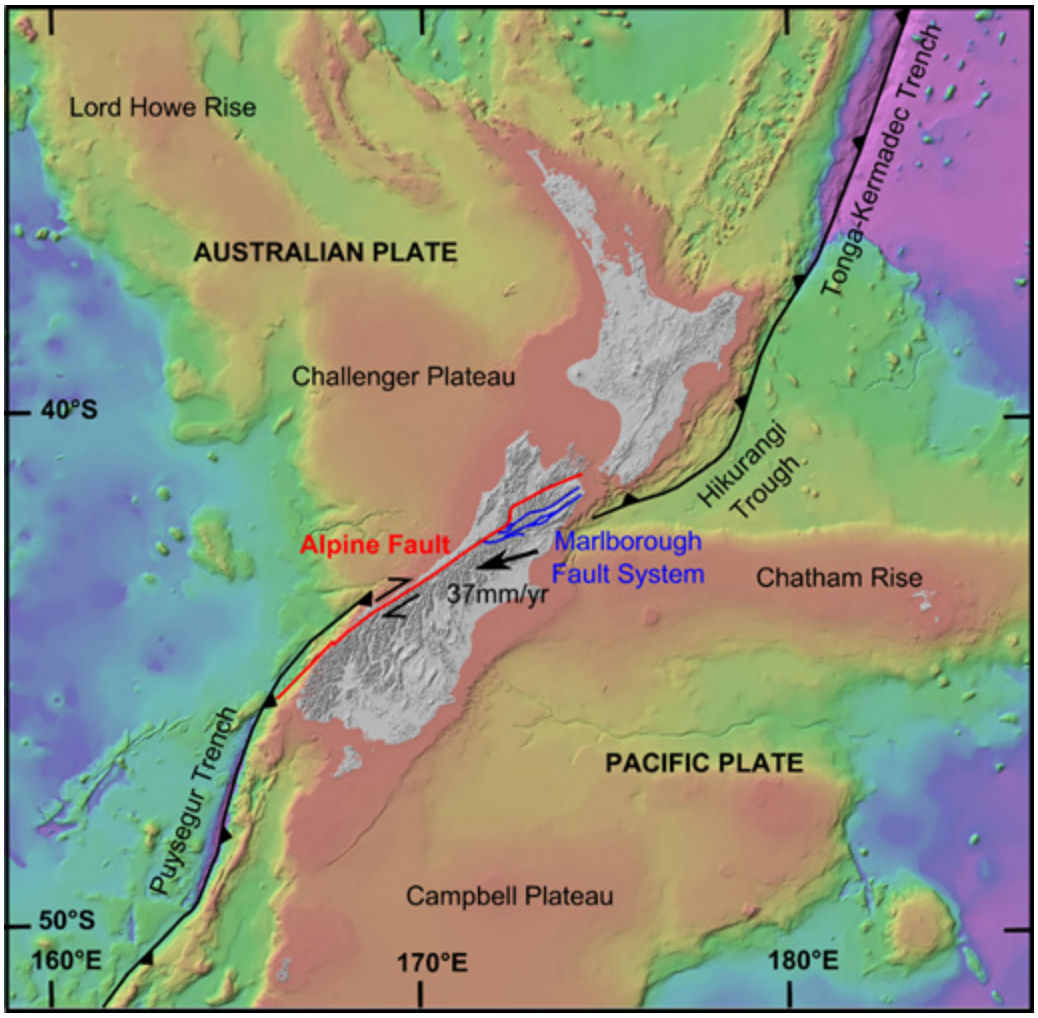

Figure 1.9 The plate tectonic setting of the Alpine Fault, New Zealand with the plate vector (DeMets et al., 1994) of the Pacific Plate relative to the Australian Plate shown. Bathymetic image from National Institute of Water and Atmospheric Research (2008).

New Zealand straddles the boundary between the Pacific and Australian plates (Fig. 1.9). The Alpine Fault is the active plate-bounding fault running through the South Island, accommodating right lateral oblique transpressional motion between these plates (Okaya et al., 2007). In the north, the Pacific plate is being subducted to the north-west beneath the Australian plate at the Hikurangi Subduction Zone, whereas to the south of South Island the Pacific plate overrides the Australian plate at the south-easterly dipping Puysegur Subduction Zone (Sutherland et al., 2006). Displacement on the Alpine Fault has offset the basement rocks that form the spine of New Zealand by 480 km as well as uplifting rocks of the Pacific plate to form the Southern Alps (Benson, 1952; Cox and Sutherland, 2007).

1.3.2 Geological history and stratigraphic units

The basement rocks of New Zealand consist of a number of terranes (Fig. 1.10), formed during convergence at the continental margin of Gondwana. These terranes are grouped together into the Western and Eastern Provinces but collectively known as the Austral Superprovince (Mortimer et al., 2014). All basement rocks have experienced varying degrees of deformation and metamorphism since their development, with fabrics and assemblages exhumed and modified during Cenozoic orogenic uplift (See section 1.4.3). Overlying Cretaceous to Recent cover sediments and igneous rocks, which postdate the accretion and assembly of the basement terranes are termed the Zealandia Megasequence (Mortimer et al., 2014).

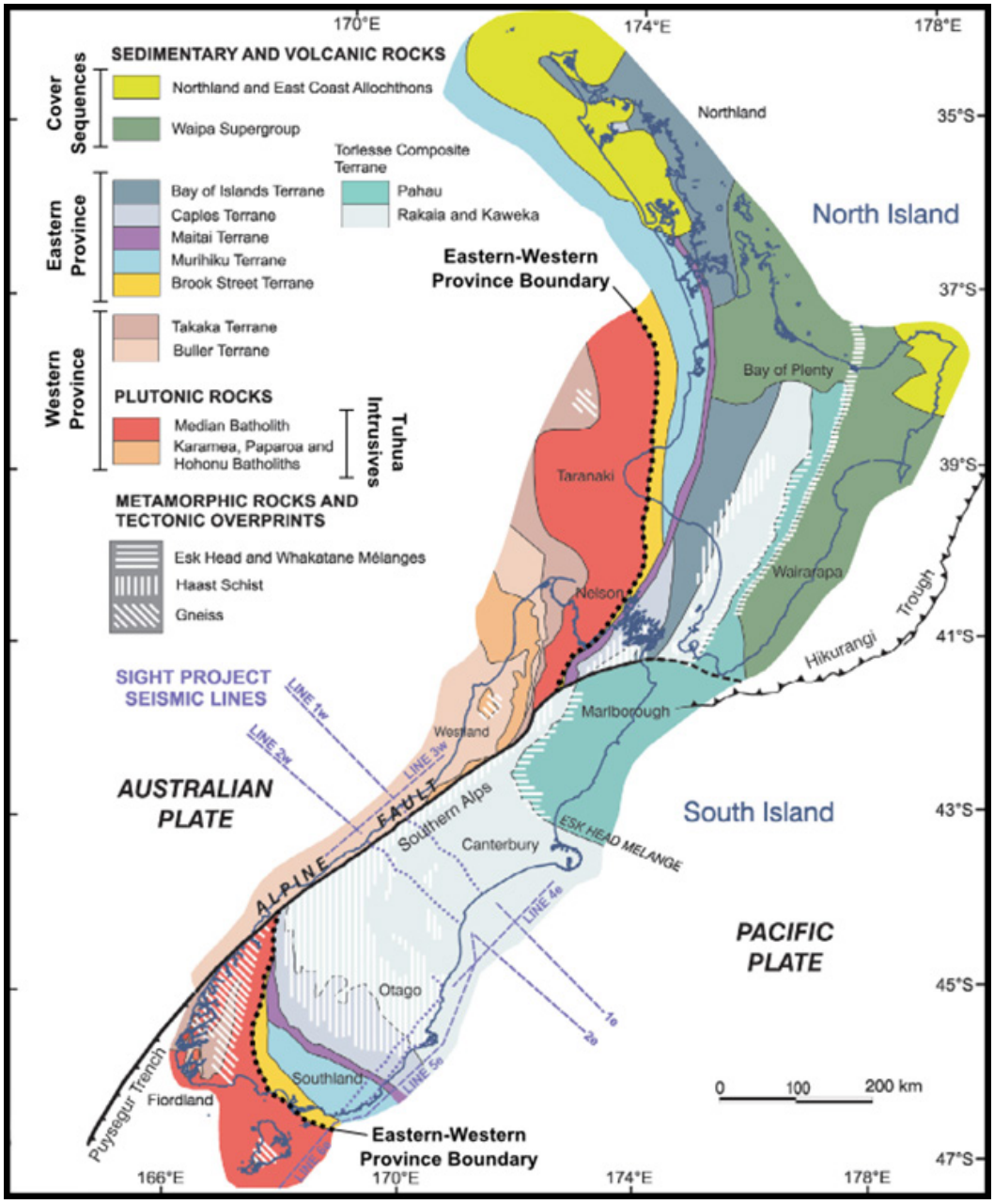

Figure 1.10 The major stratigraphic units of New Zealand. Adapted from Cox and Sutherland (2007).

The Western Province rocks formed in island arc and passive margin settings between the middle Cambrian (ca. 509 Ma) and the early Cretaceous (ca. 110 Ma) (Fig. 1.11) (Mortimer, 2004; Mortimer et al., 2014). The most westerly unit is the Buller Terrane, which is formed of continent-derived turbidite sandstones and black shales and is inferred to have been deposited in submarine fans and slope basins on the continental margin of Gondwana (Cooper, 1989). The Takaka Terrane comprises a Cambrian sedimentary succession rich in volcanic content, thought to have been deposited in close proximity to an island arc, which is overlain by Ordovician to Silurian carbonate and siliciclastic sediments, reflecting a transition to passive margin sedimentation (Cooper, 1989; Mortimer, 2004). The Tuhua Intrusives are a group of batholiths and other igneous suites within the Western Province (Mortimer et al., 2014). The group includes the Median Batholith, a subduction related composite cordilleran batholith, which forms the boundary with the Eastern Province (Mortimer et al., 1999).

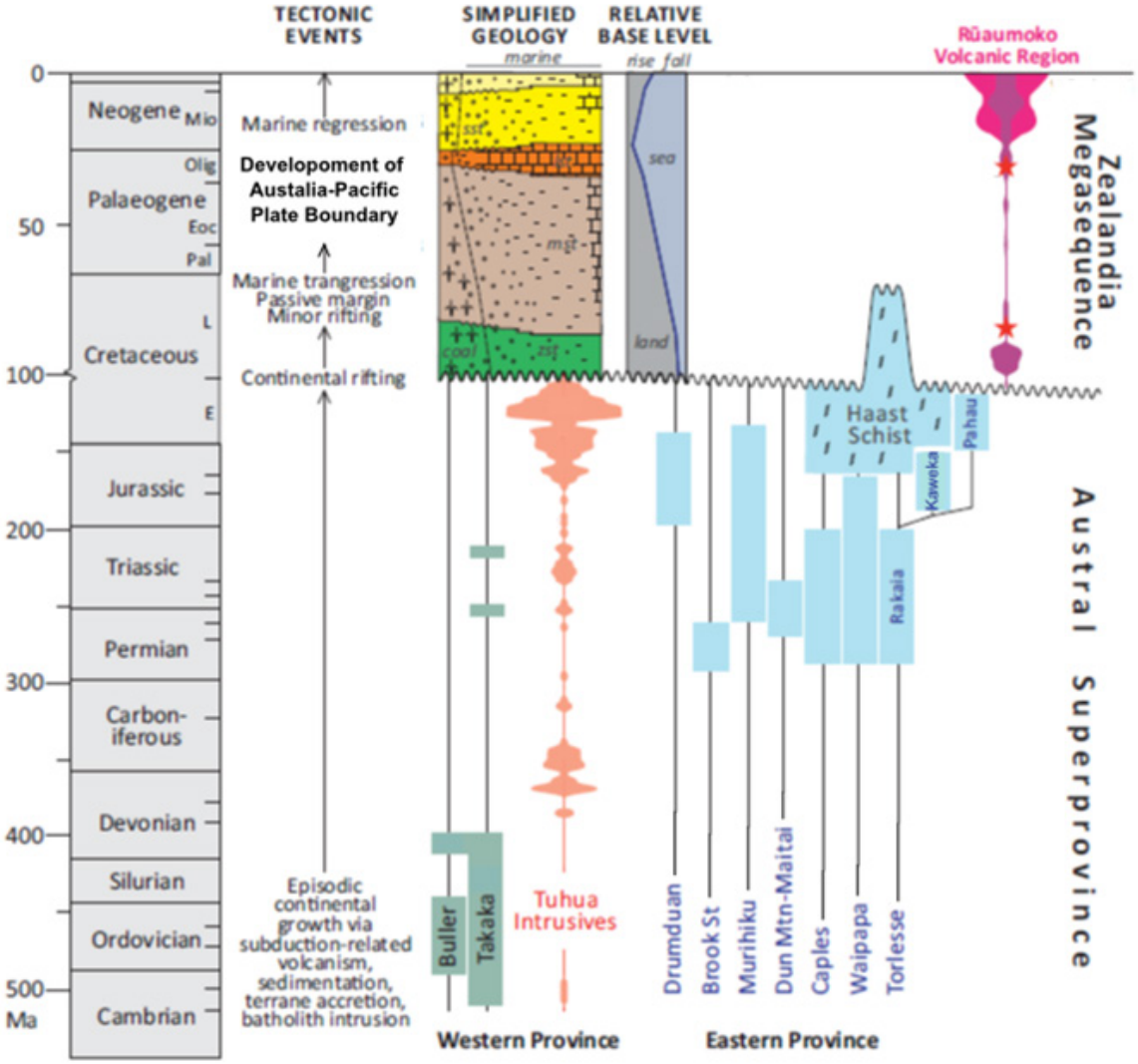

Figure 1.11 Ages of New Zealand terranes, with summarised tectonic history. Adapted from Mortimer et al. (2014).

The terranes of the Eastern Province are early Permian (ca. 292 Ma) to middle Cretaceous (ca. 100 Ma) in age (Fig. 1.11) (Cawood et al., 1999; Kamp, 2000; Mortimer, 2004; Mortimer et al., 1999, 2014). The Drumduan Terrane is formed from sediments produced by arc volcanism and lies between the Median Batholith and the Brook Street Terrane (Bradshaw, 1993). The Brook Street Terrane comprises predominantly ankaramitic and basaltic intrusives, together with basaltic to andesitic volcanic rocks and volcaniclastic sediments, interpreted to have formed in an intra oceanic island arc (Houghton and Landis, 1989; Spandler et al., 2005). Clastic and volcanoclastic sediments, with minor andesitic tuffs, ignimbrite rocks and intrusives in the neighbouring Murihiku Terrane are thought to have been formed in a forearc or backarc basin (Coombs et al., 1992; Noda et al., 2004; Roser et al., 2002). The Dun Mountain-Maitai Terrane consists of the partially serpentinised Dun Mountain Ophiolite Belt, with ophiolite derived and volcaniclasic sediments unconformably overlying it (Coombs et al., 1976; Howell, 1980; Mortimer, 2004; Mortimer et al., 2014). The Caples, Waipapa and Torlesse Terranes of the Eastern Province are interpreted to have been deposited in oceanic trench and turbidite fan settings before being juxtaposed in an accretionary prism (Fig. 1.12), adjacent to the island arc system (Gray and Foster, 2004; Mortimer, 2004; Pickard et al., 2000). These terranes are dominated by greywackes, which contain abundant volcanic material in the Caples and Waipapa Terranes but are predominantly quartzofeldspathic in the Torlesse Terrane (Adams et al., 2009a, 2009b; Mortimer and Roser, 1992). The Torlesse Terrane is commonly sub-divided into three further sub-terranes- the Rakaia, Kaweka and Pahau (Mortimer et al., 2014).

The basement terranes of New Zealand were accreted together by ca. 110 Ma (Mortimer, 2004). The mid Cretaceous (110-85 Ma) was marked by an end to convergence at the Gondwana margin and the onset of rifting (Bradshaw, 1989; Cox and Sutherland, 2007). During this time, deposition of cover sequences, which lack the deformation present in basement rocks, began (Adams et al., 2013; Mortimer, 2004). Generation of new crust at ridges in the Tasman Sea and Southern Ocean initiated before 83 Ma, ceasing at the former by 52 Ma, but continuing at the latter until the present day (Fig. 1.13) (Cox and Sutherland, 2007). During the Eocene-Miocene (38-23 Ma) the Pacific-Australian plate boundary developed (Carter and Norris, 1976; Cooper et al., 1987; Cox and Sutherland, 2007; Kamp, 1986; Molnar et al., 1975). Sea floor spreading began to the south of New Zealand around 40-38 Ma (Wood et al., 1996). Initially New Zealand experienced only diffuse continental deformation, which was transtensional in nature, as it lay close to the pole of relative plate rotation (Cande and Stock, 2004; Cox and Sutherland, 2007; Sutherland et al., 2000; Walcott, 1998).

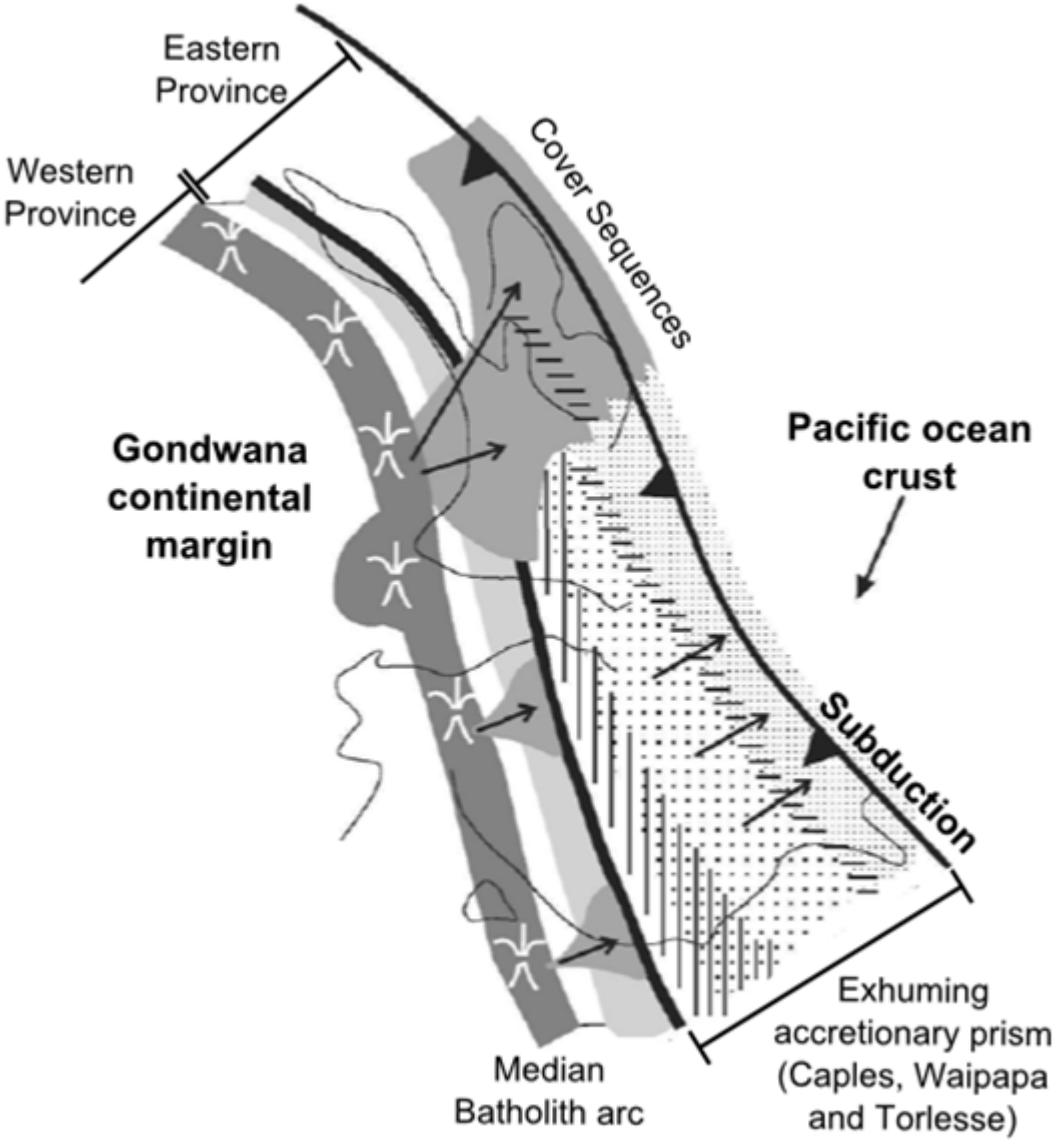

Figure 1.12 Palaeogeographic reconstruction of the possible positions of New Zealand terranes on the Gondwana margin at ca. 120 Ma, prior to the onset of rifting. Adapted from Kear and Mortimer (2003) and Mortimer (2004).

During this time passive margins formed to the east and the west of the spreading ridge (Fig. 1.13) (Sutherland et al., 2000). In the late Oligocene (29–24 Ma) the pole of rotation moved away from New Zealand to the south-east and plate motion became dominantly strike-slip (Cande and Stock, 2004; Cox and Sutherland, 2007; Sutherland, 1995; Walcott, 1998). As a result, the western passive margin was translated into the zone of continental deformation in New Zealand, where it acted as a suitably oriented discontinuity along which displacement could be accommodated, leading to the formation of the present day plate-bounding structure, the Alpine Fault (Sutherland et al., 2000). Although displacement on the Alpine Fault was initially largely strike-slip, a change in

plate vectors at ca. 6 Ma increased convergent motion, resulting in the uplift of the Southern Alps Mountain belt on the Alpine Fault (Cande and Stock, 2004; Cox and Sutherland, 2007; Sutherland, 1995; Walcott, 1998).

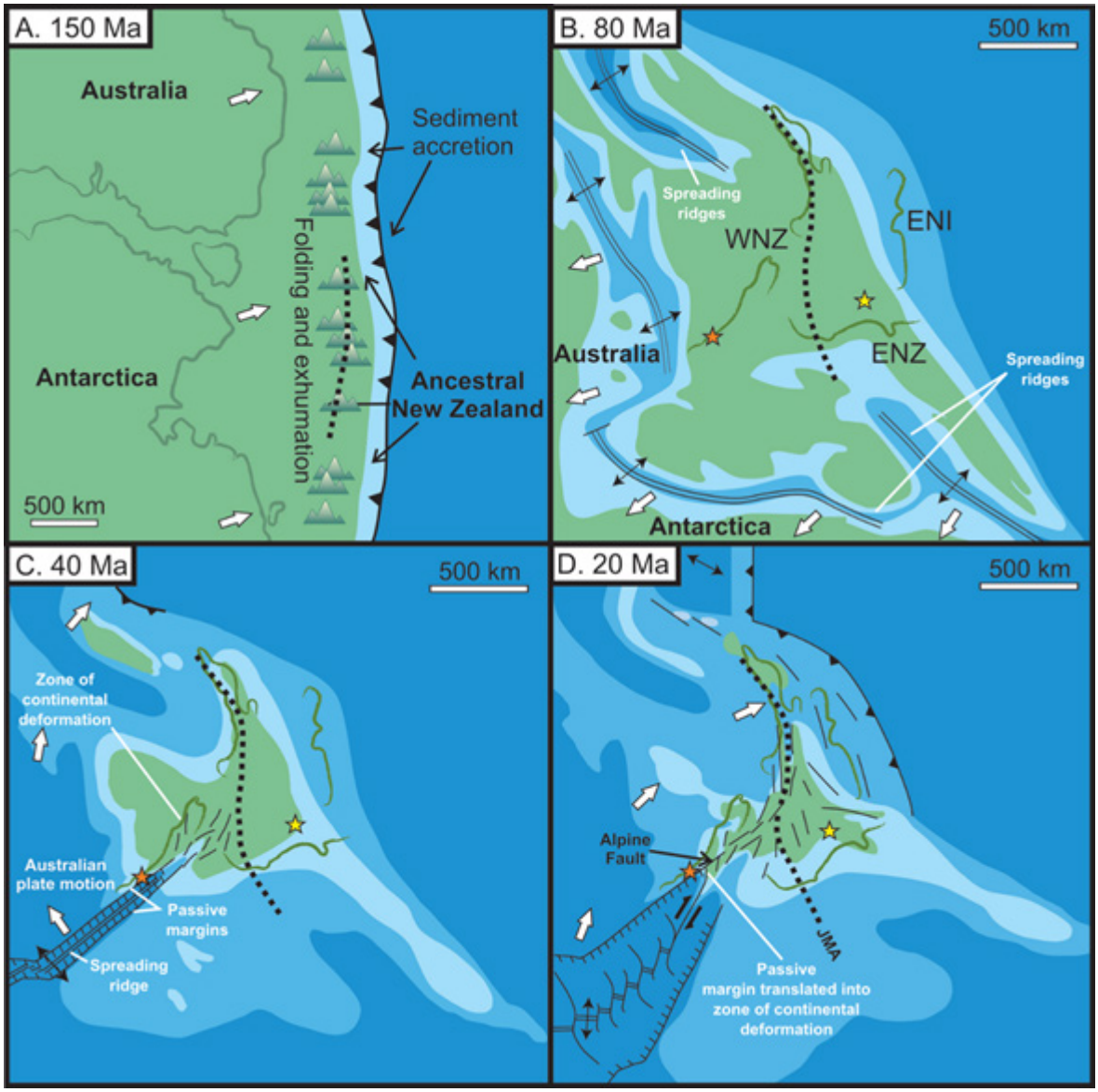

Figure 1.13 Palaeogeographic reconstruction for New Zealand between 150 Ma and 20 Ma. Stars represent points on either side of the Alpine Fault at Franz Josef (Fig. 1.17), JMA indicates the changing position of a magnetic anomaly (The Junction Magnetic Anomaly), WNZ indicates the position of the Western Province, ENZ indicates the position of Eastern Province and ENI indicates the position of Eastern North Island. Adapted from Cox and Sutherland (2007).

1.4 The Southern Alps orogen

1.4.1 The Alpine Fault

The onshore section of the Alpine Fault runs approximately parallel to the western coast of South Island for >400 km (Fig. 1.14). At Milford Sound, the fault runs offshore toward the Puysegur Subduction zone (Sutherland et al., 2006). At its northern end, the fault splays into the Marlborough Fault System, being obliquely intersected by the Hope Fault near the Taramakau River (Cox and Sutherland, 2007; Norris and Cooper, 2001). The Marlborough Fault System links the Alpine Fault with the Hikurangi subduction zone to its north (Sutherland et al., 2006) and its intersection with the Alpine Fault has migrated southwards over time (Craw et al., 2008). The extension of the fault north of Lake Rotiti is termed the Wairau Fault (Fig. 1.14), (Sutherland et al., 2007).

Aerial views of the Alpine Fault show a straight surface trace, which has an average strike of 055, up to its intersection of the Hope Fault near the Taramakau River (Norris and Cooper, 1995, 2007). Mylonitic foliations (Sibson et al. 1979), seismic reflection data (Davey et al., 1995) and GPS observations (Powrie and Beaven, 1999) indicate that at depth the Alpine Fault dips at 40-60° to the south-east, beneath the Southern Alps, along its central section. Seismic refection profiles across the central Alpine Fault indicate that it has a listric shape, dipping as steeply as 60° at 15 km depth, before becoming sub-horizontal at ~35 km depth (Fig. 1.15), (Stern et al., 2007). The southern section of the fault, to the south of the Haast River, shows almost pure strike-slip displacement and steep easterly to vertical dip (Berryman et al., 1992; Norris and Cooper, 2001; Sutherland and Norris, 1995).

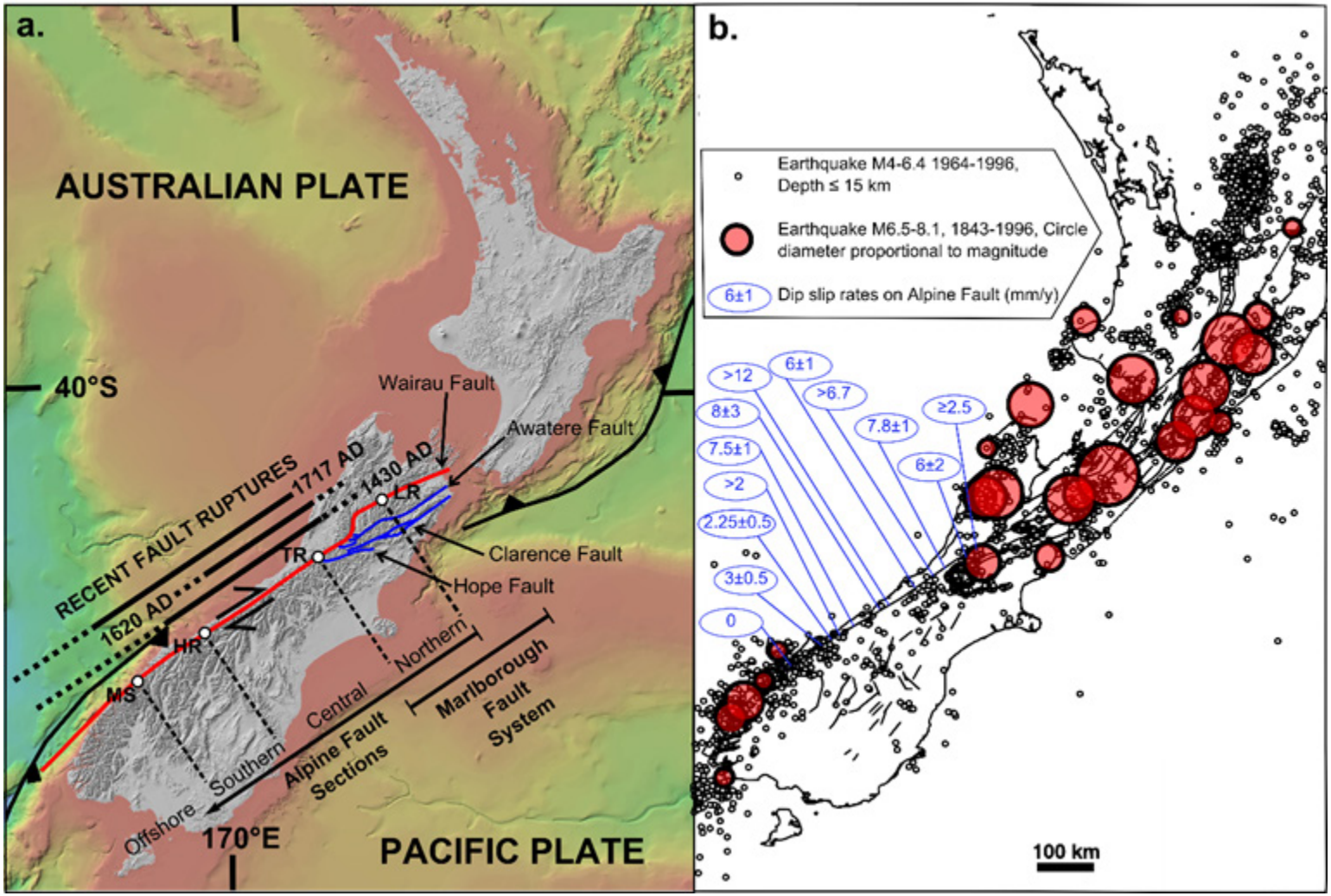

Figure 1.14 Caption overleaf.

Figure 1.14 (Overleaf) a. Map of the southern (predominantly strike-slip), central (dextral transpression, rapid uplift) and northern (intersection by Marlborough Fault System) sections of the fault (Norris and Cooper, 2001; Sutherland et al., 2006), with rupture lengths for the three most recent Alpine Fault earthquakes (Sutherland et al., 2007). MS- Milford Sound; HR- Haast River; TR- Taramakau River, LR- Lake Rotiti. Bathymetic image from National Institute of Water and Atmospheric Research (2008). b. Map to show the uplift rates on the Alpine Fault and the distribution of recent earthquakes in New Zealand. The central section of the Alpine Fault has the highest uplift rates but no recent large earthquakes. Earthquake map adapted from Stirling et al. (1998), with uplift rates adapted from Norris and Cooper (2001).

At the surface, the central section of the Alpine Fault is divided into more northerly striking oblique thrust segments and more easterly strike-slip dominated segments, which merge into a single plane at depths of 3-4 km (Norris and Cooper, 1995). Segmentation coincides with topographic variation, with thrust segments generally located at the north-eastern side of major valleys and is therefore interpreted to result from differences in stress field (Savage and Swolfs, 1986; Savage et al., 1985) that result from topographic relief (Norris and Cooper, 1995).

The significant proportion of plate motion portioned onto the Alpine Fault is evidenced by a 480 km strike slip offset of the Dun Mountain Ophiolite Belt (Benson, 1952) and the absence of late Quaternary displacement other than at the Alpine Fault and Marlborough Fault System (Cox and Sutherland, 2007). Estimates of Late Quaternary slip on the fault, based on offset landforms and marine deposits, indicate that that from Milford Sound to the Taramakau River, strike slip rates are near constant, averaging at 23-25 $mm \cdot yr^{-1}$, whereas dip slip rates vary from ~0 $mm \cdot yr^{-1}$ on the southern section of the fault, to >10 $mm \cdot yr^{-1}$ in the central section (Norris and Cooper, 2001, 2007; Sutherland et al., 2006). Comparison with plate vectors (DeMets et al., 1994) indicates that to the south of the Taramakau River, the Alpine Fault takes up 70-75 % of fault parallel plate motion, meaning that ~25 % of plate motion must be accommodated elsewhere (Norris and Cooper, 2001, 2007). The zone of plate boundary deformation has reverse faults approximately parallel to the Alpine Fault at its margins, however these are inferred to have low slip rates and are therefore unlikely to accommodate a significant amount of this deformation (Sutherland et al., 2006). Deformation may be taken up by faults within an 80 km region southeast of the Alpine Fault, although the exact structures responsible have not been identified (Norris and Cooper, 2001; Sutherland et al., 2006). As variations in dip-slip along the fault are too large to be explained by changes in plate vector alone, the degree of partitioning of deformation onto other structures must vary along the fault (Norris and Cooper, 2001). To the north of the

Taramakau River slip on the Alpine Fault is reduced as strain is portioned across the faults of the Marlborough Fault System (Berryman et al., 1992; Norris and Cooper, 2001).

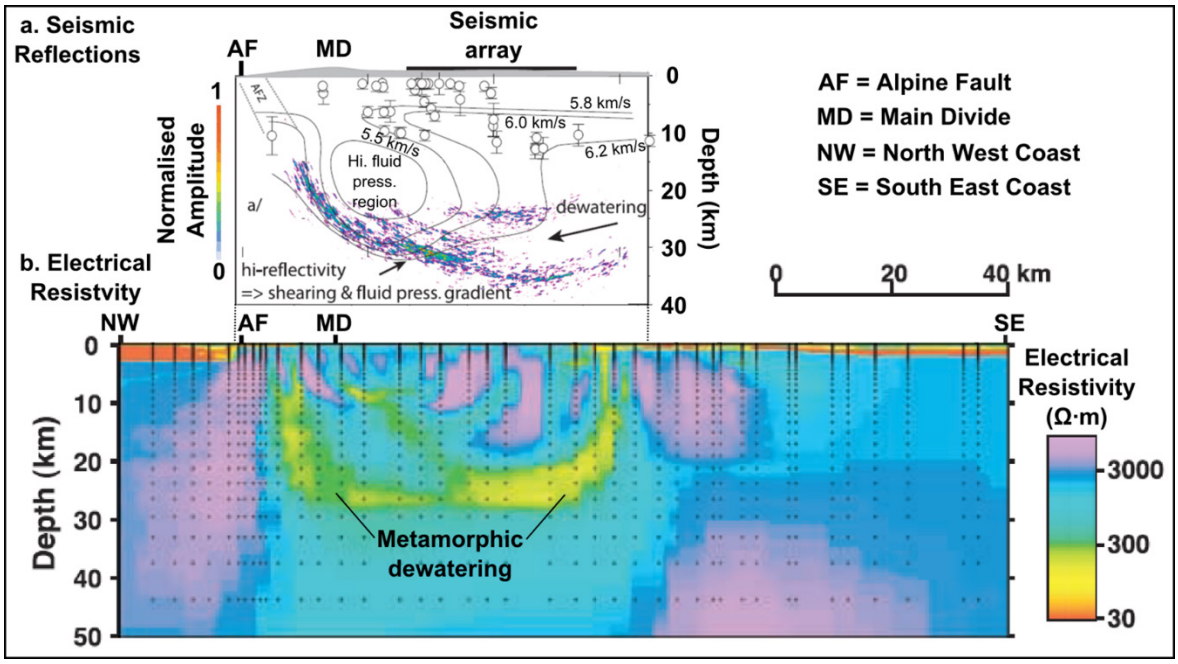

Figure 1.15 Geophysical profiles across the Southern Alps based on data collected as part of the SIGHT project. a. Stacked and migrated seismic reflection profile corresponding to SIGHT Line 2w (Fig. 1.10). Also shown are contours for P-wave speed and locations of earthquakes with local magnitude, M_L > 2 from (Leitner et al., 2001), with interpretations of data regarding the distribution of fluid. Adapted from Stern et al. (2007). b. Electrical resistivity profiles corresponding SIGHT Line 1w (Fig. 1.10), with a zone of high conductivity interpreted as representing a region of highly interconnected fluid associated with metamorphic dewatering. Adapted from Wannamaker et al. (2002).

Although large earthquakes occur relatively regularly in New Zealand, no large (moment magnitude, M_w > 7) earthquakes have occurred on the Alpine Fault since European settlement (Wells et al., 1999), despite evidence for high uplift rates on the fault (Fig. 1.14). Lack of evidence for displacement of structures that cross the Alpine Fault, such as roads, monitoring walls and tunnels, as well as recently formed river terraces indicates that significant creep has not occurred on the surface (<1 km depth) portion of the fault during the last 40 years (Sutherland et al., 2007). Although low magnitude earthquakes have been recorded near to the Alpine Fault in most seismic studies, these are less frequent on the central section of the Alpine Fault, where uplift rates are highest, than elsewhere in New Zealand (Anderson and Webb, 1994; Eberhart-Phillips, 1995; Evison, 1971; Leitner et al., 2001). This has drawn comparison to the locked Mojave section of the San Andreas fault, which experiences lower levels of body wave magnitude, M_b > 2.5 earthquakes

in comparison to creeping sections of this fault but has failed in two large (M_w > 7) earthquakes since the start of the 19th century (Eberhart-Phillips, 1995; Leitner et al., 2001). Low level seismicity on the fault ends at a depth of 8 ± 2 km, and this depth is postulated to define the base of the brittle crust and the depth to which the fault is thought to be locked (Boese et al., 2012; Leitner et al., 2001). GPS data also indicate that the fault is locked to a depth of 5-18 km, below which it creeps (Beavan et al., 1999, 2004; Wallace et al., 2007). Seismic tremor, a low amplitude, low frequency seismic signal that correlates with slow slip (Obara, 2002; Obara et al., 2004) has been detected beneath the Southern Alps (Wech et al., 2012). It occurs on a deep section of the Alpine Fault at 20-30 km depth and is interpreted as resulting from asperities on an otherwise asiesmically creeping section of the fault (Chamberlain et al., 2014; Ide, 2008).

This evidence, suggesting that the Alpine Fault is locked above 5-18 km implies that failure in large earthquakes should be expected (Leitner et al., 2001; Sutherland et al., 2007). Evidence for past ruptures of the Alpine Fault has been obtained from trenching of the Alpine Fault trace (e.g. Berryman et al., 1998; Yetton, 1998), forest damage (e.g. Norris et al., 1990) landslides (e.g. Wells et al. 1999) and sediment flux responses to past earthquakes (e.g. Cochran et al., 2017; Howarth et al., 2012). Recovery of carbon bearing material enables past events to be dated (Wells et al., 1999). Records from the southern section of the Alpine Fault indicate an average recurrence interval of 291 ± 23 between ruptures (Berryman et al., 2012; Cochran et al., 2017). Studies of the central and northern sections of the fault indicate slightly lower values, between ~200 years (Wells et al., 1999) and 260 ± 70 years (Howarth et al., 2012).

The most recent of these ruptures was in 1717 A.D. (Wells et al., 1999). As a result, the time elapsed since the last rupture has exceeded estimates for average recurrence interval, suggesting that the fault is currently late in its seismic cycle (Cochran et al., 2017). Palaeoseismic records indicate that during the last earthquake, and the two that preceded it in ca. 1620 A.D. and ca. 1430 A.D., the fault ruptured over length scales from 200-300 km to 350-600 km (Sutherland et al., 2007) (Fig. 1.14). Displacements up to 8-9 m have been estimated for the two most recent rupture events (Berryman et al., 1998) and these fit with estimates from plate motions of the accumulated strain (300 yr × 27 mm·yr^{-1} = ~8 m). Based on these dimensions of rupture, it has been estimated that these most recent rupture events produced earthquakes with M_w of 7.6 ± 0.3 to 7.9 ± 0.4, suggesting that future ruptures may generate large (M_w > 7) to great (M_w ≥ 8) earthquakes (Sutherland et al., 2007).

In addition to the damage to buildings and infrastructure that pose a significant hazard associated with any future Alpine Fault earthquake, past earthquakes are interpreted to have triggered rock avalanches, which have the potential to inundate large areas and dam or displace large volumes

of water (Barth, 2014). The consequences of a major Alpine Fault earthquake are unlikely to be limited to coseismic events. Lacustrine deposits indicate a threefold increase in sediment flux lasting for ~50 years following Alpine Fault earthquakes, which could hamper reconstruction of vital infrastructure (Howarth et al., 2012).

1.4.2 The Southern Alps

The Southern Alps, containing peaks with elevations up to >3700 m above sea level, have been formed as a result of the rapid uplift of Pacific Plate rocks on the Alpine Fault. Plate motions, estimated using magnetic anomaly and fracture zone data from the Southeast Indian Ridge, indicate that the rate of convergence along the Alpine Fault has progressively increased since 20 Ma, with distinct changes in plate kinematics at 11 Ma and 6 Ma, and an earlier onset of convergence on the northern section of the fault than further south (Cande and Stock, 2004). A range of thermochronological studies indicate the onset of rapid cooling associated with the uplift and exposure of rocks in the Southern Alps at 12-5 Ma (Adams and Gabites, 1985; Batt et al., 1999, 2004; Herman et al., 2009; Kamp et al., 1992; Tippett and Kamp, 1993). This rapid uplift may not have begun at the same time along the whole of the fault, with fission track and structural data indicating that high topography may have developed earlier in the south of the orogen (8 Ma) than in the north (5 Ma) (Craw, 1995; Tippett and Kamp, 1993). Sediments in the Waiho-1 borehole, north-west of the Alpine Fault show rapid increases in sedimentation at ca. 12 Ma and 5 Ma, which correlate with changes in plate kinematics, with the later increase interpreted as indicating the inception of widespread uplift on the Alpine Fault (Sutherland, 1996). Thus all lines of evidence indicate that widespread uplift on the Alpine Fault is likely to have begun after ~12 Ma, and possibly younger than 5 Ma. Effective crustal shortening estimates since the onset of convergence are 43 ± 8 km in the central Southern Alps, 66 ± 16 km in the north and 43 ± 8 km in the south (Lamb et al., 2015).

The orogen has an asymmetrical geometry, with the two sides, known as the inboard and outboard regions, characterised by significantly different climatic, erosional and topographic regimes and separated by the highest topography at the Main Divide (Fig. 16, 17) (Cox and Sutherland, 2007; Koons, 1990). The reason for this is that uplift on the Alpine Fault has produced a topographic barrier in the form of the Southern Alps, which interacts with the prevailing westerly air circulation in the Southern Ocean. This results in strong orographic precipitation concentrated on the north-western inboard side of the orogen, with a rain shadow to the south-east in the outboard region (Cox and Sutherland, 2007). The resulting high precipitation rates in the inboard region are up to ~13 $m \cdot yr^{-1}$ (Tait et al., 2006). This climatic regime also produces an asymmetry in erosion rates, which correlate strongly with precipitation rates (Cox and Sutherland,

2007). Consequently, while topographic elevation increases rapidly between the Alpine Fault and the Main Divide in the inboard region, the outboard region, where erosion rates are lower, consists of a broad topographic plateau. This topographic geometry mas been reproduced in models for deformation by a rigid indentor (the Australian plate) allowing removal of material (erosion) from the inboard region, which results in the formation of asymmetric inboard and outboard wedges, uplifted along thrusts with opposing dips rising from a basal decollement, with the basal inboard thrust representing the Alpine Fault (Koons, 1990). Thermally coupled models by Batt and Braun (1999) indicate that development of topographic asymmetry may not occur until several million years after initiation of uplift, as a result of the time required for the effects of asymmetrical erosion to become significant.

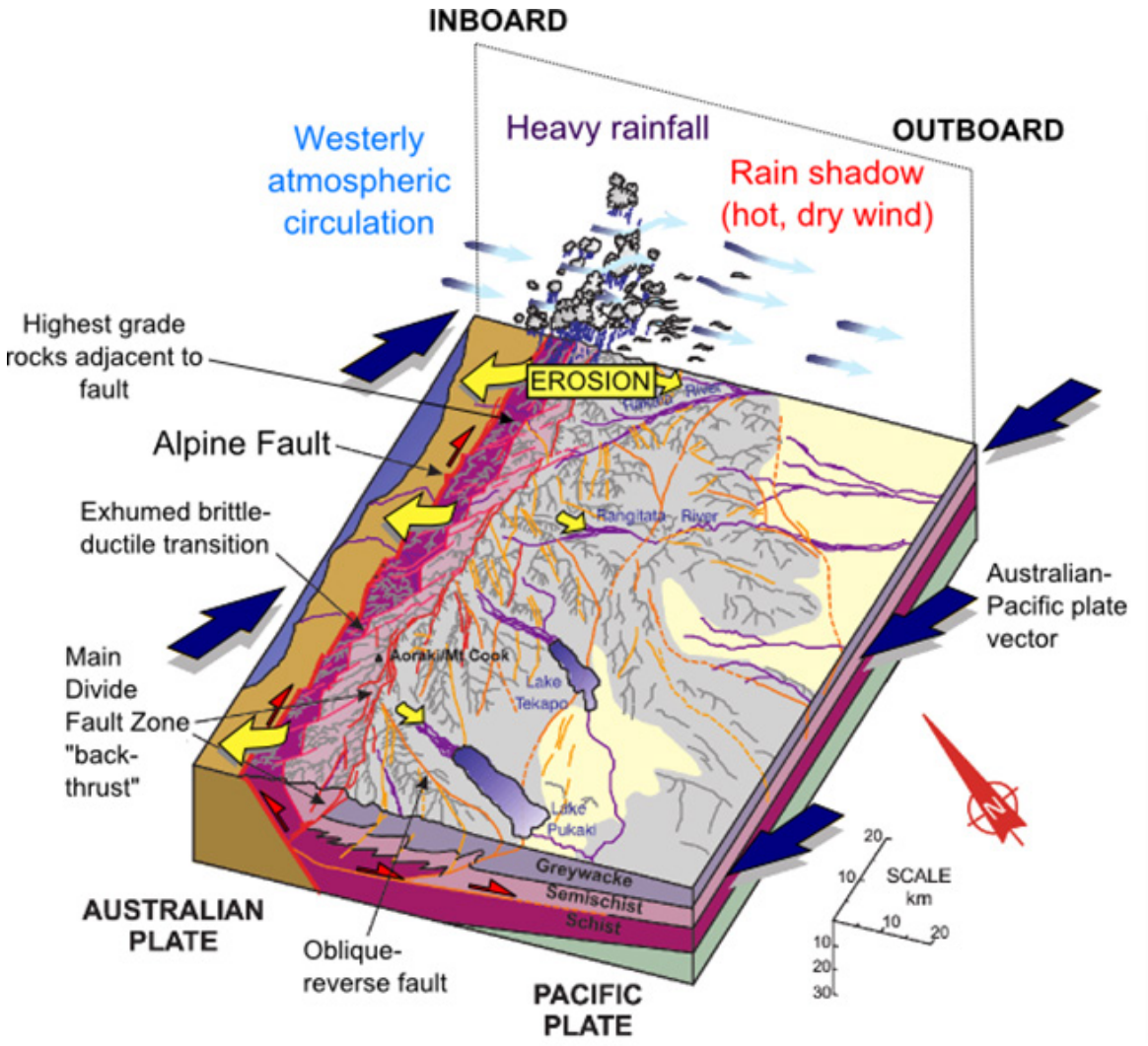

Figure 1.16 Block diagram showing the climatic and erosional systems acting upon the Southern Alps. Adapted from Cox and Sutherland (2007).

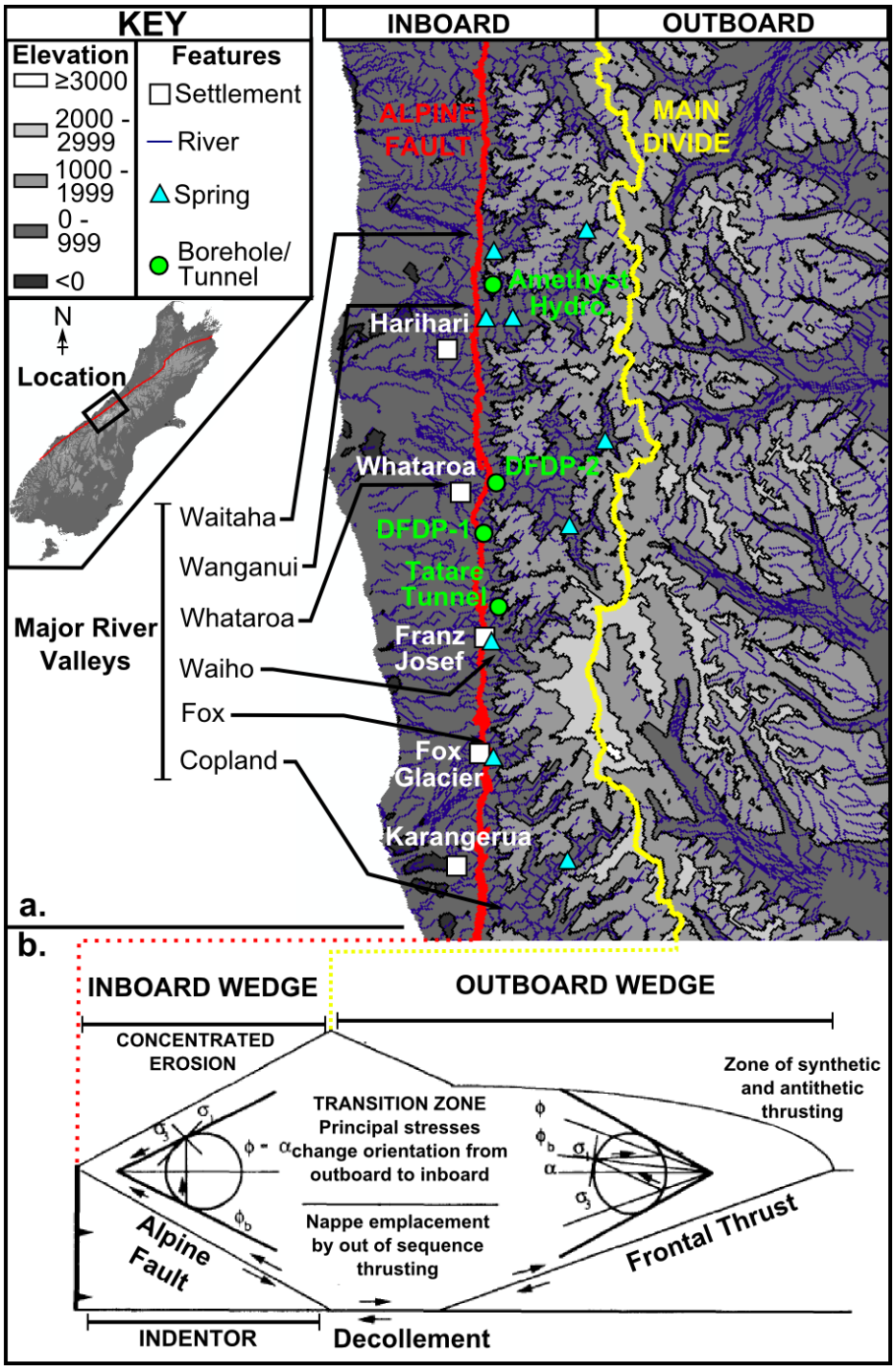

Figure 1.17 (a) The inboard region of the central Southern Alps consists of a series of river valleys containing warm springs, separated by ridges, running between the Main Divide and the Alpine Fault. The locations of boreholes and tunnels from which hydrogeologic information has been obtained are also shown. (b) Asymmetrical uplift and erosion results in two orogenic wedges, an inboard wedge with steeply tapering topography and an outboard wedge. Adapted from Koons (1990).

The inboard Southern Alps is characterised by a topographic regime in which a series of parallel ridges and valleys run between the Alpine Fault and the range of highest topography at the Main Divide (Fig. 1.17). Rocks adjacent to the fault have the highest metamorphic grade indicating the greatest total uplift (Fig. 1.16), with lower grade rocks forming the highest peaks at the Main Divide uplift (Cox and Barrell, 2007). Time-integrated vertical exhumation rates highest rates (6-9 $mm \cdot yr^{-1}$) are also highest immediately adjacent to the Alpine Fault (Little et al., 2005). This structure, in which the highest topography does not occur at the region of greatest total uplift has been shown to be an intrinsic property of mountain belt geometry over a range of uplift rates and mass transport diffusivities (Koons, 1989).

1.4.3 Rocks of the Alpine Fault Zone and Southern Alps

The rocks that have been uplifted to form the Southern Alps are the Haast Schist Group and their protoliths from the Torlesse, Waipapa and Caples terranes (Cox and Barrell, 2007; Cox and Sutherland, 2007; Mortimer et al., 2014). The Haast Schist Group rocks in a band running parallel to the Alpine Fault that have experienced brittle-ductile overprinting during exhumation on the fault are termed the Alpine Schist (Cox and Sutherland, 2007). Peak metamorphism in the Alpine Schist, which produced mineral assemblages up to the garnet-oligoclase zone of the amphibolite facies, occurred at some stage between the Cretaceous and the Miocene and predates the onset of convergent tectonics in the region (Grapes, 1995; Little et al., 2002). The absence of even higher-grade metamorphic rocks in the Southern Alps is consistent with the shallowing of the Alpine Fault at depth (Little et al., 2005). Metamorphic grade decreases away from the Alpine Fault, with the exposed sequence including an exhumed brittle-ductile transition zone (Fig. 1.18), (Little et al., 2002).

To the south-east of this transition zone are semi-schists, with ductile fabrics pre-dating uplift on the Alpine Fault, and greywackes, which form much of the outboard region to the south-east of the Main Divide (Cox and Barrell, 2007; Cox and Findlay, 1995; Cox and Sutherland, 2007; Cox et al., 1997). Veins occur across the Southern Alps, from the Main Divide region to the Alpine Fault. Quartz and calcite are the dominant vein forming minerals with chlorite and adularia also common (Craw, 1997; Menzies et al., 2014; Teagle et al., 1998; Toy et al., 2010). These were formed at a range of depths from below the top of the brittle-ductile transition zone (below 6 km depth) to the shallow subsurface above 3 km depth (Menzies et al., 2014). Veins near to the Main Divide are enriched in gold and arsenic, reflecting concentration of these elements by fluid flow (Campbell et al., 2004; Craw and Campbell, 2004; Craw et al., 2009; Pitcairn et al., 2006). Although arsenic bearing veins are present near to the Alpine Fault near its intersection with the Hope

Fault, gold bearing veins are absent from the Alpine Fault Zone itself (Campbell et al., 2004; Craw and Campbell, 2004).

In addition to the original bedding, preserved in rocks with little deformation, Alpine Schist rocks show evidence for multiple generations of metamorphic fabric (Cox and Barrell, 2007; Little et al., 2002). A crenulation foliation, inherited from peak metamorphism, has been constructively reinforced by transpressional deformation to form the steeply dipping dominant foliation in the Alpine Fault Zone more than ~1 km from the fault (Fig. 1.19), (Little et al., 2002). In a 1 to 1.5 km wide mylonite zone adjacent to the fault, the synmetamorphic fabric has been overprinted by mylonitic foliation with a less steep dip, approximately parallel to the Alpine Fault plane (Little et al., 2002; Norris and Cooper, 2007; Sibson et al., 1979).

Typical architecture of the mylonite zone varies between thrust and strike slip segments of the fault, with classic sections of fault architecture describing thrust segments, which are better exposed (Fig 1.20), (Norris and Cooper, 1995, 2007). In these sections hanging wall rocks are juxtaposed adjacent to Quaternary sediments and Western Province basement rocks in the Alpine Fault footwall (Cox and Barrell, 2007; Norris and Cooper, 2007). The base of the hanging wall is marked by a sharp contact between the footwall rocks and a zone of fault gauge (Norris and Cooper, 2007). This gouge forms the base of a zone of fault breccia and retrogressively altered green cataclasites, which is up to ca. 40 m thick in outcrops (Norris and Cooper, 1995; White and White, 1983). Analysis of the clay-sized fraction from the cataclasites showed the phyllosilicate components to be chlorite, illite-muscovite, biotite, smectite and vermiculite (Warr and Cox, 2001). Pseudotachylite veins, which are formed as a result of frictional melting in the fault zone, are most abundant within 200 m of the fault, but are absent from fault gouge (Norris and Cooper, 2007; Sibson et al., 1979). These observations indicate initial alteration by anhydrous cataclasis and frictional melting, followed by hydrothermal alteration at <320 °C and swelling clay formation at <120 °C (Warr and Cox, 2001). Above the cataclasites in thrust segments are ultramylonites, which may be dark in colour where pseudotachylite veins are abundant (Norris and Cooper, 1995, 2007). Within the Alpine Fault Zone ultramylonites, cataclasis is restricted to minor fault and shear zones, some of which show evidence of hydrothermal alteration (Norris and Cooper, 2007). With increasing distance from the fault, ultramylonites are replaced by mylonites, which commonly show imbrication into duplexes (Norris and Cooper, 1995, 2007). Further structurally above the fault, mylonites grade into protomylonites and then schist (Norris and Cooper, 1995, 2007). Strike-slip segments of the fault have narrow anastomosing zones of fault gouge and mylonite zones that are not imbricated or absent, with protomylonite up to the fault plane (Norris and Cooper, 1995).

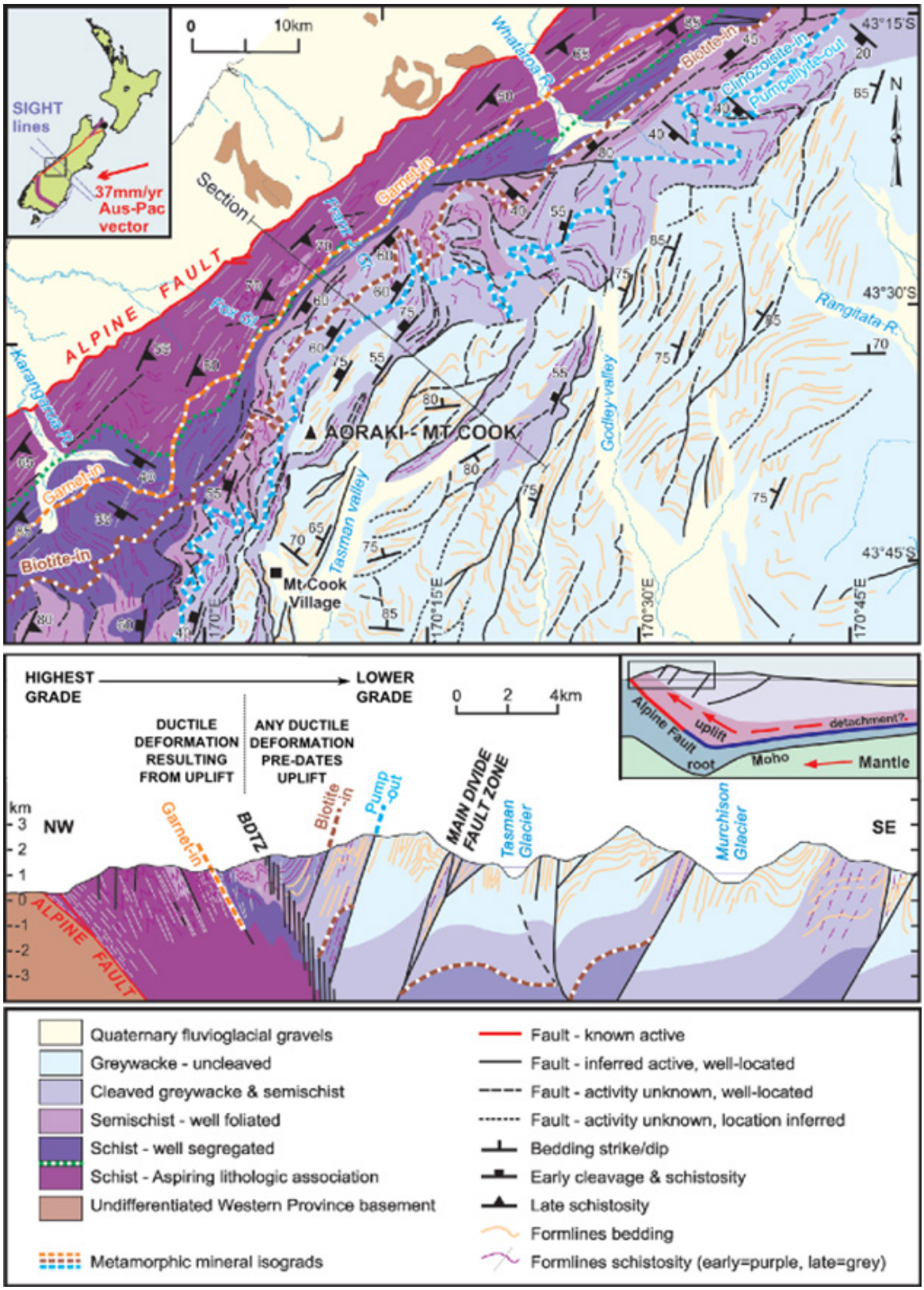

Figure 1.18 Map and cross section of the geology of the central Southern Alps. There is a broad decrease in metamorphic grade away from the fault, with no ductile deformation associated with uplift to the south-east of the exhumed brittle-ductile transition zone (BDTZ). Adapted from Cox and Sutherland (2007).

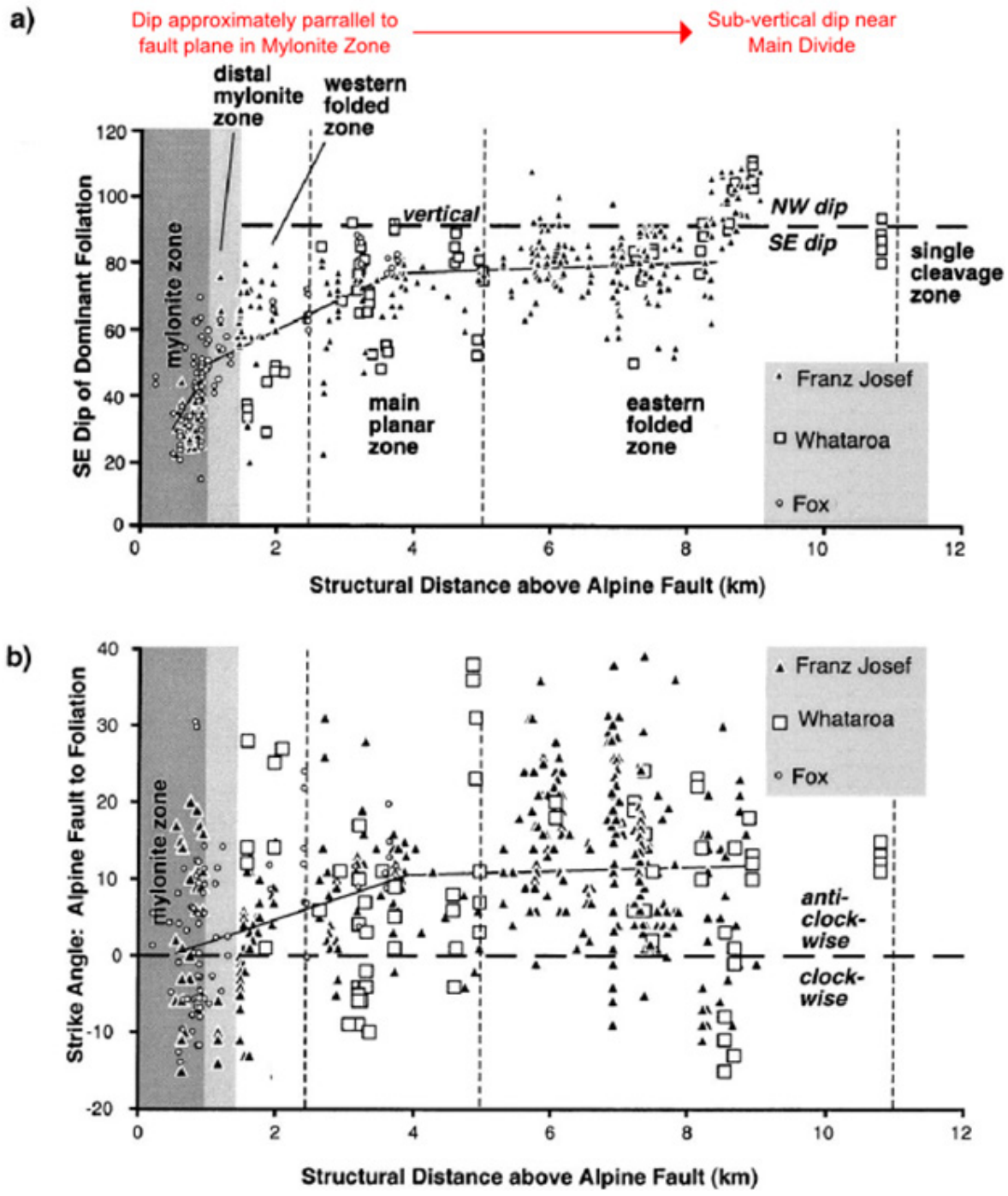

Figure 1.19 a. Dip and b. strike of dominant foliation in Alpine Schist rocks along profiles near Franz Josef, Whataroa and Fox. Adapted from Little et al. (2002).

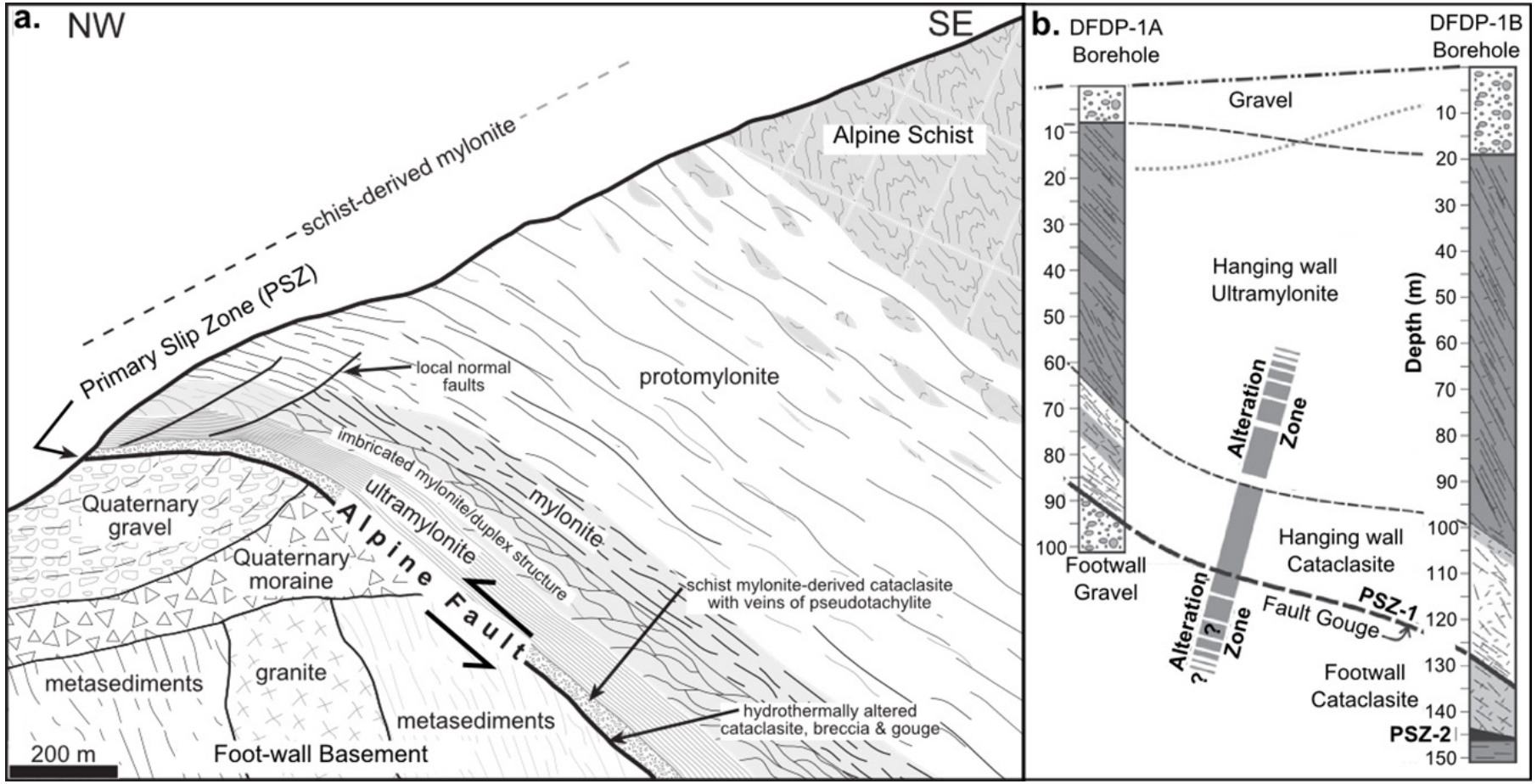

Figure 1.20 a. Cross section of typical Alpine Fault Zone architecture based on thrust segment outcrops in the central Alpine Fault region, adapted from Norris and Cooper (2007). b. Fault zone architecture from the DFDP-1A and B boreholes, adapted from Sutherland et al. (2012).

Fault zone architecture at depth was investigated by boreholes drilled as part of the Deep Fault Drilling Program (DFDP). The DFDP-1A and B boreholes were drilled at Gault Creek in 2011 (Sutherland et al., 2012) and the DFDP-2B borehole in the Whataroa valley in 2014 (Sutherland et al., 2017) (Fig. 1.17), during the period of PhD candidature of the author. The DFDP-1A and 1B boreholes penetrated through ultramylonites and altered cataclasites in the hanging wall of the fault, showing a fault zone architecture consistent with that exposed in outcrops (Fig. 1.20) (Norris and Cooper, 2007; Toy et al., 2015). DFDP-1A penetrated through the fault principal slip zone (PSZ) at 91 m depth, below which were gravels of fluvial origin (Sutherland et al., 2011, 2012). DFDP-1B encountered a PSZ forming the base of the hanging wall at 150 m depth, below which was a zone of footwall cataclasites, with a second zone of gouge, termed PSZ-2, below (Sutherland et al., 2012; Toy et al., 2015). Analysis of mineral assemblages and fabrics in recovered hanging wall ultramylonites and cataclasites indicates mixing of protoliths of both hanging wall and footwall origin, consistent with the fault having multiple high strain zones at depth or temporal variation of the position of a single high strain zone (Toy et al., 2015).

The DFDP-2B borehole in the Whataroa valley reached a depth of 818 m in the Alpine Fault hanging wall, penetrating through a sedimentary sequence into schist, protomylonite and mylonite (Sutherland et al., 2017). The 240 m thick sequence of sediments encountered is thicker than was predicted based seismic surveys, gravity modelling and from projecting the topographic slope gradients in the region. The sedimentary fill records a range of depositional environments in the Whataroa valley, and includes glacial, lacustrine and fluvial deposits (Cox et al., 2015).

1.4.4 Thermal structure (existing work)

Following rapid uplift, the Southern Alps are inferred to exist at approximate thermal as well as topographic steady state (Koons, 1987, 1989, 1990; Little et al., 2002). Allis et al. (1979) modelled the thermal regime beneath the Southern Alps based on an analytical solution for one-dimensional uplift of 500 °C rocks from 15 km depth to the surface for a range of vertical uplift rates from 10 $mm \cdot yr^{-1}$ to 20 $mm \cdot yr^{-1}$. The models indicated that for these uplift rates, rocks advect a significant amount of heat, raising temperatures in the shallow part of the orogen. Elevated temperature gradients were predicted in the areas of rapid uplift based on these results (Fig. 1.21) (Allis et al., 1979).

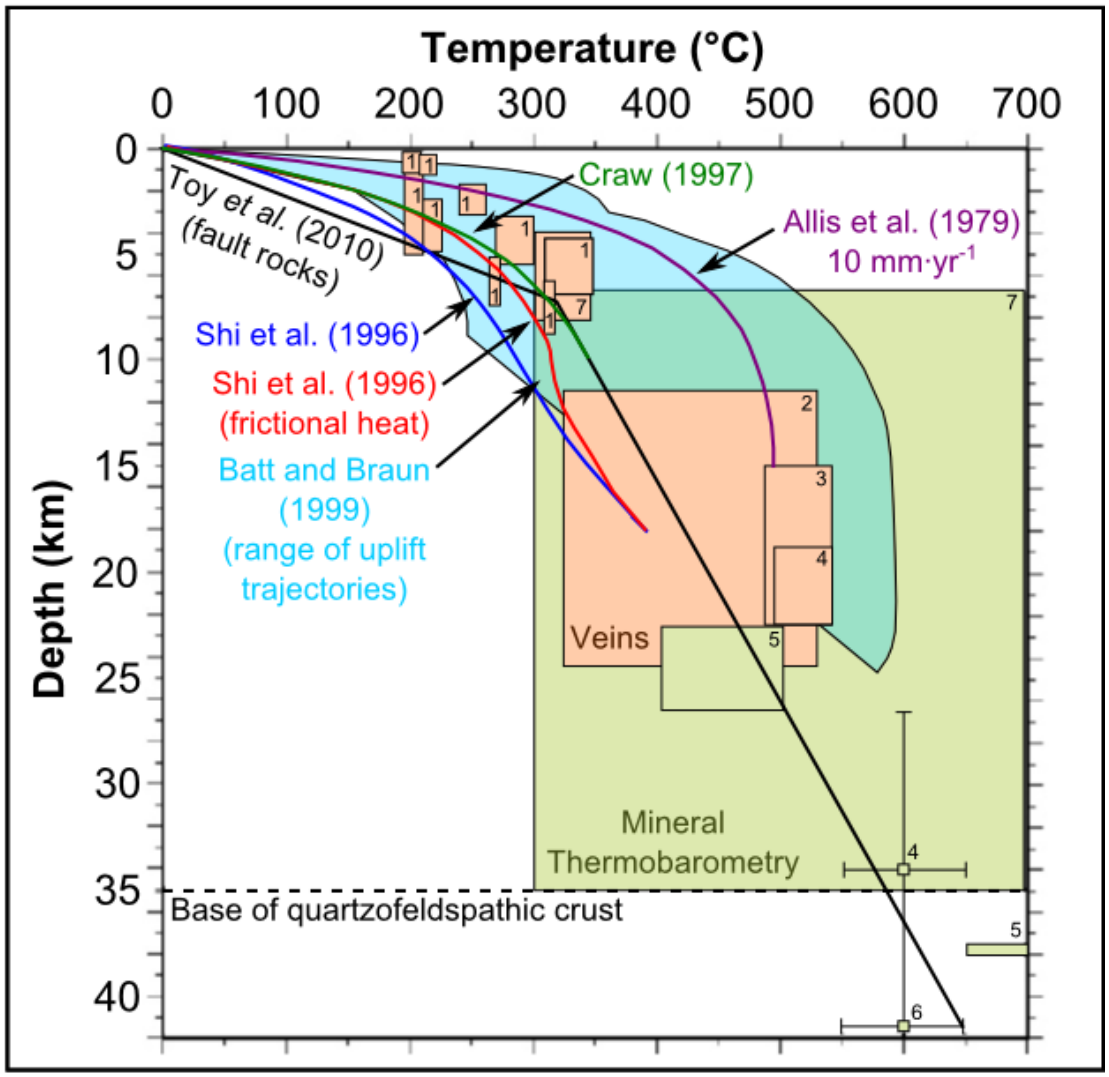

Figure 1.21 Estimated temperatures beneath the Southern Alps based on mineral thermobaromety and data from veins from (1) Craw (1997); (2) Holm et al. (1989); (3) Green (1992); (4) Grapes (1995); (5) Cooper (1980); (6) Vry et al. (2004) and (7) Toy et al. (2010), with model (Allis et al., 1979; Batt and Braun, 1999; Shi et al., 1996) and inferred (Craw, 1997; Toy et al., 2010) thermal exhumation profiles. The base of the quartzofeldspathic crust is based on Stern et al. (2007). Adapted from Toy et al. (2010).

Koons (1987) modelled temporal variation in temperature at a two-dimensional plate boundary and showed that the brittle-ductile transition beneath the Southern Alps is likely to occur at shallower depth compared to elsewhere in the region. Following 1.5 Ma of uplift in these models the brittle-ductile transition was raised from 13 km depth to 5 km and eventually reached a depth of 3 km (Koons, 1987). The shallowing of the brittle-ductile transition beneath the Southern Alps has been confirmed by seismic data, which show that the base of seismicity beneath the Southern Alps is 8 ± 2 km near to the Alpine Fault, compared to 10-15 ± 2 km elsewhere (Boese et al., 2012; Leitner et al., 2001). Subsequent 2D numerical models for the thermal consequences of uplift and

erosion by Shi et al. (1996) predicted that in addition to elevation of isotherms near to the Alpine Fault, isotherms would be depressed and heat flow reduced to the south-east of the Main Divide as a result of crustal thickening. A model by Batt and Braun (1999) in which erosion was coupled to model topography did not show this depression of isotherms. In addition to an uplifted brittle-ductile transition, this model predicted further structural consequences of the thermal regime, indicating that thermal weakening is likely to focus deformation along the Alpine Fault and faults near to the Main Divide (Batt and Braun, 1999). These existing thermal models, which invoke different assumptions and boundary conditions, predict a range of different temperature gradients for the orogen (Fig. 1.21). In addition to constraints from seismic data on the depth of the brittle-ductile transition, modelled temperatures can be tested against palaeo-thermal data from rock samples and temperature measurements from boreholes. Collated temperature estimates from fluid inclusions in veins and mineral thermobarometry (Fig. 1.21) indicate an elevated geothermal gradient above the brittle-ductile transition, with temperatures of >200 °C persisting to depths of 1-2 km and a shallower gradient of ca. 10 °C·km^{-1} below the brittle-ductile transition (Toy et al., 2010). Borehole data from across South Island showed reduced heat fluxes in the distal outboard region and elevated heat fluxes adjacent to the Alpine Fault, consistent with model predictions (Allis and Shi, 1995; Shi et al., 1996). Observed heat fluxes ranged from 320 mW·m^{-2} at a borehole in the Waiho valley, near to the Alpine Fault to 43 mW·m^{-2} in the outboard region. Heat fluxes adjacent to the Alpine Fault near the Haast River are lower (90 mW·m^{-2}) than in the Waiho valley (Allis and Shi, 1995; Shi et al., 1996), consistent with the transition to principally strike slip motion on the Alpine Fault south of the Haast River (Berryman et al., 1992; Norris and Cooper, 2001; Sutherland and Norris, 1995).

Published temperature gradients for the central Southern Alps are available from the Waiho valley borehole (Shi et al., 1996) and from DFDP boreholes (Sutherland et al., 2012, 2017). Like the Waiho valley borehole, the DFDP-2B borehole is located in a major river valley, the Whataroa valley. By contrast the DFDP-1B borehole, which lies between these two boreholes, is located in a minor ravine. Of these boreholes, the highest temperature gradient was measured in DFDP-2B, with data from an optic fibre along the drilled interval showing a geothermal gradient averaging 125 ± 55 °C·km^{-1}, following relaxation of perturbations associated with drilling (Sutherland et al., 2017). A steep temperature gradient was also observed at the Waiho valley borehole, averaging 95 °C·km^{-1} below ~150 m, with decreasing temperature with depth in the near-surface attributed to the retreat of the Franz Josef glacier in this valley ~25 years prior to drilling (Shi et al. 1996). The DFDP-1B borehole recorded the shallowest temperature gradient of the three, averaging 62.6 ± 2.1 °C·km^{-1} (Sutherland et al., 2012).

Existing studies have largely focussed on modelling the variations in temperature normal to the strike of the fault, with some consideration of along-strike variation as resulting from the changing angle of plate vectors relative to the fault (Batt and Braun, 1999), but with little consideration of along-strike variations between ridges and valleys. Possible short wavelength along-strike variations were illustrated by Upton et al. (1995), who hypothesised differences in isotherms between ridges and valleys on the basis of boiling textures in fluid inclusions. Models have also focussed largely on the role of deformation, uplift and erosion in controlling thermal structure (e.g. Batt and Braun, 1999; Koons, 1987; Shi et al., 1996). Although hot springs are found in numerous valleys across the Southern Alps, the influence of these springs and of groundwater circulation in general, has been considered negligible (Allis and Shi, 1995).

1.4.5 Fluid flow regime (existing work)

The present day fluid flow regime in the Southern Alps produces warm springs, with temperatures up to 65 °C (Barnes et al., 1978; Reyes et al., 2010). These occur in valleys along the Southern Alps, but are restricted to the hanging wall side of the Alpine Fault (Fig. 1.17). At Welcome Flat in the Copland valley (Fig. 1.17), spring water temperature of the Copland spring responds to distal large earthquakes, which has been interpreted as indicating the influence of stress state on the apertures of fractures modulating flow at depth (Cox et al., 2015).

Veins and secondary alteration zones in exposed rocks of the Southern Alps provide evidence for the passage of fluids during the uplift of rocks to the surface (Craw et al., 2009; Menzies et al., 2014; Norris and Cooper, 1995; Toy et al., 2010; Warr and Cox, 2001). This fluid flow is also key in concentrating gold and arsenic in the orogen (Campbell et al., 2004; Craw et al., 2009; Pitcairn et al., 2006). Fluid-rock interaction varies with depth, with gold bearing rocks near to the Main Divide showing a transition from alteration by fluids near chemical equilibrium with their host rock at the greatest depths, to alteration in veins and their host rocks by disequilibrium fluids at intermediate depths, with the shallowest alteration restricted to veins (Craw et al., 2009).

On the basis of the distribution of alteration and mineralisation, fluid flow is inferred to be controlled by faults and fractures (Campbell et al., 2004; Craw et al., 2009). Evidence of boiling at shallow depths (~150 m) within veins in some high elevation (>1400 m above sea level) rocks may reflect transient events of short duration in the flow system, which may be linked to seismicity (Craw, 1997). The thick zones of hydrothermal alteration directly above the Alpine Fault (Norris and Cooper, 1995; Sutherland et al., 2012) are consistent with the fault acting as a conduit for focussed fluid flow along the fault in its hanging wall damage zone (Fig. 1.22), (Menzies et al., 2016). Slug test permeability measurements in the DFDP-1B borehole indicate reduced

permeability in the damage zone closest to the fault, which has experienced significant alteration, relative to more distal parts of the damage zone (Sutherland et al., 2012). This is consistent with permeability reduction through mineral precipitation associated with fluid flow through the interseismic period (Sibson, 1990; Sutherland et al., 2012).

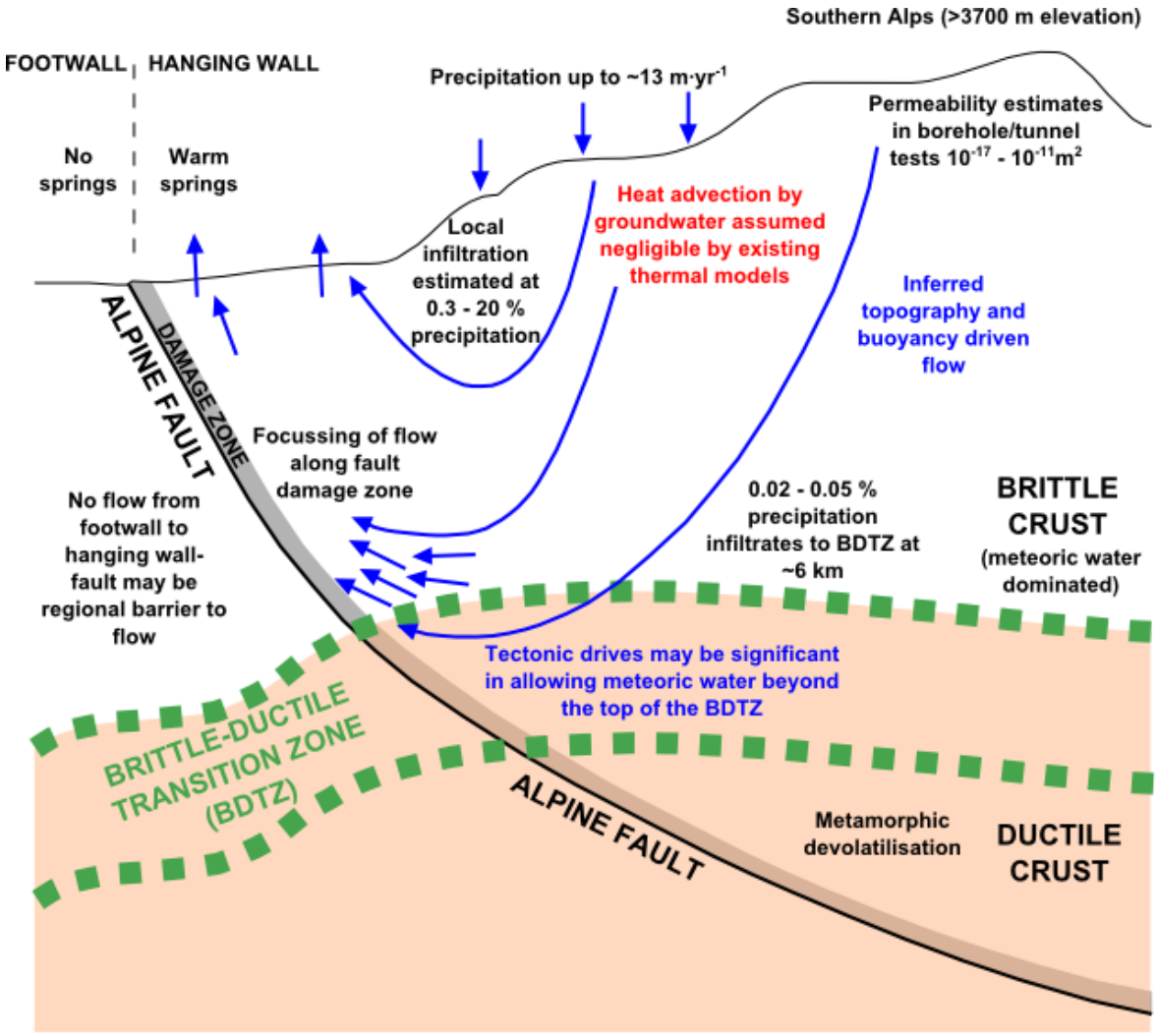

Figure 1.22 Summary of existing knowledge of the fluid flow regime in the Southern Alps. Estimated values are shown for surface infiltration (Sims et al., 2015), infiltration to 6 km depth (Menzies et al., 2016) and permeability (Cox et al., 2015; Sutherland et al., 2012). Annual precipitation rate is from Tait et al. (2006). Adapted from (Menzies et al., 2016).

At DFDP-1B significantly lower fluid pressures were recorded in the fault footwall compared to the hanging wall, with a 0.53 MPa pressure drop across the fault PSZ (Sutherland et al., 2012). Laboratory measurements of samples from DFDP-1 cores (Carpenter et al., 2014) and outcrops (Boulton et al., 2012) show low permeabilities of the order of 10^{-20} m^2 for fault gouge. These observations suggest that the fault may act as a barrier to fluid flow between the hanging wall and the footwall, at least at shallow depths. Furthermore $^{87}Sr/^{86}Sr$ ratios in warm springs and

hydrothermal mineral veins from the Alpine Fault Zone show that all have values within range of hanging wall rocks, indicating that the fault may act as a barrier to flow down to the brittle-ductile transition (Menzies et al., 2016).

There are few in situ permeability estimates for the Haast Schist Group, with the only published values, prior to the drilling of DFDP-2B, those from the DFPD-1B borehole (Sutherland et al., 2012) and from regional hydroelectric engineering reports (collated by Cox et al. (2015)). These show permeabilities in the range 10^{-17} m^2 to 10^{-11} m^2. Observations of water outflow rates at the 19th century tunnel Tatare Tunnel near Franz Josef provide the only published infiltration estimate for the Southern Alps, indicating that 0.3% to 20% of precipitation recharges groundwater (Fig. 1.22), if a measured catchment area (0.54 km^2) of is assumed to drain into the tunnel (Sims et al., 2015).

Geophysical and geochemical studies have provided insights into fluid sources and distribution at depth in the orogen, which are valuable constraints on flow regime. Magnetotelluric surveys have revealed a u-shaped high electrical conductivity zone in the mid to lower crust (Wannamaker et al., 2002), coinciding with a region of low seismic velocities (Stern et al., 2001) (Fig.1.15). As there is no magmatism associated with the orogen, this can be best explained in terms of the presence of a highly interconnected, saline fluid (Upton et al., 2003; Wannamaker et al., 2002). Studies of quartz fluid inclusion hydrogen isotopes and vein quartz oxygen isotopes that have experienced ductile deformation indicate that compositions can be most easily explained in terms of an originally meteoric fluid, with variable degrees of fluid-rock interaction (Menzies et al., 2014). This is supported by fluid flux estimations (Fig. 1.22), which suggest that the potential downward flux of meteoric fluid is at least two orders of magnitude greater than the production of a metamorphic fluid from depth (Menzies et al., 2016). The steep topography of the Southern Alps provides a strong driving force for deep meteoric water circulation, with thermally driven buoyancy also inferred to play a significant role in driving fluid flow in the orogen (Koons and Craw, 1991). However, additional driving forces are required to explain flow of meteoric water into the brittle-ductile transition zone. Localised dilation due to lithological variations (McCaig, 1988; Upton et al., 1995) and movement of a dynamic brittle-ductile transition through seismic cycles, sweeping neutrally buoyant fluids near the transition downwards (Connolly and Podladchikov, 2004), have been suggested as possible mechanisms for movement of meteoric fluids into the ductile regime. Although evidence suggests that meteoric water is the dominant fluid down to the brittle-ductile transition, most groundwater circulation must occur at much shallower depths, as warm spring geochemistry indicates fluid-rock interaction limited to <150 °C (Menzies et al., 2014, 2016; Reyes et al., 2010) .

Thus, existing studies show that fluid flow plays a significant role in alteration and mineralisation in the orogen and that meteoric groundwater is the dominant fluid in the brittle upper crust. However, what influence groundwater flow has on the Alpine Fault is not well understood, as uncertainty remains in a number of areas, such as the role of groundwater in transporting heat and the fluid pressures and flow rates at depth near to the fault. Suitable regional values for key parameters such as permeability and surface infiltration rate are poorly known, with only a few estimates from boreholes and tunnels, which may only reflect local conditions.

1.5 Thesis aims and structure

1.5.1 Aims

The overarching aim of this thesis is to better understand the fluid flow system within the Southern Alps and its potential to influence other orogenic processes. To do so, it sets out to answer the following questions:

1. What is the permeability structure of the Southern Alps?

Permeability is a key control on fluid flow, which remains poorly constrained for the Southern Alps. The only existing estimates come either from laboratory measurements, which are unlikely to reflect larger scale permeability or from a very limited number of borehole and tunnel hydraulic tests, which may also only sample small volumes of rock. This thesis aims to obtain estimates for regional-scale permeability/hydraulic conductivity, as well as additional local estimates of permeability/hydraulic conductivity from borehole data in the Alpine Fault Zone to complement this.

2. What are the regional infiltration rates at the surface?

Meteoric water infiltration rates at the surface provide an upper bound on the flux of fluid available for processes such as alteration at depth. Only one estimate currently exists and relies on an uncertain assumed catchment area (Sims et al., 2015). This thesis aims to provide an estimate for regional infiltration rate.

3. What are the fluid fluxes to depth?

Although the fluxes of meteoric water at the brittle-ductile transition have been quantified (Menzies et al., 2016), the variation in fluid flux between the surface and the brittle-ductile transition has not. This thesis aims to estimate how fluid flux varies at depths shallower than the brittle-ductile transition.

4. What are the fluid pressure conditions in the Alpine Fault Zone?

Fluid pressure conditions influence effective confining stress on the Alpine Fault. The deepest existing fluid pressure measurements from the Alpine Fault Zone are at <150 m depth in DFDP-1B. This thesis aims to obtain estimates for fluid pressure at greater depths in the Alpine Fault Zone.

5. What are the fluid flow rates (Darcy velocities) in the Alpine Fault Zone?

Flow rates influence rates of reaction and may vary spatially across the orogen. This thesis aims to provide quantification of Darcy velocities in the Alpine Fault Zone.

6. How significant is the influence of fluid flow on subsurface heat flow and temperature field?

Past thermal models (e.g. Shi et al. 1996) have assumed that fluid flow plays an insignificant role in heat transport in the orogen. This thesis aims to quantify the significance of fluid flow in advecting heat in the Southern Alps.

7. How does permeability structure influence the temperature and fluid pressure fields at depth in the Southern Alps and in particular, near to the Alpine Fault?

The temperature and fluid pressure conditions at depth affect alteration and deformation and are therefore important for understanding the behaviour of the Alpine Fault. The fluid pressure field at depth remains poorly constrained and existing models for the temperature field do not account for the thermal effects of fluid flow. This thesis aims to model the fluid pressure and temperature field and investigate the influence of permeability structure on these variables.

8. What role does thermal buoyancy play in driving groundwater circulation and how significant is the temperature dependence of water viscosity?

Topography and thermal buoyancy have been inferred to be important drivers for fluid flow in the Southern Alps. This thesis aims to investigate the significance of buoyancy-driven fluid flow and the influence of the temperature dependence of fluid viscosity on the flow regime in the orogen.

1.5.2 Structure overview

In order to answer the questions outlined, the thesis utilises a range of modelling methods and datasets. Different but complementary lines of investigation are used to study different aspects of the flow system. Regional numerical models simulate the complexity of the three-dimensional system. Simplified analytical models are used to provide insights into the fundamental processes within the orogen, which may not be obvious within the complexity of numerical models. Estimates of local conditions provide a point of comparison for larger scale simulations of the flow

system and regionally estimated parameter values, which in turn provide context for more localised studies.

Chapters 3, 4 and 5 utilise new data collected from the DFDP-2B borehole, drilled in 2014 in the Whataroa valley, during the period of candidature. The author formed part of the onsite science team for this drilling, collecting hydraulic data and acting as a custodian of the hydraulic dataset (including periodic borehole mud level, mud properties and mud pit level observations) following the project. Thesis Chapters 2-5 are presented as manuscripts intended for journal submission, one of which is a technical note (Chapter 3). Each addresses a number of the key questions outlined, with values for permeability being obtained through multiple lines of investigation in more than one chapter in order to find complementary bulk regional estimates and local estimates from the Alpine Fault Zone using different approaches.

1.5.3 Chapter 2

(Questions 1, 2 and 3)

The thesis begins by obtaining the first regional-scale estimates for key parameters in the flow system- surface infiltration rate, hydraulic conductivity (K), permeability (k) and the variation of fluid flux with depth, in order to obtain a broad understanding of the regional fluid flow regime. Water level data from boreholes drilled as part of a hydroelectric power project in the Amethyst Ravine, near the Wanganui valley is used to contain minimum water table positions, against which analytical and numerical model results are tested, in order to estimate these regional parameter values. The implications of k based on packer test estimates from these boreholes, k variation with depth, k anisotropy, k of the Alpine Fault and coupled fluid and heat flow are investigated. The applicability of analytical models based on the Dupuit assumptions for modelling shallow fluid flow in the orogen is discussed. The chapter is written as a manuscript for future submission to *Hydrogeology Journal*.

1.5.4 Chapter 3

(Questions 1 and 4)

Chapter 3 provides an introduction to the DFDP-2B borehole and the datasets collected, as well as analysing and discussing the hydraulic ‘slug test’ dataset. This dataset is used to provide estimates of steady state borehole fluid pressures (hydraulic head), which give insights into the fluid pressure conditions in the Alpine Fault Zone that are greater than have been measured before and were published as part of a contribution to *Nature* (Appendix A; Sutherland et al., 2017).

Further analysis is used to estimate the possible difference between borehole and ambient hydraulic heads. Idealised slug test models are used to provide basic hydraulic conductivity estimates for rocks in the Alpine Fault hanging wall, which can be compared to regional-scale bulk hydraulic conductivity. Insights into hydraulic conditions at the borehole are used to set out improved strategies for hydraulic data collection during any future Alpine Fault drilling projects or other scientific drilling in other Southern Alps valleys, in order to obtain the best estimates of permeability and in situ fluid pressure. Chapter 3 is written as a manuscript for future submission to the *New Zealand Journal of Geology and Geophysics*.

1.5.5 Chapter 4

(Questions 1, 5 and 6)

Having considered the hydraulic data obtained from DFDP-2B, temperature data from the borehole is investigated using one-dimensional analytical thermal models, incorporating rock advection and groundwater flow. Models provide estimates of Darcy velocity and heat flux, which are used to quantify the importance of heat transport by groundwater in the shallow Southern Alps. Local hydrogeological structure is interpreted based on variations of Darcy velocity with depth. Model Darcy velocities are combined with hydraulic head data to provide estimates of hydraulic conductivity in Alpine Schist basement rocks and overlying sediments, which supplement and improve upon estimates obtained in the previous chapter from rates of response in the slug test dataset. Chapter 4 is written as a manuscript for future submission to *Geophysical Research Letters*.

1.5.6 Chapter 5

(Questions 1, 7 and 8)

Having gained insights into the role of fluid flow in heat transport from simple one-dimensional models in Chapter 4, coupled fluid and heat flow are investigated using three-dimensional regional models. Numerical models for the Whataroa valley region, incorporating the thermal effects of rock advection, are used to quantify the effect of permeability structure on temperature and fluid pressure conditions in the Southern Alps, focussing on conditions at the Alpine Fault. Common features across modelled permeability structures are identified and the influence of buoyancy driven flow and thermally coupled viscosity are demonstrated. Results are compared to temperature and hydraulic measurements from the DFDP-1B and 2B boreholes. The chapter is written as a manuscript for future submission, with the target journal yet to be agreed. A sub-set

of the model suite presented in this chapter were provided by the author for a published contribution to *Nature* (Appendix A).

1.6 References

Achtziger-Zupančič, P., Loew, S., Mariéthoz, G., 2017. A new global database to improve predictions of permeability distribution in crystalline rocks at site scale. J. Geophys. Res. Solid Earth 122, 3513–3539. doi:10.1002/2017JB014106

Adams, C.J., Campbell, H.J., Griffin, W.L., 2009. Tracing the Caples Terrane through New Zealand using detrital zircon age patterns and radiogenic isotope signatures. New Zeal. J. Geol. Geophys. 52, 223–245. doi:10.1080/00288300909509888

Adams, C.J., Gabites, J.E., 1985. Age of metamorphism and uplift in the Haast Schist Group at Haast Pass, Lake Wanaka and Lake Hawea, South Island, New Zealand. New Zeal. J. Geol. Geophys. 28, 85–96. doi:10.1080/00288306.1985.10422278

Adams, C.J., Mortimer, N., Campbell, H.J., Griffin, W.L., 2013. Detrital zircon geochronology and sandstone provenance of basement Waipapa Terrane (Triassic–Cretaceous) and Cretaceous cover rocks (Northland Allochthon and Houhora Complex) in northern North Island, New Zealand. Geol. Mag. 150, 89–109. doi:10.1017/s0016756812000258

Adams, C.J., Mortimer, N., Campbell, H.J., Griffin, W.L., 2009. Age and isotopic characterisation of metasedimentary rocks from the Torlesse Supergroup and Waipapa Group in the central North Island , New Zealand Age and isotopic characterisation of metasedimentary rocks from the Torlesse Supergroup and Waipapa Group i. New Zeal. J. Geol. Geophys. 52, 149–170. doi:10.1080/00288300909509883

Ague, J.J., 2003. Fluid Flow in the Deep Crust, in: Treatise on Geochemistry. pp. 195–228.

Ague, J.J., 2003. Fluid infiltration and transport of major, minor, and trace elements during regional metamorphism of carbonate rocks, Wepawaug Schist, Conneticut, USA. Am. J. Sci. 303, 753–816.

Ague, J.J., Baxter, E.F., 2007. Brief thermal pulses during mountain building recorded by Sr diffusion in apatite and multicomponent diffusion in garnet. Earth Planet. Sci. Lett. 261, 500–516. doi:10.1016/j.epsl.2007.07.017

Allaby, M. (Ed.), 2008. A Dictionary of Earth Sciences, 3rd ed. Oxford University Press, Oxford.

Allis, R.G., Henley, R.W., Carman, A.F., 1979. The Thermal Regime Beneath the Southern Alps. Bull. R. Soc. New Zeal. 18, 79–85.

Allis, R.G., Shi, Y., 1995. New insights to temperature and pressure beneath the central Southern Alps, New Zealand. New Zeal. J. Geol. Geophys. 38, 585–592. doi:10.1080/00288306.1995.9514687

Anderson, H., Webb, T., 1994. New Zealand seismicity: Patterns revealed by the upgraded National Seismograph Network. New Zeal. J. Geol. Geophys. 37, 477–493. doi:10.1080/00288306.1994.9514633

Anderson, M.P., 2005. Heat as a ground water tracer. Ground Water 43, 951–968. doi:10.1111/j.1745-6584.2005.00052.x

Avouac, J., Meng, L., Wei, S., Wang, T., Ampuero, J., 2015. Lower edge of locked Main Himalayan Thrust unzipped by the 2015 Gorkha earthquake. Nat. Geosci. 8, 3–8. doi:10.1038/NGEO2518

Aydin, A., Johnson, A.M., 1978. Development of faults as zones of deformation bands and as slip surfaces in sandstone. Pure Appl. Geophys. PAGEOPH 116, 931–942. doi:10.1007/BF00876547

Balsamo, F., Storti, F., 2010. Grain size and permeability evolution of soft-sediment extensional sub-seismic and seismic fault zones in high-porosity sediments from the Crotone basin, southern Apennines, Italy. Mar. Pet. Geol. 27, 822–837. doi:10.1016/j.marpetgeo.2009.10.016

Barnes, I., Downes, C.J., Hulston, J.R., 1978. Warm springs, South Island, New Zealand, and their potentials to yield laumontite. Am. J. Sci. doi:10.2475/ajs.278.10.1412

Barth, N.C., 2014. The Cascade rock avalanche: Implications of a very large Alpine Fault-triggered failure, New Zealand. Landslides 11, 327–341. doi:10.1007/s10346-013-0389-1

Batt, G.E., Baldwin, S.L., Cottam, M. A., Fitzgerald, P.G., Brandon, M.T., Spell, T.L., 2004. Cenozoic plate boundary evolution in the South Island of New Zealand: New thermochronological constraints. Tectonics 23, 1–17. doi:10.1029/2003TC001527

Batt, G.E., Braun, J., 1999. The tectonic evolution of the Southern Alps, New Zealand: insights from fully thermally coupled dynamical modelling. Geophys. J. Int. 136, 403–420.

Batt, G.E., Kohn, B.P., Braun, J., McDougall, I., Ireland, T.R., 1999. New insight into the dynamic development of the Southern Alps, New Zealand, from detailed thermochronological investigation of the Mataketake Range pegmatites. Geol. Soc. London, Spec. Publ. 154, 261–282. doi:10.1144/GSL.SP.1999.154.01.12

Bear, J., 1972. Dynamics of Fluids in Porous Materials. Elsevier, New York.

Beaumont, C., 1981. Foreland basins. Geophys. J. R. Astron. Soc. 65, 291–329.

Beavan, J., Matheson, D., Denys, P., Denham, M., Herring, T., Hager, B., Molnar, P., 2004. A vertical deformation profile across the Southern Alps, New Zealand, from 3.5 years of continuous GPS data. Proc. Cah. du Cent. Eur. Géodynamique Séismologie Work. State GPS Vert. Position. Precis. Sep. Earth Process. by Sp. Geod. Luxemb. 23, 111–123.

Beavan, J., Moore, M., Pearson, C., Henderson, M., Parsons, B., Bourne, S., England, P., Walcott, D., Blick, G., Darby, D., Hodgkinson, K., 1999. Crustal deformation during 1994-1998 due to oblique continental collision in the central Southern Alps, New Zealand, and implications for seismic potential of the Alpine Fault. J. Geophys. Res. 104, 25233–25255.

Bense, V.F., Gleeson, T., Loveless, S.E., Bour, O., Scibek, J., 2013. Fault zone hydrogeology. Earth-Science Rev. 127, 171–192. doi:10.1016/j.earscirev.2013.09.008

Benson, W.N., 1952. Meeting of the Geological Division of the Pacific Science Congress in New Zealand, February 1949. Interim Proc. Geol. Soc. Am. Feb 1950 1, 11–13.

Berryman, K., Cooper, A.F., Norris, R.J., Sutherland, R., Villamor, P., 1998. Paleoseismic investigation of the Alpine Fault at Haast and Okuru. Geol. Soc. New Zeal. Misc. Publ. 101A, 44.

Berryman, K.R., Beanland, S., Cooper, A.F., Cutten, H.N., Norris, R.J., Wood, P.R., 1992. The Alpine Fault, New Zealand: Variation in Quaternary structural style and geomorphic expression. Ann. Tectonicae VI, 126–163.

Berryman, K.R., Cochran, U.A., Clark, K.J., Biasi, G.P., Langridge, R.M., Villamor, P., 2012. Major Earthquakes Occur Regularly on an Isolated Plate Boundary Fault. Science. 336, 1690–1693. doi:10.1126/science.1218959

Bickle, M.J., 1992. Transport mechanisms by fluid-flow in metamorphic rocks; oxygen and strontium decoupling in the Trois Seigneurs Massif; a consequence of kinetic dispersion? Am. J. Sci. 292, 289–316.

Bickle, M.J., McKenzie, D., 1987. The transport of heat and matter by fluids during metamorphism. Contrib. to Mineral. Petrol. 95, 384–392. doi:10.1007/BF00371852

Blanpied, M.L., Lockner, D.A., Byerlee, J.D., 1992. An earthquake mechanism based on the rapid sealing of faults. Nature 356, 133–135.

Boese, C.M., Townend, J., Smith, E., Stern, T., 2012. Microseismicity and stress in the vicinity of the Alpine Fault, central Southern Alps, New Zealand. J. Geophys. Res. 117, 1–20. doi:10.1029/2011JB008460

Boulton, C., Carpenter, B.M., Toy, V., Marone, C., 2012. Physical properties of surface outcrop cataclastic fault rocks, Alpine Fault, New Zealand. Geochemistry, Geophys. Geosystems 13, 1–13. doi:10.1029/2011GC003872

Bouwer, H., Rice, R.C., 1976. A slug test for determining hydraulic conductivity of unconfined aquifers with completely or partially penetrating wells. Water Resour. Res. 12, 423. doi:10.1029/WR012i003p00423

Brace, W.F., 1984. Permeability of crystalline rocks: new in situ measurements. J. Geophys. Res. 89, 4327–4330.

Brace, W.F., Kohlstedt, D.L., 1980. Limits on Lithospheric Stress Imposed by Laboratory Experiments. J. Geophys. Res. 85, 6248–6252.

Brace, W.F., Paulding, B.W., Scholz, C., 1966. Dilatancy in the fracture of crystalline rocks. J. Geophys. Res. 71, 3939–3953. doi:10.1029/JZ071i016p03939

Bradshaw, J.D., 1993. A review of the Median Tectonic Zone : Terrane boundaries and terrane amalgamation near the Median A review of the Median Tectonic Zone : terrane boundaries and terrane amalgamation near the Median Tectonic Li. New Zeal. J. Geol. Geophys. 36, 117–125. doi:10.1080/00288306.1993.9514559

Bradshaw, J.D., 1989. Cretaceous Geotectonic Patterns in the New Zealand Region. Tectonics 8, 803–820.

Brott, C.A., Blackwell, D.D., Ziagos, J.P., 1981. Thermal and tectonic implications of heat flow in the Eastern Snake River Plain, Idaho. J. Geophys. Res. 86, 11709. doi:10.1029/JB086iB12p11709

Byerlee, J., 1993. Model for episodic flow of high-pressure water in fault zones before earthquakes. Geology 21, 303–306.

Byerlee, J., 1978. Friction of rocks. Pure Appl. Geophys. PAGEOPH 116, 615–626. doi:10.1007/BF00876528

Byerlee, J.D., 1968. Brittle-ductile transition in rocks. J. Geophys. Res. 73, 4741–4750. doi:10.1029/JB073i014p04741

Caine, J.S., Evans, J.P., Forster, C.B., 1996. Fault zone architechture and permeability structure. Geology 24, 1025–1028. doi:10.1130/0091-7613(1996)024<1025

Campbell, J.R., Craw, D., Frew, R., Horton, T., Chamberlain, C.P., 2004. Geochemical signature of orogenic hydrothermal activity in an active tectonic intersection zone, Alpine Fault, New Zealand. Miner. Depos. 39, 437–451. doi:10.1007/s00126-004-0421-4

Cande, S.C., Stock, J.M., 2004. Pacific-Antarctic-Australia motion and the formation of the Macquarie Plate. Geophys. J. Int. 157, 399–414. doi:10.1111/j.1365-246X.2004.02224.x

Carpenter, B.M., Kitajima, H., Sutherland, R., Townend, J., Toy, V.G., Saffer, D.M., 2014. Hydraulic and acoustic properties of the active Alpine Fault, New Zealand: Laboratory measurements on DFDP-1 drill core. Earth Planet. Sci. Lett. 390, 45–51. doi:10.1016/j.epsl.2013.12.023

Carter, R.M., Norris, R.J., 1976. Cainozoic history of Southland New Zealand: an accord between geological observations and plate tectonic predictions. Earth Planet. Sci. Lett. 31, 85–94.

Cawood, P.A., Nemchin, A.A., Leverenz, A., Saeed, A., Ballance, P.F., 1999. U/Pb dating of detrital zircons: Implications for the provenance record of Gondwana margin terranes. Bull. Geol. Soc. Am. 111, 1107–1119. doi:10.1130/0016-7606(1999)111<1107:UPDODZ>2.3.CO;2

Chamberlain, C.J., Shelly, D.R., Townend, J., Stern, T.A., 2014. Low-frequency earthquakes reveal punctuated slow slip on the deep extent of the Alpine Fault, New Zealand. Geochemistry, Geophys. Geosystems 15, 2984–2999. doi:10.1002/2014GC005436.Received

Clauser, C., 1992. Permeability of crystalline rocks. Eos, Trans. Am. Geophys. Union 73, 233–238. doi:10.1029/91EO00190

Cochran, U.A., Clark, K.J., Howarth, J.D., Biasi, G.P., Langridge, R.M., Villamor, P., Berryman, K.R., Vandergoes, M.J., 2017. A plate boundary earthquake record from a wetland adjacent to the Alpine fault in New Zealand refines hazard estimates. Earth Planet. Sci. Lett. 464, 175–188. doi:10.1016/j.epsl.2017.02.026

Connolly, J.A.D., Podladchikov, Y.Y., 2004. Fluid flow in compressive tectonic settings: Implications for midcrustal seismic reflectors and downward fluid migration. J. Geophys. Res. B Solid Earth 109, 1–12. doi:10.1029/2003JB002822

Coombs, D.S., 1993. Dehydration veins in diagenetic and very-low-grade metamorphic rocks: features of the crustal seismogenic zone and their significance to mineral facies. J. Metamorph. Geol. 11, 389–399. doi:10.1111/j.1525-1314.1993.tb00156.x

Coombs, D.S., Cook, N.D.J., Campbell, J.D., Terrane, T.M., Island, S., Zealand, N., 1992. The Park Volcanics group : Field relations of an igneous suite emplaced in the Triassic - Jurassic Murihiku Terrane , South Island , New Zealand The Park Volcanics Group : field relations of an igneous suite emplaced in the. New Zeal. J. Geol. Geophys. 35, 337–351. doi:10.1080/00288306.1992.9514527

Coombs, D.S., Landis, C.A., Norris, R.J., Sinton, J.M., Borns, D.J., Craw, D., 1976. The Dun Mountain Ophiolite Belt, New Zealand, its tectonic setting, constitution, and origin, with special reference to the southern portion. Am. J. Sci. 276, 561–603.

Cooper, A.F., Barreiro, B.A., Kimbrough, D.L., Mattinson, J.M., 1987. Lamprophyre dyke intrusion and the age of the Alpine Fault, New Zealand. J. R. Soc. New Zeal. 21, 373–384. doi:10.1130/0091-7613(1987)15<941:LDIATA>2.0.CO;2

Cooper, A.F., 1980. Retrograde Alteration of Chromian Kyanite in Metachert and Amphibolite Whiteschist from the Southern Alps, New Zealand, with Implications for Uplift on the Alpine Fault. Contrib. to Mineral. Petrol. 75, 153–164.

Cooper, R.A., 1989. Early Paleozoic terranes of New Zealand. J. R. Soc. New Zeal. 19, 73–112. doi:10.1080/03036758.1989.10426457

Cox, S.C., Barrell, D.J.A., 2007. Geology of the Aoraki area. Institute of Geological and Nuclear Sciences 1:250,000 geological map 15.

Cox, S.C., Craw, D., Chamberlain, C.P., 1997. Structure and fluid migration in a late Cenozoic duplex system forming the Main Divide in the central Southern Alps, New Zealand. New Zeal. J. Geol. Geophys. 40, 359–373. doi:10.1080/00288306.1997.9514767

Cox, S.C., Findlay, R.H., 1995. The Main Divide Fault Zone and its role in formation of the Southern Alps, New Zealand. New Zeal. J. Geol. Geophys. 38, 489–499. doi:10.1080/00288306.1995.9514675

Cox, S.C., Menzies, C.D., Sutherland, R., Denys, P.H., Chamberlain, C., Teagle, D.A.H., 2015. Changes in hot spring temperature and hydrogeology of the Alpine Fault hanging wall, New Zealand, induced by distal South Island earthquakes. Geofluids 15, 216–239. doi:10.1111/gfl.12093

Cox, S.C., Sutherland, R., 2007. Regional Geological Framework of South Island, New Zealand, and its Significance for Understanding the Active Plate Boundary, in: Okaya, D., Stern, T., Davey, F. (Eds.), A Continental Plate Boundary: Tectonics at South Island, New Zealand. American Geophysical Union, Washington DC, pp. 19–46. doi:10.1029/175GM03

Cox, S., Howarth, J.D., Upton, P., Sutherland, R., Langridge, R., Barth, N.C., Atkins, C., DFDP-2 Science Team, 2015. Abstract T11G-02, Quaternary geology of the DFDP-2 drill holes, Alpine Fault, New Zealand presented at 2015 Fall Meeting, AGU, San Francisco, Calif., 14-18 Dec.

Craw, D., 1997. Fluid inclusion evidence for geothermal structure beneath the Southern Alps, New Zealand. New Zeal. J. Geol. Geophys. 40, 43–52. doi:10.1080/00288306.1997.9514739

Craw, D., 1995. Reinterpretation of the erosion profile across the southern portion of the Southern Alps, Mt Aspiring area, Otago, New Zealand Southern Alps, Mt Aspiring area, Otago, New Zealand. New Zeal. J. Geol. Geophys. 38, 501–507. doi:10.1080/00288306.1995.9514676

Craw, D., Burridge, C.P., Upton, P., Rowe, D.L., Waters, J.M., 2008. Evolution of biological dispersal corridors through a tectonically active mountain range in New Zealand. J. Biogeogr. 35, 1790–1802. doi:10.1111/j.1365-2699.2008.01936.x

Craw, D., Campbell, J.R., 2004. Tectonic and structural setting for active mesothermal gold vein systems, Southern Alps, New Zealand. J. Struct. Geol. 26, 995–1005. doi:10.1016/j.jsg.2003.11.012

Craw, D., Koons, P.O., Horton, T., Chamberlain, C.P., 2002. Tectonically driven fluid flow and gold mineralisation in active collisional orogenic belts: Comparison between New Zealand and western Himalaya. Tectonophysics 348, 135–153. doi:10.1016/S0040-1951(01)00253-0

Craw, D., Upton, P., Mackenzie, D.J., 2009. Hydrothermal alteration styles in ancient and modern orogenic gold deposits, New Zealand. New Zeal. J. Geol. Geophys. 52, 11–26. doi:10.1080/00288300909509874

Davey, F.J., Henyey, T., Kleffmann, S., Melhuish, A., Okaya, D., Stern, T.A., Woodward, D.J., the South Island Geophysical Transect (SIGHT) Working Group, 1995. Crustal reflections from the Alpine Fault Zone, South Island, New Zealand. New Zeal. J. Geol. Geophys. 38, 601–604.

DeCelles, P.G., Giles, K.A., 1996. Foreland basin systems. Basin Res. 8, 105–123.

DeMets, C., Gordon, R.G., Argus, D.F., Stein, S., 1994. Effects of recent revision to the geomagnetic reversal timescale on estimates of current plate motion. Geophys. Res. Lett. 21, 2191–2194.

Deming, D., 1994. Fluid flow and heat transport in the upper continental crust. Geol. Soc. London, Spec. Publ. 78, 27–42. doi:10.1144/GSL.SP.1994.078.01.04

Derry, L.A., Evans, M.J., Darling, R., France-Lanord, C., 2009. Hydrothermal heat flow near the Main Central Thrust, central Nepal Himalaya. Earth Planet. Sci. Lett. 286, 101–109. doi:10.1016/j.epsl.2009.06.036

Diersch, H.J.G., Kolditz, O., 2002. Variable-density flow and transport in porous media; approaches and challenges. 25 years, Adv. Water Resour. 25, 899–944. doi:10.1016/S0309-1708(02)00063-5

Dipple, G.M., Ferry, J.M., 1992. Metasomatism and fluid flow in ductile fault zones. Contrib. to Mineral. Petrol. 112, 149–164. doi:10.1007/BF00310451

Doan, M.L., Brodsky, E.E., Kano, Y., Ma, K.F., 2006. In situ measurement of the hydraulic diffusivity of the active Chelunepu Fault, Taiwan. Geophys. Res. Lett. 33, 1–5. doi:10.1029/2006GL026889

Domenico, P.A., Schwartz, F.W., 1990. Physical and Chemical Hydrogeology. John Wiley and Sons, New York.

Dzikowski, M., Josnin, J.Y., Roche, N., 2016. Thermal Influence of an Alpine Deep Hydrothermal Fault on the Surrounding Rocks. Groundwater 54, 55–65. doi:10.1111/gwat.12313

Eberhart-Phillips, D., 1995. Examination of seismicity in the central Alpine Fault region , South Island , New Zealand. New Zeal. J. Geol. Geophys. 38, 571–578. doi:10.1080/00288306.1995.9514685

England, P., Thompson, A., 1984. Pressure-Temperature-Time Paths of Regional Metamorphism 1. Heat Transfer During the Evolution of Regions of Thickened Continental Crust. J. Petrol. 25, 894–928. doi:10.1093/petrology/25.4.894

Etheridge, M.A., Wall, V.J., Vernon, R.H., 1983. The role of the fluid phase during regional metamorphism and deformation. J. Metamorph. Geol. 1, 205–226. doi:10.1111/j.1525-1314.1983.tb00272.x

Evans, J.P., Forster, C.B., Goddard, J.V., 1997. Permeability of fault-related rocks, and implications for hydraulic structure of fault zones. J. Struct. Geol. 19, 1393–1404. doi:10.1016/S0191-8141(97)00057-6

Evison, F.F., 1971. Seismicity of the Alpine Fault, in: Collins, B.W., Fraser, R. (Eds.), Recent Crustal Movements. Royal Society of New Zealand Bulletin 9. pp. 161–165.

Faulkner, D.R., Jackson, C.A.L., Lunn, R.J., Schlische, R.W., Shipton, Z.K., Wibberley, C.A.J., Withjack, M.O., 2010. A review of recent developments concerning the structure, mechanics and fluid flow properties of fault zones. J. Struct. Geol. 32, 1557–1575. doi:10.1016/j.jsg.2010.06.009

Faulkner, D.R., Lewis, A. C., Rutter, E.H., 2003. On the internal structure and mechanics of large strike-slip fault zones: Field observations of the Carboneras fault in southeastern Spain. Tectonophysics 367, 235–251. doi:10.1016/S0040-1951(03)00134-3

Ferry, J.M., 1994. Overview of the petrologic record of fluid flow during regional metamorphism in northern New England. Am. J. Sci. doi:10.2475/ajs.294.8.905

Ferry, J.M., Dipple, G.M., 1991. Fluid flow, mineral reactions, and metasomatism. Geology 19, 211–214. doi:10.1130/0091-7613(1991)019<0211:FFMRAM>2.3.CO

Ferry, J.M., Winslow, N.W., Penniston-Dorland, S.C., 2013. Re-evaluation of infiltration-driven regional metamorphism in northern New England: Newtransport models with solid solution and cross-layer equilibration of fluid compositio. J. Petrol. 54, 2455–2485. doi:10.1093/petrology/egt053

Fetter, C.W., 1999. Contaminant Hydrogeology. Prentice Hall, Upper Saddle River, N.J.

Forster, C., Smith, L., 1989. The influence of groundwater flow on thermal regimes in mountainous terrain: A model study. J. Geophys. Res. Solid … 94, 9439–9451. doi:10.1029/JB094iB07p09439

Freeze, R.A., Cherry, J.A., 1979. Groundwater. Prentice-Hall, Englewood Cliffs, NJ.

Fyfe, W.S., Price, N.J., Thompson, A.B., 1978. Fluids In The Earth's Crust. Elsevier, New York.

Garabedian, S.P., Leblanc, D.R., 1991. Large-scale natural gradient tracer test in sand and gravel, Cape Cod, Massachusetts: 2. Analysis of Spatial Moments for a Nonreactive Tracer. Water Resour. Res. 27, 895–910.

Germanovich, L.N., Lowell, R.P., 1992. Percolation Theory, Thermoelasticity, and Discrete Hydrothermal Venting in the Earth's Crust. Science. 255, 1564–1567.

Goldfarb, R.J., Groves, D.I., Gardoll, S.J., 2001. Orogenic gold and geologic time: a global synthesis. Ore Geol. Rev. 18, 1–75.

Grapes, R.H., 1995. Uplift and exhumation of Alpine Schist, Southern Alps, New Zealand: Thermobarometric constraints. New Zeal. J. Geol. Geophys. 38, 525–533. doi:10.1080/00288306.1995.9514679

Gray, D.R., Foster, D.A., 2004. 40Ar/39Ar thermochronologic constraints on deformation, metamorphism and cooling/exhumation of a Mesozoic accretionary wedge, Otago Schist, New Zealand. Tectonophysics 385, 181–210. doi:10.1016/j.tecto.2004.05.001

Green, D.C., 1992. High P Petrology and Geodynamics of Collision Processes. PhD thesis, University of Otago.

Groves, D.I., Goldfarb, R.J., Gebre-Mariam, M., Hagemann, S.G., Robert, F., 1998. Orogenic gold deposits: A proposed calssification in the context of their crustal contribution and relationship to other gold deposit types. Ore Geol. Rev. 13, 7–27. doi:10.1016/S0169-1368(97)00012-7

Harris, N., Massey, J., 1994. Decompression and anatexis of Himalayan metapelites. Tectonics 13, 1537–1546.

Herman, F., Cox, S.C., Kamp, P.J.J., 2009. Low-temperature thermochronology and thermokinematic modeling of deformation, exhumation, and development of topography in the central Southern Alps, New Zealand. Tectonics 28. doi:10.1029/2008TC002367

Hess, K.M., Wolf, S.H., Celia, M.A., 1992. Large-scale natural gradient tracer test in sand and gravel, Cape Cod, Massachusetts: 3. Hydraulic conductivity variability and calculated macrodispersivities. Water Resour. Res. 28, 2011–2027. doi:10.1029/92WR00668

Holdsworth, R.E., Strachan, R.A., 1991. Interlinked system of ductile strike slip and thrusting formed by Caledonian sinistral transpression in northeastern Greenland. Geology 19, 510–513.

Holm, D.K., Norris, R.J., David, C., 1989. Brittle and ductile deformation in a zone of rapid uplift: Central Southern Alps, New Zealand. Tectonics 8, 153–168.

Houghton, B.F., Landis, C.A., 1989. Sedimentation and volcanism in a Permian arc-related basin, southern New Zealand. Bull. Volcanol. 51, 433–450.

Houlsby, A.C., 1976. Routine Interpretation of the Lugeon Water-test. Q. J. Eng. Geol. Hydrogeol. 9, 303–313.

Howarth, J.D., Fitzsimons, S.J., Norris, R.J., Jacobsen, G.E., 2012. Lake sediments record cycles of sediment flux driven by large earthquakes on the Alpine fault, New Zealand. Geology 40, 1091–1094. doi:10.1130/G33486.1

Howell, D.G., 1980. Mesozoic accretion of exotic terranes along the New Zealand segment of Gondwanaland. Geology 8, 487–491.

Hubbert, M.K., 1940. The Theory of Ground-Water motion. J. Geol. 48, 785–944.

Hubbert, M.K., Rubey, W.W., 1959. Role of fluid pressure in overthrust faulting: I. Mechanics of fluid-filled porous solids and its application to overthrust faulting. Bull. Geol. Soc. Am. 70, 115–166. doi:10.1130/0016-7606(1959)70

Hvorslev, M.J., 1951. Time Lag and Soil Permeability in Ground-Water Observations. Bull. (Waterways Exp. Stn. Corps Eng. U.S. Army, Vicksburg, Mississippi) 36.

Ide, S., 2008. A Brownian walk model for slow earthquakes. Geophys. Res. Lett. 35, 3–7. doi:10.1029/2008GL034821

Imber, J., Holdsworth, R.E., Butler, C.A., 2001. A reappraisal of the Sibson-Scholz fault zone model: The nature of the frictional to viscous (“brittle-ductile”) transition along a long-lived, crustal-scale fault, Outer Hebrides, Scotalnd. Tectonics 20, 601–624.

Ingebritsen, S.E., Manning, C.E., 2010. Permeability of the Continental Crust: Dynamic Variations Inferred from Seismicity and Metamorphism. Geofluids 193–205. doi:10.1002/9781444394900.ch13

Ingebritsen, S.E., Manning, C.E., 2002. Diffuse fluid flux through orogenic belts: implications for the world ocean. Proc. Natl. Acad. Sci. U. S. A. 99, 9113–6. doi:10.1073/pnas.132275699

Ingebritsen, S.E., Manning, C.E., 1999. Geological implications of a permeability-depth curve for the continental crust. Geology 27, 1107–1110. doi:10.1130/0091-7613(1999)027<1107:GIOAPD>2.3.CO

John, T., Klemd, R., Gao, J., Garbe-Schönberg, C.D., 2008. Trace-element mobilization in slabs due to non steady-state fluid-rock interaction: Constraints from an eclogite-facies transport vein in blueschist (Tianshan, China). Lithos 103, 1–24. doi:10.1016/j.lithos.2007.09.005

Kamp, P.J.J., 2000. Thermochronology of the Torlesse accretionary complex, Wellington region, New Zealand. J. Geophys. Res. Earth 105, 19253–19272. doi:10.1029/2000jb900163

Kamp, P.J.J., 1986. The mid-Cenozoic Challenger Rift System of western New Zealand and its implications for the age of Alpine fault inception. Geol. Soc. Am. Bull. 97, 255–281. doi:10.1130/0016-7606(1986)97<255:tmcrso>2.0.co;2

Kamp, P.J.J., Green, P.F., Tippett, J.M., 1992. Tectonic Architecture of the Mountain-Foreland Basin Transition, South Island, New Zealand, Assessed by Fission Track Analysis. Tectonics 11, 98–113.

Kao, H., Chen, W., 2000. The Chi-Chi Earthquake Sequence: Active , Out-of-Sequence Thrust Faulting in Taiwan. Science. 288, 2346–2350.

Kear, D., Mortimer, N., 2003. Waipa Supergroup, New Zealand: A proposal. J. R. Soc. New Zeal. 33, 149–163. doi:10.1080/03014223.2003.9517725

Kohlstedt, D.L., Evans, B., Mackwell, S.J., 1995. Strength of the lithosphere: Constraints imposed by laboratory experiments. J. Geophys. Res. doi:10.1029/95JB01460

Koons, P.O., 1989. The topographic evolution of collisional mountain belts: a numerical look at the Southern Alps, New Zealand. Am. J. Sci. doi:10.2475/ajs.289.9.1041

Koons, P.O., 1987. Some thermal and mechanical consequences of rapid uplift: an example from the Southern Alps, New Zealand. Earth Planet. Sci. Lett. 86, 307–319. doi:10.1016/0012-821X(87)90228-7

Koons, P.O., Craw, D., 1991. Gold mineralization as a consequence of continental collision: an example from the Southern Alps, New Zealand. Earth Planet. Sci. Lett. 103, 1–9. doi:10.1016/0012-821X(91)90145-8

Koons, P.O., Kirby, E., 2007. Topography, denudation, and deformation: the role of surface processes on fault evolution, in: Handy, M.R., Hirth, G., Hovius, N. (Eds.), Tectonic Faults: Agents of Change on A Dynamic Earth. MIT Press, Cambridge, Massachusetts, pp. 205–230.

Koons, P.O., 1990. Two-sided orogen: Collision and erosion from the sandbox to the Southern Alps, New Zealand. Geology 18, 679–682. doi:10.1130/0091-7613(1990)018<0679

Lachenbruch, A.H., Sorey, M.L., Lewis, R.E., Sass, J.H., 1976. The Near-Surface Hydrothermal Regime of Long Valley Caldera for two dates. J. Geophys. Res. 81.

Lamb, S.H., Smith, E., Stern, T., Warren-Smith, E., 2015. Continent-scale strike-slip on a low-angle fault beneath New Zealand's Southern Alps: Implications for crustal thickening in oblique collision zones. Geochemistry, Geophys. Geosystems 3076–3096. doi:10.1002/2015GC005990.Received

Lancaster, P.J., Baxter, E.F., Ague, J.J., Breeding, C.M., Owens, T.L., 2008. Synchronous peak Barrovian metamorphism driven by syn-orogenic magmatism and fluid flow in southern Connecticut, USA. J. Metamorph. Geol. 26, 527–538. doi:10.1111/j.1525-1314.2008.00773.x

Lazear, G.D., 2006. Evidence for deep groundwater flow and convective heat transport in mountainous terrain, Delta County, Colorado, USA. Hydrogeol. J. 14, 1582–1598. doi:10.1007/s10040-006-0058-8

Leblanc, R., Hess, K.M., Gelhar, L.W., Wood, W., 1991. Large-scale natural gradient tracer test in sand and gravel, Cape Cod, Massachusetts: 1. Experimental Design and Observed Tracer Movement. Water Resour. 27, 895–910.

Leitner, B., Eberhart-Phillips, D., Anderson, H., Nabelek, J.L., 2001. A focused look at the Alpine Fault, New Zealand: Seismicity, focal mechanisms, and stress observations. J. Geophys. Res. 106, 2193–2220.

Little, T.A., Holcombe, R.J., Ilg, B.R., 2002. Ductile fabrics in the zone of active oblique convergence near the Alpine Fault, New Zealand: Identifying the neotectonic overprint. J. Struct. Geol. 24, 193–217. doi:10.1016/S0191-8141(01)00059-1

Little, T.A., Cox, S., Vry, J.K., Batt, G., 2005. Variations in exhumation level and uplift rate along the oblique-slip Alpine fault, central Southern Alps, New Zealand. Bull. Geol. Soc. Am. 117, 707–723. doi:10.1130/B25500.1

Lockner, D.A., Tanaka, H., Ito, H., Ikeda, R., Omura, K., Naka, H., 2009. Geometry of the Nojima fault at Nojima-Hirabayashi, Japan - I. A simple damage structure inferred from borehole core permeability. Pure Appl. Geophys. 166, 1649–1667. doi:10.1007/s00024-009-0515-0

Lopez, D.L., Smith, L., 1996. Fluid flow in fault zones: Influence of hydraulic anisotropy and heterogeneity on the fluid flow and heat transfer regime. Water Resour. Res. 32, 3227–3235.

Manga, M., Beresnev, I., Brodsky, E.E., Elkhoury, J.E., Elsworth, D., Ingebritsen, S.E., Mays, D.C., Wang, C., 2012. Changes in Permeability Caused By Transient Stresses : Field Observations ,

Experiments , and Mechanisms. Rev. Geophys. 50, 1–24. doi:10.1029/2011RG000382.1.INTRODUCTION

Manning, C.E., Ingebritsen, S.E., 1999. Permeability Implications of the Continental of Geothermal Data and Metamorphic Systems. Rev. Geophys. 37, 127–150.

McCaig, A.M., 1988. Deep fluid circulation in fault zones. Geology 16, 867–870. doi:10.1130/0091-7613(1988)016<0867

Menzies, C.D., Teagle, D.A.H., Craw, D., Cox, S.C., Boyce, A.J., Barrie, C.D., Roberts, S., 2014. Incursion of meteoric waters into the ductile regime in an active orogen. Earth Planet. Sci. Lett. 399, 1–13. doi:10.1016/j.epsl.2014.04.046

Menzies, C.D., Teagle, D.A.H., Niedermann, S., Cox, S.C., Craw, D., Zimmer, M., Cooper, M.J., Erzinger, J., 2016. The fluid budget of a continental plate boundary fault: Quantification from the Alpine Fault, New Zealand. Earth Planet. Sci. Lett. 445, 125–135. doi:10.1016/j.epsl.2016.03.046

Micarelli, L., Benedicto, A., Wibberley, C.A.J., 2006. Structural evolution and permeability of normal fault zones in highly porous carbonate rocks. J. Struct. Geol. 28, 1214–1227. doi:10.1016/j.jsg.2006.03.036

Miller, D.J., Dunne, T., 1996. Topographic perturbations of regional stresses and consequent bedrock fracturing. J. Geophys. Res. 101, 25523. doi:10.1029/96JB02531

Mitchell, T.M., Faulkner, D.R., 2009. The nature and origin of off-fault damage surrounding strike-slip fault zones with a wide range of displacements: A field study from the Atacama fault system, northern Chile. J. Struct. Geol. 31, 802–816. doi:10.1016/j.jsg.2009.05.002

Mitchell, T.M., Faulkner, D.R., 2012. Towards quantifying the matrix permeability of fault damage zones in low porosity rocks. Earth Planet. Sci. Lett. 339-340, 24–31. doi:10.1016/j.epsl.2012.05.014

Molnar, P., Atwater, T., Mammerickx, J., Smith, S.M., 1975. Magnetic Anomalies, Bathymetry and the Tectonic Evolution of the South Pacific since the Late Cretaceous. Geophys. J. R. astr. Soc. 40, 383–320. doi:10.1111/j.1365-246X.1975.tb04139.x

Molnar, P., England, P., Martinod, J., 1993. Mantle dynamics, uplift of the Tibetan Plateau and the Indian Monsoon. Rev. Geophys. 31, 357–396.

Morin, R.H., 2002. Topographic stress perturbations in southern Davis Mountains, west Texas 2. Hydrogeologic implications. J. Geophys. Res. 107, 1–10. doi:10.1029/2001JB000488

Mortimer, N., 2004. New Zealand's Geological Foundations. Gondwana Res. 7, 261–272. doi:10.1016/S1342-937X(05)70324-5

Mortimer, N., Gans, P., Calvert, A., Walker, N., 1999. Geology and thermochronometry of the east edge of the Median Batholith (Median Tectonic Zone): A new perspective on Permian to Cretaceous crustal growth of New Zealand. Isl. Arc 8, 404–425. doi:10.1046/j.1440-1738.1999.00249.x

Mortimer, N., Rattenbury, M.S., King, P.R., Bland, K.J., Barrell, D.J.A., Bache, F., Begg, J.G., Campbell, H.J., Cox, S.C., Crampton, J.S., Edbrooke, S.W., Forsyth, P.J., Johnston, M.R., Jongens, R., Lee, J.M., Leonard, G.S., Raine, J.I., Skinner, D.N.B., Timm, C., Townsend, D.B., Tulloch, A.J., Turnbull, I.M., Turnbull, R.E., 2014. High-level stratigraphic scheme for New Zealand rocks. New Zeal. J. Geol. Geophys. 57, 402–419. doi:10.1080/00288306.2014.946062

Mortimer, N., Roser, B.P., 1992. Geochemical evidence for the position of the Caples-Torlesse boundary in the Otago Schist, New Zealand. J. Geol. Soc. London. 149, 967–977. doi:10.1144/gsjgs.149.6.0967

Mortimer, N., Tulloch, A.J., Spark, R.N., WaLker, N.W., Ladey, E., Allibone, A., Kimbrough, D.L., 1999. Overview of the Median Batholith, New Zealand: a new interpretation of the geology of the Median Tectonic Zone and adjacent rocks. J. African Earth Sci. 29, 257–268.

National Institute of Water and Atmospheric Research, 2008. Southwest Pacific Region Bathymetry [WWW Document]. URL https://www.niwa.co.nz/our-science/oceans/bathymetry/download-the-data (accessed 13.01.2014).

Noda, A., Takeuchi, M., Adachi, M., 2004. Provenance of the Murihiku Terrane , New Zealand : evidence from the Jurassic conglomerates and sandstones in Southland. Sediment. Geol. 164, 203–222. doi:10.1016/j.sedgeo.2003.10.003

Norris, R.J., Cooper, A.F., 1995. Origin of small-scale segmentation and transpressional thrusting along the Alpine Fault, New Zealand. Geol. Soc. Am. Bull. 107, 231–240. doi:10.1130/0016-7606(1995)107<0231:OOSSSA>2.3.CO;2

Norris, R.J., Cooper, A.F., 2001. Late Quaternary slip rates and slip partitioning on the Alpine Fault, New Zealand. J. Struct. Geol. 23, 507–520. doi:10.1016/S0191-8141(00)00122-X

Norris, R.J., Cooper, A.F., 2007. The Alpine Fault, New Zealand: Surface geology and field relationships, in: Okaya, D., Stern, T., Davey, F. (Eds.), A Continental Plate Boundary: Tectonics at South Island, New Zealand. pp. 157–176. doi:10.1029/175GM09

Norris, R.J., Henley, R.W., 1976. Dewatering of a metamorphic pile. Geology 4, 333–336. doi:10.1130/0091-7613(1976)4<333:DOAMP>2.0.CO;2

Norris, R.J., Koons, P.O., Cooper, A. F., 1990. The obliquely-convergent plate boundary in the South Island of New Zealand: implications for ancient collision zones. J. Struct. Geol. 12, 715–725. doi:10.1016/0191-8141(90)90084-C

Obara, K., 2002. Nonvolcanic Deep Tremor Associated with Subduction in Southwest Japan. Science. 296, 1679–1681. doi:10.1126/science.1070378

Obara, K., Hirose, H., Yamamizu, F., Kasahara, K., 2004. Episodic slow slip events accompanied by non-volcanic tremors in southwest Japan subduction zone. Geophys. Res. Lett. 31, 1–4. doi:10.1029/2004GL020848

Okaya, D., Stern, T., Davey, F., Henrys, S., Cox, S., 2007. Continent-Continent Collision at the Pacific/Indo-Australian Plate Boundary: Background, Motivation, and Principal Results. A Cont. Plate Bound. Tectonics South Island, New Zeal. 1–18. doi:10.1029/175GM02

Owens, T.J., Zandt, G., 1997. Implications of crustal property variations for models of Tibetan plateau evolution. Nature 387, 37–43.

Phillips, O.M., 2009. Geological Fluid Dynamics. Cambridge University Press, Cambridge.

Pickard, A.L., Adams, C.J., Barley, M.E., 2000. Australian provenance for Upper Permian to Cretaceous rocks forming accretionary complexes on the New Zealand sector of the Gondwanaland margin. Aust. J. Earth Sci. 47, 987–1007. doi:10.1046/j.1440-0952.2000.00826.x

Pitcairn, I.K., Craw, D., Teagle, D.A.H., 2014. The gold conveyor belt: Large-scale gold mobility in an active orogen. Ore Geol. Rev. 62, 129–142. doi:10.1016/j.oregeorev.2014.03.006

Pitcairn, I.K., Teagle, D.A.H., Craw, D., Olivo, G.R., Kerrich, R., Brewer, T.S., 2006. Sources of metals and fluids in orogenic gold deposits: Insights from the Otago and Alpine schists, New Zealand. Econ. Geol. 101, 1525–1546. doi:10.2113/gsecongeo.101.8.1525

Powrie, W., Beaven, R.P., 1999. Hydraulic properties of household waste and implications for landfills. Proc. ICE - Geotech. Eng. 137, 235–247. doi:10.1680/geng.1997.137.4.235

Putnis, A., Austrheim, H., 2010. Fluid-induced processes: metasomatism and metamorphism. Geofluids 10, 254–269. doi:10.1111/j.1468-8123.2010.00285.x

Rau, G.C., Andersen, M.S., Acworth, R.I., 2012. Experimental investigation of the thermal dispersivity term and its significance in the heat transport equation for flow in sediments. Water Resour. Res. 48, 1–21. doi:10.1029/2011WR011038

Rau, G.C., Andersen, M.S., McCallum, A.M., Roshan, H., Acworth, R.I., 2014. Heat as a tracer to quantify water flow in near-surface sediments. Earth-Science Rev. 129, 40–58. doi:10.1016/j.earscirev.2013.10.015

Reyes, A.G., Christenson, B.W., Faure, K., 2010. Sources of solutes and heat in low-enthalpy mineral waters and their relation to tectonic setting, New Zealand. J. Volcanol. Geotherm. Res. 192, 117–141. doi:10.1016/j.jvolgeores.2010.02.015

Rojstaczer, S.A., Ingebritsen, S.E., Hayba, D.O., 2008. Permeability of continental crust influenced by internal and external forcing. Geofluids 8, 128–139. doi:10.1111/j.1468-8123.2008.00211.x

Roser, B.P., Coombs, D.S., Korsch, R.J., Campbell, J.D., 2002. Whole-rock geochemical variations and evolution of the arc-derived Murihiku Terrane , New Zealand. Geol. Mag. 139, 665–685. doi:10.1017/S0016756802006945

Saar, M.O., Manga, M., 2004. Depth dependence of permeability in the Oregon Cascades inferred from hydrogeologic, thermal, seismic, and magmatic modeling constraints. J. Geophys. Res. B Solid Earth 109, 1–19. doi:10.1029/2003JB002855

Savage, W.Z., Swolfs, H.S., 1986. Tectonic and Gravitational Stress in Long Symmetric Ridges and Valleys. J. Geophys. Res. 91, 3677–3685.

Savage, W.Z., Swolfs, H.S., Powers, P.S., 1985. Gravitational stresses in long symmetric ridges and valleys in anisotropic rock. Int. J. Rock Mech. Min. Sci. Geomech. 22, 291–302. doi:10.1016/0148-9062(94)90899-0

Schmid, S.M., Bernoulli, D., Fugenschuh, B., Matenco, L., Schefer, S., Schuster, R., Tischler, M., Ustaszewski, K., 2008. The Alpine-Carpathian-Dinaridic orogenic system: correlation and evolution of tectonic units. Swiss J. Geosci. 101, 139–183. doi:10.1007/s00015-008-1247-3

Scholz, C.H., 1998. Earthquakes and friction laws. Nature 391, 37–42. doi:10.1038/34097

Searle, M.P., Cottle, J.M., Streule, M.J., Waters, D.J., 2010. Crustal melt granites and migmatites along the Himalaya: melt source, segregation, transport and granite emplacement mechanisms. Earth Environ. Sci. Trans. R. Socitey Edinburgh 100, 219–233. doi:10.1017/S175569100901617X

Searle, M.P., Simpson, R.L., Law, R.D., Parrish, R.R., Waters, D.J., 2003. The structural geometry, metamorphic and magmatic evolution of the Everest massif, High Himalaya of Nepal – South Tibet. J. Geol. Soc. London. 160, 345–366.

Segall, P., Rice, J.R., 2006. Does shear heating of pore fluid contribute to earthquake nucleation? J. Geophys. Res. Solid Earth 111, 1–17. doi:10.1029/2005JB004129

Shankar, R., Guha, S.K., Seth, N.N., Muthuraman, K., 1991. Geothermal Atlas of India. Geological Survey of India, Calcutta.

Shapiro, A.M., Ladderud, J.A., Yager, R.M., 2015. Interpretation of hydraulic conductivity in a fractured-rock aquifer over increasingly larger length dimensions. Hydrogeol. J. 23, 1319–1339. doi:10.1007/s10040-015-1285-7

Shi, Y., Allis, R., Davey, F., 1996. Thermal modeling of the Southern Alps, New Zealand. Pure Appl. Geophys. 146, 469–501. doi:10.1007/BF00874730

Shmonov, V.M., Vitiovtova, V.M., Zharikov, A.V., Grafchikov, A.A., 2003. Permeability of the continental crust: implications of experimental data. J. Geochemical Explor. 78-79, 687–699.

Sibson, R.H., 1996. Structural permeability of fluid-driven fault-fracture meshes-Sibson-J Struct Geol-1996.pdf. J. Struct. Geol. 18, 1031–1042.

Sibson, R.H., 1992. Implications of fault-valve behaviour for rupture nucleation and recurrence. Tectonophysics 211, 283–293. doi:10.1016/0040-1951(92)90065-E

Sibson, R.H., 1990. Conditions for fault-valve behaviour. Geol. Soc. London, Spec. Publ. 15–28.

Sibson, R.H., 1983. Continental fault structure and the shallow earthquake source. J. Geol. Soc. London. 140, 741–767. doi:10.1144/gsjgs.140.5.0741

Sibson, R.H., 1973. Interactions between Temperature and Pore-Fluid Pressure during Earthquake Faulting and a Mechanism for Partial or Total Stress Relief. Nat. Phys. Sci. 243, 66–68.

Sibson, R.H., White, S.H., Atkinson, B.K., 1979. Fault rock distribution and structure within the Alpine Fault Zone: A preliminary account. Bull. R. Soc. New Zeal. 18, 55–66.

Sims, A., Cox, S.C., Fitzsimons, S., Holland, P., 2015. Seasonal infiltration and groundwater movement in schist bedrock, Southern Alps, New Zealand. J. Hydrol. 54, 33–52.

Spandler, C., Worden, K., Arculus, R., Eggins, S., 2005. Igneous rocks of the Brook Street Terrane, New Zealand: Implications for Permian tectonics of eastern Gondwana and magma genesis in modern intra-oceanic volcanic arcs. New Zeal. J. Geol. Geophys. 48, 167–183. doi:10.1080/00288306.2005.9515107

Stein, C.A., 1995. Heat Flow of the Earth, in: Global Earth Physics – A Handbook of Physical Constants, AGU Reference Shelf 1. American Geophysical Union, Washington DC, pp. 144–158. doi:10.1112/S0024609301008396

Stern, T., Kleffmann, S., Okaya, D., Scherwath, M., Bannister, S., 2001. Low seismic wave-speeds and enhanced fluid pressure beneath the Southern Alps of. New Zealand, Geol. 29, 679–682.

Stern, T., Okaya, D., Kleffmann, S., Scherwath, M., Henrys, S., Davey, F., 2007. Geophysical Exploration and Dynamics of the Alpine Fault Zone 207–234.

Stirling, M.W., Wesnousky, S.G., Berryman, K.R., 1998. Probabilistic seismic hazard analysis of New Zealand. New Zeal. J. Geol. Geophys. 41, 355–375. doi:10.1080/00288306.1998.9514816

Stober, I., Bucher, K., 2015. Hydraulic conductivity of fractured upper crust: Insights from hydraulic tests in boreholes and fluid-rock interaction in crystalline basement rocks. Geofluids 15, 161–178. doi:10.1002/9781119166573.ch15

Stober, I., Bucher, K., 2007. Hydraulic properties of the crystalline basement. Hydrogeol. J. 15, 213–224. doi:10.1007/s10040-006-0094-4

Sutherland, R., 1996. Transpressional development of the Australia-Pacific boundary through southern South Island, New Zealand: Constraints from Miocene-Pliocene sediments, Waiho-1 borehole, South Westland. New Zeal. J. Geol. Geophys. 39, 251–264. doi:10.1080/00288306.1996.9514709

Sutherland, R., 1995. The Australia-Pacific in the SW Pacific : boundary and Cenozoic plate motions. Tectonics 14, 819–831.

Sutherland, R., Berryman, K., Norris, R., 2006. Quaternary slip rate and geomorphology of the Alpine fault: Implications for kinematics and seismic hazard in southwest New Zealand. Bull. Geol. Soc. Am. 118, 464–474. doi:10.1130/B25627.1

Sutherland, R., Davey, F., Beaven, J., 2000. Plate boundary deformation in South Island, New Zealand, is related to inherit lithospheric structure. Earth Planet. Sci. Lett. 177, 141–151.

Sutherland, R., Harris, R.A., Stern, T., Beavan, J., Ellis, S., Henrys, S., Cox, S., Norris, R.J., Berryman, K.R., Townend, J., Bannister, S., Pettinga, J., Leitner, B., 2007. Do Great Earthquakes Occur on the Alpine Fault in Central South Island, New Zealand?, in: Okaya, D., Stern, T., Davey, F. (Eds.), A Continental Plate Boundary: Tectonics at South Island, New Zealand. American Geophysical Union, Washington DC, pp. 235–251.

Sutherland, R., Norris, R.J., 1995. Late Quaternary displacement rate, paleoseismicity, and geomorphic evolution of the Alpine Fault: Evidence from Hokuri Creek, South Westland, New Zealand. New Zeal. J. Geol. Geophys. 38, 419–430. doi:10.1080/00288306.1995.9514669

Sutherland, R., Townend, J., Toy, V., Upton, P., Coussens, J., Allen, M., Baratin, L.-M., Barth, N., Becroft, L., Boese, C., Boles, A., Boulton, C., Broderick, N.G.R., Janku-Capova, L., Carpenter, B.M., Célérier, B., Chamberlain, C., Cooper, A., Coutts, A., Cox, S., Craw, L., Doan, M.-L., Eccles, J., Faulkner, D., Grieve, J., Grochowski, J., Gulley, A., Hartog, A., Howarth, J., Jacobs, K., Jeppson, T., Kato, N., Keys, S., Kirilova, M., Kometani, Y., Langridge, R., Lin, W., Little, T., Lukacs, A., Mallyon, D., Mariani, E., Massiot, C., Mathewson, L., Melosh, B., Menzies, C., Moore, J., Morales, L., Morgan, C., Mori, H., Niemeijer, A., Nishikawa, O., Prior, D., Sauer, K., Savage, M., Schleicher, A., Schmitt, D.R., Shigematsu, N., Taylor-Offord, S., Teagle, D., Tobin, H., Valdez, R., Weaver, K., Wiersberg, T., Williams, J., Woodman, N., Zimmer, M., 2017. Extreme hydrothermal conditions at an active plate-bounding fault. Nature 546, 137–140. doi:10.1038/nature22355

Sutherland, R., Toy, V., Townend, J., Eccles, J., Prior, D.J., Norris, R.J., Mariani, E., Faulkner, D.R., Pascale, G. de, Carpenter, B.M., Boulton, C., Menzies, C.D., Cox, S., Little., T.A., Hasting, M., Cole-Baker, J., Langridge, R., Scott, H.R., Lindroos, Z.R., Fleming, B., Wing, R., 2011. Operations and well completion report for boreholes DFDP-1A and DFDP-1B, Deep Fault Drilling Project, Alpine Fault, Gaunt Creek, New Zealand.

Sutherland, R., Toy, V.G., Townend, J., Cox, S.C., Eccles, J.D., Faulkner, D.R., Prior, D.J., Norris, R.J., Mariani, E., Boulton, C., Carpenter, B.M., Menzies, C.D., Little, T.A., Hasting, M., De Pascale, G.P., Langridge, R.M., Scott, H.R., Reid Lindroos, Z., Fleming, B., Kopf, J., 2012. Drilling reveals fluid control on architecture and rupture of the Alpine fault, New Zealand. Geology 40, 1143–1146. doi:10.1130/G33614.1

Tait, A., Henderson, R., Turner, R., Zheng, X., 2006. Thin plate smoothing spline interpolation of daily rainfall for New Zealand using climatological rainfall surface. Int. J. Climatol. 26, 2097–2115. doi:10.1002/joc

Teagle, D.A.H., Hall, C.M., Cox, S.C., Craw, D., 1998. Ar/Ar dating of hydrothermal minerals in the Southern Alps, New Zealand. Mineral. Mag. 62A, 1496–1497.

Theis, C.V., 1935. The relation between the lowering of the Piezometric surface and the rate and duration of discharge of a well using ground-water storage. Trans. Am. Geophys. Union 519–524.

Thiem, G., 1906. Hydrologische Methoden. Gebhardt, Leipzig.

Thompson, A.B., England, P.C., 1984. Pressure Temperature Time Paths of Regional Metamorphism .2. Their Inference and Interpretation Using Mineral Assemblages in Metamorphic Rocks. J. Petrol. 25, 929–955.

Tippett, J.M., Kamp, P.J.J., 1993. Fission Track Analysis of the Late Cenozoic Veritical Kinematics of Continental Crust, South Island, New Zealand. J. Geophys. Res. 98, 16119–16148.

Tóth, J., 1963. A theoretical analysis of groundwater flow in small drainage basins. J. Geophys. Res. 68, 4795–4812. doi:10.1029/JZ068i016p04795

Tóth, J., 1962. A Theory of Groundwater Motion in Small Drainage Basins Hydrology in Central Alberta, Canada. J. Geophys. Res. 67, 4375–4387. doi:10.1029/JZ067i011p04375

Townend, J., Zoback, M.D., 2000. How faulting keeps the crust strong. Geology 28, 399–402.

Toy, V.G., Boulton, C.J., Sutherland, R., Townend, J., Norris, R.J., Little, T.A., Prior, D.J., Mariani, E., Faulkner, D., Menzies, C.D., Scott, H., Carpenter, B.M., 2015. Fault rock lithologies and architecture of the central Alpine fault, New Zealand, revealed by DFDP-1 drilling. Lithosphere 7, 155–173. doi:10.1130/l395.1

Toy, V.G., Craw, D., Cooper, A.F., Norris, R.J., 2010. Thermal regime in the central Alpine Fault zone, New Zealand: Constraints from microstructures, biotite chemistry and fluid inclusion data. Tectonophysics 485, 178–192. doi:10.1016/j.tecto.2009.12.013

U.S. Geological Survey, 2017. Geologic Province Map [WWW Document]. URL https://earthquake.usgs.gov/data/crust/type.html (accessed 26.07.2017).

Upton, P., Craw, D., Caldwell, T., Koons, P., James, Z., Wannamaker, P., Jiracek, G., Chamberlain, C., 2003. Upper crustal fluid flow in the outboard region of the Southern Alps, New Zealand. Geofluids 3, 1–12. doi:10.1046/j.1468-8123.2003.00046.x

Upton, P., Koons, P.O., Chamberlain, C.P., 1995. Penetration of deformation driven meteoric water into ductile rocks: Isotopic and model observations from the Southern Alps, New Zealand. New Zeal. J. Geol. Geophys. 38, 535–543. doi:10.1080/00288306.1995.9514680

Upton, P., Sutherland, R., 2014. High permeability and low temperature correlates with proximity to brittle failure within mountains at an active tectonic boundary, Manapouri tunnel, Fiordland, New Zealand. Earth Planet. Sci. Lett. 389, 176–187. doi:10.1016/j.epsl.2013.12.032

Van Orstrand, V.E., 1934. Temperature gradient, in: Problems of Petroleum Geology. American Association of Petroleum Geologists, pp. 989–1021.

Vance, D., Strachan, R.A., Jones, K.A., 1998. Extensional versus compressional settings for metamorphism: Garnet chronometry and pressure-temperature-time histories in the Moine Supergroup , northwest Scotland. Geology 26, 927–930.

Vry, J.K., Baker, J., Maas, R., Little, T.A., Grapes, R., Dixon, M., 2004. Zoned (Cretaceous and Cenozoic) garnet and the timing of high grade metamorphism, Southern Alps, New Zealand. J. Metamorph. Geol. 22, 137–157. doi:10.1111/j.1525-1314.2004.00504.x

Walcott, R.I., 1998. Modes of oblique compression: Late Cenozoic tectonics of the south island of New Zealand. Rev. Geophys. 36, 1–26. doi:10.1029/97RG03084

Wallace, L.M., Beavan, J., McCaffrey, R., Berryman, K., Denys, P., 2007. Balancing the plate motion budget in the South Island, New Zealand using GPS, geological and seismological datas. Geophys. J. Int. 168, 332–352. doi:10.1111/j.1365-246X.2006.03183.x

Wannamaker, P.E., Jiracek, G.R., Stodt, J.A., Caldwell, T.G., Gonzalez, V.M., McKnight, D.J., Porter, A.D., 2002. Fluid generation and pathways beneath an active compressional orogen, the New Zealand Southern Alps, inferred from magnetotelluric data. J. Geophys. Res. 107, 1–21. doi:10.1029/2001JB000186

Warr, L.N., Cox, S., 2001. Clay mineral transformations and weakening mechanisms along the Alpine Fault, New Zealand. Geol. Soc. London, Spec. Publ. 186, 85–101. doi:10.1144/GSL.SP.2001.186.01.06

Wech, a. G., Boese, C.M., Stern, T.A., Townend, J., 2012. Tectonic tremor and deep slow slip on the Alpine Fault. Geophys. Res. Lett. 39, 1–6. doi:10.1029/2012GL051751

Wells, A., Yetton, M.D., Duncan, R.P., Stewart, G.H., 1999. Prehistoric dates of the most recent Alpine fault earthquakes, New Zealand. Geology 27, 995–998. doi:10.1130/0091-7613(1999)027<0995:PDOTMR>2.3.CO;2

Whipp, D.M., Ehlers, T.A., 2007. Influence of groundwater flow on thermochronometer-derived exhumation rates in the central Nepalese Himalaya. Geology 35, 851–854. doi:10.1130/G23788A.1

White, J.C., White, S.H., 1983. Semi-brittle deformation within the Alpine fault zone, New Zealand. J. Struct. Geol. 5, 579–589. doi:10.1016/0191-8141(83)90070-6

Wibberley, C.A.J., Shimamoto, T., 2005. Earthquake slip weakening and asperities explained by thermal pressurization. Nature 436, 689–692. doi:10.1038/nature03901

Wibberley, C.A.J., Shimamoto, T., 2003. Internal structure and permeability of major strike-slip fault zones: The Median Tectonic Line in Mie Prefecture, Southwest Japan. J. Struct. Geol. 25, 59–78. doi:10.1016/S0191-8141(02)00014-7

Wood, R., Lamarche, G., Herzer, R., Delteil, J., Davy, B., 1996. Paleogene seafloor spreading in the southeast Tasman Sea. Tectonics 15, 966–975. doi:10.1029/96TC00129

Yardley, B.W.D., 2009. The role of water in the evolution of the continental crust. J. Geol. Soc. London 166, 585–600. doi:10.1144/0016-76492008-101.Review

Yardley, B.W.D., Rochelle, C.A., Barnicoat, A.C., Lloyd, G.E., 1991. Oscillatory Zoning in Metamorphic Minerals - an Indicator of Infiltration Metasomatism. Mineral. Mag. 55, 357–365. doi:10.1180/minmag.1991.055.380.06

Yetton, M.D., 1998. Progress in understanding the paleoseismicity of the central and northern Alpine Fault, Westland, New Zealand. New Zeal. J. Geol. Geophys. 41, 475–483. doi:10.1080/00288306.1998.9514824

Yin, A., 2006. Cenozoic tectonic evolution of the Himalayan orogen as constrained by along-strike variation of structural geometry, exhumation history, and foreland sedimentation. Earth-Science Rev. 76, 1–131. doi:10.1016/j.earscirev.2005.05.004

Zhang, S., Paterson, M.S., Cox, F., 1994. Porosity and permeability evolution during hot isostatic pressing of calcite aggregates. J. Geophys. Res. 99, 15741–15760.

Zheng, Y.F., Fu, B., Gong, B., Li, L., 2003. Stable isotope geochemistry of ultrahigh pressure metamorphic rocks from the Dabie-Sulu orogen in China: Implications for geodynamics and fluid regime. Earth-Science Rev. 62, 105–161. doi:10.1016/S0012-8252(02)00133-2

Zhisheng, A., Kutzbach, J.E., Prell, W.L., Porter, S.C., 2001. Evolution of Asian monsoons and phased uplift of the Himalaya-Tibetan plateau since Late Miocene times. Nature 411, 62–66.

Chapter 2:

Regional groundwater flow in an active orogenic mountain belt; evidence from the Amethyst Ravine, Southern Alps, New Zealand

Abstract

Meteoric water penetrates to the brittle-ductile transition in the Southern Alps and can influence orogenic processes through heat and mass transport and through the influence of pore fluid pressure on deformation. To understand how meteoric and shallow ground waters affect deformation, mineralization, and the thermal structure of mountain belts, better knowledge is required of key parameters such as permeability and infiltration rate. The construction of a hydroelectric power station on the Amethyst Ravine in the Southern Alps allowed borehole water level and packer test permeability measurements to be undertaken. Here, borehole water levels from the Amethyst Ravine are combined with hydrogeological models to determine possible ranges of regional-scale permeability and infiltration rate. Models consistent with borehole data require a high elevation water table across the Southern Alps, which is up to 1.4 km above the adjacent valley floor at interfluves, with widespread seeps on valley sides and some rivers, up to at least 1750 m elevation, in continuity with groundwater. Regional infiltration must be ≥0.02 % of precipitation but is >20 % precipitation if measured hydraulic conductivity values from the Amethyst Ravine are representative of rocks at similar depths across the region. For investigated permeability structures, the majority (>70 %) of infiltrating water travels on shallow flow paths <500 m below ground surface. If treated as a homogeneous, regional parameter, hydraulic conductivity must be $\leq 5 \times 10^{-7}$ m·s^{-1} in models to reproduce water levels observed in the Amethyst boreholes. The corresponding upper bound for intrinsic permeability is ~10^{-13} m^2.

2.1 Introduction

The Alpine Fault, New Zealand is a major transpressional plate-bounding fault (Fig. 2.1a), accommodating the majority of the ~10 mm·yr^{-1} convergent and 37-40 mm·yr^{-1} dextral strike slip motion between the Australian and Pacific plates (DeMets et al., 1994; Norris and Cooper, 2001). Rapid uplift on the Alpine Fault, which is estimated to dip at 40-60° (Sibson et al., 1979; Stern et al., 2007), has resulted in the formation of the Southern Alps (Little et al., 2005) and elevated temperatures in the shallow orogen, raising the brittle-ductile transition in the region to 6 - 10 km

depth (Boese et al., 2012; Koons, 1987; Leitner et al., 2001). Although uplift rates are high, there have been no large (M_w > 7) earthquakes on the central Alpine Fault since European settlement ca. 1800 A.D., and there is no evidence for aseismic creep at the surface (Sutherland et al., 2007). However, studies of landslides, forest damage and palaeoseismic excavations have suggested that in the past, the Alpine Fault has generated large (M_w > 7) to great (M_w ≥ 8) earthquakes (Sutherland et al., 2007). Recent statistical analyses suggest average recurrence intervals of 291 ± 23 years between these events (Cochran et al., 2017). The last of these was in 1717 A.D. (Wells et al., 1999), 300 years ago, suggesting that the fault is late in its seismic cycle.

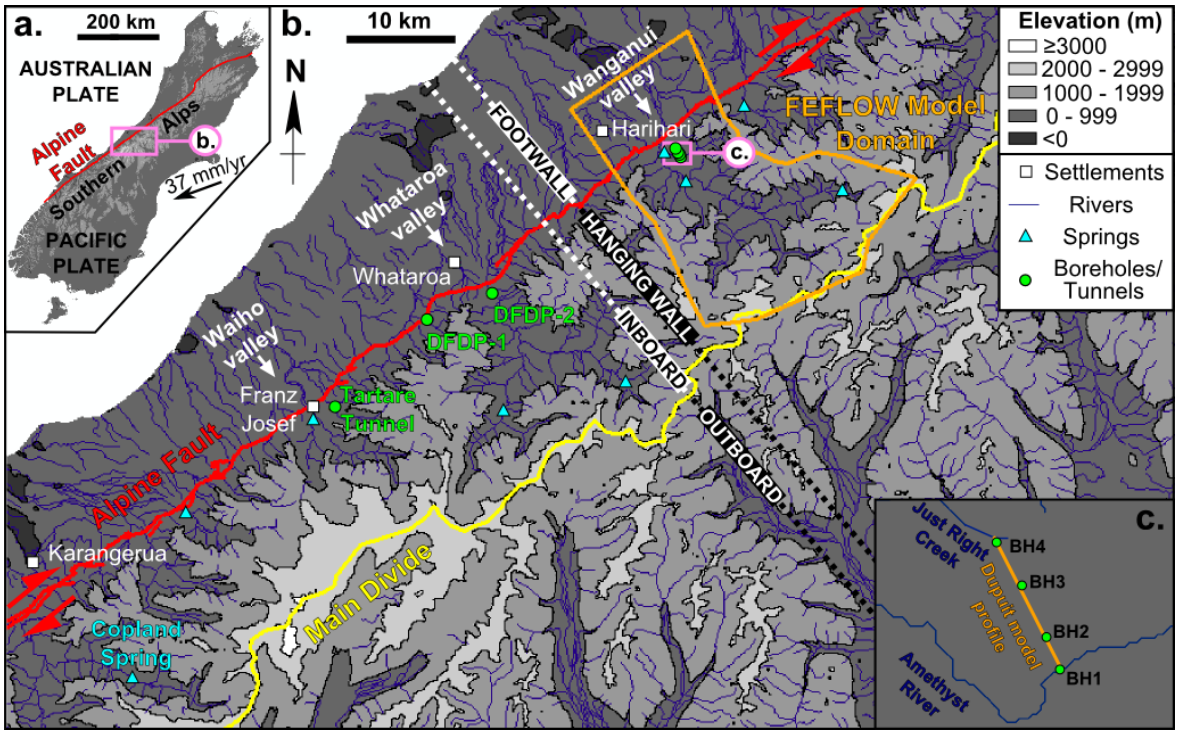

Figure 2.1 a. The tectonic setting. b. The three-dimensional model domain in the context of the central Southern Alps. River positions are based on the National Institute of Water and Atmospheric Research (2010) dataset. c. The Amethyst boreholes and profile of one-dimensional models (A1-A2).

Abundant warm springs in the Southern Alps (Fig. 2.1b) and the common presence of hydrothermal veins testify to past and ongoing fluid flow within the orogen (Barnes et al., 1978; Menzies et al., 2016). Furthermore, magnetotelluric surveys have revealed a u-shaped high electrical conductivity zone in the mid- to lower crust, interpreted as a highly interconnected, saline fluid (Upton et al., 2003; Wannamaker et al., 2002). Fluids have the potential to influence the mechanical behaviour of faults. Increased fluid pressures reduce effective confining stress on a fault, meaning that changes in fluid pressure could influence if and when a fault fails (Hubbert and Rubey 1959). Furthermore, fluid flow can cause alteration and precipitation of secondary minerals in fault zone rocks, which can further influence fault strength by modifying the fault's

frictional properties and by infilling pore spaces, causing changes in permeability that may play a crucial role in fluid pressure modulation on or near fault planes (Blanpied et al., 1992; Byerlee, 1993; Sibson, 1992). By modifying heat flow through advection, fluid flow is also able to influence the thermal structure of collisional mountain belts. The temperature regime controls the depths at which minerals undergo a transition from brittle to ductile deformational behaviour and also the interval over which they display velocity weakening frictional behaviour, necessary for earthquake nucleation (Blanpied et al., 1992; Chester, 1994; Nakatani, 2001; Rice et al., 2001). Detailed knowledge of groundwater flow in the crust below the Southern Alps would therefore provide important insights into the mechanical behaviour of the Alpine Fault.

Stable isotopic measurements of fluids and vein minerals and fluid flux estimates indicate that meteoric fluids penetrate down to the brittle-ductile transition zone and are the dominant fluids throughout the brittle crust (Menzies et al., 2014). To better understand fluid flow throughout the brittle crust, down to depths where fluids may influence earthquake nucleation and the behaviour of the Alpine Fault (>6 km Fagereng and Toy, 2011), knowledge of the shallow (<6 km depth) groundwater flow regime is required. Of particular interest are infiltration rates, which place an upper bound on amount of meteoric water available for processes at depth, and permeability structure, a control on fluid flow at depth. Aqueous fluids can play a key role in metamorphic reactions and mineral assemblages are commonly used to calculate required fluid fluxes (Ague, 1997; Bickle, 1992; Dipple and Ferry, 1992). Infiltration rate at the surface provides an upper bound on available meteoric water. Permeability values must be assigned for numerical modelling of the roles of fluids in mass transport and mineralization (e.g. Garven et al., 1999), heat transport (e.g. Whipp and Ehlers, 2007) and deformation (e.g. Strayer et al., 2001). Permeability is often not well constrained (Garven et al., 1999). The scale dependence of permeability estimates from laboratory tests and some in-situ measurements indicates that these methods often sample too small a volume to give representative estimates of regional-scale permeability and therefore may be of limited use (Clauser, 1992; Manning and Ingebritsen, 1999). Furthermore, where the fluid flow regime of interest is no longer active, permeability may have changed significantly since fluid processes of interest took place. In studies of metamorphism and mineralization, estimates of regional permeability in such extinct fluid flow systems are obtained based on the time-integrated fluid fluxes required for reactions (Dipple and Ferry, 1992).

This study seeks to establish constrained estimates of regional infiltration rate and permeability structure and to identify characteristics of the active shallow flow system in Southern Alps, using data from the Amethyst Power Project. To do this, a range of hydrogeological models are tested, some with permeability calibrated to measurements from Amethyst dataset, against minimum water table elevations, based on observations from the same dataset. Features of the shallow

flow regime in models consistent with these data are documented. Both simplified analytical models and three-dimensional finite element models are used, in order identify the features of the Southern Alps orogen that are a fundamental in controlling its flow regime.

2.2 Regional setting

The study begins by reviewing the existing knowledge of the system, which will inform decisions in the modelling process, such as choices of boundary conditions and parameters.

2.2.1 Geography and hydrology

The highest average precipitation rates across the Southern Alps are ~13 $m \cdot yr^{-1}$ (Tait et al., 2006). The predominantly westerly winds in the Southern Ocean interact with the Southern Alps to concentrate rainfall and erosion on the western slopes of the Main Divide, producing a rain shadow to the east (Cox and Sutherland, 2007). The resulting asymmetry in erosion has resulted in a two-sided geometry in the orogen, with a steep inboard wedge and an outboard wedge with a topographic plateau (Koons 1990). In the inboard region (Fig. 2.1b), rapid uplift and erosion has formed a series of parallel ridges and valleys that trend perpendicular to the Alpine Fault, away from the Main Divide (Koons, 1989). These valleys contain rivers, some fed by upstream glaciers, which carry precipitation toward the Alpine Fault and low lying footwall. Hence orogenic processes have established a topographic drive for groundwater flow that converges into valleys from interfluves either side, and descends from the Main Divide toward the footwall. Warm springs, located within valleys and restricted to the hanging wall side of the fault, attest to such convergence. In addition to outflow at warm springs within valleys, groundwater seeps have been observed along valley margins at a sub-set of locations in the region during fieldwork by the author. Regional maps of the positions of these seeps are not currently available, due to the densely vegetated steep terrain and the need for prolonged dry periods in order to distinguish seeps from run-off.

2.2.2 Geology

The Alpine Fault exhumes quartzo-feldspathic metamorphic Alpine Schist in its hanging wall, which is juxtaposed against metasediments and granitoids on the Australian Plate in the footwall (Cox and Barrell, 2007). The Alpine Schist is part of the Haast Schist Group, which consists of rocks deformed during the Jurassic-Cretaceous. A near full crustal section is exposed from the Alpine Fault towards the Main Divide, with garnet-oligoclase-zone amphibolite facies schists exposed at low altitudes adjacent to the fault and sub-greenschist facies semi-schists and greywackes

(Mortimer, 2004) forming the highest peaks to the east. Uplift on the Alpine Fault since the Neogene has resulted in further deformation, with mylonites developed within ~1 km and cataclasis within 10-100 m of the fault (Norris and Cooper, 2007). As a result, the Alpine Schist contains multiple generations of foliation, with a transition in the dominant foliation from a dip of 30-50° near to the fault, to sub-vertical at the Main Divide (Little et al. 2002). Alpine Schist rocks to the west of the Main Divide (Fig. 2.1b) display seismic anisotropy, in contrast to the unfoliated greywackes to the east which are isotopic (Christensen and Okaya, 2007). Multiple generations of veins, which have formed along fractures, joints, faults and shears as well as within foliation boundinage, attest to past fluid flow in hanging wall rocks (Menzies et al., 2014). Cataclastic rocks in the hanging wall of the Alpine Fault are partially altered to clay minerals, calcite and quartz as a result of fluid flow (Norris and Cooper, 2007; Sutherland et al., 2012; Warr and Cox, 2001).

2.2.3 Hydrogeology

The rocks of the Southern Alps are pervasively fractured (Clarke and Burbank, 2011). Because primary permeability in metamorphic rocks is typically minimal (Freeze and Cherry, 1979), the secondary permeability provided by these fractures is inferred to provide the main pathways for groundwater flow. There is a lack of hydrogeologic data for the orogen, in particular the inboard region, as a result of a low population density and relative inaccessibility. Data that are available have been obtained from studies of hot springs, hydrothermal veins and measurements in tunnels and boreholes.

Copland spring is a warm spring in the Copland valley near Karangarua (Fig. 2.1b). Spring temperature has been observed to show responses to large earthquakes (Cox et al., 2015). It was inferred that these changes reflect changes in fracture apertures associated with stress field variations.

Tatare Tunnel was excavated during the 19th century in the Tatare Gorge near Franz Josef township (Fig. 2.1b). Rapid responses to major rainfall events observed in tunnel water discharge are consistent with flow through highly fractured rocks (Maréchal and Etcheverry, 2003; Sims et al., 2015). Outflow data from the tunnel provides the only known published infiltration estimate for the Southern Alps. This gives values of 0.3 % to 20 % of precipitation, based on an assumed catchment area for the tunnels of 0.54 km^3 (Sims et al., 2015). However, a reliable estimate of the catchment area is hard to make, given the lack of understanding of the groundwater flow system in the vicinity of the tunnel.

The DFDP-1A and B boreholes (Fig. 2.1b) were drilled <200 m from the Alpine Fault trace, penetrating the fault at depths of 91 m and 128 m respectively (Sutherland et al., 2011). Slug tests

were carried out in these boreholes, yielding permeability, k, estimates of the order 10^{-14} m^2 (hydraulic conductivity, K = 10^{-8} m·s^{-1} to 10^{-7} m·s^{-1} at 0.01-10 °C, 1 atm). Significantly lower fluid pressures were recorded in the fault footwall compared to the hanging wall in the DFDP-1B borehole, with a 0.53 MPa pressure drop across fault core, suggesting that the fault may act as a barrier to fluid flow, at least at shallow depths (Sutherland et al., 2012). This is supported by laboratory measurements of samples from DFDP-1 cores (Carpenter et al., 2014) and outcrops (Boulton et al., 2012) that indicate permeabilities of the order of 10^{-20} m^2 (K = 10^{-14} m·s^{-1} at 0.01-10 °C, 1 atm) for the fault gouge. A series of further permeability estimates in unpublished engineering reports from across the Southern Alps were collated by Cox et al. (2015). These include data from the Amethyst Ravine, discussed in this study, as well as from a number of studies near the Main Divide. Estimated K in these studies ranges from 10^{-10} m·s^{-1} to 10^{-4} m·s^{-1} (k = 10^{-17} m^2 to 10^{-11} m^2 at 0.01-10 °C, 1 atm).

Geochemical studies of hydrothermal vein minerals and spring water provide insights into the flow regime on a regional scale. Spring waters and veins from the Alpine Fault Zone all have $^{87}Sr/^{86}Sr$ ratios within the range of hanging wall rocks, which suggests that fluids circulating on the hanging wall side of the Alpine Fault have not interacted with highly radiogenic rocks of the Australian plate footwall (Menzies et al., 2016), consistent with the fault acting as a barrier to flow down to the brittle-ductile transition. Estimates from geochemical tracer transport modelling, based on oxygen and hydrogen stable isotopic compositions of quartz veins and fluid inclusions, suggest 0.02 % to 0.05 % of precipitation penetrates to the top of the brittle-ductile transition zone at ~6 km depth (Menzies et al., 2016).

2.3 The Amethyst Ravine

The Amethyst Ravine lies approximately 1 km south-east of the Alpine Fault (Fig. 2.1b-c.), adjacent to the Wanganui valley. This valley runs for approximately 14 km between the Main Divide and the Alpine Fault and has a span of approximately 2.5 km at its widest point. Elevation increases from <100 m where the valley meets the fault to peaks of >2500 m at the Main Divide to the south-east of the valley. All elevations given in this study are relative to reference ellipsoid GRS80 (for further information on the NZGD2000 geodetic datum see Land Information New Zealand, 2008).

Table 2.1 Hydrogeological data used in hydrogeological modelling of the Amethyst Ravine region. Grid references are in the New Zealand 1949 Geodetic Datum. Continued overleaf.

CONSTRAINT	DATA				SOURCE
Borehole information	**Borehole name**	**Grid reference (NZ 1949 GD)**	**Borehole plunge, length (m)**	**Surface elevation at borehole above mean sea level (m)**	Geotech Consulting Ltd. (2006)
	BH1	N5778850, E2318710	12°, 200.0	525 (±5)	
	BH2	N5779081, E2318620	90°, 180.1	684 (±5)	
	BH3	N5779446, E2318445	90°, 309.1	725 (±9)	
	BH4	N5779756, E2318265	0°, 201.5	322 (±5)	
Hydraulic conductivity, K	**Location**	**Depth of base of packer from surface (m)**	**Elevation of base of packer, above mean sea level (m)**	**Hydraulic Conductivity, K (m·s^{-1})**	Geotech Consulting Ltd. (2006)
	BH2	165	519 (±5)	4.89×10^{-6}	
	BH3	232	493 (±9)	1.50×10^{-5}	
	BH3	232	493 (±9)	1.50×10^{-5}	
	BH3	301.6	423.4 (±9)	1.40×10^{-5}	
	Waikukupa River	1.16×10^{-20} to 1.71×10^{-20}			

CONSTRAINT (CONT.)	DATA (CONT.)			SOURCE (CONT.)
Borehole water levels	**Location**	**Observed water level, above mean sea level (m)**		Geotech Consulting Ltd. (2006)
		Minimum	**Maximum**	
	BH2	552.98 (±5)	556.21 (±5)	
	BH1	Water flowing out of hole at 40 to 60 m borehole length		
Seeps	**Location**	**Seeps locations**		Field observations by the author
	Whataroa and Wanganui valleys	Seeps observed at the foot of ridges in both river valleys		
Amethyst tunnel observations	**Location**	**Observations**		S. Cox pers. comm.
	Amethyst tunnel	Most of the flow into the tunnel occurs in the eastern 1/3 of the tunnel.		

CONSTRAINT (CONT.)	DATA (CONT.)				SOURCE (CONT.)
Rainfall	**Location**	**Minimum Average Annual Rainfall ($m \cdot yr^{-1}$)**	**Maximum Average Annual Rainfall ($m \cdot yr^{-1}$)**	**Dataset**	Tait et al. (2006)
	New Zealand wide data	2.571	12.6081	Estimated mean annual rainfall for the period 1960-2004, derived using thin plate smoothing spline interpolation method.	
Alpine Fault gouge permeability	**Location**	**Permeability, k (m^2)**			
	DFDP-1	1.62×10^{-20}			Carpenter et al. (2014)
	Gaunt Creek	7.45×10^{-20}			Boulton et al. (2012)

During 2005-2006 four boreholes (BH1, BH2, BH3 and BH4) were drilled and measurements taken (Fig. 2.2), as part of a project to redirect the Amethyst river to a hydroelectric power station (Geotech Consulting Ltd., 2006). All boreholes were left uncased and open to flow along their entire length. Packer test measurements of K were taken at BH2 and BH3 and these range from 4.9×10^{-6} m·s^{-1} to 2.7×10^{-5} m·s^{-1} (Table 2.1; see also supplementary information from Cox et al., 2015). Borehole water level data was recorded at BH1 and BH2. At BH2, the water levels were monitored using a piezometer for several months following borehole drilling. The water level recorded was 49 m to 52 m above the base of the borehole at 504 ± 5 m elevation throughout the measurement period. Water levels in BH1 were not monitored, but artesian flow occurred when the borehole reached 40 to 60 m length (517-513 ± 5 m above sea level).

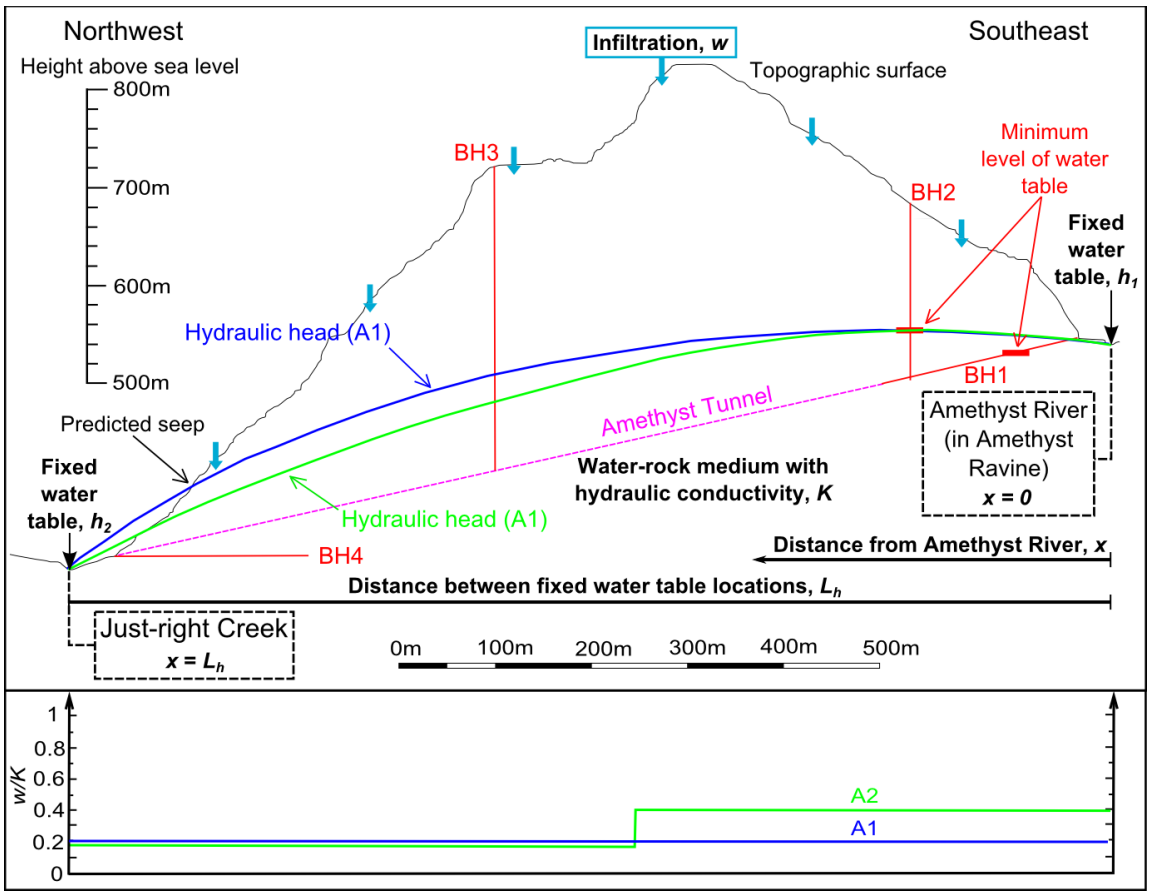

Figure 2.2 Cross section through the drilled region at the Amethyst Ravine. Positions of boreholes BH1-BH4 are indicated, together with minimum water table levels where appropriate. Two one-dimensional analytical solutions, based on Dupuit's assumptions for the position of the water table are plotted, with infiltration to hydraulic conductivity ratio (w/K) adjusted to cause the simulated head to intersect the observed minimum position of the water table, based on borehole measurements. Model A1 has a constant w/K, Model A2 has a stepped w/K, as might be produced by greater infiltration on the southeast hill slope.

2.3.1 Water table location

Since the boreholes at Amethyst were open to flow along their entire length during drilling and observation, water levels do not precisely record the position of the water table, nor the hydraulic head at a specified depth, unless there is no head gradient along the drilled interval. If one considers a system in only two dimensions, for topography-controlled flow from a ridge to a valley in a medium of uniform permeability, the hydraulic head decreases vertically beneath the central portion of the ridge (Hubbert, 1940; Tóth, 1962). If it is assumed that this is true beneath the south-eastern section of the Amethyst ridge, near to where BH2 was drilled, the hydraulic head will decrease down the borehole. Thus, the water level in the borehole will be lower than the water table would be at that point in the absence of the borehole. This is because the open borehole provides a pathway for water to move downwards, to the lower hydraulic heads at depth. Based on this assumption, the lowest measured water level in BH2, 553 ± 5 m above mean sea level, is taken to represent the minimum position of the water table at BH2, against which models are tested (Fig. 2.2). Consistency of three-dimensional model results with these assumptions is considered further in the discussion of results of these models.

The observation of water flowing out of the near horizontal (12° plunge) BH1 once borehole length reached 40-60 m, provides an estimate of the minimum depth of the water table in that location. Due to the low angle of this borehole, flow is likely to result from a lateral head gradient, rather than reflecting a vertical increase in hydraulic head along the borehole. Irrespective of hydraulic gradients, it is assumed that the water table cannot be lower than the elevation of the tunnel when water began flowing (i.e. at 40-60 m along the borehole). A minimum of 513 ± 5 m for the water table at 60 m down BH1 is therefore adopted for testing models.

2.4 Modelling approaches

Two types of model were used to study the Amethyst Ravine region. Analytical models, in which hydraulic head varies in one dimension, allow for an initial simplified analysis of the key parameters that may control the regional hydrology. Finite element models are then used to give a fuller three-dimensional study of the region. Given that spatial variability in infiltration and permeability may both feasibly span orders of magnitude and given that the water level data gives minimum, rather than exact water levels, the study does not seek to find a particular optimum permeability structure or infiltration distribution. Rather, a range of pre-defined permeability and infiltration scenarios are investigated in order to explore the effects that different permeability structures and infiltration values have on the flow regime and to eliminate those that are inconsistent with data.

The study utilises models that assume homogeneous water properties and those where water density, ρ and viscosity, μ are state dependent. Both ρ and μ have the potential to influence Darcian flow, which is given by:

$$\boldsymbol{q} = -\frac{\boldsymbol{k}}{\mu} \cdot (\nabla p + \rho g \hat{\boldsymbol{n}}) \tag{2.1}$$

Where $\boldsymbol{q}$ is the Darcy velocity vector, $\boldsymbol{k}$ is the intrinsic permeability tensor, p is the pressure, g is the acceleration due to gravity and $\hat{\boldsymbol{n}}$ is a unit vector oriented vertically upward. The assumption of homogeneous water properties allows for straightforward insights into the system, which are then built upon using the results of more the complex models with inhomogeneous fluid properties. In addition to intrinsic permeability, k, it proves useful to consider models assuming homogeneous fluid properties in terms of hydraulic conductivity, K, which also describes ρ and μ of the fluid flowing. K is defined as $k\rho g/\mu$ and is the parameter estimated in most borehole hydraulic tests to characterise permeability (e.g. Hvorslev, 1951; Bouwer and Rice, 1976), including the packer tests carried out in the Amethyst boreholes (Houlsby, 1976).

2.5 One-dimensional analytical modelling

One-dimensional models of the profile containing the boreholes (Fig. 2.1c) interpolate the position of the water table in the locality and can be calibrated based on the borehole measurements. The models use the Dupuit assumptions for flow of a homogeneous fluid between two fixed heads in an unconfined aquifer, which are that flow is horizontal, with vertical equipotentials, that the gradient of the water table is small and that the hydraulic head gradient is proportional to the slope of the water table. These models are described here as 'one-dimensional' because although they have a vertical dimension, in which the elevation of the water table is expressed, hydraulic head only varies in one dimension, which is horizontal. The first model, Model A1, assumes constant hydraulic conductivity and infiltration rate. For this case, the phreatic surface is described by the equation:

$$h = \sqrt{{h_1}^2 - \frac{({h_1}^2 - {h_2}^2)x}{L_h} + \frac{w}{K}(L_h - x)x} \tag{2.2}$$

Where h is the elevation of the water table at x; h_1 and h_2 are the fixed water table elevations at either end of the model; L_h is the distance between h_1 and h_2; x is the distance from fixed head h_1; w is the infiltration rate; and K is the hydraulic conductivity. Fixed heads equal to the surface elevation were assumed at the Amethyst River (x = 0) and at Just Right Creek (x = L_h), (Fig. 2.2). The validity of this assumption is evaluated further in the Discussion. w/K, the ratio of infiltration to hydraulic conductivity, is the unknown parameter in Eq. 2.2 and was varied to find which conditions produce a water table compatible with the borehole water levels. As well as constant

w/K, a model with a spatial step in w/K simulating higher infiltration on the south-eastern side of the ridge was investigated (Model A2). This is based on observations of greater inflow to the Amethyst hydroelectric tunnel (Fig. 2.2) in this location by S. Cox. In this model, there is a transition in w/K at D_h, where D_h is the distance from the Amethyst River (x = 0) to the peak of the ridge, such that:

For $x \leq D_h$: (2.3)

$$\frac{w}{K} = \frac{w_1}{K_1}$$

For $x > D_h$: (2.4)

$$\frac{w}{K} = \frac{w_2}{K_2}$$

In this case:

For $x \leq D_h$: (2.5)

$$h = \sqrt{C_1 x + C_2 - \frac{w_1}{K_1} x^2}$$

For $x > D_h$: (2.6)

$$h = \sqrt{C_3 x + C_4 - \frac{w_2}{K_2} x^2}$$

Where:

$$C_1 = C_3 - 2D_h \left(\frac{w_2}{K_2} - \frac{w_1}{K_1}\right) \quad (2.7)$$

$$C_2 = {h_1}^2 \quad (2.8)$$

$$C_3 = \frac{1}{L_h}\left({h_2}^2 + \frac{w_2}{K_2} L_h^2 - C_4\right) \quad (2.9)$$

$$C_4 = {h_1}^2 - D_h^2 \left(\frac{w_2}{K_2} - \frac{w_1}{K_1}\right) \quad (2.10)$$

2.5.1 Results and discussion from one-dimensional analytical modelling

For Model A1, the minimum w/K ratio required to produce a water table consistent with the lower bounds from Amethyst borehole measurements was 0.29. Because the head exceeds the ground elevation, a seep is predicted on the north-western hillside of the model (Fig. 2.2). Setting w/K = 0.29 and using K = 4.9 × 10^{-6} m·s^{-1}, the minimum hydraulic conductivity measured during borehole packer tests, requires w = 44 m·yr^{-1} (1.4 × 10^{-6} m·s^{-1}). However, the highest average precipitation rates across the Southern Alps are ~13 m·yr^{-1} (Tait et al., 2006). As no glaciers are present within 5 km of the Amethyst boreholes or in the vicinity of the sources of the Amethyst River or Just Right Creek, glacial meltwater would seem unlikely to produce the major additional contribution to infiltration required.

For Model A2, with $K_{1,2}$ = 4.9 × 10^{-6} m·s^{-1} and infiltration on the western slope set to the maximum precipitation rate, w_2 = 13 m·yr^{-1}, an infiltration rate of 62 m·yr^{-1}, greatly in excess of the precipitation rate, is still required on the south-eastern slope.

Although Model A2 does not offer a clear solution to the incompatibility between observed K and water table constraints, it does demonstrate the capacity for variations in permeability structure and infiltration rate to influence the shape and elevation of the water table. Thus, there are three possible explanations for the unrealistically high w required by models A1 and A2:

1) Packer test measurements overestimate K at the ridge. This could result from damage during drilling. $K \leq 1.4 \times 10^{-7}$ m·s^{-1} is required for infiltration ≤100 % precipitation.

2) w/K variation is significant and more complex than considered in these simple models.

3) The Dupuit assumptions break down and are not useful for this setting.

Three-dimensional finite element modelling allows for further investigation of points 2) and 3) as these models are not constrained by the Dupuit assumptions and w and K may be varied with greater complexity.

2.6 Finite element modelling

Three-dimensional finite element models (Fig. 2.3) were built using the groundwater simulation software FEFLOW (Diersch, 2014). Five sets of models were created. Model sets have different k features, to investigate the effect that each feature would have on flow in the region (Table 2.2), with the absolute values assigned for k and w varied within models of the set. Four sets of models constructed (B1 to B4) assume homogeneous water properties. As such, these models can be described in terms of K. However, to allow comparison with other model sets in which water properties are not homogeneous, a corresponding k is also defined. A set of minimum temperature reference surface conditions (0.01 °C, 1 atm) are used to define k in these models, which give k = 2 × 10^{N-7} m^2 for K = 1 × 10^N m·s^{-1}. Changes in water ρ and μ between 0.01 °C to 10 °C at 1 atm are relatively minor, meaning that corresponding k values are not heavily dependent (varying by a factor <1.4) on the exact choice of reference temperature within this range. The conditions chosen provide a low temperature baseline against which a fifth, thermally coupled model set (B5) can be compared. B5 models have k assigned to equal values in equivalent uncoupled models and simulate coupled fluid and heat flow, with water properties that are temperature and pressure dependent (Table 2.2).

Table 2.2 Features of three-dimensional model sets. IAF = Impermeable Alpine Fault, VK = Variable *k* with depth, A = Anisotropic *k*, TC = Thermal coupling.

Model Set	**IAF**	**VD**	**A**	**TC**	K **(m·s^{-1})**	k **(m^2)**	w
B1 'Homogeneous k'	No	No	No	No	5×10^N and 1×10^N for integers N = -6 to -11	9×10^N and 2×10^N for integers N = -13 to -18	Spatially variable: 1×10^N % and 2×10^N % precipitation for integers N = -3 to 3 (all sets); 1.5×10^N % and 3×10^N % precipitation for integers N = 0 to 1 (B5 only) Homogeneous: Calibrated to 1 s.f. (B1 and B2 only)
B2 'Low k fault'	Yes	No	No	No	5×10^N and 1×10^N for integers N = -6 to -11	9×10^N and 2×10^N for integers N = -13 to -18	
B3 'Variable k with depth'	Yes	Yes	No	No	Depth < 301.6 m: 1×10^{-6}; Depth > 301.6 m: 1×10^N for integers N = -6, -7, -8, and -10	Depth < 301.6 m: 2×10^{-13}; Depth > 301.6 m: 2×10^N for integers N = -13, -14, -15, and -16	
B4 'Anisotropic k'	Yes	No	Yes	No	k_p = 10 k_n = 1.3×10^N for integers N = -6, -7, -8 (calibrated to equal BH2 water table elevation in B2 for w = 1 %, 10 % and 100 % precipitation)	k_p = 10 k_n = 2.4×10^N for integers N = -13, -14, -15 (calibrated to equal BH2 water table elevation in B2 for w = 1 %, 10 % and 100 % precipitation)	
B5 'Thermally coupled'	Yes	No	No	Yes*	N/A	9×10^{-15}, 2×10^{-15} and 9×10^{-16}	

*In B5 models the groundwater flow equation includes variable density and viscosity as a function of temperature, T, and pressure, p, making the Boussinesq approximation. The equations of state for water density $\rho(T, p)$ and viscosity $\mu(T)$ are estimated using the approximations given by Magri et al. (2009) and Mercer and Pinder (1974) respectively, which are valid for conditions in the range 0 °C ≤ T ≤ 300 °C; 0.1 MPa ≤ p ≤ 100 MPa.

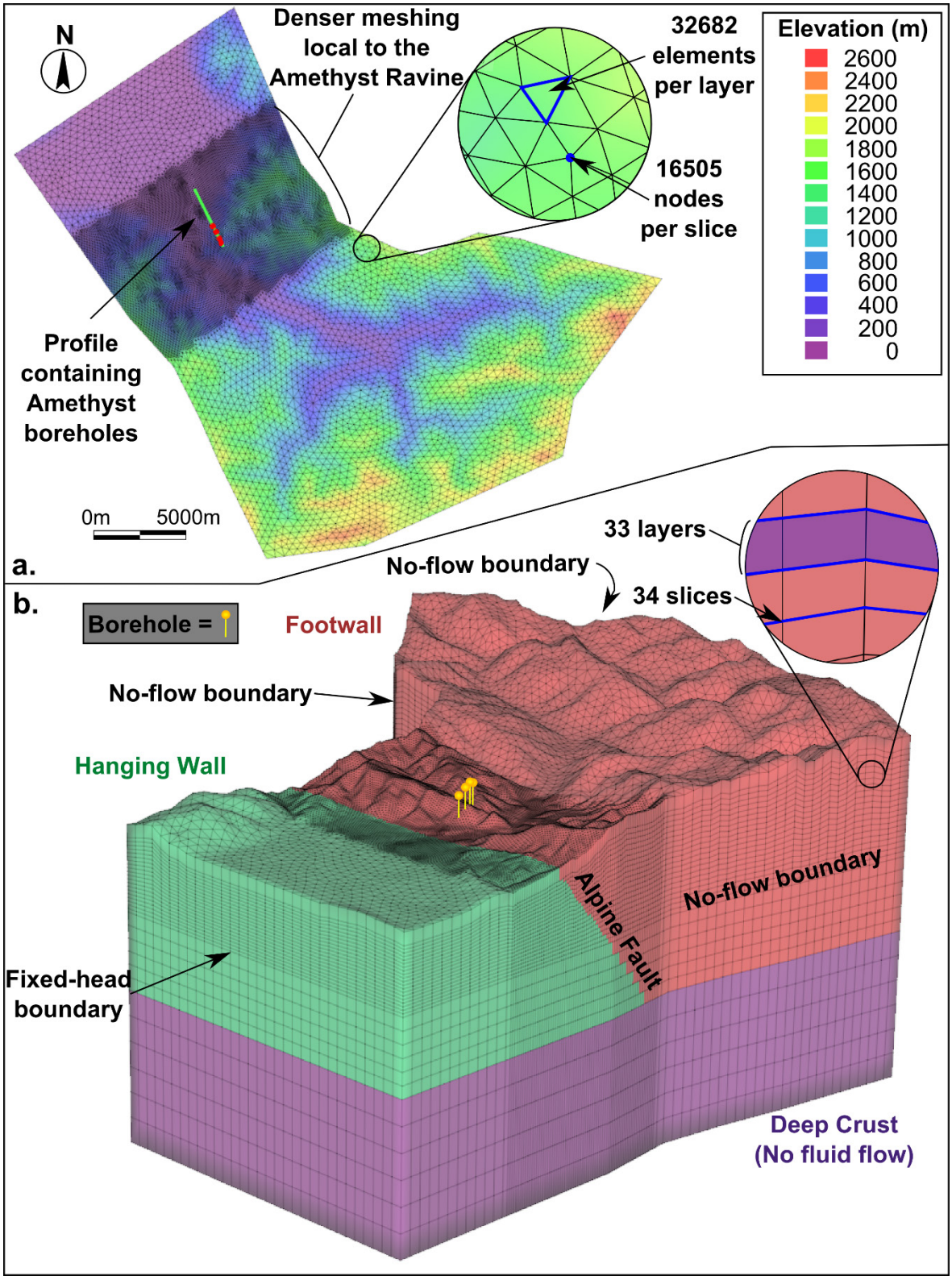

Figure 2.3 Caption opposite.

Figure 2.3 (Opposite) a. Top down view on the large-scale FEFLOW model, showing the location of the Amethyst boreholes within the model domain. b. Three-dimensional view of the FEFLOW model illustrating the model Alpine Fault, which is impermeable in some models. On the top slice of the model a fixed-head condition is automatically applied where the water table reaches the surface. All other boundaries are no-flow with respect to fluid, apart from the downstream boundary of the model, where a fixed head condition at surface elevation is applied in order to allow outflow along this boundary. At the base of the model (below -6 km) is a low permeability zone (k = 2 × 10^{-20} m^2; K = 10^{-13} $m \cdot s^{-1}$) with a no-fluid flow boundary at its base. This zone was deactivated in model sets B1-B4 and only activated in set B5 during a set-up phase of simulation, to establish fixed temperatures at the -6 km. Thus for final flow simulation, the top of this zone was a no-fluid flow boundary for all model sets.

The top boundary of the model domain is the ground surface. The presence of abundant warm springs in river valleys in the Southern Alps, the evidence for groundwater seeps from fieldwork and the water tables rising above surface elevation produced by models A1 and A2 all suggest that up-flow of groundwater into rivers and out of seeps may be significant. In order to allow models to simulate this, a fixed head (Dirichlet) boundary condition at surface elevation is automatically applied to any model node where the water table reaches the surface, thereby simulating the location of a seep or river. Infiltration rate is set as a fixed fluid flux (Neumann) boundary condition on the top slice of the model. Both spatially constant infiltration and infiltration as a fixed percentage of spatially variable precipitation rate (Tait et al., 2006) are investigated. Spatially variable precipitation rate averaged across the model domain equates to a rate of 6 $m \cdot yr^{-1}$. It is assumed that flow through the unsaturated zone does not limit infiltration rates.

The model domain has lateral no-fluid flow boundaries set along the drainage divides of the Wanganui River catchment, which are assumed to correspond to groundwater divides, and a downstream fixed head boundary, set at the ground surface elevation above each boundary node. Meshing density is increased for the immediate region surrounding the Amethyst Ravine, to improve the accuracy of the solution in this region.

The basal boundary is horizontal at -12 km elevation, however, it is assumed that the shallow topographically driven groundwater flow system ends at the top of brittle-ductile transition zone, set at -6 km elevation in models, and allocate a relatively low permeability (k = 2 × 10^{-20} m^2; i.e. K = 10^{-13} $m \cdot s^{-1}$) to the region below. This lower portion of the model domain is activated only in

thermally coupled models (B5), for an initial set-up phase. Thus for final flow simulation, all models have a no-fluid flow boundary at -6 km.

For the thermally coupled model set B5, a fixed temperature (Dirichlet) boundary condition of 10 °C is applied to the surface of the model. The thermal effects of rock advection are implemented though application of a rock advection velocity field to represent rock movement throughout the model domain, with a conductive heat flux field applied to the base of the model, with no conductive heat flow across lateral boundaries. Values used for this simulation of rock advection are generated by the FLAC model described by Sutherland et al. (2017), assuming a convergence rate of 12 $mm \cdot yr^{-1}$ and are applied to the FEFLOW model using the same method as employed in that study (see Chapter 5, section 5.11.1, for a full outline of this method). For consistency with this FLAC model, a homogeneous porosity of 0.1 is assumed for the purposes of calculating thermal conductivity and volumetric heat capacity of bulk water-rock medium (Table 2.3). Although fracture porosity is commonly much smaller than this ($<10^{-3}$) and is also expected to vary with depth (Freeze and Cherry, 1979; Ingebritsen and Manning, 2003; Snow, 1968), the uncertainty associated with this choice of porosity (rather than a much lower value) is small compared to the possible range in these parameters, based on measured rock properties (Eppelbaum et al., 2014). The exact contribution of rock advection to groundwater movement is, however, heavily dependent on porosity. Because of this, the simple model employed to simulate the thermal effects of rock advection is not also employed to simulate transport of fluid by rock advection (i.e. the mass flux field is implemented only for the purposes of heat flow simulation). Rather, it is assumed that groundwater average linear velocities are sufficiently high that the contribution of rock advection to movement of water is negligible in comparison. This assumption is reasonable for models of the Southern Alps, as geochemical evidence for penetration of meteoric water to beneath the brittle-ductile transition suggests that the groundwater movement in the brittle crust is not dominated by uplift (Menzies et al., 2014, 2016). Model flow rates, which are discussed subsequently, also prove to be consistent with this assumption.

To establish thermal structure, B5 models are initially run with the lower portion of the model (to -12 km) activated. During this set-up phase, hydraulic head is fixed at the surface, to avoid excessively long convergence timescales. Following this phase, temperature is fixed at -6 km, based on simulated values. The lower portion of the model is deactivated and the fixed head condition at the model surface replaced by a recharge condition for the main phase of flow simulation.

The Alpine Fault is modelled as a plane with a strike of 052, dipping at 50° to the south-east. Elements to the north-west of this plane were designated the model footwall. For fully

homogeneous models (set B1) these elements were undifferentiated from the rest of the model. The effect of a regionally extensive impermeable Alpine Fault is investigated by deactivating hanging wall elements, making the fault a no-flow boundary to the model hanging wall. For B5 models footwall elements are assigned relatively low permeability (k = 2 × 10^{-20} m^2*;* i.e. K = 10^{-13} $m \cdot s^{-1}$) for initial heat flow simulation and are then deactivated for the main phase of flow simulation, similar to the deep zone below -6 km.

Table 2.3 Thermal parameter values used for simulating heat flow in B5 models, based on the convective form of the energy conservation equation.

Parameter	**Value**
Rock advection rate (dip slip)	12 $mm \cdot yr^{-1}$
Thermal conductivity (water)	0.6 $W \cdot m^{-1} \cdot K^{-1}$
Thermal conductivity (rock)	2.0 $W \cdot m^{-1} \cdot K^{-1}$
Volumetric heat capacity (water)	4.2 $MJ \cdot m^{-3} \cdot K^{-1}$
Volumetric heat capacity (rock)	2.7 $MJ \cdot m^{-3} \cdot K^{-1}$
Porosity	0.1

B1 and B2 models were simulated for w set at 1 × 10^N % precipitation and 2 × 10^N % for integers N = -3 to 3 and for homogeneous k = 9 × 10^N m^2 and 2 × 10^N m^2 for integers N = -13 to -18 (i.e. K = 5 × 10^N $m \cdot s^{-1}$ and 1 × 10^N $m \cdot s^{-1}$ for integers N = -6 to -11). These k values are applied to the entire model domain above -6 km in fully homogeneous B1, but restricted to the hanging wall in B2. The position of the water table was recorded to find the minimum K and equivalent k value able to reproduce a water table consistent with that observed at the Amethyst boreholes for these spatially variable infiltration rates. To allow for comparison of B1 and B2 models with model A1, a model with k = 9 × 10^{-15} m^2 (K = 5 × 10^{-8} $m \cdot s^{-1}$) was also run with spatially constant w, calibrated to find the minimum w/K required to produce a consistent water table.

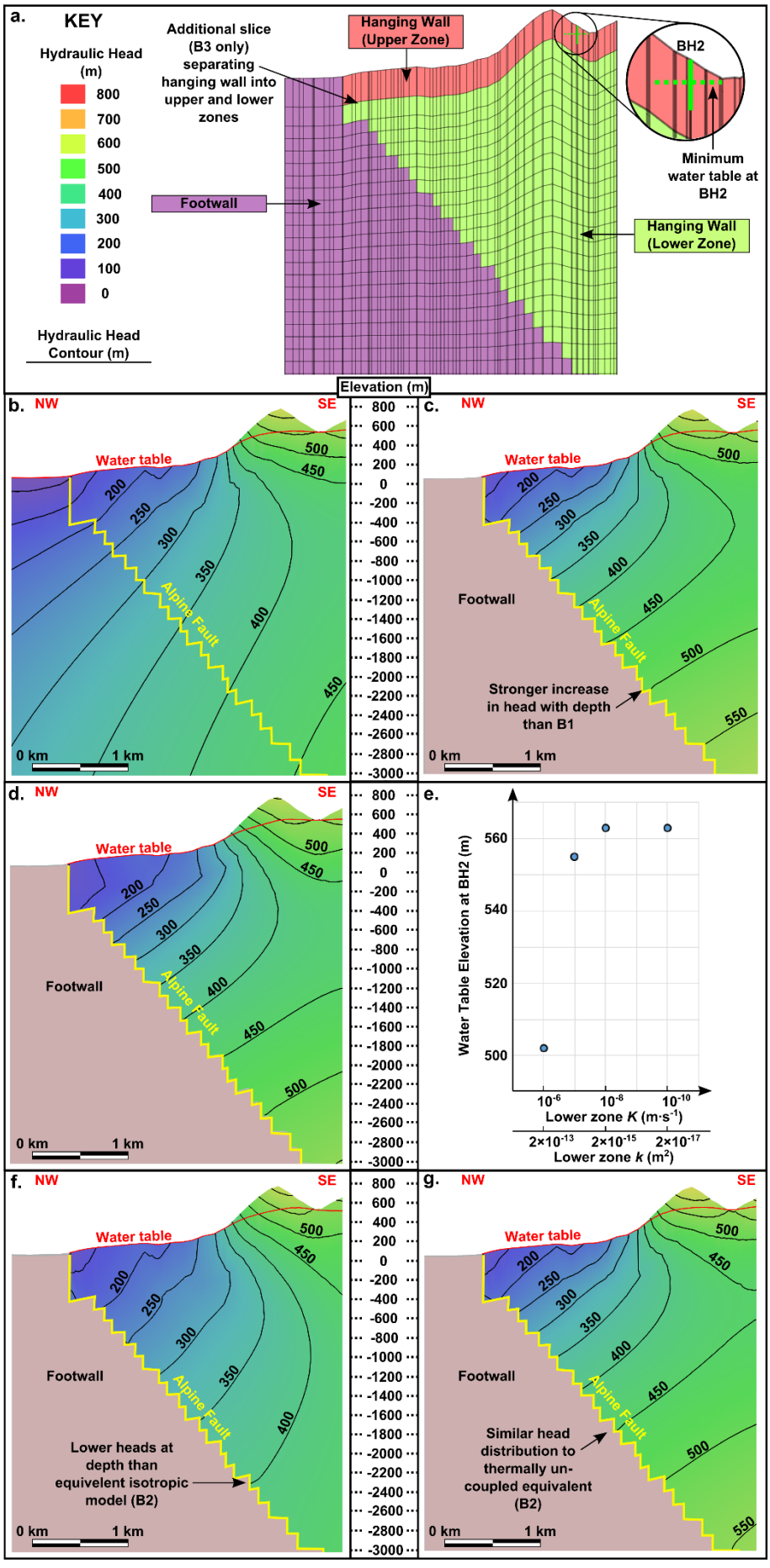

Figure 2.4 Caption opposite.

Figure 2.4 (Opposite) a. Overview of model structure in the vicinity of the Amethyst boreholes. b. Hydraulic head and water table cross section for B1 model with k = 9 × 10^{-15} m^2 (K = 5 × 10^{-8} m·s^{-1}) and w = 10 % of precipitation. c. Cross section for B2 model with k = 9 × 10^{-15} m^2 (K = 5 × 10^{-8} m·s^{-1}) and w = 10 % of precipitation. d. Cross section for B3 model. In the upper zone k = 2 × 10^{-13} m^2 (K = 1 × 10^{-6} m·s^{-1}) and in the lower zone k = 2 × 10^{-14} m^2 (K = 1 × 10^{-7} m·s^{-1}), w = 100 % of precipitation. e. Effect of changing lower zone k in B3 models. f. Cross section for B4 model with k_p = 2.4 × 10^{-14} m^2, k_n = 2.4 × 10^{-15} m^2 (K_p= 1.3 × 10^{-7} m·s^{-1}, K_n = 1.3 × 10^{-8} m·s^{-1}) and w = 10 % of precipitation. g. Cross section for B5 model with k = 9 × 10^{-15} m^2 and w = 15 % of precipitation.

Model set B3 has k varied with depth. Models have an upper high k zone and a lower low k zone (Fig. 2.4a), with k in the upper zone based on measured K values in the Amethyst boreholes. This set aims to test whether models with near-surface k based on these measured values could produce a water table consistent with measured levels, without requiring unrealistically high w values (w > 100 % precipitation). In order to place a constraint on the minimum w required to produce a consistent water table, the extent of the upper zone is limited to the depth of the deepest packer test measurement (301.6 m), with k set at 2 × 10^{-13} m^2 (K = 1 × 10^{-6} m·s^{-1}), based on the lower bound of measured values (K = 4.9 × 10^{-6} m·s^{-1}). An additional slice is added to the model at 301.6 m to define the boundary between upper and lower zones. The k of the lower zone beneath is varied between 2 × 10^{-13} m^2 (K = 1 × 10^{-6} m·s^{-1}), equal to k in the upper zone, and 2 × 10^{-17} m^2 (K = 1 × 10^{-10} m·s^{-1}). B3 Models were run for w = 20 % and w = 100 % of precipitation.

The effect of anisotropy in the presence of an impermeable Alpine Fault is investigated in Set B4, on the basis of the seismic anisotropy observed in foliated rocks in the Southern Alps (Christensen and Okaya, 2007). Foliated rocks typically have a higher k parallel to their foliation than normal to it (Singhal and Gupta, 2010). In set B4, the effect of introducing a 10 × anisotropy to models for the Amethyst Ravine is investigated by assuming a simplified regional foliation parallel to the dip and strike of the model Alpine Fault. k normal to this foliation (k_n) is modelled as 10 × smaller than k parallel to it (k_p). To allow comparison, k in these models is calibrated to give the same water level at BH2 as Set B2 models, with the same w applied.

Model set B5 represent thermally coupled equivalents of set B2, focusing on a sub-set of k values (Table 2.2). For some B5 models, the w values used in B1 and B2 models were found to either produce too low a water table or invoke surface infiltration exceeding the limit of $w/K \leq 1$ for infiltration under gravity, for K based on model surface conditions (Nimmo, 2005; Nimmo et al.,

2005). Therefore additional recharge values of 1.5×10^N % precipitation and 3×10^N % were also simulated for this set.

2.6.1 Results from finite element modelling

For B1 models, with w = 100% precipitation, $k \leq 9 \times 10^{-14}$ m·s^{-1} ($K \leq 5 \times 10^{-7}$ m·s^{-1}) is required to produce a water table consistent with the water level data. Maximum k decreases by a factor of ten when w is decreased by this amount, such that for w = 10 % precipitation, $k \leq 9 \times 10^{-15}$ m·s^{-1} ($K \leq 5 \times 10^{-8}$ m·s^{-1}) is required (Fig. 2.4b). For $k \leq 2 \times 10^{-13}$ m·s^{-1} ($K \leq 1 \times 10^{-6}$ m·s^{-1}), which represents a lower bound of Amethyst measurements ($K \geq 4.9 \times 10^{-6}$ m·s^{-1}), w = 200 % precipitation is required. When infiltration is simplified to a spatially constant value, $w/K > 0.3$ is required to produce a consistent water table. Thus the combinations of w and K or k that give a water table consistent with data can be mapped (Fig. 2.5).

The introduction of an impermeable Alpine Fault in set B2 does not change the maximum k values for a given w from those in set B1, with $k \leq 9 \times 10^{-14}$ m·s^{-1} ($K \leq 5 \times 10^{-7}$ m·s^{-1}) required for w = 100 % precipitation and similar scaling of K and k with w (Fig. 2.4c). Calculated minimum w/K based on constant infiltration is also unchanged (Fig. 2.5).

In set B3, the w required for near-surface $k = 2 \times 10^{-13}$ m·s^{-1} ($K = 1 \times 10^{-6}$ m·s^{-1}) is reduced from w = 200 %, when rocks at depth also have $k = 2 \times 10^{-13}$ m·s^{-1}, to w = 100 % when $k = 2 \times 10^{-14}$ m·s^{-1} ($K = 1 \times 10^{-7}$ m·s^{-1}) in rocks at depth (Fig. 2.4d). Further reduction in minimum w cannot be achieved by further decreases in lower zone k and changes in water table position minimal beyond $k = 2 \times 10^{-15}$ m·s^{-1} ($K = 1 \times 10^{-8}$ m·s^{-1}) (Fig. 2.4e).

Anisotropic models (set B4) require a maximum of $k_p = 2.4 \times 10^{-14}$ m^2, $k_n = 2.4 \times 10^{-15}$ m^2 ($K_p = 1.3 \times 10^{-7}$ m·s^{-1}, $K_n = 1.3 \times 10^{-8}$ m·s^{-1}) for w = 10 % precipitation (Fig. 2.4f), with reductions in w by a factor of 10 reducing maximum k_n by the same factor, similar to those in isotropic models.

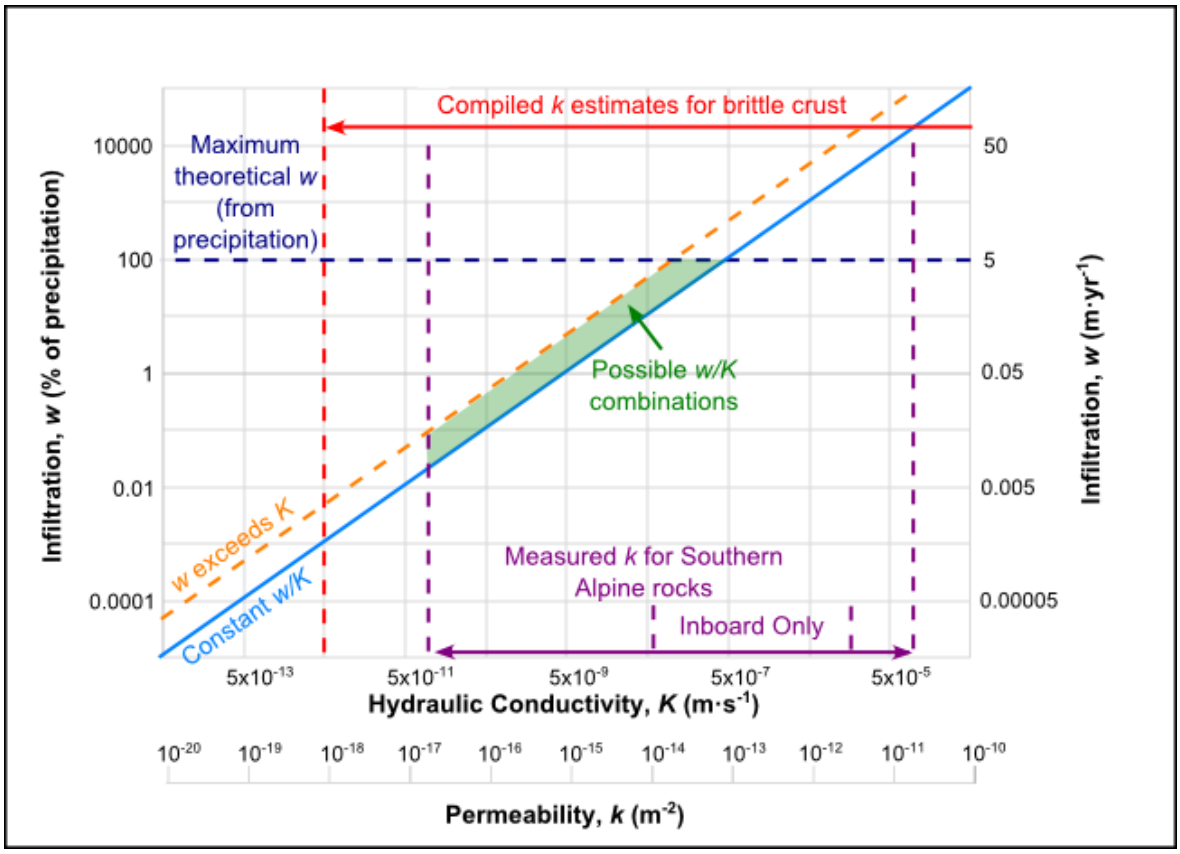

Figure 2.5 Log-log plot showing minimum w/K combinations that produce a water table consistent with Amethyst borehole water level constraints for models sets B1 and B2, for w as a percentage of spatially variable precipitation and as a homogeneous value. Corresponding w/k values based on low temperature reference conditions (0.01 °C, 1 atm) also represent an absolute minimum, as higher temperatures in models incorporating heat flow and coupled fluid properties act to slightly increase the minimum w required for a given k. The possible range of w/K and w/k values can be narrowed based on the maximum infiltration rate (100 % precipitation), the estimated range of large scale k in the brittle crust (Ingebritsen and Manning, 2010; Manning and Ingebritsen, 1999) and by limit of $w/K \leq 1$ based on the assumption of Darcian flow in the unsaturated zone under a unity head gradient. This range is further limited based on k estimates for rocks from the Southern Alps (Cox et al., 2015; Sutherland et al., 2012).

Models incorporating temperature and pressure dependent water properties (set B5), produce lower water table elevations for a given w and k than their thermally uncoupled counterparts in set B2 (Fig. 2.6a). Taking k and the average density and viscosity for water in the domain of flow, an effective average K for these models can be calculated. This is higher than the specified K in equivalent B2 models for all B5 models (Fig. 2.6b), reflecting the reduction in water viscosity with temperature relative to the low temperature reference conditions. For Darcian flow (Eq. 2.1),

reduced viscosity increases the flow rate under a given pressure gradient, increasing the w required to sustain a given water table. Buoyancy effects also have the potential to increase flow rates, increasing the required w. Changes in water table elevation relative to B2 models with the same w are greatest in the B5 models with the lowest k, as in these models average temperatures are highest, due to reduced advective cooling of the system by groundwater circulation (Fig. 2.6).

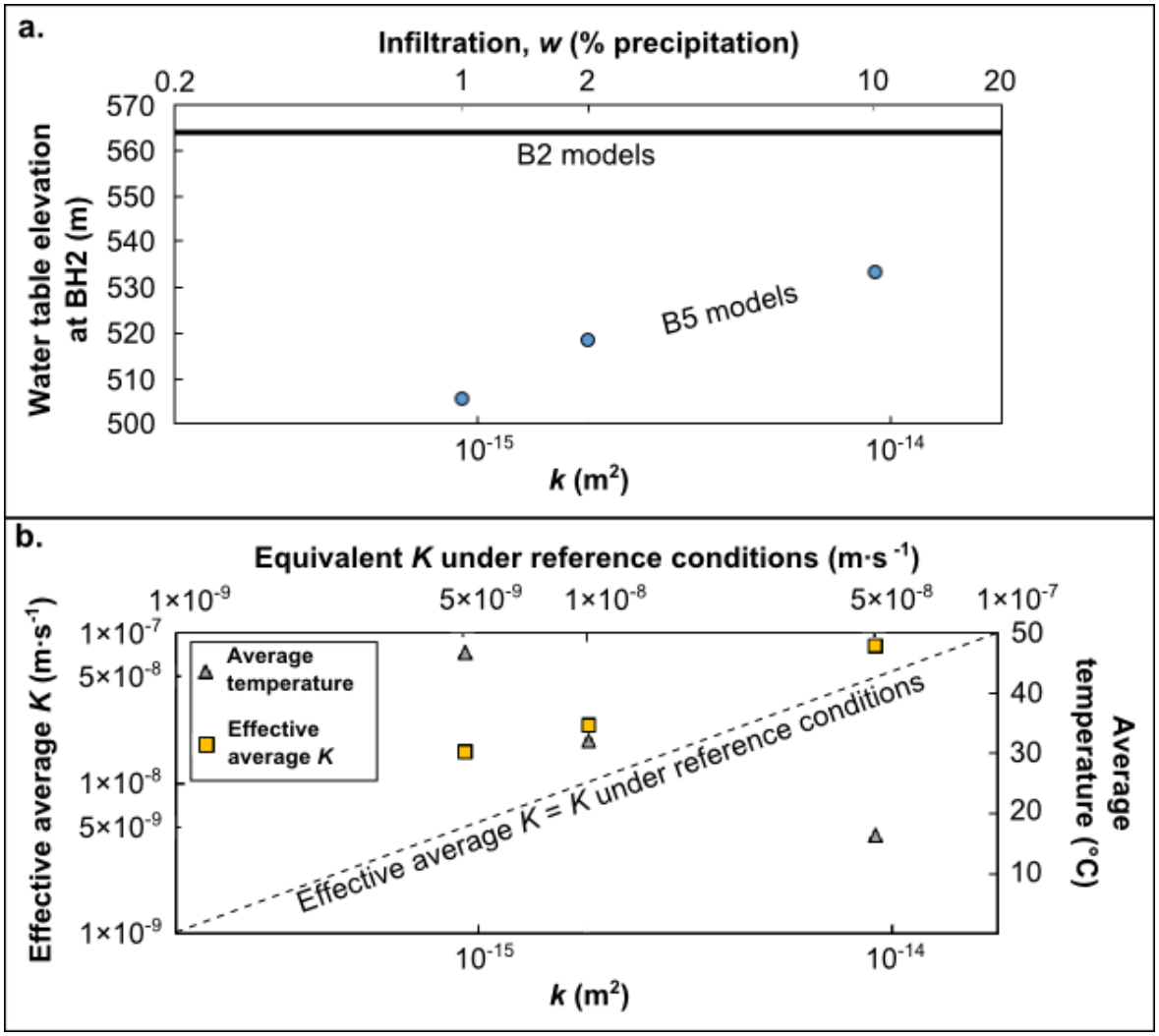

Figure 2.6 a. Water level at BH2 is lower in B5 models relative to equivalent B2 models and does not remain constant for fixed w/k. b. Average temperature above -6 km in B5 models and effective average K for these models, based on average water properties in the model domain. Effective average K becomes progressively larger with decreasing k compared to equivalent K under reference conditions (0.01 °C, 1 atm) assumed for uncoupled models.

As a result of these lowered water tables, the minimum w is slightly increased for B5 models relative to B2 counterpart models. For example, in the B2 model with k = 9 × 10^{-15} m·s^{-1} (K = 5 × 10^{-8} m·s^{-1}), w = 10 % produces a sufficiently high water table, but in the B5 model with equivalent k, the same w value produces too low a water table. As for some B5 models an

increase in w to the next highest value in the range used by B1 and B2 models requires unrealistically high infiltration in areas of the model (w/K > 1, based on surface K), B5 models simulated w that was 1.5 × higher than minimum values in corresponding B2 models (e.g. w = 15 % for k = 9 × 10^{-15} m·s^{-1}). These w values produce a sufficiently high water table in all B5 models, while maintaining $w/K \leq 1$.

Three-dimensional simulations for all sets (B1-B5) that are consistent with borehole water table constraints also predict seeps at the base of many of the ridges (Fig. 2.7), similar to predictions from analytical models. Seeps are also predicted beneath streams, to over 1750 m elevation, with seepage across almost the entire surface below ~250 m elevation. There is little variation in the hanging wall seep distribution between B1, B2 and B5 models. Anisotropy (B4) has the effect of altering the shape of the water table to reduce the area of seepage relative to isotropic models (Fig. 2.7c).

The hydraulic heads beneath the Amethyst ridge vary between model sets (Fig. 2.4, 2.8). Set B1 models, which are differentiated from other models sets by the absence of an impermeable Alpine Fault, show lower heads at the fault than equivalent models (B2) with an impermeable Alpine Fault (Fig. 2.8a-b.). Anisotropic (B3) models predict lower heads at depth than their isotropic equivalent, B2. The effect of coupled water properties in B5 is to produce a slight decrease in heads at depth, relative to B2. However, these differences in head between model sets do not persist into the shallow region penetrated by the Amethyst borehole (Fig. 2.7a.).

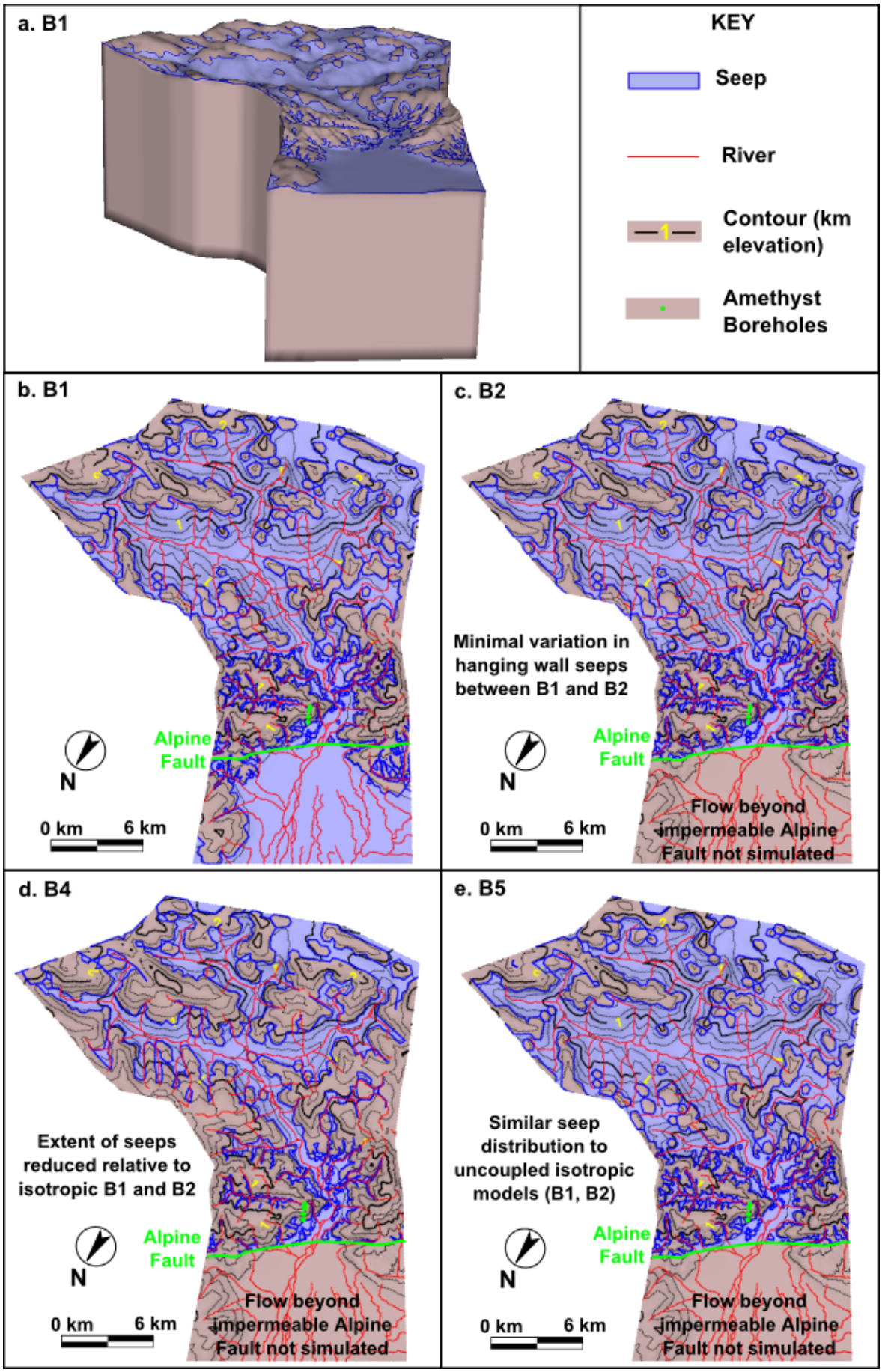

Figure 2.7 Caption opposite.

Figure 2.7 (Opposite) Comparison of spatial distribution of seeps (blue area) generated by models from set B1 (a., b.), B2 (c.), B4 (d.) and B5 (e.) models. w = 10 % of precipitation for B1, B2 and B4. w = 15 % of precipitation for B5. For isotropic models (B1, B2, B5), k = 9 × 10^{-15} m^2 (K = 5 × 10^{-8} m·s^{-1} in uncoupled models) and for anisotropic B4, k_p = 2.4 × 10^{-7} m^2, k_n = 2.4 × 10^{-8} m^2 (K_p = 1 × 10^{-7} m·s^{-1}, K_n = 1 × 10^{-9} m·s^{-1}). All models shown produce a sufficiently high water table position at the Amethyst boreholes to fit borehole observations and models B1, B2 and B3 have the same water table elevation at borehole BH2.

Downward vertical volumetric flow rates (flow throughout the model domain) and equivalent fluxes (flow per unit area) of water are reported though a surface at 500 m depth and through surfaces at -3 km and -5 km elevation. Where the Alpine Fault is a barrier to flow (B2-B5), the area across which flow is distributed decreases with depth, and as a result fluxes as a percentage of the average infiltration flux are slightly higher than flow rates as a percentage of the infiltration flow rate. The water fluxes scale with w and show little variation (≤1 % infiltration) between model sets B1, B2, indicating a flux equivalent to <30 % of the average infiltration flux at 500 m depth (Table 2.4) and much lower fluxes at -3 km and -5 km. Anisotropy in model set B4 has the effect of slightly increasing these fluxes relative to isotropic B1 and B2 models, whereas decreasing k with depth in model set B3 decreases the fluxes (Table 2.5). In the B5 model set, fluxes as a percentage of precipitation are similar to those in the corresponding B2 model for k = 9 × 10^{-15} m·s^{-1} (K = 5 × 10^{-8} m·s^{-1} in B2), but become progressively larger as k is decreased (Table 2.4). The higher percentages of infiltrating water reaching the investigated model surfaces with decreasing k can be understood in light of the increases in average temperature that also occur with decreasing k (Fig. 2.6a.). Higher average temperatures relative to the fixed temperature model surface indicate steeper average temperature gradients and result in greater reductions in water viscosity with depth. Decreasing viscosity promotes higher flow rates and therefore reduces the fall in groundwater fluxes with depth.

In interpreting average linear velocities corresponding to these fluxes, porosity of ≤5 × 10^{-5} is assumed for rocks at 500 m depth, based on compiled fracture porosity estimates for rocks below ~60 m depth (Snow, 1968). For rocks at -3 km and -5 km elevation, porosities of ≤3 × 10^{-5} and ≤1 × 10^{-5} respectively are assumed, based on the porosity depth relationship of Ingebritsen and Manning (2003) for fractured rocks. Based on these porosities, spatially averaged linear velocities corresponding to fluxes across the 500 m depth, -3 km and -5 km surfaces are more than an order of magnitude (and in most cases multiple orders of magnitude) greater than the maximum model uplift velocity. This is the case for all models presented and thus model fluxes support the assumption of a negligible contribution to groundwater movement from rock advection.

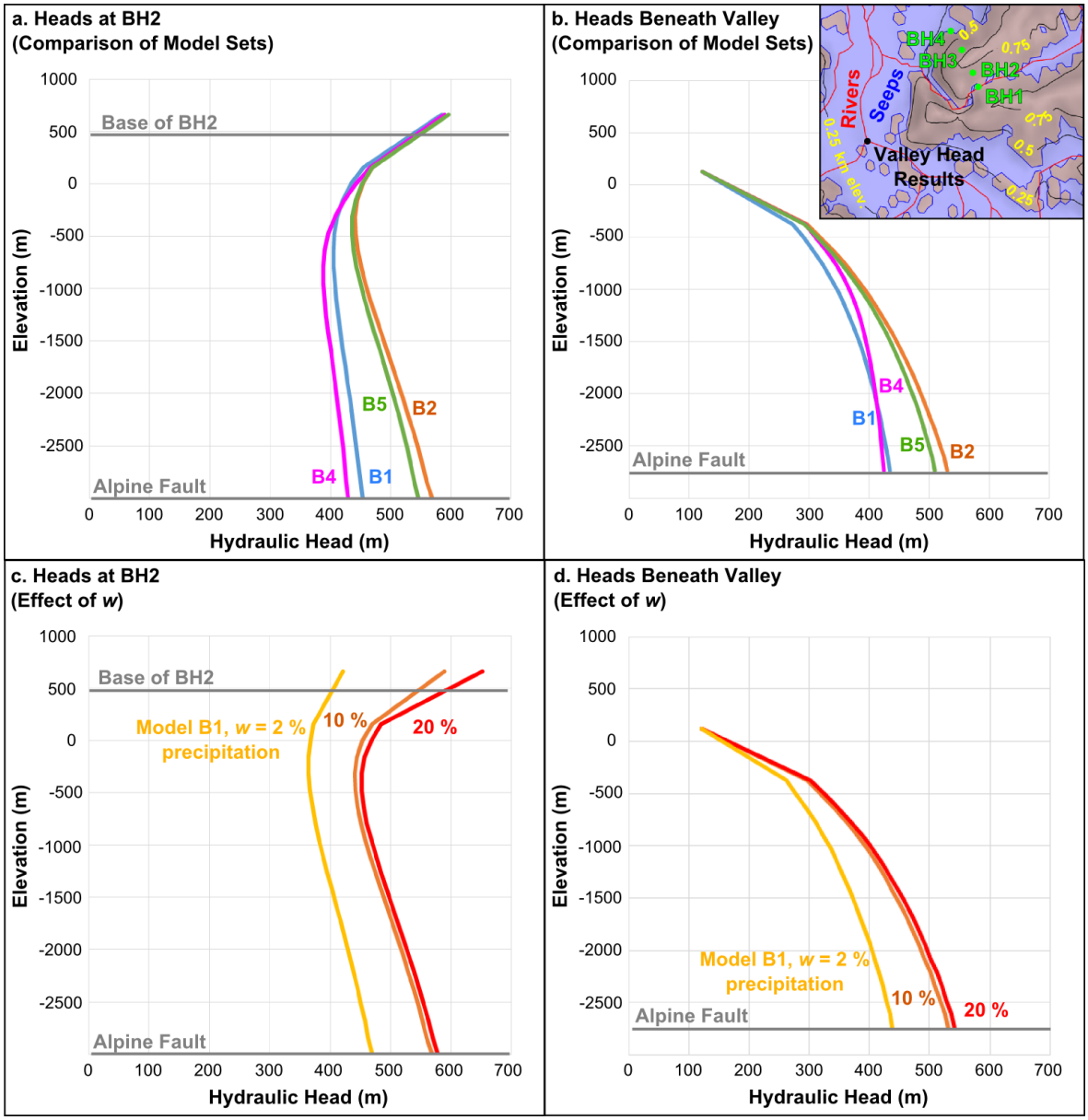

Figure 2.8 a-b. Head vs elevation profiles at BH2 (a.) and beneath the Wanganui valley (b., location inset) for model sets B1, B2, B4 and B5. w = 10 % of precipitation for uncoupled models (B1, B2 and B4), 15 % of precipitation for B5. For isotropic models (B1, B2, B5), k = 9 × 10^{-15} m^2 (K = 5 × 10^{-8} m·s^{-1} in uncoupled models) and for anisotropic B4, k_p = 2.4 × 10^{-7} m^2, k_n = 2.4 × 10^{-8} m^2 (K_p = 1 × 10^{-7} m·s^{-1}, K_n = 1 × 10^{-9} m·s^{-1}). C-D. Profiles at BH2 (c.) and beneath the Wanganui valley (d.) for model sets B2 with K = 5 × 10^{-8} m·s^{-1} for w = 2 %, 10 % and 20 % of precipitation.

Table 2.4 Downward groundwater volumetric flow rates and fluxes through surfaces at 500 m depth (i.e. parallel to the topographic surface), -3000 m elevation and -5000 m elevation compared to infiltration for a range of models (all with water tables consistent with borehole data).

Model Set	**B1**	**B2**	**B2**	**B4**	**B5**	**B5**	**B5**
K **(m·s^{-1})**	5×10^{-8}	5×10^{-8}	5×10^{-7}	1.3×10^{-7} (K_P)	N/A		
k **(m^2)**	9×10^{-15}	9×10^{-15}	9×10^{-14}	2.4×10^{-14} (k_P)	9×10^{-16}	2×10^{-15}	9×10^{-15}
w **(% precipitation)**	10	100	10	10	1.5	3	15
	Volumetric Flow Rate (m^3·s^{-1}) [Volumetric flow rate as a percentage of infiltration flow rate in square brackets]						
Infiltration	9.8 [100]	8.4 [100]	84 [100]	8.4 [100]	1.3 [100]	2.5 [100]	13 [100]
500 m depth	2.1 [22]	1.8 [21]	18 [21]	2.4 [28]	0.3 [25]	0.6 [23]	3 [20]
-3000 m	0.3 [3]	0.2 [2]	2 [2]	0.3 [3]	<0.1 [7]	<0.1 [5]	<1 [3]
-5000 m	<0.1 [1]	<0.1 [<1]	<1 [<1]	<0.1 [<1]	<0.1 [3]	<0.1 [2]	<1 [1]
	Flux (×10^{-8} m·s^{-1}) [Flux as a percentage of average infiltration flux in square brackets]						
Infiltration	2.1 [100]	2.3 [100]	23 [100]	2.3 [100]	0.34 [100]	0.68 [100]	3.4 [100]
500 m depth	0.5 [22]	0.5 [21]	5 [21]	0.6 [28]	0.09 [25]	0.15 [23]	0.7 [20]
-3000 m	0.1 [3]	0.1 [3]	1 [3]	0.1 [3]	0.03 [8]	0.04 [6]	0.1 [3]
-5000 m	<0.1 [1]	<0.1 [1]	<1 [1]	<0.1 [1]	0.01 [4]	0.02 [3]	<0.1 [1]

Table 2.5 Downward volumetric flow rates and fluxes through surfaces at 500 m depth, -3000 m elevation and -5000 m elevation for B3 models with a range of k values for the lower zone (>301.6 m depth). Fluxes decrease with decreasing k. A lower zone with k = 2 × 10^{-13} m^2 (K = 1 × 10^{-6} m·s^{-1}) produces too low a water table to be consistent with Amethyst borehole water levels, in contrast to other models for which fluxes are presented.

Model Set	**B3**		
Lower zone K (m·s^{-1})	1 × 10^{-6}	1 × 10^{-7}	1 × 10^{-8}
Lower zone k (m^2)	2 × 10^{-13}	2 × 10^{-14}	2 × 10^{-15}
w (% precipitation)	100		
	Volumetric Flow Rate (m^3·s^{-1}) [Volumetric flow rate as a percentage of infiltration flow rate in square brackets]		
Infiltration	84 [100]	84 [100]	84 [100]
500 m depth	29 [35]	4 [5]	<1 [<1]
-3000 m	4 [5]	<1 [<1]	<1 [<1]
-5000 m	1 [1]	<1 [<1]	<1 [<1]
	Flux (×10^{-8} m·s^{-1}) [Flux as a percentage of average infiltration flux in square brackets]		
Infiltration	23 [100]	23 [100]	23 [100]
500 m depth	8 [35]	1 [5]	<1 [1]
-3000 m	1 [5]	<1 [1]	<1 [<1]
-5000 m	<1 [2]	<1 [<1]	<1 [<1]

2.7 Discussion

2.7.1 Infiltration, hydraulic conductivity and permeability values

B1, B2 and B5 models are discussed first, in order to consider appropriate values for regional bulk K and k. B1 and B2 models show a dependence of water table elevation on w and K similar to that in analytical (A1) models, as changes in K can be accommodated by changes in w to maintain a water table consistent with observations (Fig. 2.5). As such, the conditions required to produce a sufficiently high water table can be described in terms of a minimum w/K or corresponding minimum w/k. Values for k in coupled B5 models, which simulate the thermal structure of the Southern Alps, correspond to k in B1 and B2 models, assuming uniform low temperature reference conditions (0.01 °C, 1 atm) in these uncoupled model sets. The higher temperatures in B5 models, compared to those assumed for uncoupled models, result in higher groundwater flow rates due to decreased water viscosities and increased buoyancy effects, which act to increase the minimum w required to sustain a given high water table elevation. This means that the elevation of the water table in B5 models does not remain unchanged for constant w/k, as temperatures are also dependent on k. Consequently a minimum w/k cannot be defined based on B5 models. However, because the effect of increased temperature in B5 models is to increase the minimum w, the straightforward minimum for w/k in uncoupled B1 and B2 models (based on the lower bound for w/K under minimum temperature reference conditions), provides a suitable absolute lower bound.

For the minimum w/K and w/k ratios indicated by these models, the range of possible w and K or k combinations can be narrowed down based on other constraints on these parameters (Fig. 2.5). The limit of $w/K \leq 1$ for infiltration under gravity at the surface provides a straightforward bound on w/K (Nimmo, 2005; Nimmo et al., 2005). Additionally, w cannot be greater than 100 % precipitation, in the absence of significant alternative sources of infiltration. If 25 % of the entire 53.3 km^3 volume of glaciers in the Southern Alps (Chinn, 1989) melted in just one year, >20 % of the melt water would need to drain into the Wanganui valley, to produce an input equal to 100 % of precipitation. Thus although locally glacial melt may contribute to infiltration at the southerly end of the Wanganui valley, the total glacial input into the area encompassed by the finite element model domain is likely to be orders of magnitude less than 100 % precipitation. Losing streams are not likely to be a major source, not only because the positions of many streams correspond to the positions of seeps in three-dimensional models, suggesting they are gaining, but also because water in losing streams will be predominantly sourced from precipitation in the

catchment. This means that although they may cause localised redistribution of infiltration, they are unlikely to increase it regionally.

The percentage of precipitation infiltrating is likely to vary laterally with greater complexity than modelled in this study. The amount and type of vegetation, soil and snow cover, the slope of the ground surface and the angle of rock fabric with respect to the ground surface may all cause spatial variation in w and could cause it to exceed 100 % precipitation in limited, localised areas. However, the conclusions drawn from B1 and B2 models with spatially variable w are the same as those drawn from those with homogeneous w – that models with homogeneous $k \geq 9 \times 10^{-13}$ m^2 ($K \geq 5 \times 10^{-7}$ m·s^{-1}), require w greater than can be supplied by precipitation in the catchment. This suggests that conclusions drawn are unlikely to be significantly improved by modelling more complex spatial variations in w.

Based on compiled estimates of large-scale k for the brittle crust (Ingebritsen and Manning, 2010; Manning and Ingebritsen, 1999), which show $k > 10^{-18}$ m^2 ($K > 5 \times 10^{-12}$ m·s^{-1} for uncoupled model reference conditions), w must be 0.001 to 100 % of precipitation in homogeneous models (Fig. 2.5). This range narrows to 0.02 to 100 % of precipitation for k values for the unaltered Haast Schist Group rocks (Sutherland et al., 2012; Cox et al., 2015). The range is further reduced to 10 to 100 % if only values from the inboard region of the Southern Alps, north-west of the Main Divide are included, although this permeability range is based on data from the Amethyst and DFDP-1 boreholes alone. For models with $k = 2 \times 10^{-13}$ m·s^{-1} ($K = 1 \times 10^{-6}$ m·s^{-1}), as a lower bound for measured values at the Amethyst boreholes, w = 200 % rainfall is required in B1 and B2 models. This may be because measured values represent rocks damaged during the drilling process, with k raised above undisturbed values. Alternatively, measured values may represent a local high in k. Packer tests were carried out at only two boreholes, over a narrow depth interval and may have only sampled a small volume of rock, meaning that there is significant scope for spatial variability. B3 models show that limiting the vertical extent of this high k does significantly reduce the infiltration required, producing a water table consistent with borehole data for w = 100 %, but not for w = 20 % precipitation. The insensitivity of water table elevations in B3 models to decreases in k in the lower zone beyond values two orders of magnitude less than the value in the upper zone suggests that water table position is largely controlled by the k of rocks nearer the surface. Because of this and because the upper zone was restricted to the minimum depth extent possible based on borehole measurements, with k corresponding to the minimum measured K, it seems unlikely that any other k-depth relationship could produce a significantly greater reduction in the infiltration required. Therefore if the K values measured at the Amethyst Ravine are representative of the properties of near-surface rocks across the region, w must be in the range >20 % to 100 % of precipitation. Consequently, although this study indicates a possible a

range in w based on based on k in Haast Schist Group rocks (0.02-100 % precipitation) which is broadly consistent with the range estimated by Sims et al. (2015) (0.3-20 % precipitation), it shows that w values slightly above this existing estimated range (i.e. >20 % precipitation) are a realistic possibility.

There are numerous ways in which k may vary laterally. k is likely to vary spatially around the Alpine Fault and around other local faults, with increased k where fracturing is greater and reduced k where fluid flow has caused mineral precipitation and reduced porosity (Sutherland et al., 2012). The variation of k with stress state modelled for the Manapouri region of Fiordland, New Zealand (Upton and Sutherland, 2014), indicated that the highest k is beneath mountains and ridges, with lower values beneath valleys, and these findings may also be applicable to the Amethyst region.

2.7.2 Regional water table

Three-dimensional models predict a bulging water table beneath the Amethyst Ridge, producing seeps on its northwest flank, similar to those predicted by models A1 to A2. Regionally, three-dimensional models predict water table elevations of up to 1.4 km above the adjacent valley floor in some ridges with seepage over a large area. The presence of seeps at the sites of all streams below 250 m suggests that streams below this elevation are in hydraulic continuity with groundwater, receiving water from the saturated zone ('gaining'). Seeps are also present along many streams above this elevation too, including the Amethyst River and Just Right Creek. Anisotropy has a strong influence on seep distribution, with B3 models showing significantly less extensive seepage than other model sets. The variation in the extent of seepage in analytical models (A1-A2) also highlights the potential for lateral variations in k to locally alter the distribution of seeps.

2.7.3 Hydraulic heads at depth

The high water table has important consequences for vertical hydraulic head gradients beneath valleys in the region. Models (e.g., B1) show increasing vertical hydraulic head gradients at depth with increasing water table elevation (Fig. 2.8c-d.). The high elevation water table required to be consistent with the Amethyst borehole water levels generates high heads at depth, with rapid increases in head beneath valleys (Fig. 2.8b). Significant artesian flow within valleys in the Southern Alps predicted by these models was observed during drilling of DFPD-2B boreholes in the adjacent Whataroa valley (Chapter 3, this thesis; Sutherland et al., 2017). The head values reached are dependent on k structure, with the presence of an impermeable Alpine Fault acting

to increase heads at depth in the hanging wall of the fault and the presence of anisotropy parallel to the fault acting to reduce them. Decreasing heads with depth beneath BH2 in all three-dimensional model sets (Fig. 2.4, 2.8) are consistent with the assumptions made in considering borehole water levels as minimum water table elevations.

2.7.4 Applicability of analytical models

The presence of seeps at the Amethyst River and Just Right Creek in finite element models supports the assumption made by analytical models that these watercourses are in hydraulic continuity with groundwater. The similar w/K values required by homogeneous B1 and B2 models (0.3) to the value predicted by model A1 (0.29) and their similar predictions for the shape of the water table and presence of seeps suggests that this type of simple analytical model, based on the Dupuit assumptions can provide straightforward insights into the position on the water table and regional w and K values, in spite of the presence of significant vertical head gradients (Fig. 2.8). However, the presence of vertical head gradients within models B1-B5 does indicate that models based on the Dupuit assumptions are not suitable for every modelling application within the Southern Alps. For example, by neglecting vertical flow, calculated Darcy velocity vectors are likely to be inaccurate for much of the orogen.

2.7.5 Water fluxes to depth

With the exception of model set B3, three-dimensional models in this study do not simulate any decrease in k with depth. The anticipated effect of decreasing k with depth is to reduce flow rates at depth. This is supported by decreasing fluxes in set B3 models as k in the lower zone is reduced (Table 2.5). As such, fluxes from model set B1, B2, B4 and B5 provide upper bounds on fluxes of water to depth. Anisotropy in model set B4 acts to increase the percentage of infiltrating water flowing to depth, relative to corresponding isotropic models (B2). Fluxes in B5 models reflect the influence of temperature, with increasing average temperature gradients acting to minimise the decreases in groundwater flux with depth that occur in all models, through decreases in water viscosity, which promote higher flow rates.

Models that produce water tables consistent with Amethyst borehole water levels show that fluid flow penetrating beyond 500 m depth represents <30 % of the average infiltration flux at the surface (and equivalently <30 % of the total infiltrating volume per unit time). The majority (>70 %) of infiltrating water must travel on relatively short, shallow flow paths before leaving the groundwater system through seeps. The decrease in infiltration beyond 500 m depth associated with just an order of magnitude decrease in k at depth in model set B3 is much greater than

changes associated with anisotropy or temperature regime. Therefore ~30 % of the average surface infiltration would appear to be an appropriate upper limit for the fluid flux beyond 500 m depth.

Models from this study show fluxes equivalent to ≤8 % of the average infiltration flux reaching -3 km elevation and ≤4 % of the average infiltration flux reaching -5 km. These fluxes, given as percentages of the average flux of water infiltrating into the groundwater system, may also be expressed in terms of the average precipitation rate, which includes both water that infiltrates to the saturated zone and water that does not. Where w is of the order of 1 % of precipitation or greater, the predicted maximum flux at -5 km of 4 % of the average infiltration flux represents at least 0.04 % of the average precipitation rate. In this case ($w \gtrsim 1$ % precipitation), results from this study are consistent with geochemical tracer modelling, which indicates a fluid flux at ~6 km depth equivalent to 0.02-0.05 % of the precipitation rate (Menzies et al., 2016).

Because the drop in fluid fluxes with depth is reduced under higher temperature gradients in B5 models, high uplift rates in the Southern Alps, which have increased temperature gradients in the shallow orogen, may facilitate flow of increased fluxes of meteoric water to the base of the brittle crust than would occur under lower temperature gradient conditions in the absence of uplift. A scenario in which uplift velocities were large enough to overwhelm downward penetration of fluid within the brittle crust would represent an exception to this. However, evidence for meteoric fluids penetrating beneath the brittle-ductile transition (Menzies et al., 2014, 2016), as well as average linear velocities in models (based on likely porosity values) that are sufficiently high that uplift velocities are negligible in comparison, suggest that this is not the case in the Southern Alps.

2.8 Conclusions

The shallow flow regime in the Amethyst region of the Southern Alps is characterised by a high elevation water table in the interfluves, which is up to 1.4 km above the adjacent valley floor, with widespread seeps on valley sides. The majority of infiltrating water (>70 % for modelled k structures) travels on shallow flow paths (<500 m below ground level) before leaving the groundwater system (Fig. 2.9). Mapped rivers in the inboard Southern Alps are in hydraulic continuity with groundwater below 250 m elevation in all cases. In some locations, this continues to >1750 m elevation.

The infiltration flux to the groundwater table, w for the region must be ≥0.02 % of precipitation, but is >20 % precipitation if packer test estimates for K from the Amethyst Ravine are representative of rocks at similar depths across the inboard Southern Alps. Regional w > 100 %

precipitation is not possible as other sources of infiltration such as glacial melt are minor compared to the contribution from precipitation.

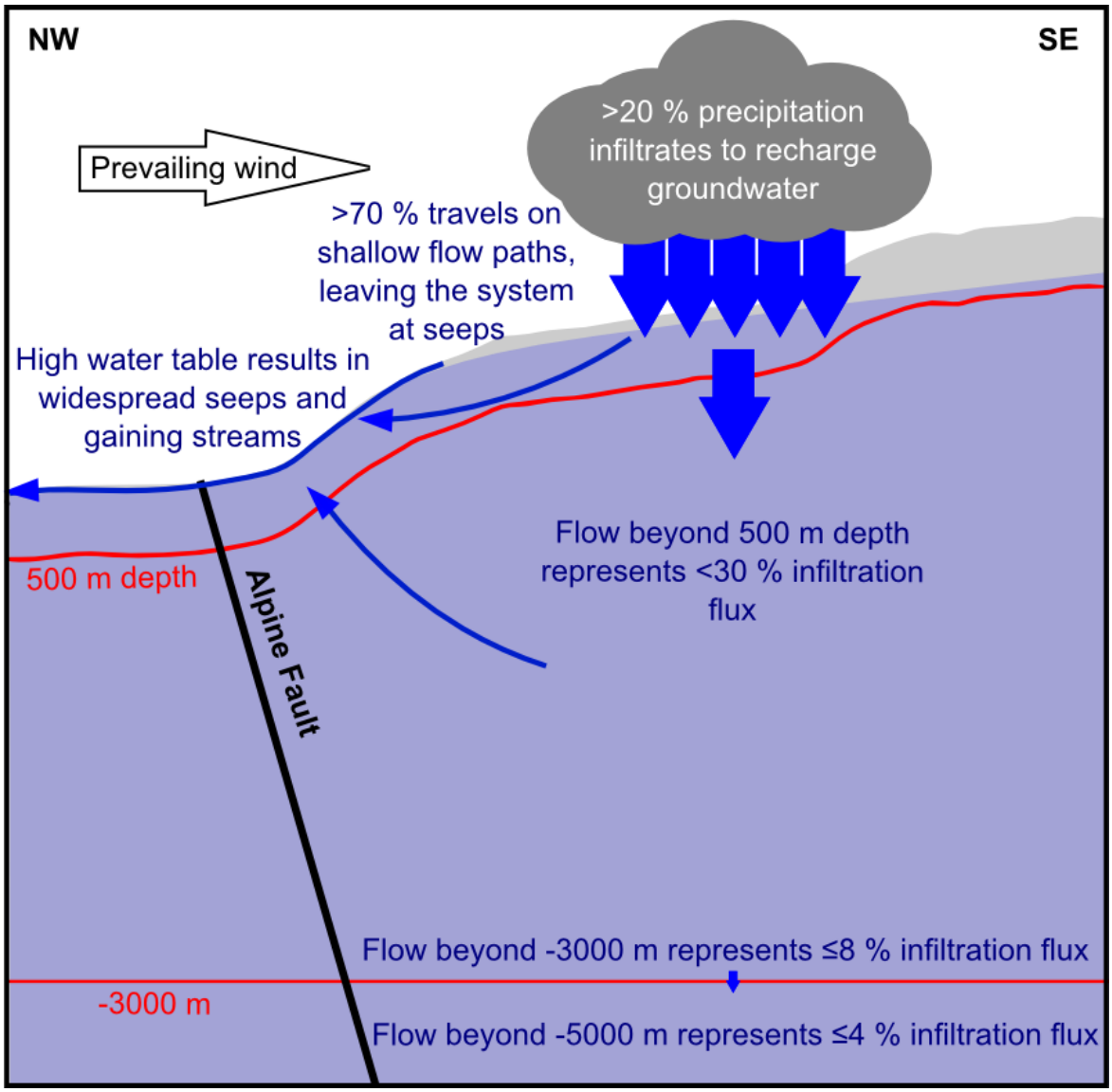

Figure 2.9 Vertically exaggerated cross section to illustrate shallow flow in the Southern Alps, which is characterised by a high water table and widespread seeps, with >70 % of infiltrating waters seeping out without reaching depths greater than 500 m. Estimated down-flow beyond -5000 m is equivalent to a maximum of 4 % of the average infiltration flux. For w of the order 1 % precipitation or greater, this represents at least 0.04 % of the average precipitation rate and is consistent with geochemical tracer modelling, which indicates a fluid flux at the brittle-ductile transition (~6 km depth) equivalent to 0.02-0.05 % of the precipitation rate (Menzies et al., 2016).

Decreases in fluid fluxes with depth are less significant under higher temperature gradients in models. Increased temperature gradients in the shallow Southern Alps resulting from rapid uplift

may therefore promote flow of greater fluxes of meteoric water to the base of the brittle crust than under lower temperature gradient conditions.

If treated as a homogeneous regional parameter for the brittle crust, K must be of the order 5×10^{-7} m·s^{-1} or less, based on the requirement that $w \leq 100$ % precipitation. The corresponding upper bound for k is 9×10^{-14} m^2 ≈ 10^{-13} m^2 and is established by assuming uniform low temperature conditions, as higher temperatures in thermally coupled models act to increase the minimum w required. K values measured in boreholes at the Amethyst Ravine ($K \geq 4.9 \times 10^{-6}$ m·s^{-1}) are therefore inferred to characterise local conditions, restricted to the shallowest rocks and potentially those in fault damage zones.

2.9 References

Ague, J.J., 1997. Crustal mass transfer and index mineral growth in Barrow's garnet zone, northeast Scotland. Geology 25, 73–76. doi:10.1130/0091-7613(1997)025<0073:CMTAIM>2.3.CO;2

Barnes, I., Downes, C.J., Hulston, J.R., 1978. Warm springs, South Island, New Zealand, and their potentials to yield laumontite. Am. J. Sci. doi:10.2475/ajs.278.10.1412

Bickle, M.J., 1992. Transport mechanisms by fluid-flow in metamorphic rocks; oxygen and strontium decoupling in the Trois Seigneurs Massif; a consequence of kinetic dispersion? Am. J. Sci. 292, 289–316.

Blanpied, M.L., Lockner, D.A., Byerlee, J.D., 1992. An earthquake mechanism based on the rapid sealing of faults. Nature 356, 133–135.

Boese, C.M., Townend, J., Smith, E., Stern, T., 2012. Microseismicity and stress in the vicinity of the Alpine Fault, central Southern Alps, New Zealand. J. Geophys. Res. 117, 1–20. doi:10.1029/2011JB008460

Boulton, C., Carpenter, B.M., Toy, V., Marone, C., 2012. Physical properties of surface outcrop cataclastic fault rocks, Alpine Fault, New Zealand. Geochemistry, Geophys. Geosystems 13, 1–13. doi:10.1029/2011GC003872

Bouwer, H., Rice, R.C., 1976. A slug test for determining hydraulic conductivity of unconfined aquifers with completely or partially penetrating wells. Water Resour. Res. 12, 423. doi:10.1029/WR012i003p00423

Byerlee, J., 1993. Model for episodic flow of high-pressure water in fault zones before earthquakes. Geology 21, 303–306.

Carpenter, B.M., Kitajima, H., Sutherland, R., Townend, J., Toy, V.G., Saffer, D.M., 2014. Hydraulic and acoustic properties of the active Alpine Fault, New Zealand: Laboratory measurements on DFDP-1 drill core. Earth Planet. Sci. Lett. 390, 45–51. doi:10.1016/j.epsl.2013.12.023

Chester, F.M., 1994. Effects of temperature on friction: constitutive equations and experiments with quartz gouge. J. Geophys. Res. 99, 7247–7261. doi:10.1029/93JB03110

Chinn, T.H.H., 1989. Glaciers of New Zealand, in: Satellite Image Atlas of Glaciers in the World. U.S. Geological Survey Professional Paper 1386-H. p. P 1386–H.

Christensen, N.I., Okaya, D.A., 2007. Compressional and Shear Wave Velocities in South Island, New Zealand Rocks and Their Application to the Interpretation of Seismological Models of the New Zealand Crust, in: Continental Plate Boundary: Tectonics At South Island, New Zealand. pp. 123–155. doi:10.1029/175GM08

Clarke, B.A., Burbank, D.W., 2011. Quantifying bedrock-fracture patterns within the shallow subsurface: Implications for rock mass strength, bedrock landslides, and erodibility. J. Geophys. Res. Earth Surf. 116, 1–22. doi:10.1029/2011JF001987

Clauser, C., 1992. Permeability of crystalline rocks. Eos, Trans. Am. Geophys. Union 73, 233–238. doi:10.1029/91EO00190

Cochran, U.A., Clark, K.J., Howarth, J.D., Biasi, G.P., Langridge, R.M., Villamor, P., Berryman, K.R., Vandergoes, M.J., 2017. A plate boundary earthquake record from a wetland adjacent to the Alpine fault in New Zealand refines hazard estimates. Earth Planet. Sci. Lett. 464, 175–188. doi:10.1016/j.epsl.2017.02.026

Cox, S.C., Barrell, D.J.A., 2007. Geology of the Aoraki area. Institute of Geological and Nuclear Sciences 1:250,000 geological map 15.

Cox, S.C., Menzies, C.D., Sutherland, R., Denys, P.H., Chamberlain, C., Teagle, D.A.H., 2015. Changes in hot spring temperature and hydrogeology of the Alpine Fault hanging wall, New Zealand, induced by distal South Island earthquakes. Geofluids 15, 216–239. doi:10.1111/gfl.12093

Cox, S.C., Sutherland, R., 2007. Regional Geological Framework of South Island, New Zealand, and its Significance for Understanding the Active Plate Boundary, in: Okaya, D., Stern, T., Davey,

F. (Eds.), A Continental Plate Boundary: Tectonics at South Island, New Zealand. American Geophysical Union, Washington DC, pp. 19–46. doi:10.1029/175GM03

DeMets, C., Gordon, R.G., Argus, D.F., Stein, S., 1994. Effects of recent revision to the geomagnetic reversal timescale on estimates of current plate motion. Geophys. Res. Lett. 21, 2191–2194.

Diersch, H.-J.G., 2014. FEFLOW: Finite Element Modeling of Flow, Mass and Heat Transport in Porous and Fractured Media. Springer-Verlag, Berlin, Heidelberg.

Dipple, G.M., Ferry, J.M., 1992. Metasomatism and fluid flow in ductile fault zones. Contrib. to Mineral. Petrol. 112, 149–164. doi:10.1007/BF00310451

Eppelbaum, L., Kutasov, I., Pilchin, A., 2014. Applied Geothermics, Applied Geothermics. doi:10.1007/978-3-642-34023-9

Freeze, R.A., Cherry, J.A., 1979. Groundwater. Prentice-Hall, Englewood Cliffs, NJ.

Garven, G., Appold, M.S., Toptygina, V.I., Hazlett, T.J., 1999. Hydrogeologic modeling of the genesis of carbonate-hosted lead-zinc ores. Hydrogeol. J. 7, 108–126. doi:10.1007/s100400050183

Geotech Consulting Ltd., 2006. Amethyst Hydro Scheme 2006 Drilling Investigation Summary Report. Prepared for Westpower Ltd. Reference 2745.

Houlsby, A.C., 1976. Routine Interpretation of the Lugeon Water-test. Q. J. Eng. Geol. Hydrogeol. 9, 303–313.

Hubbert, M.K., 1940. The Theory of Ground-Water motion. J. Geol. 48, 785–944.

Hvorslev, M.J., 1951. Time Lag and Soil Permeability in Ground-Water Observations. Bull. (Waterways Exp. Stn. Corps Eng. U.S. Army, Vicksburg, Mississippi) 36.

Ingebritsen, S.E., Manning, C.E., 2010. Permeability of the Continental Crust: Dynamic Variations Inferred from Seismicity and Metamorphism. Geofluids 193–205. doi:10.1002/9781444394900.ch13

Ingebritsen, S.E., Manning, C.E., 2003. Implications of crustal permeability for fluid movement between terrestrial fluid reservoirs. J. Geo 79, 1–6. doi:10.1016/S0375-6742(03)00037-2

Koons, P.O., 1989. The topographic evolution of collisional mountain belts: a numerical look at the Southern Alps, New Zealand. Am. J. Sci. doi:10.2475/ajs.289.9.1041

Koons, P.O., 1987. Some thermal and mechanical consequences of rapid uplift: an example from the Southern Alps, New Zealand. Earth Planet. Sci. Lett. 86, 307–319. doi:10.1016/0012-821X(87)90228-7

Land Information New Zealand, 2008. Land Information Fact Sheet: New Zealand Geodetic Datum 2000 Projections [WWW Document]. URL http://www.linz.govt.nz/system/files_force/media/regulatory-documents/25702-LINZG25702 Fact sheet - New Zealand Geodetic Datum 2000 Projections_4.pdf?download=1&download=1 (accessed 23.02.2015).

Leitner, B., Eberhart-Phillips, D., Anderson, H., Nabelek, J.L., 2001. A focused look at the Alpine Fault, New Zealand: Seismicity, focal mechanisms, and stress observations. J. Geophys. Res. 106, 2193–2220.

Little, T.A., Cox, S., Vry, J.K., Batt, G., 2005. Variations in exhumation level and uplift rate along the oblique-slip Alpine fault, central Southern Alps, New Zealand. Bull. Geol. Soc. Am. 117, 707–723. doi:10.1130/B25500.1

Magri, F., Bayer, U., Maiwald, U., Otto, R., Thomsen, C., 2009. Impact of transition zones, variable fluid viscosity and anthropogenic activities on coupled fluid-transport processes in a shallow salt-dome environment. Geofluids 9, 182–194. doi:10.1111/j.1468-8123.2009.00242.x

Manning, C.E., Ingebritsen, S.E., 1999. Permeability Implications of the Continental of Geothermal Data and Metamorphic Systems. Rev. Geophys. 37, 127–150.

Maréchal, J.C., Etcheverry, D., 2003. The use of 3H and 18O tracers to characterize water inflows in Alpine tunnels. Appl. Geochemistry 18, 339–351. doi:10.1016/S0883-2927(02)00101-4

Menzies, C.D., Teagle, D.A.H., Craw, D., Cox, S.C., Boyce, A.J., Barrie, C.D., Roberts, S., 2014. Incursion of meteoric waters into the ductile regime in an active orogen. Earth Planet. Sci. Lett. 399, 1–13. doi:10.1016/j.epsl.2014.04.046

Menzies, C.D., Teagle, D.A.H., Niedermann, S., Cox, S.C., Craw, D., Zimmer, M., Cooper, M.J., Erzinger, J., 2016. The fluid budget of a continental plate boundary fault: Quantification from the Alpine Fault, New Zealand. Earth Planet. Sci. Lett. 445, 125–135. doi:10.1016/j.epsl.2016.03.046

Mercer, J., Pinder, G., 1974. Finite element analysis of hydrothermal systems, in: Oden, J.T., Zienkiewicz, O.C., Gallagher, R.., Taylor, C. (Eds.), Finite Element Methods in Flow Problems:

Proceedings of the International Symposium on Finite Element Methods in Flow Problems, Swansea, January 1974. University of Alabama Press, Huntsville, pp. 401–414.

Mortimer, N., 2004. New Zealand's Geological Foundations. Gondwana Res. 7, 261–272. doi:10.1016/S1342-937X(05)70324-5

Nakatani, M., 2001. Conceptual and physical clarification of rate and state friction: Frictional sliding as a thermally activated rheology. J. Geophys. Res. 106, 13347. doi:10.1029/2000JB900453

National Institute of Water and Atmospheric Research, 2010. The River Environment Classification system dataset.

Nimmo, J.R., 2005. Unsaturated Zone Flow Processes, in: Encyclopedia of Hydrological Sciences. Wiley, Chichester, UK, pp. 2299–2322. doi:10.1002/0470848944.hsa161

Nimmo, J.R., Healy, R.W., Stonestrom, D.A, 2005. Aquifer Recharge, in: Encyclopedia of Hydrological Sciences. Wiley, Chichester, UK, pp. 2229–2246. doi:10.1002/0470848944.hsa161a

Norris, R.J., Cooper, A.F., 2001. Late Quaternary slip rates and slip partitioning on the Alpine Fault, New Zealand. J. Struct. Geol. 23, 507–520. doi:10.1016/S0191-8141(00)00122-X

Norris, R.J., Cooper, A.F., 2007. The Alpine Fault, New Zealand: Surface geology and field relationships, in: Okaya, D., Stern, T., Davey, F. (Eds.), A Continental Plate Boundary: Tectonics at South Island, New Zealand. pp. 157–176. doi:10.1029/175GM09

Rice, J.R., Lapusta, N., Ranjith, K., 2001. Rate and state dependent friction and the stability of sliding between elastically deformable solids. J. Mech. Phys. Solids 49, 1865–1898. doi:10.1016/S0022-5096(01)00042-4

Sibson, R.H., 1992. Implications of fault-valve behaviour for rupture nucleation and recurrence. Tectonophysics 211, 283–293. doi:10.1016/0040-1951(92)90065-E

Sibson, R.H., White, S.H., Atkinson, B.K., 1979. Fault rock distribution and structure within the Alpine Fault Zone: A preliminary account. Bull. R. Soc. New Zeal. 18, 55–66.

Sims, A., Cox, S.C., Fitzsimons, S., Holland, P., 2015. Seasonal infiltration and groundwater movement in schist bedrock, Southern Alps, New Zealand. J. Hydrol. 54, 33–52.

Singhal, B.B.S., Gupta, R.P., 2010. Applied Hydrogeology of Fractured Rocks, 2nd Editio. ed. Springer, New York.

Snow, D.T., 1968. Rock fracture spacings, openings, and porosities. J. Soil Mech. Found. Div. Proc. Am. Soc. Civ. Eng. 94, 73–62.

Stern, T., Okaya, D., Kleffmann, S., Scherwath, M., Henrys, S., Davey, F., 2007. Geophysical Exploration and Dynamics of the Alpine Fault Zone 207–234.

Strayer, L.M., Hudleston, P.J., Lorig, L.J., 2001. A numerical model of deformation and fluid-flow in an evolving thrust wedge. Tectonophysics 335, 121–145. doi:10.1016/S0040-1951(01)00052-X

Sutherland, R., Harris, R.A., Stern, T., Beavan, J., Ellis, S., Henrys, S., Cox, S., Norris, R.J., Berryman, K.R., Townend, J., Bannister, S., Pettinga, J., Leitner, B., 2007. Do Great Earthquakes Occur on the Alpine Fault in Central South Island, New Zealand?, in: Okaya, D., Stern, T., Davey, F. (Eds.), A Continental Plate Boundary: Tectonics at South Island, New Zealand. American Geophysical Union, Washington DC, pp. 235–251.

Sutherland, R., Townend, J., Toy, V., Upton, P., Coussens, J., Allen, M., Baratin, L.-M., Barth, N., Becroft, L., Boese, C., Boles, A., Boulton, C., Broderick, N.G.R., Janku-Capova, L., Carpenter, B.M., Célérier, B., Chamberlain, C., Cooper, A., Coutts, A., Cox, S., Craw, L., Doan, M.-L., Eccles, J., Faulkner, D., Grieve, J., Grochowski, J., Gulley, A., Hartog, A., Howarth, J., Jacobs, K., Jeppson, T., Kato, N., Keys, S., Kirilova, M., Kometani, Y., Langridge, R., Lin, W., Little, T., Lukacs, A., Mallyon, D., Mariani, E., Massiot, C., Mathewson, L., Melosh, B., Menzies, C., Moore, J., Morales, L., Morgan, C., Mori, H., Niemeijer, A., Nishikawa, O., Prior, D., Sauer, K., Savage, M., Schleicher, A., Schmitt, D.R., Shigematsu, N., Taylor-Offord, S., Teagle, D., Tobin, H., Valdez, R., Weaver, K., Wiersberg, T., Williams, J., Woodman, N., Zimmer, M., 2017. Extreme hydrothermal conditions at an active plate-bounding fault. Nature 546, 137–140. doi:10.1038/nature22355

Sutherland, R., Toy, V., Townend, J., Eccles, J., Prior, D.J., Norris, R.J., Mariani, E., Faulkner, D.R., Pascale, G. de, Carpenter, B.M., Boulton, C., Menzies, C.D., Cox, S., Little., T.A., Hasting, M., Cole-Baker, J., Langridge, R., Scott, H.R., Lindroos, Z.R., Fleming, B., Wing, R., 2011. Operations and well completion report for boreholes DFDP-1A and DFDP-1B, Deep Fault Drilling Project, Alpine Fault, Gaunt Creek, New Zealand.

Sutherland, R., Toy, V.G., Townend, J., Cox, S.C., Eccles, J.D., Faulkner, D.R., Prior, D.J., Norris, R.J., Mariani, E., Boulton, C., Carpenter, B.M., Menzies, C.D., Little, T.A., Hasting, M., De Pascale, G.P., Langridge, R.M., Scott, H.R., Reid Lindroos, Z., Fleming, B., Kopf, J., 2012. Drilling reveals fluid control on architecture and rupture of the Alpine fault, New Zealand. Geology 40, 1143–1146. doi:10.1130/G33614.1

Tait, A., Henderson, R., Turner, R., Zheng, X., 2006. Thin plate smoothing spline interpolation of daily rainfall for New Zealand using climatological rainfall surface. Int. J. Climatol. 26, 2097–2115. doi:10.1002/joc

Tóth, J., 1962. A Theory of Groundwater Motion in Small Drainage Basins Hydrology in Central Alberta, Canada. J. Geophys. Res. 67, 4375–4387. doi:10.1029/JZ067i011p04375

Upton, P., Craw, D., Caldwell, T., Koons, P., James, Z., Wannamaker, P., Jiracek, G., Chamberlain, C., 2003. Upper crustal fluid flow in the outboard region of the Southern Alps, New Zealand. Geofluids 3, 1–12. doi:10.1046/j.1468-8123.2003.00046.x

Upton, P., Sutherland, R., 2014. High permeability and low temperature correlates with proximity to brittle failure within mountains at an active tectonic boundary, Manapouri tunnel, Fiordland, New Zealand. Earth Planet. Sci. Lett. 389, 176–187. doi:10.1016/j.epsl.2013.12.032

Wannamaker, P.E., Jiracek, G.R., Stodt, J.A., Caldwell, T.G., Gonzalez, V.M., McKnight, D.J., Porter, A.D., 2002. Fluid generation and pathways beneath an active compressional orogen, the New Zealand Southern Alps, inferred from magnetotelluric data. J. Geophys. Res. 107, 1–21. doi:10.1029/2001JB000186

Warr, L.N., Cox, S., 2001. Clay mineral transformations and weakening mechanisms along the Alpine Fault, New Zealand. Geol. Soc. London, Spec. Publ. 186, 85–101. doi:10.1144/GSL.SP.2001.186.01.06

Wells, A., Yetton, M.D., Duncan, R.P., Stewart, G.H., 1999. Prehistoric dates of the most recent Alpine fault earthquakes, New Zealand. Geology 27, 995–998. doi:10.1130/0091-7613(1999)027<0995:PDOTMR>2.3.CO;2

Whipp, D.M., Ehlers, T.A., 2007. Influence of groundwater flow on thermochronometer-derived exhumation rates in the central Nepalese Himalaya. Geology 35, 851–854. doi:10.1130/G23788A.1

Chapter 3:

Estimating fluid pressure and permeability conditions in the Alpine Fault Zone, New Zealand: insights from the DFDP-2B borehole

Abstract

The DFDP-2B borehole was drilled in 2014, to investigate conditions at depth on the Alpine Fault, the right-lateral transpressional boundary between the Pacific and Australian plates that runs through the South Island of New Zealand. The borehole penetrated to a vertical depth of 818 m through 240 m of valley sediments and Alpine Fault Zone basement rocks below. During borehole construction, drilling mud levels were monitored. Exponential models presented here provide insights into fluid pressure conditions in the Alpine Fault Zone by estimating steady state borehole hydraulic head based on observed changes in mud level (slug tests) in DFDP-2B. Borehole head increases from a relatively low value of approximately 2 m at 35 m below the base of the sediments to >60 m head in the full depth borehole. The small increase in head across the sediments is consistent with these units having a higher permeability than the basement below. Finite element models are used to provide estimates of the possible ambient head field that could produce the borehole heads. Ambient head profiles, fitted to estimated borehole heads using these models, show that ambient head may be >120 m at the base of the borehole. Application of Bouwer and Rice and Hvorslev slug test models to the data yields hydraulic conductivity estimates in the range 10^{-9} m·s^{-1} to 10^{-7} m·s^{-1}. Although conditions are likely to have deviated from the idealised scenarios assumed by conventional slug test models and the long open interval of the borehole prevents retrieval of information on permeability variations with depth, the bulk estimates obtained are consistent with values obtained based on modelling of borehole temperature data. To obtain better estimates in the future, fault zone drilling projects in the Southern Alps should aim to limit the hydraulic perturbations caused by drilling and the presence of the borehole. In particular, the uncased interval of the borehole should be minimised for periods of hydraulic testing, for example through regular insertion of casing and packer test permeability estimates also obtained.

3.1 Introduction

Fluid flow has the potential to play important roles in fault zone processes. Changes in fluid pressure can influence if and when a fault fails, as effective confining stress is a function of pore fluid pressure (Hubbert and Rubey, 1959). Thermal pressurisation, in which frictional heating and expansion of fluids during fault movement reduces the effective confining stress on the fault as it moves, may contribute to seismogenic velocity weakening behaviour (Blanpied et al., 1992; Sibson, 1973; Wibberley and Shimamoto, 2005). Fluids transfer heat and mass within fault zones and therefore have the potential to modify the frictional properties of fault rocks (Blanpied et al., 1992; Byerlee, 1993). Mineralisation associated with fluid flow may facilitate development of high pore pressures by reducing porosity and permeability near to a fault zone (Sibson, 1992). Fault zone drilling allows conditions at depth of fault zones to be investigated (Ando, 2001; Tanaka et al., 2002; Zoback et al., 2010). This study presents analyses of new hydraulic measurements from within the hanging wall of an active plate bounding fault, the Alpine Fault.

3.1.1 The Alpine Fault

The Alpine Fault (Fig. 3.1a) accommodates ~10 mm·yr^{-1} convergent and 23-25 mm·yr^{-1} strike slip displacement, representing approximately 75 % of the relative motion between the Pacific and Australian Plates in South Island, New Zealand (Norris and Cooper, 2001, 2007; Sutherland et al., 2006). The convergent component of motion on the fault has resulted in the formation of the Southern Alps mountain belt, as well as exhuming fault zone rocks from depth in its hanging wall and uplifting the regional brittle-ductile transition to a depth of 8 ± 2 km (Koons, 1987; Leitner et al., 2001). In the past, the Alpine Fault has failed in large (M_w > 7) to great (M_w ≥ 8) earthquakes every 291 ± 23 years (Berryman et al., 2012; Cochran et al., 2017; Howarth et al., 2016; Sutherland et al., 2007). The last such event was in 1717 A.D. (Wells et al., 1999), meaning the fault is currently late in its seismic cycle, allowing its pre-rupture state to be investigated.

The convergent component of motion on the fault means that it has exhumed its own fault zone rocks from depth. The fault zone rocks of the Alpine Fault hanging wall are the Alpine Schists, which are mylonitised in a ~1 km wide zone adjacent to the fault (Norris and Cooper, 2007). Hydrothermally altered calaclasites are present within ~40 m of the fault. Granitoids and metasediments in its footwall show little deformation associated with displacement on the Alpine Fault (Cox and Barrell, 2007; Norris and Cooper, 2007; Sutherland et al., 2012).

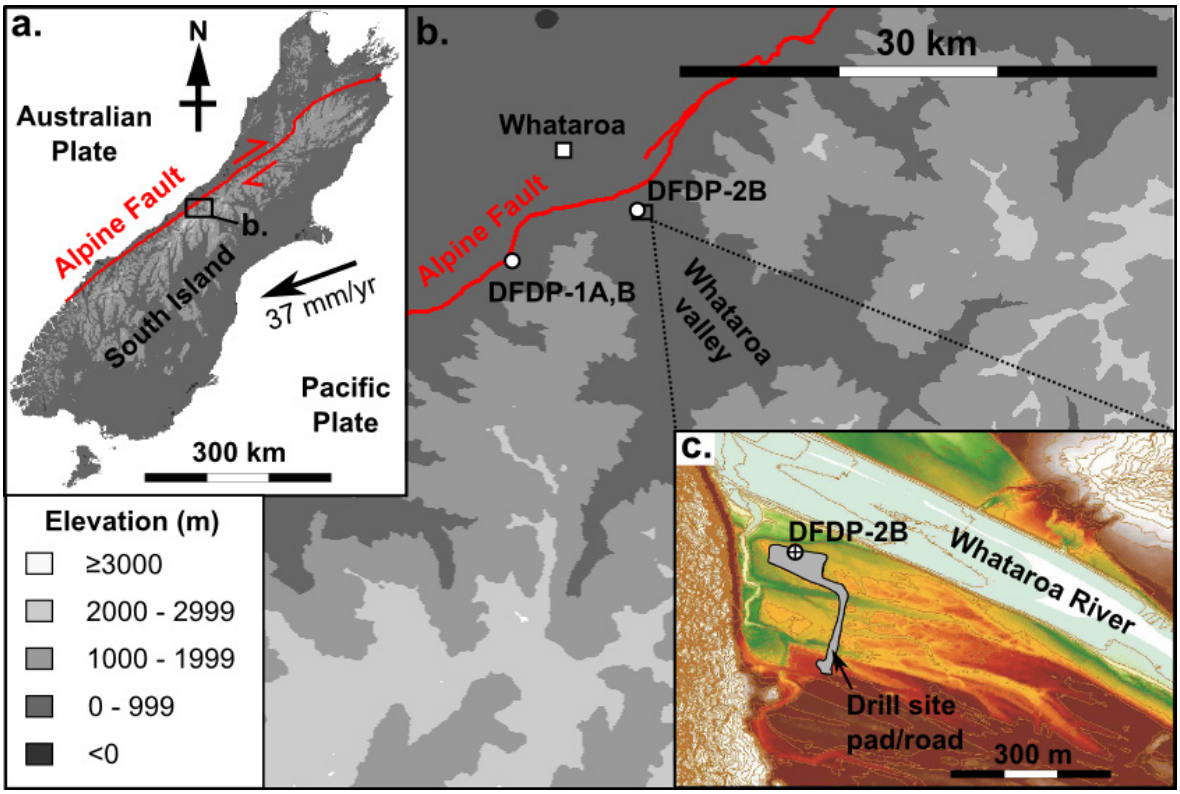

Figure 3.1 a. The tectonic setting of the Alpine Fault. b. The location of the DFDP-1A, 1B and 2B boreholes in the central Southern Alps. c. The setting of the DFDP-2B drill site and borehole within the Whataroa valley, with 1 m LIDAR contours, adapted from Sutherland et al. (2015).

Hydraulic conditions in the fault zone at shallow depth were investigated by the Deep Fault Drilling Project (DFDP) 1A and 1B boreholes (Fig. 3.1b), which intersected the fault at 91 m and 128 m respectively. Slug tests, involving the monitoring of borehole fluid level recovery following a perturbation, yielded permeability estimates of the order 10^{-14} m^2 (Sutherland et al., 2012). These estimates were interpreted to reflect permeability in fractured ultramylonites at 34-53 m depth. In DFDP-1B a fluid pressure difference of 0.53 MPa was measured across the fault, indicating that the Alpine Fault may act as a regional barrier to flow (Sutherland et al. 2012). This is supported by the distribution and chemistry of warm springs in the orogen, which are restricted to the hanging-wall side of the fault (Barnes et al., 1978) and show no isotopic evidence of interaction with high $^{87}Sr/^{86}Sr$ footwall rocks (Menzies et al., 2016).

3.1.2 DFDP-2B

The DFDP-2B borehole (Fig. 3.1b, c) was drilled in the Whataroa valley between August and December 2014 using rotary drilling, with the aim of studying the Alpine Fault Zone at greater depth than in the DFDP-1 boreholes. The first phase of DFDP-2B drilling penetrated to a drilled depth of 263 m, with a 10” diameter casing advanced to this depth (Fig. 3.2). A second phase of

drilling to form an 8.5” diameter open hole then continued to a drilled depth of 893 m. On completion of this second period of drilling, a 5.5” casing and an optical fibre (for temperature monitoring) were inserted to the bottom of the hole and cemented in place. A break in the 5.5” casing meant that cement filled the borehole interior, in addition to securing the casing. Cement within the casing was subsequently drilled out to a drilled depth of 400 m (Sutherland et al. 2017). The geometry of the borehole is not purely vertical, but instead deviates toward the Alpine Fault. As such drilled depths have been adjusted to vertical depths (Fig. 3.2) using wireline inclination data. The base of the borehole is at a vertical depth of 818 m. Depths given in this study are vertical depths, unless stated otherwise.

The lithology of the drilled interval was determined from the recovered rock cuttings. The upper 240 m of the borehole penetrates a sedimentary sequence of Pleistocene and Holocene gravels, sands, silts and diamictites, reflecting changing depositional environments in the Whataroa valley. Below this the borehole penetrated Alpine Schist basement rocks including schists, protomylonites and mylonites (Fig. 3.2).

The borehole (with the exception of upper 77 m) was drilled using a mud drilling system. As part of this drilling process, water-based drilling mud, with a greater density and viscosity than water, was pumped into the borehole during construction, in order to remove rock cut away by the drill bit and to suppress hydrogeological fluid up-flow in the borehole. When drilling was actively taking place, the mud in the borehole was circulated, so that mud continuously flowed into and out of the borehole. During breaks in drilling, wireline data such as temperature profiles were collected. Drilling encountered high temperatures, resulting in heating of the mud to >80 °C during some periods of drilling (Fig. 3.3). Differing degrees of heating of the borehole mud and of thermal perturbation of the surrounding formation by mud circulation resulted in significant variability in wireline temperature profiles. The optical fibre was used to measure downhole temperatures following the completion of the borehole. Measurements were collected over a period of months, to obtain a steady state temperature profile. This showed a steep average temperature gradient of 125 ± 55 °C·km^{-1} (Sutherland et al., 2017).

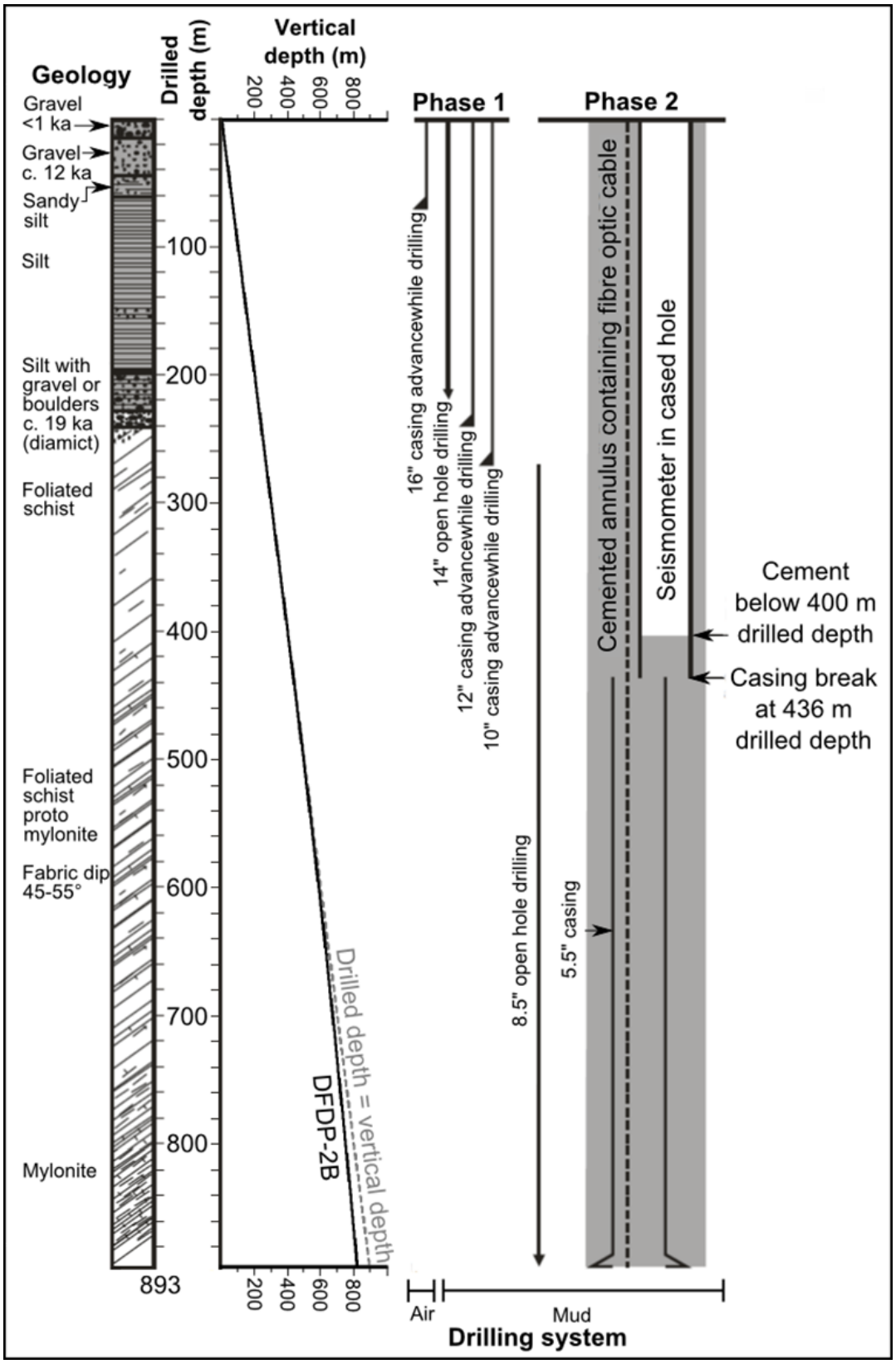

Figure 3.2 Summary of the rock types (with estimated ages for some units), relation between drilled depth and vertical depth, drilling methods and borehole structure for DFDP-2B. Borehole and casing measurements are diameters. Adapted from Sutherland et al. (2015).

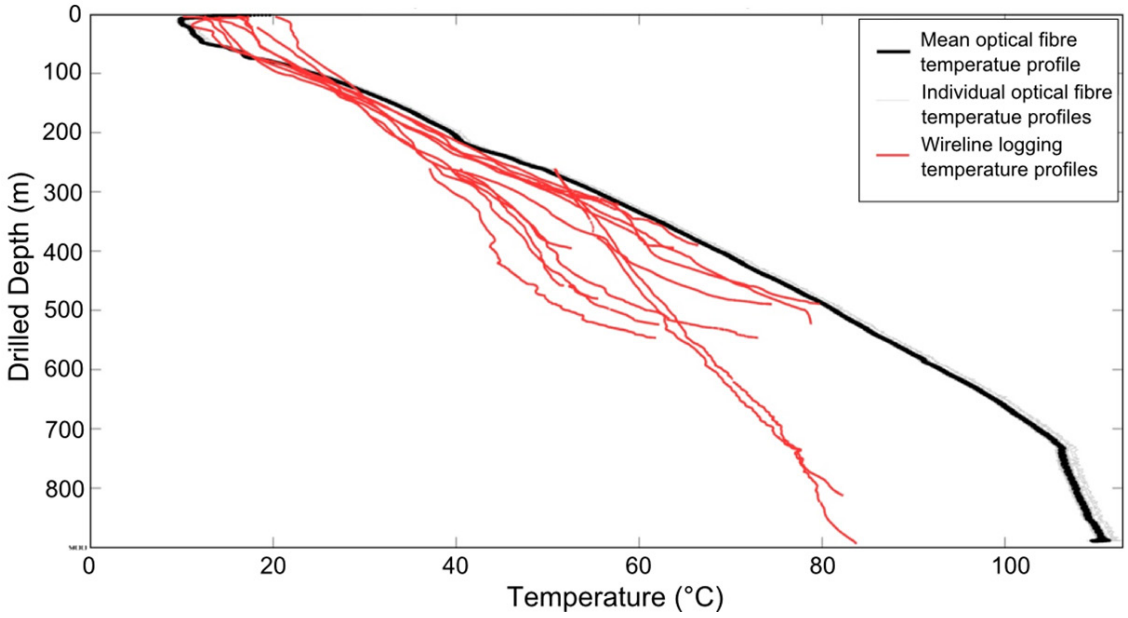

Figure 3.3 Temperature profiles from the DFDP-2B borehole. Wireline logging profiles were obtained during construction of the borehole. The optical fibre was cemented in place once the borehole had reach its full depth and was used to obtain temperature profiles following drilling. Adapted from Sutherland et al. (2015).

3.1.3 Study aims and structure

DFDP-2B data represent a rare opportunity to characterise conditions in the Alpine Fault hanging wall at a depths much greater than previously investigated. This study focusses on hydraulic data from the borehole, considering in particular the monitored mud levels. It aims to find out what this dataset can reveal about fluid pressures and permeability or hydraulic conductivity at depth, as well as to provide insights into the hydraulics of the DFDP-2B borehole, which can be used to inform planning of future fault zone drilling. Following an outline of the borehole mud system and data collection methods, estimates for steady state borehole hydraulic heads are obtained, to provide an initial indication of fluid pressure conditions across the drilled interval. These borehole head estimates were contributed by the author to combined drilling results presented by Sutherland et al. (2017) (although here additional estimates, including data originally excluded from analyses are also presented). Here the full methods used in obtaining these values are documented and results receive further discussion. Further modelling is carried out to investigate the relationship between borehole hydraulic heads (representing fluid pressure conditions at the base of the borehole at a particular depth) and ambient hydraulic heads (representing fluid pressure conditions in the undisturbed rock formation at a particular depth, in the absence of any drilling-related hydraulic perturbations) in the Alpine Fault hanging wall at DFDP-2B. Estimates for

permeability and hydraulic conductivity of rocks penetrated are obtained and discussed. Finally the implications of the findings of the study for future drilling are discussed.

3.2 Borehole hydraulic processes and data collection

Mud circulation maintained a constant mud level during drilling (Fig. 3.4). Mud was pumped into the borehole from the Suction pit and flowed out of the hole down an Overflow pipe into the Returns pit. These pits were linked by overflow pipes from one another and to an Overflow pit. Borehole mud density was controlled through addition of new mud batches, with the aim of maintaining a fluid pressure in the borehole that was slightly 'overbalanced', that is, in excess of formation fluid pressure (Azar and Samuel, 2007), such that the borehole experiences a net outflow of fluid. Maintaining an overbalance prevents net inflow into a borehole from the surrounding formation, which could become difficult to arrest and result in borehole collapse. Ensuring that the overbalance is not too large means that the amount of fluid injected into the formation is minimised.

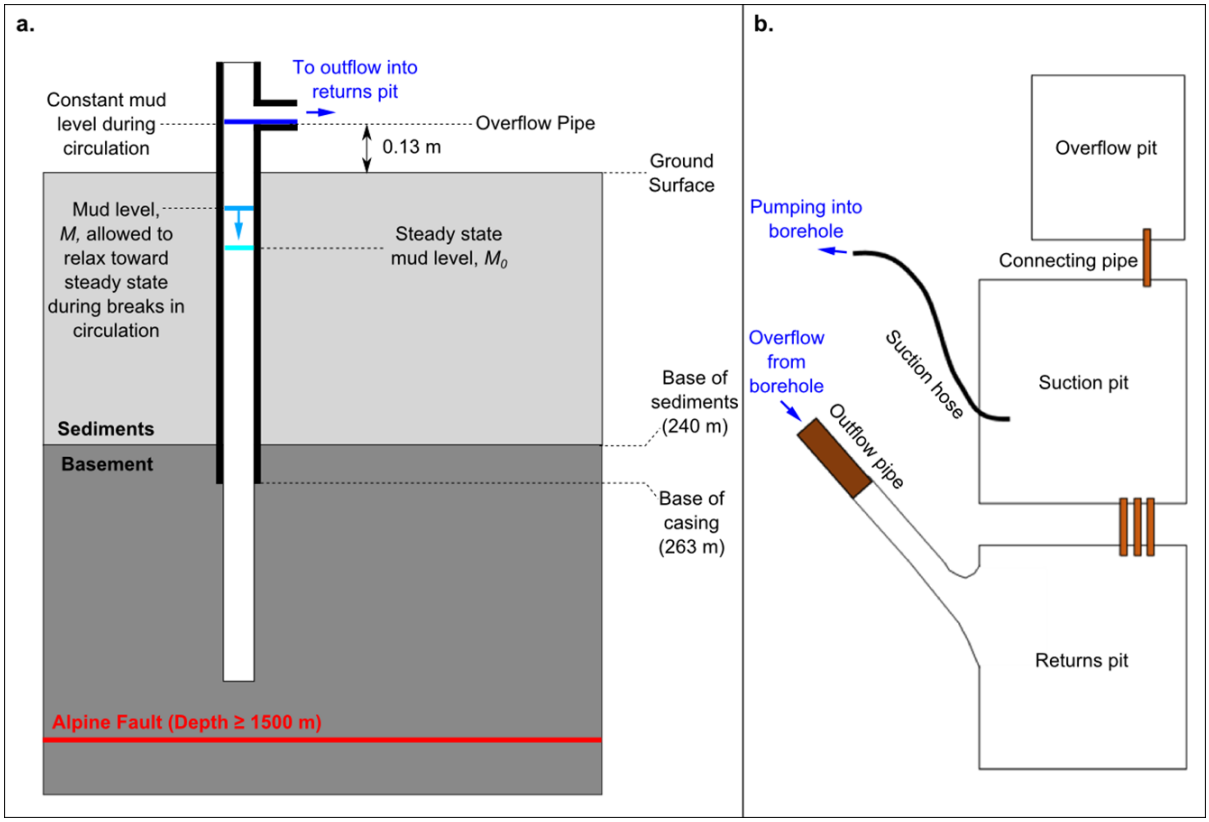

Figure 3.4 a. Flow out of an overflow maintained a constant mud level during mud circulation. Mud level was allowed to move toward a steady state level when mud was not being pumped into the borehole. b. Set-up of the mud pit system that supplied and received borehole mud.

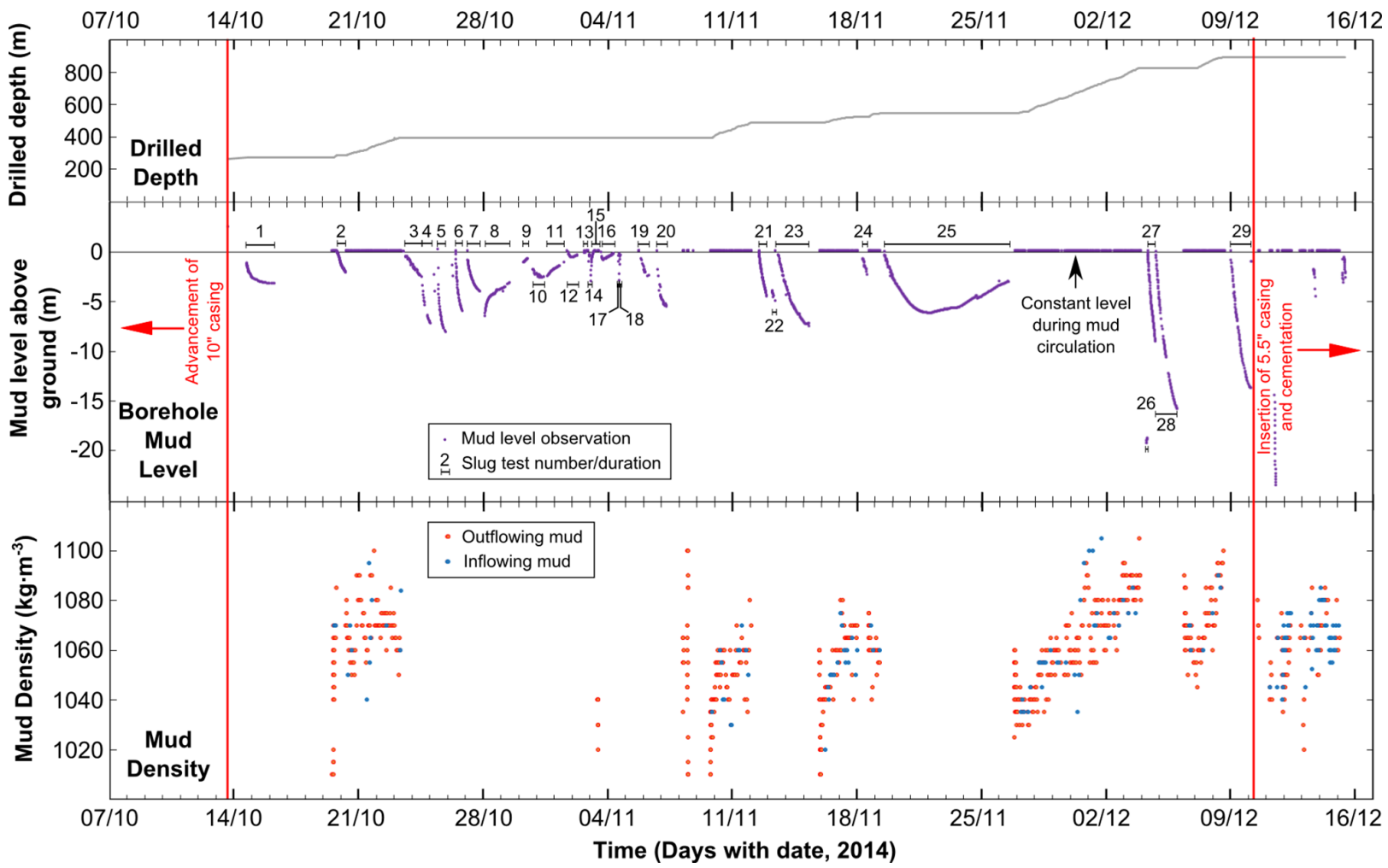

Figure 3.5 Plot of changing mud level and density in DFDP-2B with progress of drilling, following initial drilling and casing to 263 m depth. Slug tests are labelled.

When circulation was taking place, a range of properties of the inflowing and outflowing mud were measured. The procedure was to monitor outflowing mud at least hourly, although in practice, sampling intervals were sometimes slightly longer than this for operational reasons. When significant changes in the mud properties were observed and during pump-outs of mud that had remained in the borehole for significant periods during hiatuses in circulation, sampling was much more frequent, with intervals of a little as 1 minute. Inflowing mud properties (outlined below) were measured at least every 24 hours during circulation, often more frequently. In particular, inflowing mud was measured when a new batch of mud was mixed, or when circulation resumed after a hiatus.

Drilling mud density, ρ_d (kg·m^{-3}), was measured using a mud balance. The mud was also passed through a marsh funnel viscometer. The time taken for a US quart (946 mL) of mud to empty from the funnel, t_μ (s), was recorded. The following empirical formula (Pitt, 2000) was used to obtain effective mud viscosity, μ_d (mPa·s) from this data:

$$\mu_d = \frac{\rho_d}{10^3}(t_\mu - 25) \tag{3.1}$$

A digital sensor was also used to measure the conductivity and temperature of the mud. During measurements of mud properties the relative heights of the suction, returns and overflow mud pits were also noted, in order to monitor when mud loss and gain occurred.

During hiatuses in drilling and mud circulation, the mud level was allowed to adjust toward a steady state level, through fluid flow into or out of the borehole from the surrounding formation. The borehole was periodically topped up with mud, resulting in a number of distinct periods of mud level decay. Mud level was recorded using a measurement tape with inbuilt water sensor (Solinist Water Level Meter, Model 101). This was lowered down the borehole until its sensor reached the mud level, at which time the sensor gives an audible signal. Measurements were taken relative to the drill table of the drilling rig or the top of the borehole casing, when the drill rig was not in place. The elevations of these reference points relative to the ground surface at the drill site were measured and all mud levels corrected to be relative to the ground surface at the drill site.

In total 29 decay curves, described here as *slug tests*, were collected prior to cementation, numbered sequentially from slug test 1 (ST1) to slug test 29 (ST29) (Fig. 3.5). Two of these tests, ST14 and ST15, taken during activities to prevent borehole overflow were not used f or analysis on the basis of significant uncertainty in borehole mud density during the measurement period. All of the tests were carried out after the insertion of the 10” borehole casing to 263 m and prior to the insertion of the 5.5” casing to the bottom of the hole. The first test was carried when the vertical borehole depth was 275 m and the last when it was at 818 m, with tests carried out at 6

other borehole depths in between. Therefore slug tests investigate borehole conditions over a range of depth intervals.

3.3 Borehole hydraulic head

3.3.1 Modelling method

Steady state borehole head, H_0, based on fresh water with density ρ_w= 1000 kg·m^{-3}, was calculated using estimates for steady state mud level, M_0 obtained from slug test curves, together with SG_d, the specific gravity of mud with density ρ_d relative to water with density ρ_w and the vertical depth of the borehole at the time of the test, D.

$$H_0 = SG_d(D + M_0) - D \tag{3.2}$$

$$SG_d = \frac{\rho_d}{\rho_w} \tag{3.3}$$

All mud levels and heads presented represent an elevation relative to the ground surface at the drill site, such that values below the ground surface are negative.

Exponential curves were found to give a good fit (R^2≥0.93) to slug test mud data. In order to estimate steady state mud level, each slug test curve was fitted using an exponential of the form:

$$M = M_0 + Ae^{-Bt} \tag{3.4}$$

Where M is the mud level relative to ground level at time t, A is a constant representing the initial upward displacement of the mud level from steady state at t=0 and B is a decay constant. A number of slug test curves show a transition from falling mud level to rising mud level (Fig. 3.6). Application of a basic correction of thermal expansion (see 3.9 Supporting Information), treating the borehole as a one dimensional heat sink during circulation suggests that thermal expansion is only a minor contributor to these rises. They are therefore inferred to be caused by settling of drilling mud solids, resulting in significantly reduced density in sections of the borehole. Where a transition from falling to rising mud level was present, the exponential function (Eq. 3.4) was only fitted to the falling section of the curve.

A number of mud level measurements were taken while wireline logging equipment was present in the borehole. These measurements were excluded for the original modelling to produce results presented by Sutherland et al. (2017), due to concerns that the presence of this equipment may have resulted in upward displacement of the borehole mud level. Here these are included, with comparison of results showing little change in estimated borehole heads (Fig. 3.7).

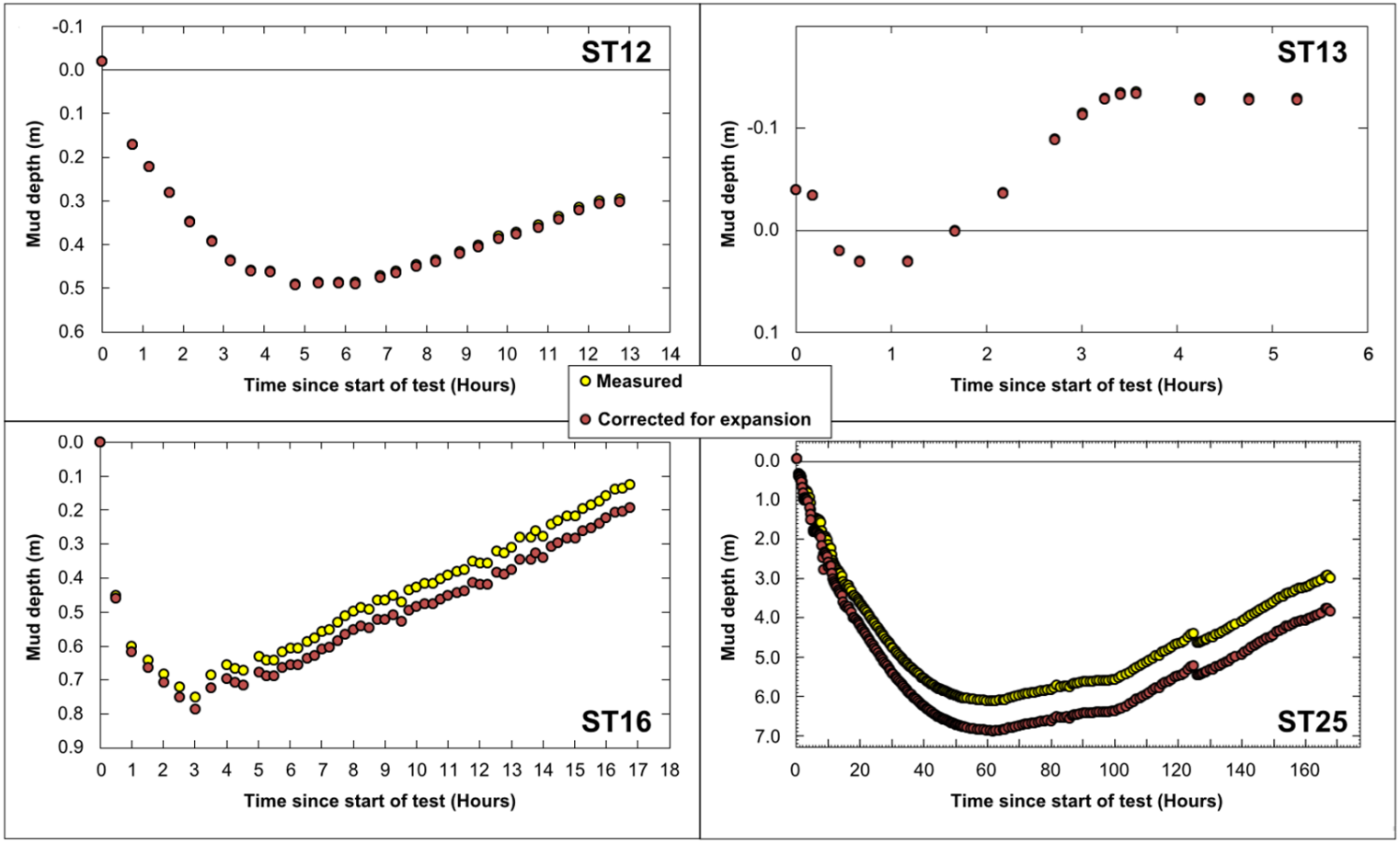

Figure 3.6 A selection of slug tests that showed a transition from falling to rising mud level. Correction of mud levels for thermal expansion (see Supporting Information 3.9.1) is not sufficient to account for this transition.

For quantification of uncertainty in M_0, slug tests were divided into sets of tests carried out at the same borehole depth, with no circulation occurring between the tests. Sequential tests at the same borehole depth where circulation had taken place between tests cannot be grouped with respect to uncertainty in M_0 as they do not share a common value for ρ_d, which itself would cause deviation in M_0 between these tests. Standard deviation, SD, in M_0 estimates was calculated for all sets. For slug tests within sets, uncertainty, δM_0, was set as two standard deviations, $2SD$. For slug tests that did not form part of a repeated set, δM_0 was specified based on the value of $2SD$ for the set incorporating the largest number of tests.

A set of 3 approaches for estimating ρ_d during each test were defined (Table 3.1), as the data available varied between tests, not allowing any one approach to work for all tests. For the 'first approach', ρ_d was calculated as the average of measurements from mud flowing out of the borehole during the 2.5 hours before the end of circulation preceding the test. 2.5 hours was chosen, rather than 2 hours as it ensured that hourly measurements that took place slightly early (e.g. 2 hours 1 minute before the end of circulation) were not excluded. Maximum and minimum ρ_d measurements from this period were combined with an estimation of the measurement error (±5 kg·m^{-3}), based on the precision of the mud balance, to set maximum and minimum mud densities for the purposes of uncertainty calculation. If no measurements of ρ_d were recorded within 2.5 hours of the end of circulation or a newly mixed batch of mud was added during this 2.5 hour period, which was not within error (±5 kg·m^{-3}) of the range of ρ_d measurements prior to addition (e.g., dense 'kill mud' was added), a second approach was applied.

The second approach was based on mud density measurements during pumping of mud out of the borehole following a test. The time for the borehole mud to be completely pumped out following a slug test was calculated based on the pumping rate and borehole volume. The average measured mud density during this pump-out period was used as the estimate for ρ_d during the preceding slug test. Maximum and minimum ρ_d measurements from this the pump-out period were combined with the term for measurement error (±5 kg·m^{-3}) to give the uncertainty in ρ_d.

A third approach was applied where new mud of significantly different density (>5 kg·m^{-3} difference) to the mud already in borehole ('old mud') was added prior to the slug test and where there were no ρ_d measurements from a borehole pump-out following the test. In this approach, estimated ρ_d was based on a volume weighted average of the measured density of the old mud and the new mud. The density of the old mud was calculated based on mud flowing out of the borehole in the 2.5 hours before the end of circulation. Density of the new mud was measured from a sample of the new batch of mud added. The volume of new mud added was recorded prior to addition. The volume of remaining old mud was calculated based on the borehole volume, with

the volume of new mud subtracted. Uncertainty was based on the maximum and minimum of all ρ_d values (including old mud flowing prior to the test and the new mud) and also incorporates ±5 kg·m^{-3} measurement error.

Table 3.1 Methods used for estimation of ρ_d values.

ρ_m estimation method	**Methodology summary**	**Tests using method**
First approach	Based on average of mud flowing out of the borehole prior to the test	ST1-2, ST21-29
Second approach	Based on average of mud pumped out of the borehole following the test	ST19-20
Third approach	Volume weighted average based on mud flowing out of borehole and new mud added prior to the test	ST3-13, ST16-18

Uncertainties in the vertical depth of the borehole were based on an estimated measurement error of 0.05 m. This represents a conservative estimate, as borehole vertical depths are constrained to within ~0.01 m (M. Linh Doan, pers. comm.).

Uncertainty in borehole head, $\delta {H_0}^2$ was calculated for individual tests based on the following rules (Taylor, 1997):

If,

$$a = b + c \tag{3.5}$$

Then uncertainty in a is calculated as:

$$\delta a^2 = \delta b^2 + \delta c^2 \tag{3.6}$$

And if,

$$a = bc \tag{3.7}$$

Then uncertainty in a is calculated as:

$$\left(\frac{\delta a}{a}\right)^2 = \left(\frac{\delta b}{b}\right)^2 + \left(\frac{\delta c}{c}\right)^2 \tag{3.8}$$

Applying these rules to Eq. 3.2 gives:

$$\delta {H_0}^2 = \delta D^2 + (SG_d D)^2 \left[\left(\frac{\delta SG_d}{SG_d}\right)^2 + \left(\frac{\delta D}{D}\right)^2\right] + (SG_d M_0)^2 \left[\left(\frac{\delta SG_d}{SG_d}\right)^2 + \left(\frac{\delta M_0}{M_0}\right)^2\right] \tag{3.9}$$

Estimates of borehole head for each borehole depth were calculated based on the mean of head estimates for all tests carried out at that borehole depth. For each, δH_0 was based on $2SD$ for

borehole depths with multiple tests. For borehole depths with only one test, uncertainty was set at the maximum of $+\delta H_0$ and $-\delta H_0$ calculated for the individual test.

3.3.2 Results and discussion

The exponential model was found to give a good fit to mud level decay curves ($R^2 \geq 0.93$ for all tests) (Table 3.2). Borehole heads calculated based on modelled M_0 values broadly increase with borehole depth, consistent with the hole experiencing increasing ambient heads with depth associated with fluid up-flow (Fig. 3.7). Because of the long uncased interval of the borehole, these borehole heads do not represent ambient head at a particular depth. In the presence of an ambient vertical head gradient, a borehole will act as a high transmissivity pathway for fluid flow from higher ambient head regions at depth to lower ambient head regions nearer the surface, resulting a perturbation of the steady state flow regime for pre-drilling conditions. Borehole heads therefore represent a value somewhere between the highest and lowest ambient heads across the uncased interval of the borehole. Further analysis, performed in the next section of this study, is required to obtain better estimates of ambient heads.

Borehole heads do, however, provide some indication of the relative permeability of the sediments penetrated by DFDP-2B compared to the basement rocks below. If the water table is assumed to correspond to the ground surface at DFDP-2B, theoretical borehole head would be 0 m at a borehole depth of 0 m. Thus the borehole head of ~2 m at 275 m borehole depth represents only a small increase in head across the upper portion of the borehole, which penetrates through sediments to 240 m depth, relative to the increases in borehole head in the basement below this depth. Assuming that changes in fluid properties can be neglected for the purposes of local consideration of the drilled interval, Darcy's Law gives:

$$q = -K\frac{dh}{dz} \tag{3.10}$$

$$K = \frac{k\rho g}{\mu} \tag{3.11}$$

Where q is vertical Darcy velocity, K is hydraulic conductivity, which is a function of fluid density, ρ, fluid viscosity, μ and the acceleration due to gravity, g and dh/dz is the vertical head gradient. If vertical q is assumed to remain approximately constant in the surrounding formation, the shallower borehole head gradient across the sediments relative to the basement implies that the sediments have a higher hydraulic conductivity and permeability, assuming that the borehole head gradients reflect the relative ambient head gradients of these units. This apparent higher permeability across the upper section of the borehole suggests that sediment units which might be expected to have a low permeability (e.g. lacustrine silts) may be of limited lateral extent.

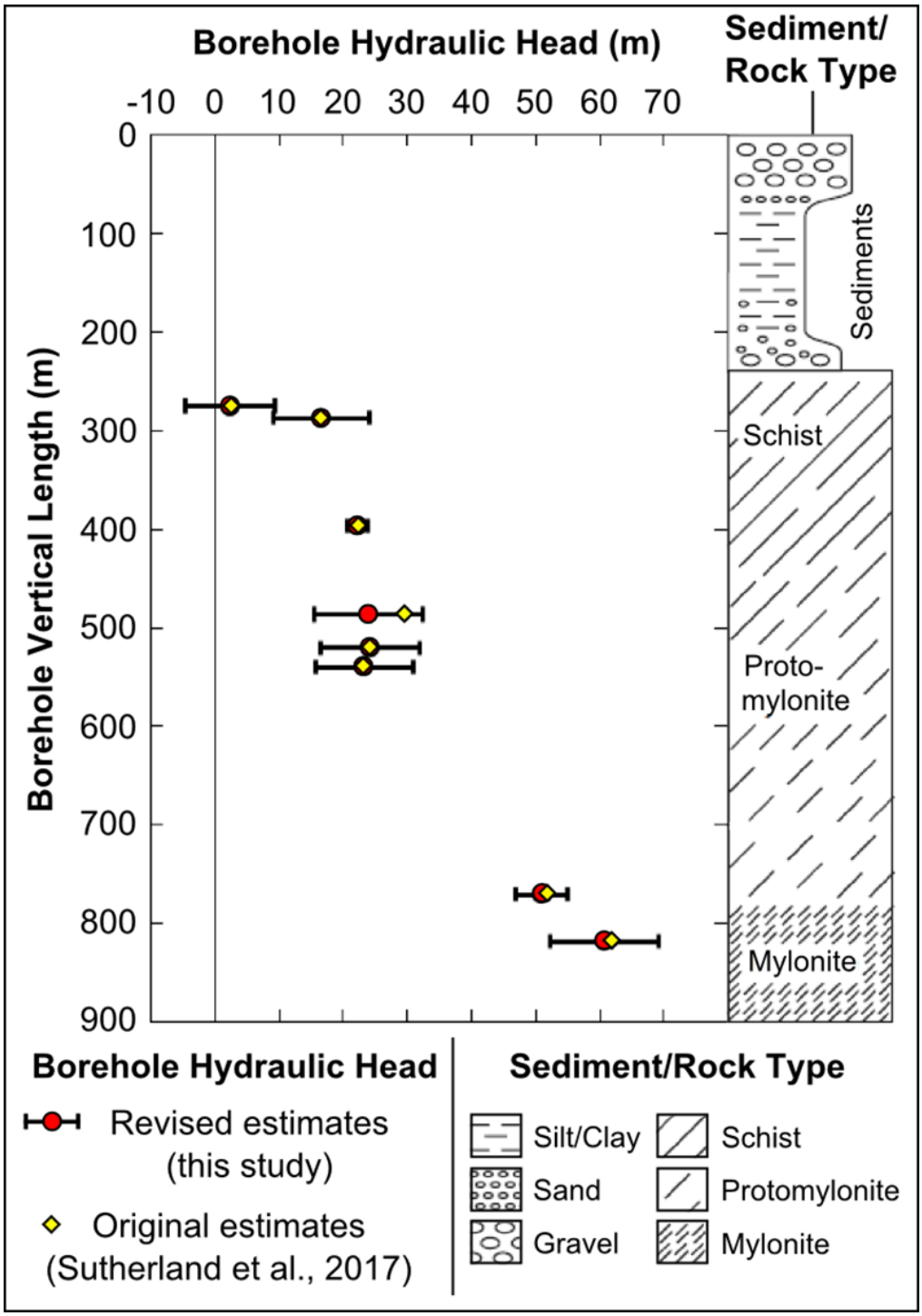

Figure 3.7 Estimated borehole heads for DFDP-2B using fitted exponential curves. Original estimates (Sutherland et al., 2017) excluding data collected while wireline logging equipment was present in the borehole during some tests lie within the uncertainty interval of revised estimates presented here, based on models that include this data. Rock type column from Sutherland et al. (2017).

Table 3.2 Borehole heads for individual slug tests and averaged values for each investigated borehole depth. δD = 0.05 m for all tests. Continued opposite.

Individual Tests													Borehole Depths		
Slug Test	L (m)	A (m)	B (s^{-1})	R^2	M_0 (m)	$\pm\delta M_0$ (m)	SG_d (-)	$+\delta SG_d$ (-)	$-\delta SG_d$ (-)	H_0 (m)	$+\delta H_0$ (m)	$-\delta H_0$ (m)	L (m)	H_0 (m)	$\pm\delta H_0$ (m)
ST01	275	1.9	4.8×10^{-5}	>0.99	-3.0	6.7	1.02	0.005	0.005	2.4	7.0	7.0	275	2.4	7.0
ST02	287	3.7	2.2×10^{-5}	>0.99	-3.4	6.7	1.071	0.005	0.005	16.6	7.4	7.4	287	16.6	7.4
ST03	396	8.2	4.1×10^{-6}	>0.99	-8.2	6.7	1.068	0.021	0.023	18.2	11.0	11.6	396	22.3	1.6
ST04		6.5	4.3×10^{-5}	>0.99	-8.4					18.0	11.0	11.6			
ST05*		5.8	1.1×10^{-4}	0.98	-7.8					18.6	11.0	11.6			
ST06		5.3	1.3×10^{-4}	0.98	-5.7					20.9	11.0	11.6			
ST07		3.7	4.3×10^{-5}	>0.99	-4.1					22.5	11.0	11.6			
ST08		-2.6	3.0×10^{-5}	0.96	-3.4					23.4	11.0	11.6			
ST09		-2.3	9.5×10^{-6}	>0.99	1.2					28.2	11.0	11.6			
ST10		0.9	5.6×10^{-5}	0.94	-2.6					24.2	11.0	11.6			
ST11		-1.4	2.2×10^{-5}	>0.99	-1.0					25.9	11.0	11.6			
ST12		0.6	1.3×10^{-4}	>0.99	-0.6					26.3	11.0	11.6			
ST13		1.0	3.5×10^{-5}	0.93	-0.9					25.9	11.0	11.6			
ST16		0.7	5.0×10^{-4}	>0.99	-0.7	0.7	1.055	0.04	0.04	21.0	15.9	15.9			
ST17		-0.90	5.4×10^{-4}	>0.99	0.0					21.7	15.9	15.9			
ST18		-2.7	5.4×10^{-4}	>0.99	-0.1					21.7	15.9	15.9			
ST19		2.2	5.3×10^{-5}	>0.99	-2.7	3.8	1.062	0.008	0.012	21.5	5.2	6.2			
ST20		5.0	8.8×10^{-5}	0.98	-5.4					18.7	5.2	6.2			

Individual Tests (cont.)													Borehole Depths (cont.)		
Slug Test	L (m)	A (m)	B (s^{-1})	R^2	M_0 (m)	$\pm\delta M_0$ (m)	SG_d (-)	$+\delta SG_d$ (-)	$-\delta SG_d$ (-)	H_0 (m)	$+\delta H_0$ (m)	$-\delta H_0$ (m)	L (m)	H_0 (m)	$\pm\delta H_0$ (m)
ST21	486	19.5	8.6×10^{-6}	>0.99	-19.5	13.7	1.075	0.005	0.005	15.5	14.9	14.9	486	23.9	8.5
ST22		2.8	1.8×10^{-3}	0.97	-6.6					29.4	14.9	14.9			
ST23		10.2	1.2×10^{-5}	>0.99	-9.1					26.7	14.9	14.9			
ST24	520	9.6	8.2×10^{-6}	0.96	-10.2	6.7	1.068	0.005	0.005	24.2	7.6	7.65	520	24.2	7.6
ST25	540	7.2	9.6×10^{-6}	>0.99	-7.3	6.7	1.058	0.005	0.005	23.3	7.6	7.6	540	23.3	7.6
ST26	770	-0.6	4.4×10^{-4}	0.99	-18.6	6.4	1.091	0.005	0.005	49.7	8.0	8.0	770	50.9	4.0
ST27		13.9	2.7×10^{-5}	>0.99	-13.9					54.9	8.0	8.0			
ST28		20.0	1.5×10^{-5}	>0.99	-19.9					48.2	8.0	8.0			
ST29	818	17.1	1.7×10^{-5}	>0.99	-17.3	6.7	1.098	0.005	0.005	60.7	8.4	8.4	818	60.7	8.4

*The first measured mud level during this test was above overflow pipe level and is therefore not included in analyses.

3.4 Ambient hydraulic head

3.4.1 Modelling method

The borehole head estimates from exponential models are built upon using a finite element model, to obtain an estimate of the possible relationship between borehole heads and the ambient head in the Alpine Fault hanging wall. Steady state Darcian finite element models for the DFDP-2B borehole were built using COMSOL. These are radially symmetric about the borehole, which was treated as vertical for the purposes of this modelling (Fig. 3.8). All model elevations are relative to the ground surface at the drill site, set at 0 m. A no-flow basal boundary was set at -1200 m elevation, representing the approximate depth of the Alpine Fault, which acts as a barrier to flow (Menzies et al., 2016; Sutherland et al., 2012). Models were split into a basement region below -240 m and a sediment region above this, as well as incorporating the borehole and its casing. A constant basement permeability, k_b = 10^{-16} m^2 was assumed. The permeability of the sediments, k_s was also assumed to be constant and higher than that of the basement, based on the shallower borehole head gradient across the upper section of the borehole and was set as $10^2 k_b$. Borehole permeability, k_{bh} was set as $10^9 k_b$ and casing permeability, k_c was set as $10^{-5} k_b$. These values give changes in head along the length of the model borehole of <0.1 m.

A fixed head boundary was applied at 120 m radius, where hydraulic head within the rock formation was assumed to be unperturbed from ambient conditions by the borehole. Head along this outer boundary of the models was fixed using a piecewise-linear function. The use of a significantly greater outer radius is inappropriate, as the borehole is <200 m from the ridge at the valley margin, where ambient heads may be significantly different. The sensitivity of results to this and other parameter choices was investigated.

For Model A, the outer head function was set to have two sections- one corresponding to the model region above the sediment-basement boundary at -240 m, the other to the region below. Model B had five equal 240 m sections of linearly increasing head. Using COBYLA optimisation, coefficients for head gradient in the outer head function were altered from initial values (0.05 in the sediments and 0.5 in the basement) to minimise the difference between borehole head simulated in these models and estimated H_0 values in the previous section of the study. These models are not thermally coupled as, due to the thermal perturbations associated with drilling and mud circulation highlighted by wireline logs, the temperature regime in the surrounding formation during slug tests, and in many cases also in the borehole, is not well constrained.

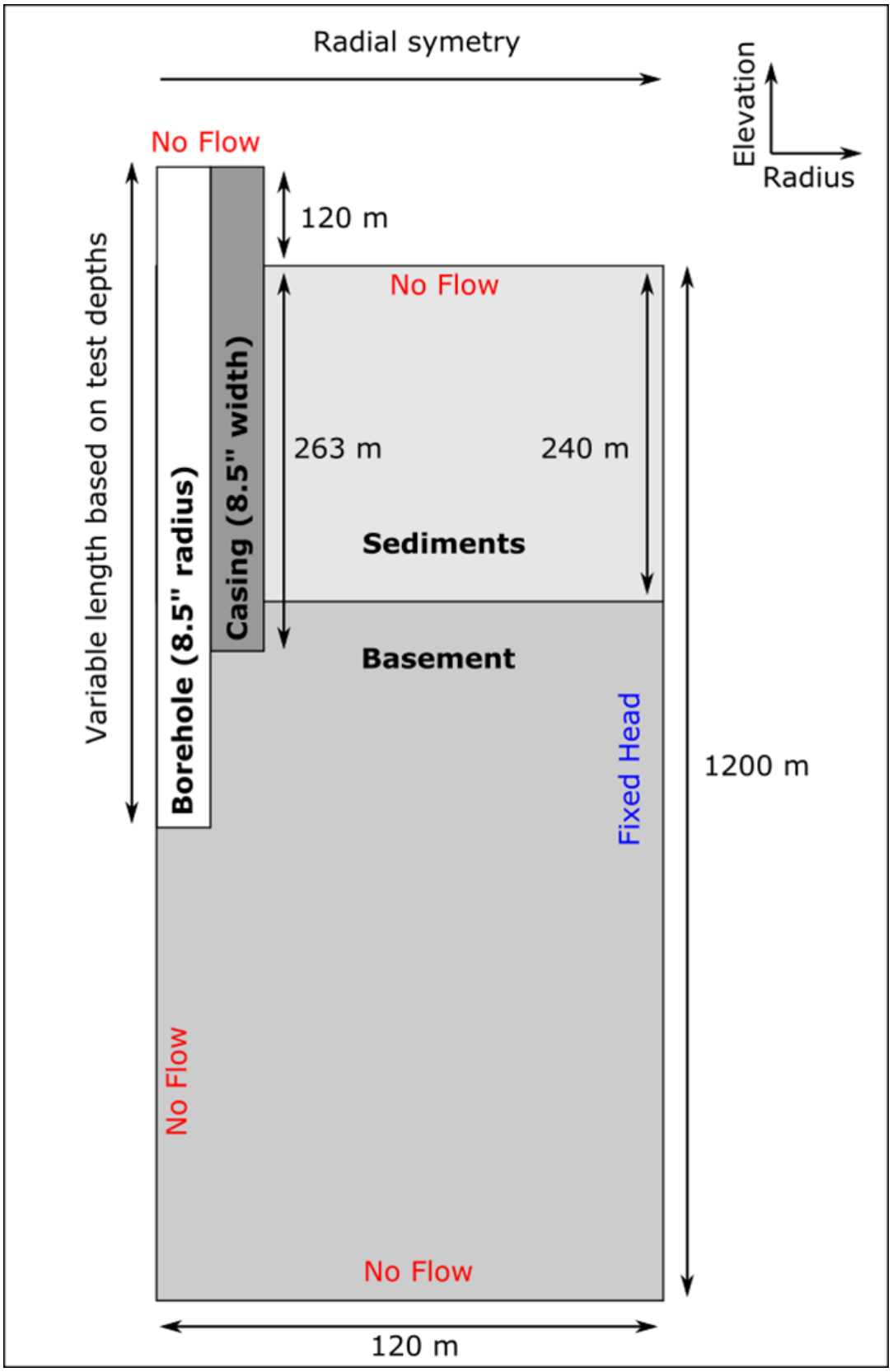

Figure 3.8 Geometry (not to scale) of the radially symmetric borehole model.

3.4.2 Results and discussion

Model borehole heads are unaffected by the choice of absolute permeability and are also relatively insensitive to doubling or halving of model outer radius, reduction in model depth to 900 m and to moderate changes in the relative permeabilities of components (Table 3.3, 3.4). Model A borehole heads lie within the uncertainty range of H_0 values for three of the eight borehole depths (Fig. 3.9a). Model B gives an improved fit to H_0 values, lying within the uncertainty range of H_0 for all but one (396 m) borehole depth.

An improved fit to estimated borehole heads may be possible through use of an alternative form of function for model fixed head or by simulating a more complex heterogeneity in permeability structure. Therefore neither Model A nor Model B is presented as a unique best representation of ambient heads, but rather these models are used to provide an approximate indication of the ambient head field that could produce the borehole heads observed, which would otherwise remain unknown. Both models indicate ambient heads at the base of the borehole that are >30 m higher than the borehole head estimated for the full depth borehole. For Model B this ambient head is more than double the borehole head value. No interpretations are made based on modelled ambient head below the extent of DFDP-2B (-818 m), as although models simulate ambient heads to an elevation of -1200 m, in an attempt to accurately represent the flow regime, measurements used to inform these models are restricted to the drilled interval.

In addition to allowing possible ambient head conditions to be investigated, these models provide an indication of variation of fluid flow rates along the borehole (Fig. 3.10). Due to the vertical head gradient, steady state borehole fluid levels represent a state of dynamic equilibrium, with flow into the borehole at depth and outflow from the borehole nearer the surface. The magnitude of flow rates between the borehole and surrounding rock formation increases toward to top and bottom of the uncased interval, with no flow at the transition between inflow and outflow. The transition from inflow to outflow corresponds approximately to the depth at which borehole head is equal to model outer ambient head. The variation in flow rates along the borehole has implications for hydraulic conductivity estimates based on DFDP-2B slug test data, discussed in the next section.

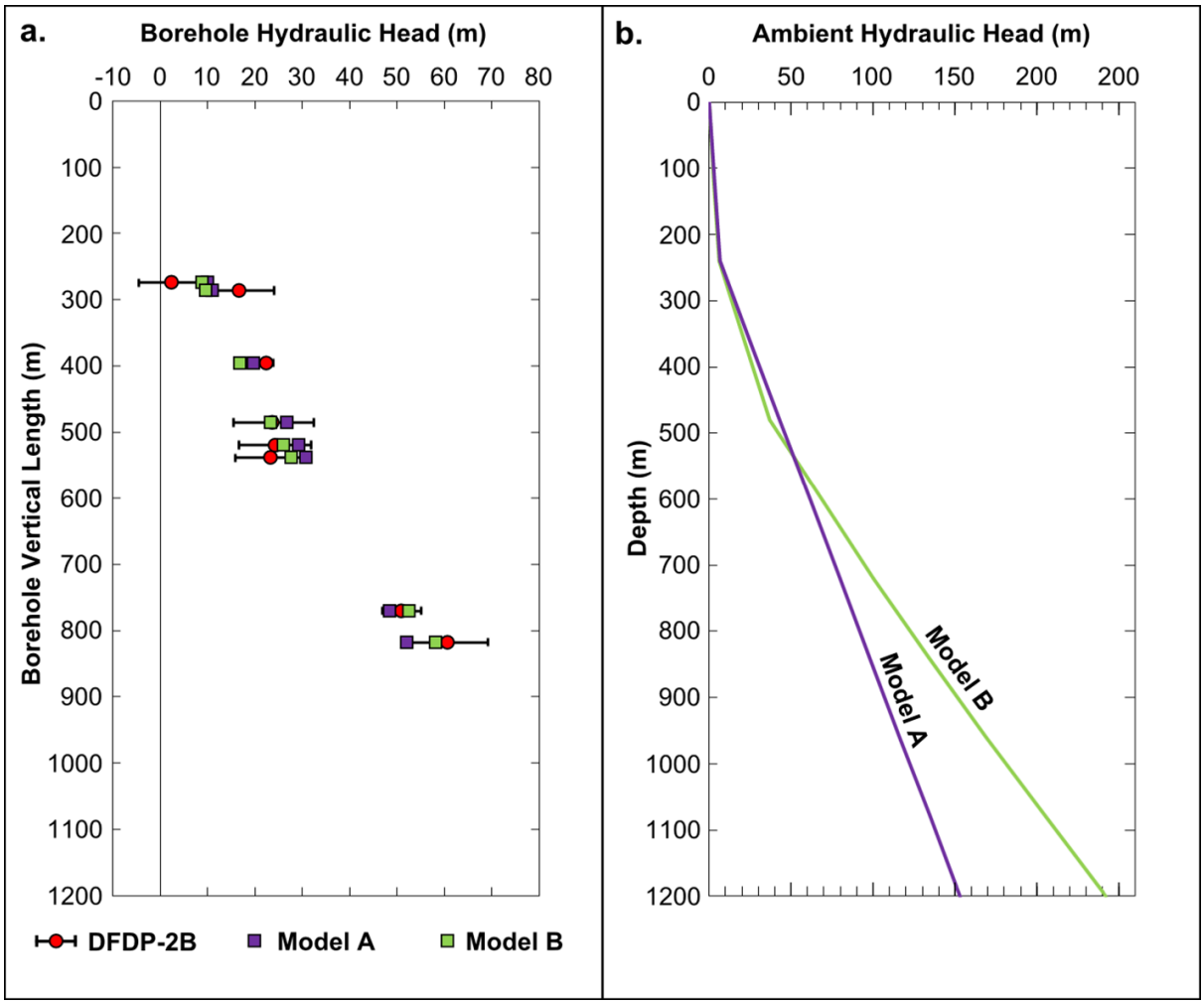

Figure 3.9 a. Borehole heads simulated by radial borehole Models A and B, compared to H_0 estimates obtained from DFDP-2B slug tests. b. Fitted ambient heads in Model A and B.

Table 3.3 Sensitivity of borehole heads simulated by Model B to changes in permeability and fluid density and viscosity.

Borehole vertical depth (m)	Model B borehole head (m)	Sensitivity											
		k_b (Basement) (m^2)		k_s (Sediment) (m^2)		k_{bh} (Borehole) (m^2)		k_c (Casing) (m^2)		Fluid viscosity (mPa·s)		Fluid density ($kg \cdot m^{-3}$)	
		10^{-14}	10^{-18}	$=k_b$	$=10^4 k_b$	$=10^8 k_b$	$=10^{10} k_b$	$=10^{-4} k_b$	$=10^{-6} k_b$	0.1	10	10000	100
275	8.8	8.8	8.8	11.7	8.8	8.8	8.8	8.8	8.8	8.8	8.8	8.8	8.8
287	9.6	9.6	9.6	12.2	9.6	9.6	9.6	9.6	9.6	9.6	9.6	9.6	9.6
396	16.8	16.8	16.8	18.1	16.8	16.8	16.8	16.8	16.8	16.8	16.8	16.8	16.8
486	23.3	23.3	23.3	24.1	23.2	23.2	23.3	23.3	23.3	23.3	23.3	23.3	23.3
520	26.0	26.0	26.0	26.8	26.0	26.0	26.0	26.0	26.0	26.0	26.0	26.0	26.0
540	27.7	27.7	27.7	28.5	27.7	27.7	27.7	27.7	27.7	27.7	27.7	27.7	27.7
770	52.4	52.4	52.4	52.9	52.4	52.1	52.4	52.4	52.4	52.4	52.4	52.4	52.4
818	58.2	58.2	58.2	58.7	58.2	57.8	58.2	58.2	58.2	58.2	58.2	58.2	58.2

Table 3.4 Sensitivity of borehole heads simulated by Model B to changes in model geometric parameter values.

Borehole vertical depth (m)	Model B borehole head (m)	Sensitivity								
		Distance of outer boundary from centre of model (m)			Elevation of top of borehole (m)			Elevation of base of model (m)		
		60	240	480	0	60	240	-1100	-1000	-900
275	8.8	9.5	8.4	9.0	8.8	8.8	8.8	8.8	8.8	8.8
287	9.6	10.2	9.3	10.1	9.6	9.6	9.6	9.6	9.6	9.6
396	16.8	16.8	17.8	20.1	16.8	16.8	16.8	16.8	16.8	16.8
486	23.3	22.6	25.3	28.5	23.3	23.3	23.3	23.3	23.3	23.3
520	26.0	25.2	28.3	31.7	26.0	26.0	26.0	26.0	26.0	26.0
540	27.7	26.9	30.1	33.6	27.7	27.7	27.7	27.7	27.7	27.7
770	52.4	51.7	54.5	56.3	52.4	52.4	52.4	52.4	52.4	52.2
818	58.2	57.6	60.1	61.1	58.2	58.2	58.2	58.2	58.2	57.8

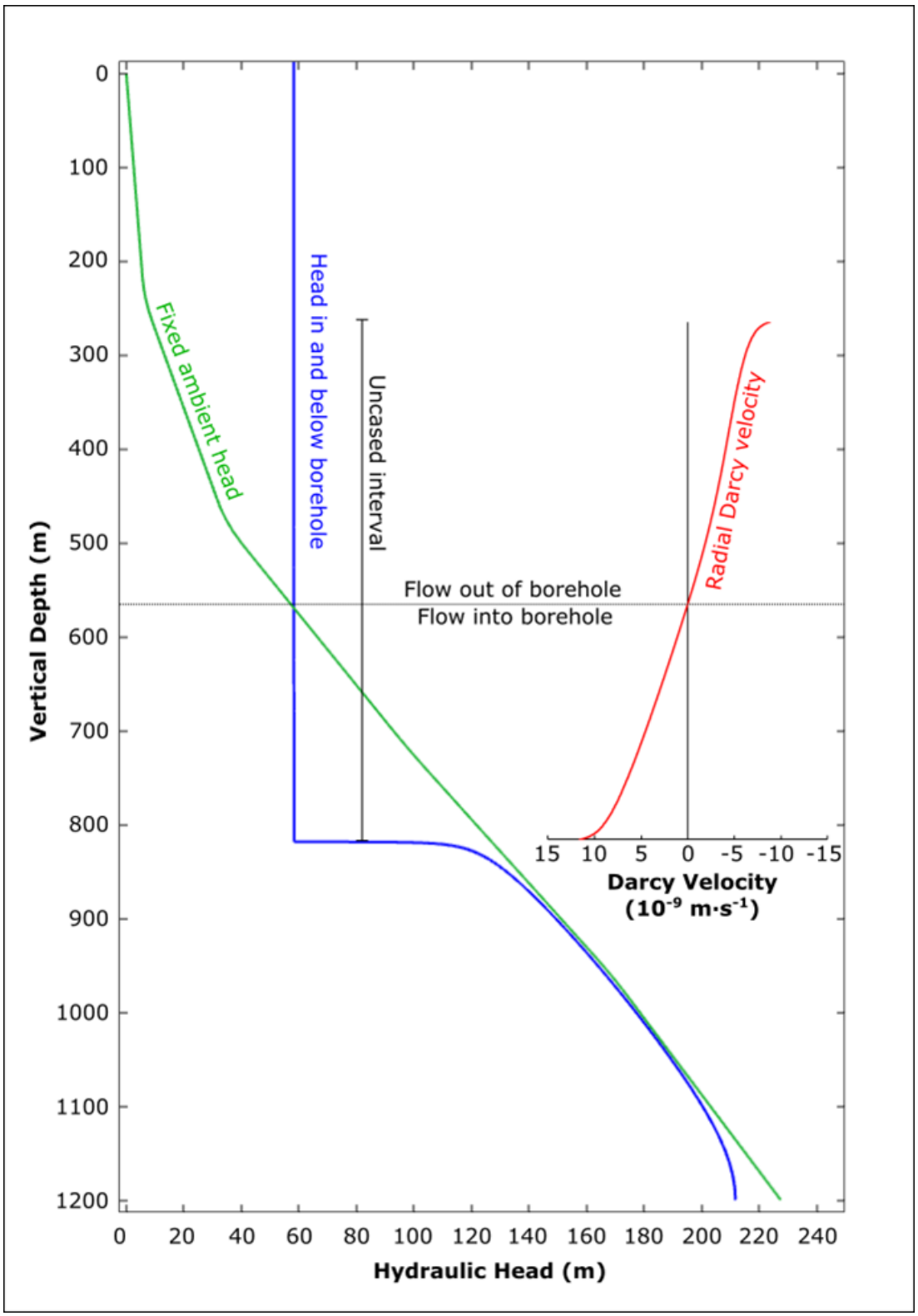

Figure 3.10 Variation in heads and radial flow rates with depth along the open section of the full 818 m long borehole in Model B, with the transition from inflow to outflow corresponding approximately to the point at which borehole head falls below ambient head. Flow rates are shown are at from within the model basement rocks, at 1 m from the borehole-rock interface.

3.5 Hydraulic conductivity and permeability

3.5.1 Modelling method

The slug test analysis methods of Bouwer and Rice (1976) and Hvorslev (1951) are commonly used to estimate hydraulic conductivity, which may be converted to an equivalent permeability, if fluid density and viscosity are known. These methods were used to estimate permeability at the DFDP-1 boreholes (Sutherland et al., 2012) and in this study were applied to DFDP-2B slug test data to estimate hydraulic conductivity and permeability. Both methods assume steady state radial flow, with negligible variation in fluid properties, into a borehole following an instantaneous perturbation in borehole fluid level. The applicability of these assumptions to DFDP-2B slug test dataset is discussed subsequently.

For the Bouwer and Rice method, hydraulic conductivity is calculated as:

$$K = \frac{r_c^2 \ln(R_e/r_w)}{2d} \frac{1}{t} \ln\left(\frac{y_i}{y(t)}\right) \tag{3.12}$$

Where r_c is the radius of the borehole casing, R_e is an effective radius, over which fluid level perturbation is dissipated (calculated using electrical analogues), r_w is the radius of the borehole or well, d is the length of the borehole which is uncased and open to fluid flow, t is the time elapsed since the initiation of the slug test, y_i is the change in borehole fluid level relative to its unperturbed level at the initiation of the test and y is the borehole fluid level relative to its unperturbed level at time t.

Using the Hvorslev method for partially penetrating wells, isotropic hydraulic conductivity is calculated as:

$$K = \frac{r_c^2 \ln(d/2r_w) + \sqrt{1 + (d/2r_w)^2}}{2d} \frac{1}{t} \ln\left(\frac{y_i}{y(t)}\right) \tag{3.13}$$

As all parameters in these equations are commonly assumed constant for a particular slug test, with the exception of y and t, data obeying these relations should plot as a straight line on a graph of $\ln(y(t))$ against t allowing estimation of $ln\left(\frac{y_i}{y(t)}\right)/t$ based on the gradient of this line (Bouwer, 1989). Commonly, slug test datasets plot as a straight line during the early part of the test only (Fig. 3.10a) (Bouwer and Rice, 1976).

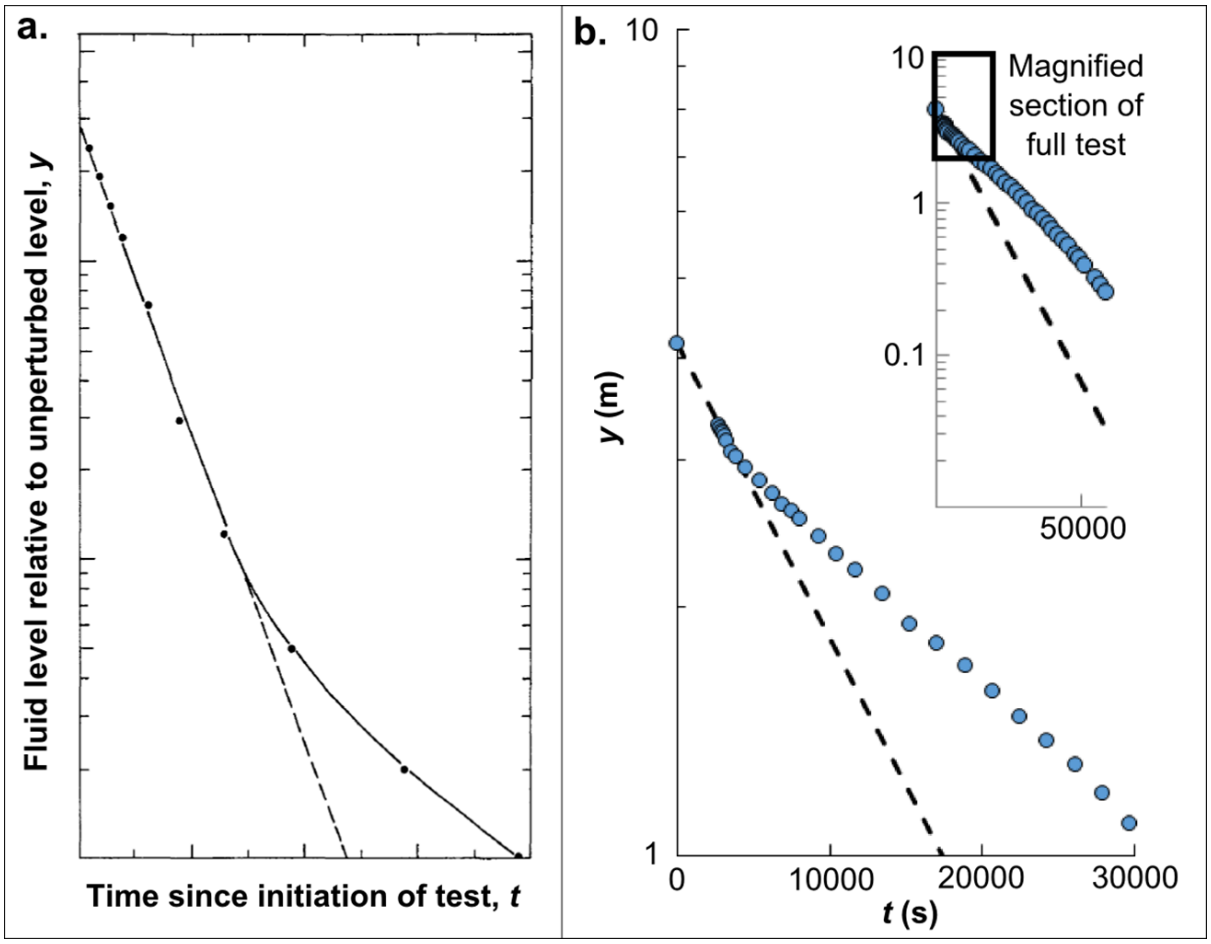

Figure 3.11 a. Example of fitting of slug test data for gradient, adapted from Bouwer and Rice (1976). b. Fitting of the initial straight section of ST7 data from DFDP-2B.

DFDP-2B slug tests used for head calculation were analysed using both Bouwer and Rice and Hvorslev methods, with y_i and y calculated based on M_0 values from exponential curve fitting and $\ln\left(\frac{y_i}{y(t)}\right)/t$ estimates obtained based on fitting initial straight line sections of these tests (Fig. 3.11b). For tests in which borehole geometry fell outside the range for which R_e values were obtained by Bouwer and Rice (1976), estimates were obtained using only the Hvorselv method.

3.5.2 Results and discussion

Hydraulic conductivity estimates from both Bouwer and Rice and Hvorslev methods fall in the range 10^{-9} m·s^{-1} to 10^{-7} m·s^{-1}, with estimates spanning this range obtained by multiple tests at a single borehole depth (396 m) and no clear systematic change with depth (Fig. 3.11). As the borehole was filled with drilling mud of different density and viscosity to water, the appropriate fluid properties for permeability calculations remain uncertain. Fluid flowing into the lower section of the borehole may have been water, whereas fluid flowing out of the top of the borehole is likely to have been mud or a mud filtrate with some mud solids lost. If fluid properties based on water are adopted, these hydraulic conductivities correspond to permeabilities of

10^{-14} m^2 to 10^{-16} m^2 for water at surface conditions (0.01-10 °C, 1 atm) or 10^{-15} m^2 to 10^{-17} m^2 for water at the bottom of the hole (100 °C, 1-10 MPa). If estimated mud properties for each test are used to calculate permeability, the range is 10^{-13} m^2 to 10^{-15} m^2.

DFDP-2B was uncased along much of its length during slug tests. Thus fluid exchange between the borehole and the surrounding formation was not restricted to a small depth interval but is likely to have occurred across the full open length of the borehole. This makes recovery of any hydraulic conductivity or permeability-depth relationship extremely challenging. No such relationships should be interpreted based on the simple slug test analyses presented here.

The significant vertical component of flow in rocks surrounding DFDP-2B, indicated by the steep increases in head along the borehole, means that slug tests deviate from the assumption of radial flow made by Bouwer and Rice and Hvorslev methods. This may result in errors in hydraulic conductivity estimates based on these methods. Furthermore, vertical flow may also contribute to scatter in data. Because flow rates between the formation and the borehole vary across the uncased interval, the influence of permeability of rocks at different depths on changes in fluid level will be not be the same. For example, a highly permeable fractured zone will have minimal influence on fluid level change if it is near the transition between fluid inflow into the borehole and outflow from it. In contrast, if it is near the top or bottom of the open interval, a highly permeable zone will have significant potential to influence mud level changes. The distribution of flow rates along the borehole is inferred to have varied both between and within tests, as a function of changing borehole head (Fig. 3.13). Flow rates are also inferred to have changed between tests with increasing borehole depth. Thus the influence of permeability at a particular depth on slug test curves will have varied between tests, potentially resulting in variability of permeability estimates based on these curves. Consideration of this effect further highlights the unsuitability of DFDP-2B slug test data for obtaining any permeability-depth relationship.

DFDP-2B slug test data also deviate from idealised slug test assumptions in that hydraulic conditions are unlikely to have been in a steady state prior to the initiation of tests. Many of the DFDP-2B slug tests were carried out shortly after drilling and mud circulation or previous slug tests. Following initiation of ST25, mud level continued to fall for over 2 days, highlighting the potential persistence of hydraulic perturbations over timescales much greater than the breaks between the end of circulation and the initiation of slug tests, and between sequential slug tests. These existing temporal perturbations are likely to cause errors in hydraulic conductivity estimates. Furthermore as the hydraulic history of the borehole prior to each test is different, the degree of existing perturbation is expected to have varied between tests. This, therefore may contribute to scatter within estimated hydraulic conductivities.

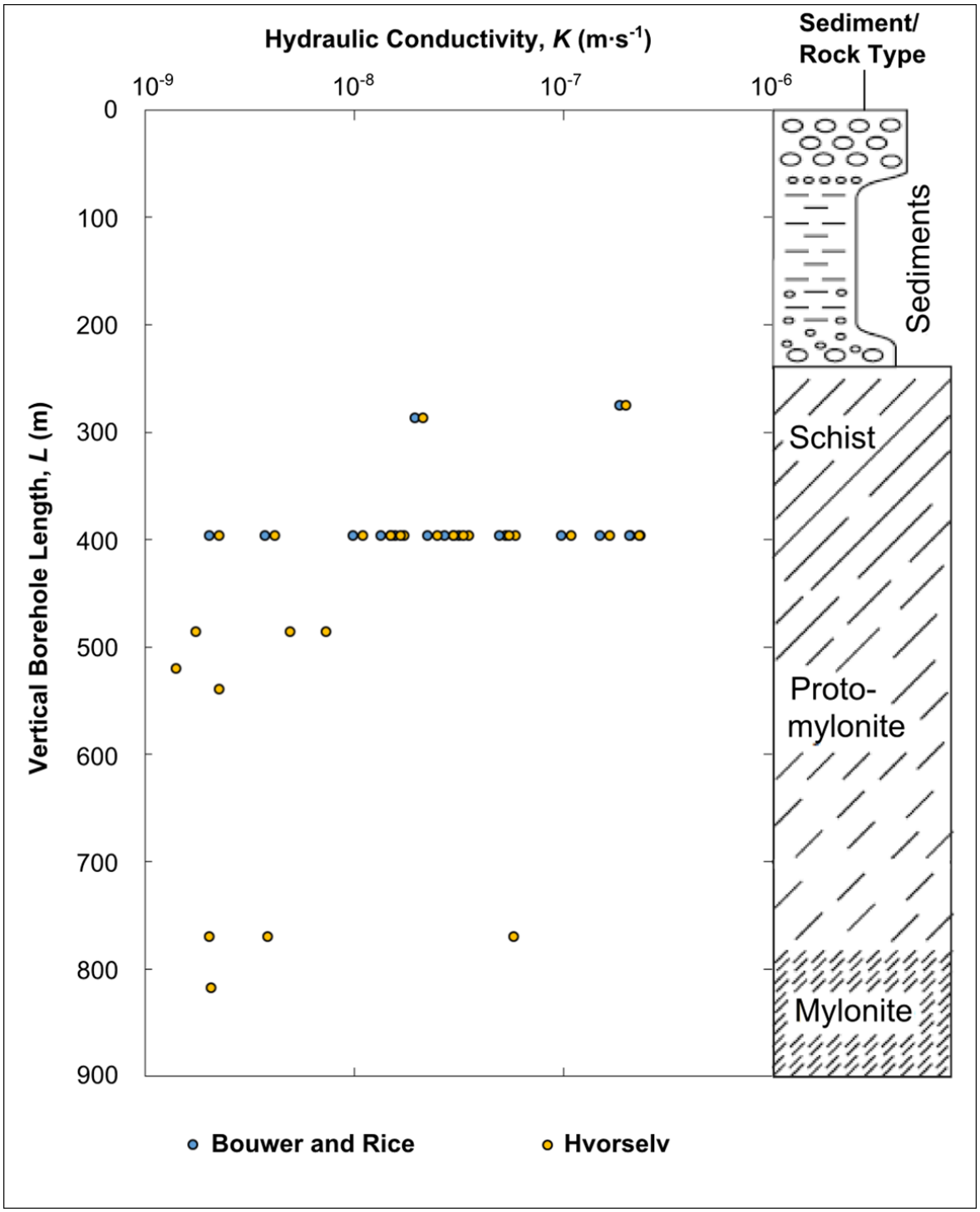

Figure 3.12 Hydraulic conductivity estimates based on application of Bouwer and Rice and Hvorslev models to DFDP-2B slug tests. r_w = 4.25"; r_c = 5"; d = $(D - 263)$m, based on the total depth of the borehole and the depth at which the borehole casing ended, with R_e based on values from Bouwer and Rice (1976). For tests at borehole depths of ≥486 m only Hvorslev model estimates are presented, as borehole geometry lies outside the range considered by Bouwer and Rice (1976) for these tests. Rock type column from Sutherland et al. (2017).

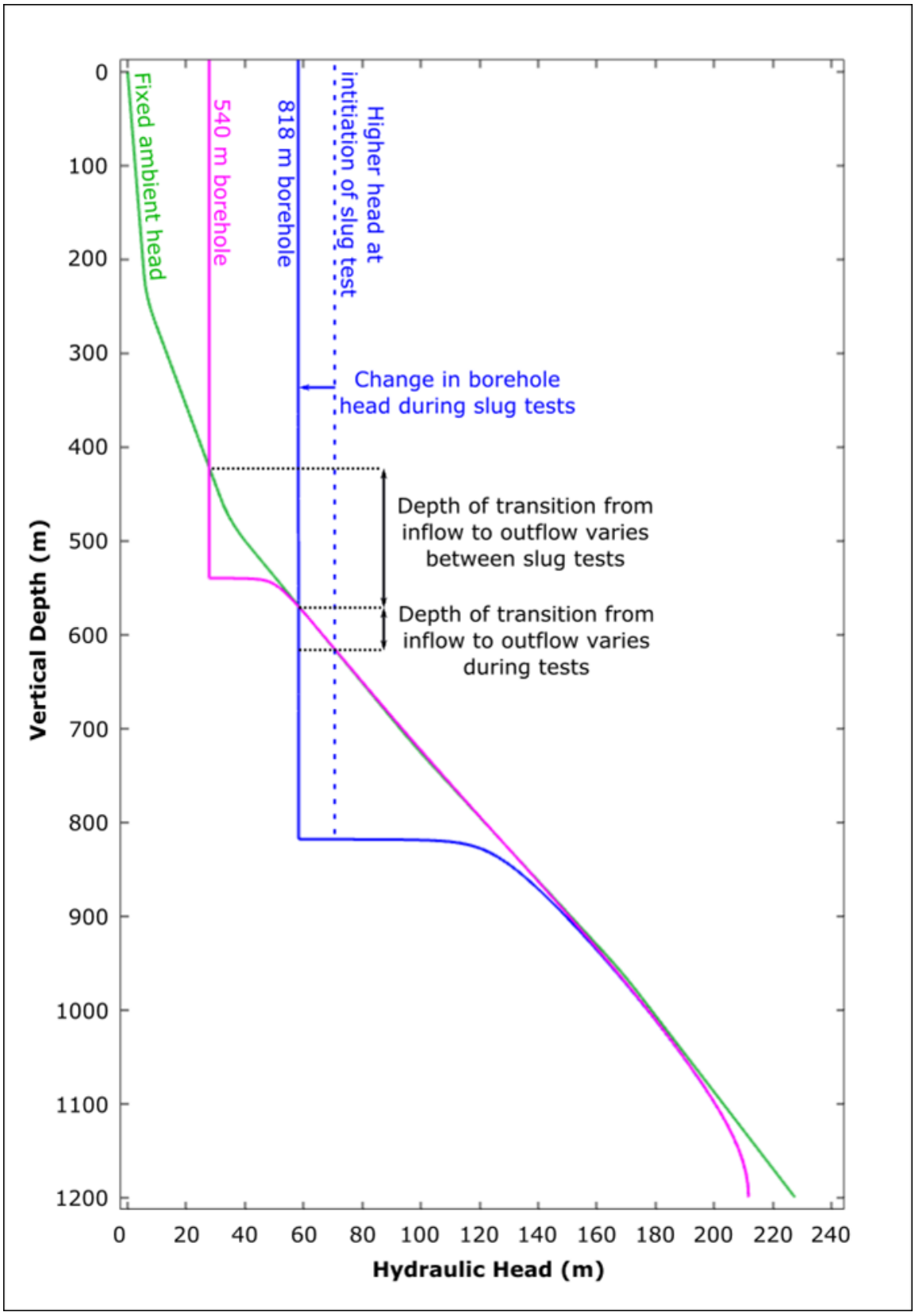

Figure 3.13 Illustration of the changing depth at which borehole head becomes lower than ambient head both between and within slug tests, using Model B steady state borehole and ambient heads, with the change in head during a falling head slug test illustrated.

Clogging of fractures and pores by drilling mud solids and thermal expansion of drilling mud may also have influenced hydraulic conductivity estimates and contributed to scatter in data. Both these processes and the degree of existing hydraulic perturbation may be expected to vary as a function of the duration of prior periods of circulation and the time elapsed since the circulation. However, simple plots of hydraulic conductivity estimates against timescales for the duration of fluid circulation prior to the slug test and against the time elapsed since the end of the last period of circulation do not show obvious correlations (Fig. 13.3), suggesting that any straightforward calculation on the basis of these timescales is unlikely to be possible.

True variations in hydraulic conductivity between tests may have resulted from differing properties of the fluid flowing, as it is a function of fluid viscosity and density. These properties are expected to differ between tests as a result of mud composition in the borehole (Table 3.2) as well as the properties of the fluid in the surrounding rock, which may have consisted of both groundwater and infiltrated drilling fluid. The density and viscosity of the water based mud, like those of water are assumed to be temperature dependent (Lemmon et al., 2017). Therefore variation between and within tests is also inferred to have occurred as a result of changing temperature conditions within the borehole. Changes in viscosity have particular potential to be significant for many of the tests, as mud viscosities vary by approximately an order of magnitude (2 mPa·s to 20 mPa·s) and are also very different from that of water (approx. 0.3 mPa·s to 2 mPa·s). However, plots of estimated fluid density and viscosity during slug tests (Fig. 13.3) against hydraulic conductivity estimates do not show obvious correlations, suggesting that changes in mud viscosity are not the single predominant cause of variation.

In addition to the factors outlined above, results may be influenced by density driven flow, not considered by idealised slug test models, the deviation of the borehole, and damage during drilling. Thus, there are multiple variables that may have caused scatter and error in these basic hydraulic conductivity estimates. However, despite these qualifications, the range of estimated hydraulic conductivity values is consistent with independent estimates obtained by using steady state temperature profiles and head gradient, which indicate hydraulic conductivity of $\geq 10^{-8}$ m·s^{-1} within the sediments and 10^{-9} m·s^{-1} within the basement (Chapter 4). They are also consistent with estimates for bulk regional hydraulic conductivity of $\leq 5 \times 10^{-7}$ m·s^{-1} (Chapter 2). Further analysis beyond that presented here may require multiple corrections as there is no clear evidence for a single process being the cause of scatter. Each correction would in itself carry significant uncertainties. Therefore it appears unlikely that additional analysis would provide further significant insights into hydraulic conductivity and permeability at DFDP-2B. Consequently, a more sophisticated analysis of hydraulic conductivity using DFDP-2B slug test curves is not pursued.

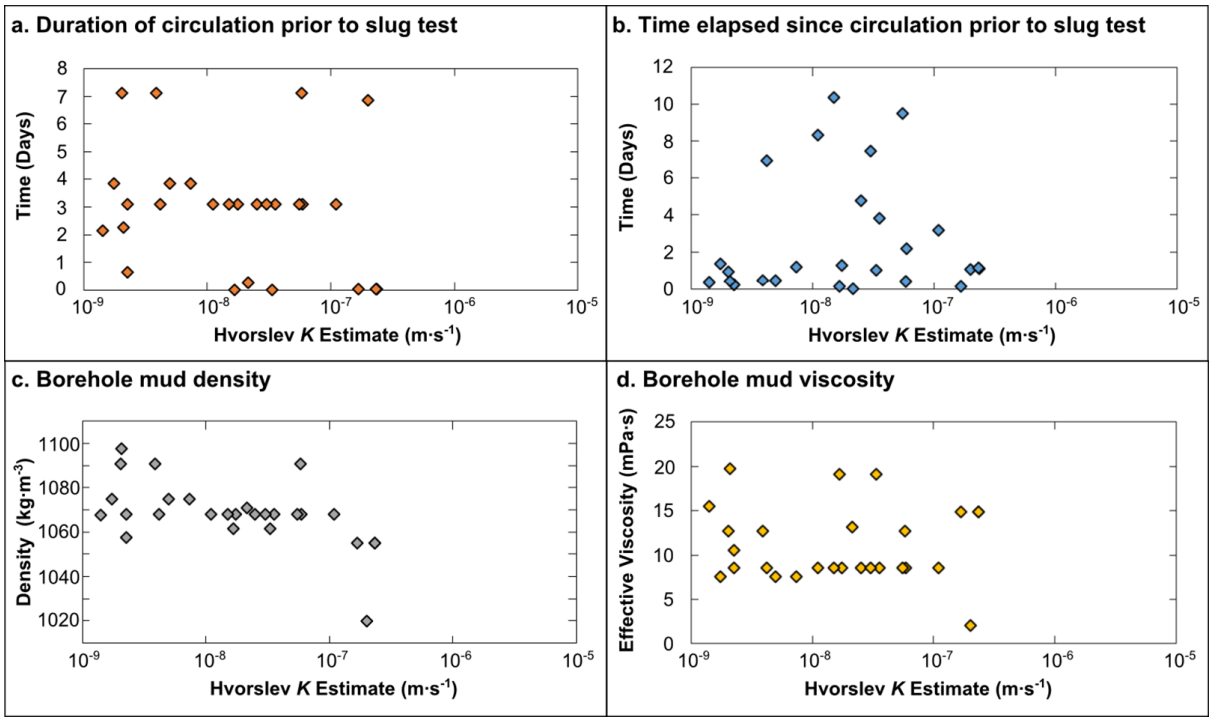

Figure 3.14 Estimated hydraulic conductivity for each slug test using the Hvorslev method plotted against a. the duration of mud circulation prior to the slug test, b. the time elapsed between the end of circulation and the start of the slug test, c. the estimated mud density in the borehole during the slug test, d. the estimated mud viscosity in the borehole during the slug test.

3.6 Future investigation

Given the potential importance of fluids in fault zone processes and the rare opportunity that fault zone drilling provides to investigate fluid pressures and permeability structure at depth, strategies to obtain data that can provide the most information about hydraulic conditions at depth should form a key part of the planning of any fault zone drilling.

The steep vertical head gradients beneath the Whataroa valley indicated by models in this study highlight the need for consideration of the effects of vertical fluid flow in any future hydraulic investigation at the DFDP-2B site. As similar steep head gradients are likely to exist in other valleys within the Southern Alps as a result of the regional topographic flow regime, or indeed in other mountainous fault zones, the hydraulic testing strategy suggested here is also applicable to drilling at other sites within the orogen or similar settings elsewhere in the world.

Even if mud density is perfectly balanced to maintain a steady state borehole fluid level, boreholes with uncased sections through regions of vertical fluid flow will experience a dynamic equilibrium with inflow at depth and outflow nearer the surface. As a result, the fluid flow regime

surrounding the borehole will be perturbed from its original state, even when temporal perturbations associated with injection of drilling mud have decayed away. This makes estimation of ambient heads from borehole mud levels significantly more challenging. In order to allow the most accurate estimation of ambient heads, it is important that the borehole should be cased to leave only a minimal open interval prior to collection of data to be used to estimate hydraulic head.

Regular insertion of casing would also minimise temporal perturbations associated with injection of overbalanced mud into the surrounding rocks during mud circulation. This has the advantage of reducing existing temporal perturbations prior to initiation of any hydraulic tests, which could influence permeability estimates obtained from these tests. Although control of mud density cannot be used to avoid perturbation of steady state conditions around the borehole, this too will act to minimise temporal perturbations. Maintenance of a minimal mud overbalance is therefore particularly important where constraints of finance, logistics or other scientific goals prevent regular casing. Estimated heads from the study can be used as a guide in calculation of appropriate mud density.

The transition from falling to rising heads in a number of DFDP-2B slug tests indicates that delaying of hydraulic tests to estimate permeability until after temporal perturbations have decayed away is unlikely to prove a successful strategy. This is because models suggest that these rises are unlikely to result from thermal expansion alone, with a probable cause being the loss of mud solids through settling and to clogging in the surrounding formation, resulting in reduced mud density. If this is the case, rather than reaching a steady state, mud level rises will continue until borehole overflow, which may prove difficult to arrest (Azar and Samuel, 2007).

In order to derive a meaningful permeability-depth relationship, sections of the borehole must be isolated for testing. This too can be achieved by regular casing, leaving a small uncased section open at the base of the hole. The permeability of this section can be estimated using slug or other hydraulic tests, minimising the influence of permeability away from the tested section.

If the borehole is uncased across a large interval during the period for hydraulic testing, permeability should be assessed using packer tests, which will allow individual sections of the borehole to be isolated and tested. This would also allow a permeability-depth relationship to be obtained and has the advantage that particular zones of interest can be investigated. Packer testing following wireline logging would allow a period for perturbations resulting from drilling to relax and zones of interest, for example zones of particularly high fracture density, to be identified and hydraulically tested. The viscosity and density of fluids injected during the packer test could

be measured prior to injection to avoid the uncertainties in conversion of hydraulic conductivity estimates to permeabilities.

Given the likelihood of significant vertical flow and superimposed effects of multiple hydraulic perturbation, which produce conditions that deviate from the assumptions of radial flow and initial steady state conditions made by common models for borehole slug and pumping tests used for determining permeability (e.g. Bouwer and Rice, 1976; Hvorslev, 1951; Theis, 1935; Thiem, 1906), alternative methods for permeability estimation that do not require fluid injection should also be considered. Vertical fluid flow rates can be calculated based on modelling of a steady state temperature profile (Bredehoeft and Papadopulos, 1965). If head data is obtained from the borehole, the vertical head gradient and fluid flow rates can be used to estimate hydraulic conductivity using Darcy's Law (Chapter 4). This alternative method of permeability estimation can be used to complement permeability estimates obtained from standard slug test modelling.

3.7 Conclusions

A simple exponential model provides a good fit ($R^2 \geq 0.93$) to slug test curves from the DFDP-2B borehole. Steady state mud level estimates obtained from these models allow estimation of borehole heads, which increase to >60 m above ground level at the base of the borehole. Due to the long open interval of DFDP-2B, borehole heads do not represent ambient heads at a specific depth, but are rather the product of a dynamic equilibrium, with inflow into the lower section of the borehole and outflow from the upper section. Finite element models of the borehole show that ambient heads may reach >120 m at the base of the DFDP-2B borehole. Although the exact ambient head values are not well constrained, modelled heads indicate that fluid pressures in the drilled section (<1000 m) Alpine Fault Zone are significantly above hydrostatic.

Simple models of thermal expansion of borehole mud suggest that transitions from rising to falling head during the latter parts of some slug tests cannot be explained by thermal expansion alone and are therefore inferred to result from reductions in borehole mud density as a result of loss of mud solids through settling or transport into the surrounding formation. Such rises are expected to continue until borehole overflow occurs, unless remedial action such as injection of fresh mud is taken.

Hydraulic conductivity and permeability estimations for the surrounding host rock formations, based on the DFDP-2B slug test data are hampered by the presence of steep vertical head gradients and the long open interval of the borehole. As flow occurs over a long interval of the borehole and variation of flow rates with depth may vary between tests, the data is unsuitable for the determination of a permeability-depth relationship. Estimates of bulk permeability based on

idealised Bouwer and Rice (1976) and Hvorslev (1951) slug test models indicate hydraulic conductivity in the range 10^{-9} m·s^{-1} to 10^{-7} m·s^{-1}, corresponding to a permeability of 10^{-13} m^2 to 10^{-17} m^2. Although the potential influence of existing hydraulic perturbations, significant vertical flow, thermal expansion, clogging of flow pathways, rock damage during drilling and variations in fluid properties, reduce the precision and accuracy of these estimates, they are consistent with other independent permeability estimates from DFDP-2B and for the Southern Alps (Chapter 2, Chapter 4).

The impact of significant ambient vertical flow on hydraulic testing, which is particularly important when large sections of a borehole are uncased, should be considered in the planning of future drilling and hydraulic investigation at the DFDP-2B site or in other Southern Alps locations. To facilitate accurate estimation of heads, casing of the borehole, followed by mud level monitoring should occur at regular intervals as drilling progresses. Packer tests or slug tests carried out over a range of borehole depths, with only a short interval of the borehole uncased during each test may allow information regarding variations in permeability with depth to be obtained. Minimisation of temporal hydraulic perturbations from flow of drilling mud into the surrounding formation may allow for more precise hydraulic conductivity and permeability estimates. Temporal hydraulic perturbations resulting from flow of drilling mud into the surrounding formation, which have the potential to influence subsequent slug tests results, may be minimised by using head estimates from this study to maintain a small pressure overbalance in the borehole. Installation of equipment to allow measurement of the temperature profile along the borehole is also important, as this can also be used to estimate hydraulic conductivity if heads have also been estimated (Chapter 4).

3.8 References

Ando, M., 2001. Geological and geophysical studies of the Nojima Fault from drilling: An outline of the Nojima Fault zone probe. Isl. Arc 10, 206–214. doi:10.1111/j.1440-1738.2001.00349.x

Azar, J.J., Samuel, G.R., 2007. Drilling Engineering. PennWell Corp., Tulsa, OK.

Barnes, I., Downes, C.J., Hulston, J.R., 1978. Warm springs, South Island, New Zealand, and their potentials to yield laumontite. Am. J. Sci. doi:10.2475/ajs.278.10.1412

Berryman, K., Cooper, A., Norris, R., Villamor, P., Sutherland, R., Wright, T., Schermer, E., Langridge, R., Biasi, G., 2012. Late Holocene rupture history of the alpine fault in South Westland, New Zealand. Bull. Seismol. Soc. Am. 102, 620–638. doi:10.1785/0120110177

Blanpied, M.L., Lockner, D.A., Byerlee, J.D., 1992. An earthquake mechanism based on the rapid sealing of faults. Nature 356, 133–135.

Bouwer, H., 1989. The Bouwer and Rice Slug Test - An Update. Ground Water 27, 304–309.

Bouwer, H., Rice, R.C., 1976. A slug test for determining hydraulic conductivity of unconfined aquifers with completely or partially penetrating wells. Water Resour. Res. 12, 423. doi:10.1029/WR012i003p00423

Bredehoeft, J.D., Papadopulos, I.S., 1965. Rates of Vertical Groundwater Movement Estimated from the Earth's Thermal Profile. Water Resour. Res. 1.

Byerlee, J., 1993. Model for episodic flow of high-pressure water in fault zones before earthquakes. Geology 21, 303–306.

Carslaw, H.S., Jaeger, J.C., 1959. Conduction of Heat in Solids, 2nd ed. Oxford University Press, Oxford.

Cochran, U.A., Clark, K.J., Howarth, J.D., Biasi, G.P., Langridge, R.M., Villamor, P., Berryman, K.R., Vandergoes, M.J., 2017. A plate boundary earthquake record from a wetland adjacent to the Alpine fault in New Zealand refines hazard estimates. Earth Planet. Sci. Lett. 464, 175–188. doi:10.1016/j.epsl.2017.02.026

Cox, S.C., Barrell, D.J.A., 2007. Geology of the Aoraki area. Institute of Geological and Nuclear Sciences 1:250,000 geological map 15.

Eppelbaum, L., Kutasov, I., Pilchin, A., 2014. Applied Geothermics, Applied Geothermics. doi:10.1007/978-3-642-34023-9

Howarth, J.D., Fitzsimons, S.J., Norris, R.J., Langridge, R., Vandergoes, M.J., 2016. A 2000 yr rupture history for the Alpine fault derived from Lake Ellery, South Island, New Zealand. Bull. Geol. Soc. Am. 128, 627–643. doi:10.1130/B31300.1

Hubbert, M.K., Rubey, W.W., 1959. Role of fluid pressure in overthrust faulting: I. Mechanics of fluid-filled porous solids and its application to overthrust faulting. Bull. Geol. Soc. Am. 70, 115–166. doi:10.1130/0016-7606(1959)70

Hvorslev, M.J., 1951. Time Lag and Soil Permeability in Ground-Water Observations. Bull. (Waterways Exp. Stn. Corps Eng. U.S. Army, Vicksburg, Mississippi) 36.

Koons, P.O., 1987. Some thermal and mechanical consequences of rapid uplift: an example from the Southern Alps, New Zealand. Earth Planet. Sci. Lett. 86, 307–319. doi:10.1016/0012-821X(87)90228-7

Leitner, B., Eberhart-Phillips, D., Anderson, H., Nabelek, J.L., 2001. A focused look at the Alpine Fault, New Zealand: Seismicity, focal mechanisms, and stress observations. J. Geophys. Res. 106, 2193–2220.

Lemmon, E.W., McLinden, M.O., Friend, D.G. Thermophysical Properties of Fluid Systems, in: Linstrom, P.J., Mallard, W.G. (Eds.), NIST Chemistry WebBook, NIST Standard Reference Database Number 69. National Institute of Standards and Technology, Gaithersburg MD. doi:10.18434/T4D303 (accessed 30.08.2017).

Menzies, C.D., Teagle, D.A.H., Niedermann, S., Cox, S.C., Craw, D., Zimmer, M., Cooper, M.J., Erzinger, J., 2016. The fluid budget of a continental plate boundary fault: Quantification from the Alpine Fault, New Zealand. Earth Planet. Sci. Lett. 445, 125–135. doi:10.1016/j.epsl.2016.03.046

Norris, R.J., Cooper, A.F., 2001. Late Quaternary slip rates and slip partitioning on the Alpine Fault, New Zealand. J. Struct. Geol. 23, 507–520. doi:10.1016/S0191-8141(00)00122-X

Norris, R.J., Cooper, A.F., 2007. The Alpine Fault, New Zealand: Surface geology and field relationships, in: Okaya, D., Stern, T., Davey, F. (Eds.), A Continental Plate Boundary: Tectonics at South Island, New Zealand. pp. 157–176. doi:10.1029/175GM09

Pitt, M.J., 2000. The Marsh Funnel and Drilling Fluid Viscosity: A New Equation for Field Use. SPE Drill. Complet. 15, 3–6.

Sibson, R.H., 1992. Fault-valve behavior and the hydrostatic-lithostatic fluid pressure interface. Earth-Science Rev. 32, 141–144. doi:10.1016/0012-8252(92)90019-P

Sibson, R.H., 1973. Interactions between Temperature and Pore-Fluid Pressure during Earthquake Faulting and a Mechanism for Partial or Total Stress Relief. Nat. Phys. Sci. 243, 66–68.

Sutherland, R., Berryman, K., Norris, R., 2006. Quaternary slip rate and geomorphology of the Alpine fault: Implications for kinematics and seismic hazard in southwest New Zealand. Bull. Geol. Soc. Am. 118, 464–474. doi:10.1130/B25627.1

Sutherland, R., Harris, R.A., Stern, T., Beavan, J., Ellis, S., Henrys, S., Cox, S., Norris, R.J., Berryman, K.R., Townend, J., Bannister, S., Pettinga, J., Leitner, B., 2007. Do Great Earthquakes Occur on the Alpine Fault in Central South Island, New Zealand?, in: Okaya, D., Stern, T., Davey, F.

(Eds.), A Continental Plate Boundary: Tectonics at South Island, New Zealand. American Geophysical Union, Washington DC, pp. 235–251.

Sutherland, R., Townend, J., Toy, V., Allen, M., Baratin, L., Barth, N., Beacroft, B.L., Boese, C., Boles, A., Boulton, C., Capova, L., Carpenter, B., Celerier, B., Chamberlain, C., Conze, R., Cooper, A., Coussens, J., Coutts, A., Cox, S., Craw, L., Doan, M., Eccles, J., Faulkner, D., Grieve, J., Grochowski, J., Gulley, a., Henry, G., Howarth, J., Jacobs, K., Jeppson, T., Kato, N., Keys, S., Kirilova, M., Kometani, Y., Kovacs, A., Langridge, R., Lin, W., Little, T., Mallyon, D., Mariani, B., Marx, R., Massiot, C., Mathewson, L., Melosh, B., Menzies, C., Moore, J., Morales, L., Morgan, C., Mori, H., Niemeijera, A., Nishikawa, O., Nitsch, O., Paris Cavailhès, J., Pooley, B., Prior, D., Pyne, A., Sauer, K., Savage, M., Schleicher, a., Schmitt, D., Shigematsu, N., Taylor-Offord, S., Tobin, H., Upton, P., Valdez, R., Weaver, K., Wiersberg, T., Williams, J., Yeo, S., Zimmer, M., 2015. Deep Fault Driling Project (DFDP), Alpine Fault Boreholes DFDP-2A and DFDP-2B Technical Completion Report. GNS Sci. Rep. 50, 269.

Sutherland, R., Townend, J., Toy, V., Upton, P., Coussens, J., Allen, M., Baratin, L.-M., Barth, N., Becroft, L., Boese, C., Boles, A., Boulton, C., Broderick, N.G.R., Janku-Capova, L., Carpenter, B.M., Célérier, B., Chamberlain, C., Cooper, A., Coutts, A., Cox, S., Craw, L., Doan, M.-L., Eccles, J., Faulkner, D., Grieve, J., Grochowski, J., Gulley, A., Hartog, A., Howarth, J., Jacobs, K., Jeppson, T., Kato, N., Keys, S., Kirilova, M., Kometani, Y., Langridge, R., Lin, W., Little, T., Lukacs, A., Mallyon, D., Mariani, E., Massiot, C., Mathewson, L., Melosh, B., Menzies, C., Moore, J., Morales, L., Morgan, C., Mori, H., Niemeijer, A., Nishikawa, O., Prior, D., Sauer, K., Savage, M., Schleicher, A., Schmitt, D.R., Shigematsu, N., Taylor-Offord, S., Teagle, D., Tobin, H., Valdez, R., Weaver, K., Wiersberg, T., Williams, J., Woodman, N., Zimmer, M., 2017. Extreme hydrothermal conditions at an active plate-bounding fault. Nature 546, 137–140. doi:10.1038/nature22355

Sutherland, R., Toy, V.G., Townend, J., Cox, S.C., Eccles, J.D., Faulkner, D.R., Prior, D.J., Norris, R.J., Mariani, E., Boulton, C., Carpenter, B.M., Menzies, C.D., Little, T.A., Hasting, M., De Pascale, G.P., Langridge, R.M., Scott, H.R., Reid Lindroos, Z., Fleming, B., Kopf, J., 2012. Drilling reveals fluid control on architecture and rupture of the Alpine fault, New Zealand. Geology 40, 1143–1146. doi:10.1130/G33614.1

Tanaka, H., Wang, C.-Y., Chen, W.-M., Sakaguchi, A., Ujiie, K., Ito, H., Ando, M., 2002. Initial Science Report of Shallow Drilling Penetration into the Chelungpu Fault Zone, Taiwan. TAO 13, 227–251.

Taylor, J.R., 1997. An Introduction to Error Analysis, 2nd editio. ed. University Science Books, Sausalito, CA.

Theis, C. V, 1935. The relation between the lowering of the Piezometric surface and the rate and duration of discharge of a well using ground-water storage. Trans. Am. Geophys. Union 519–524.

Thiem, G., 1906. Hydrologische Methoden. Gebhardt, Leipzig.

Wells, A., Yetton, M.D., Duncan, R.P., Stewart, G.H., 1999. Prehistoric dates of the most recent Alpine fault earthquakes, New Zealand. Geology 27, 995–998. doi:10.1130/0091-7613(1999)027<0995:PDOTMR>2.3.CO;2

Wibberley, C.A.J., Shimamoto, T., 2005. Earthquake slip weakening and asperities explained by thermal pressurization. Nature 436, 689–692. doi:10.1038/nature03901

Zoback, M., Hickman, S., Ellsworth, W., 2010. Scientific drilling into the San Andreas fault zone. Eos Trans. AGU 91, 197–204.

3.9 Supporting information

3.9.1 Thermal expansion modelling

Thermal expansion of drilling mud also has the potential to produce a transition to rising mud levels. Simple thermal models were used to investigate whether thermal expansion alone could explain these rises. Models were based on Carslaw's equation for radial conductive heat flow to an infinite linear heat sink was employed (Carslaw and Jaeger, 1959):

$$T_0 - T_w = \frac{Q_w}{4\pi\Lambda_e} \mathrm{W}\left(\frac{r_w^2 C_e}{4\Lambda_e t}\right) \tag{3.14}$$

Where T_0 is the initial formation temperature, T_w is the temperature at the formation-borehole boundary at time at time t; Q_w is the rate of heat extraction from the borehole; Λ_e is the effective thermal conductivity of the surrounding formation (assumed isotropic); W is the well function (Theis, 1935); r_w is the well radius and C_e is the effective volumetric heat capacity of the surrounding formation.

Thermal diffusivity, κ, is equal to Λ/C and is calculated for rocks in the drilled interval as ~1.6 × 10^{-6} m·s^{-1} based on the volume weighted geometric mean of mineral proportions (Sutherland et al., 2017). Assuming a porosity of 0.1 and a typical water thermal diffusivity of 1.5 × 10^{-7} m·s^{-1}, (Lemmon et al., 2017), this gives an effective thermal diffusivity of 1.46 × 10^{-6} m·s^{-1} (also using a volume weighted geometric mean). Adopting this value of thermal diffusivity and setting C_e as 2.5 J·m^{-3}·K^{-1}, based on the arithmetic mean (Eppelbaum et al., 2014) of values for water at 50 °C of 4.1× 10^6 J·m^{-3}·K^{-1} (Lemmon et al., 2017) and typical values for schist of 2.3 × 10^6 J·m^{-3}·K^{-1} (Eppelbaum et al., 2014) required that $\Lambda_e$is set at 3.7 W·m^{-1}·K^{-1} (which is consistent the range of reported values for schists, see Eppelbaum et al. (2014)).

An approximate rate of heat extraction was calculated based on the wireline temperature profile measured following the longest period of circulation, 613080 seconds (~7 days). The depth integrated average temperature for this profile is 10 °C cooler than the steady state temperature profile. Models indicate that the heat extraction rate required to produce a 10 °C temperature drawdown at the end of 613080 seconds of circulation is 146 W. Average temperature recovery was modelled for each slug test, assuming this heat extraction rate. On the basis of these temperature recovery curves, thermal expansion curves were calculated, assuming a coefficient of thermal expansion of 4.57 × 10^{-4} °C^{-1}, based on the value for water at 50 °C.

Application of a correction to remove the modelled effect of thermal expansion from slug test curves does not remove the transition to rising mud levels seen in some tests. Therefore, although thermal expansion will have made some contribution, rising mud levels are interpreted

as resulting predominantly from changes in borehole mud density. For all tests, modelled expansion is equivalent to <0.3 % of the total borehole mud volume at the initiation of the test and associated changes in mud level are <1 m (Table 3.5).

Table 3.5 Modelled volumetric thermal expansion for all slug tests at the time of the final mud level measurement, expressed as a percentage of the mud volume at the time of the first mud level measurement. Modelled rises in mud level associated with these volume changes are also given.

Slug Test	Expansion (% of initial mud volume)	Associated mud level change (m)
ST1	0.21	0.57
ST2	0.21	0.59
ST3	0.23	0.84
ST4	0.03	0.11
ST5	0.01	0.05
ST6	0.01	0.03
ST7	0.01	0.04
ST8	<0.01	<0.01
ST9	<0.01	0.01
ST10	<0.01	0.01
ST11	<0.01	0.01
ST12	<0.01	0.01
ST13	<0.01	<0.01
ST16	0.02	0.07
ST17	<0.01	<0.01
ST18	<0.01	<0.01
ST19	0.01	0.04
ST20	<0.01	<0.01
ST21	0.07	0.29
ST22	0.02	0.07
ST23	0.08	0.34
ST24	0.07	0.32
ST25	0.18	0.84
ST26	0.02	0.10
ST27	0.10	0.63
ST28	0.11	0.69
ST29	0.13	0.87

3.10 Supporting information references

Carslaw, H.S., Jaeger, J.C., 1959. Conduction of Heat in Solids, 2nd ed. Oxford University Press, Oxford.

Eppelbaum, L., Kutasov, I., Pilchin, A., 2014. Applied Geothermics, Applied Geothermics. doi:10.1007/978-3-642-34023-9

Lemmon, E.W., McLinden, M.O., Friend, D.G. Thermophysical Properties of Fluid Systems, in: Linstrom, P.J., Mallard, W.G. (Eds.), NIST Chemistry WebBook, NIST Standard Reference Database Number 69. National Institute of Standards and Technology, Gaithersburg MD. doi:10.18434/T4D303 (accessed 30.08.2017).

Sutherland, R., Townend, J., Toy, V., Upton, P., Coussens, J., Allen, M., Baratin, L.-M., Barth, N., Becroft, L., Boese, C., Boles, A., Boulton, C., Broderick, N.G.R., Janku-Capova, L., Carpenter, B.M., Célérier, B., Chamberlain, C., Cooper, A., Coutts, A., Cox, S., Craw, L., Doan, M.-L., Eccles, J., Faulkner, D., Grieve, J., Grochowski, J., Gulley, A., Hartog, A., Howarth, J., Jacobs, K., Jeppson, T., Kato, N., Keys, S., Kirilova, M., Kometani, Y., Langridge, R., Lin, W., Little, T., Lukacs, A., Mallyon, D., Mariani, E., Massiot, C., Mathewson, L., Melosh, B., Menzies, C., Moore, J., Morales, L., Morgan, C., Mori, H., Niemeijer, A., Nishikawa, O., Prior, D., Sauer, K., Savage, M., Schleicher, A., Schmitt, D.R., Shigematsu, N., Taylor-Offord, S., Teagle, D., Tobin, H., Valdez, R., Weaver, K., Wiersberg, T., Williams, J., Woodman, N., Zimmer, M., 2017. Extreme hydrothermal conditions at an active plate-bounding fault. Nature 546, 137–140. doi:10.1038/nature22355

Theis, C. V, 1935. The relation between the lowering of the Piezometric surface and the rate and duration of discharge of a well using ground-water storage. Trans. Am. Geophys. Union 519–524.

Thiem, G., 1906. Hydrologische Methoden. Gebhardt, Leipzig.

Chapter 4:

The significance of heat transport by shallow fluid flow at an active plate boundary; the Southern Alps, New Zealand

Abstract

Fluid flow can influence the nature and timing of failure on faults. This study quantifies the role of groundwater heat advection in establishing the thermal structure of the Alpine Fault, a major tectonic boundary in southern New Zealand that accommodates most of the motion between the Australian and Pacific Plates. Convergence on the Alpine Fault has rapidly uplifted the Southern Alps, resulting in high geothermal gradients and a thin seismogenic zone. A new equilibrium temperature profile from the 818 m-deep Deep Fault Drilling Project 2B (DFDP-2B) borehole has been interrogated using one-dimensional analytical models of fluid and rock advection. Models indicate a heat flux approximating to 720 $mW \cdot m^{-2}$ results from groundwater flow with Darcy velocities of ~10^{-9} $m \cdot s^{-1}$, which advects significantly more heat than rock advection in the shallow orogen (<6 km depth) and must act as a major control on the subsurface temperature field.

4.1 Introduction

Fluid flow can influence the nature and timing of failure on faults by changing temperatures and pore-fluid pressures, and by modifying the mechanical properties of fault materials through chemical alteration and mineralization (Hubbert and Rubey, 1959; Kohlstedt et al., 1995; Sibson, 1973, 1990). Here the role of fluids in advecting heat and controlling thermal structure of an active fault zone is quantified. The Alpine Fault is a major plate-bounding fault accommodating ~75 % of the ~10 $mm \cdot yr^{-1}$ convergent and ~36 $mm \cdot yr^{-1}$ dextral strike slip motion between the Australian and Pacific plates in South Island, New Zealand (Fig. 4.1a), (DeMets et al., 1994; Norris and Cooper, 2001, 2007). Although the relative plate motions are high there have been no large (M_w > 7) earthquakes on the central Alpine Fault since European settlement ca. 1800 A.D., and there is no evidence for aseismic creep at the surface (Sutherland et al., 2007). However, palaeoseismic records indicate that the Alpine Fault has ruptured in multiple large (M_w > 7) to great (M_w ≥ 8) earthquakes every 291 ± 23 years with the most recent event in 1717 A.D. (Berryman et al., 2012; Cochran et al., 2017; Cox and Sutherland, 2007; Howarth et al., 2016; Wells et al., 1999). Consequently, the Alpine Fault appears to be late in its seismic cycle. Convergence on the Alpine Fault has resulted in rapid uplift of the >3500 m Southern Alps and

earlier models, backed up by micro-seismicity observations, have predicted high shallow geothermal gradients, the uplift of the brittle-ductile transition and consequent thinning of the seismogenic crust (Allis et al., 1979; Koons, 1987; Leitner et al., 2001; Townend et al., 2012). Here a new equilibrium temperature profile (Sutherland et al., 2017) from the 818 m-deep International Continental Scientific Drilling Program (ICDP) Deep Fault Drilling Project 2B (DFDP-2B) borehole is interrogated, to quantify the relative roles of heat conduction, heat transfer by rock advection and heat transfer by fluid flow in establishing the local, near-surface geothermal profile of an orogen-bounding, major continental strike-slip fault. Rock advection is defined here as movement of rock, along with entrained pore water relative to a fixed reference frame and fluid flow defined as movement of water relative to rock.

The ~45 degree-dipping Alpine Fault has uplifted and juxtaposed amphibolite facies quartzofeldspathic rocks of the Alpine Schist against Cretaceous granitoids and Palaeozoic metasediments in its footwall (Cox and Barrell, 2007). Heavy orographic precipitation (~10 $m \cdot yr^{-1}$) on the western side of the Southern Alps results in high rates of physical erosion and has produced a quasi-steady state topographic regime in which the range of the highest topography, the Main Divide, runs parallel to but 15-20 km offset from the Alpine Fault, connected by a series of valleys and 1000 to 1500 m high ridges running normal to the fault (Fig. 4.1b) (Koons, 1990, 1989).

A >50 m thick zone of intense hydrothermal alteration in the hanging wall of the Alpine Fault Zone (Cooper and Norris, 1994; Sutherland et al., 2012; Warr and Cox, 2001) and numerous warm (<60 °C) geothermal springs in the Southern Alps (Fig. 4.1b) (Barnes et al., 1978; Menzies et al., 2014) issuing meteoric water attest to significant fluid flow penetrating to depth that may influence orogenic processes. The topographic geometry of the Southern Alps drives two significant components of groundwater flow in the mountain belt (Fig. 4.1c). One component is groundwater flow from ridges into the valleys that they bound. This convergence of flow from ridges on either side produces a relatively large upward vertical component to flow beneath valleys. The other component of flow is parallel to the ridges and valleys, down the topographic gradient from the Main Divide at ~3500 m to the near sea-level Alpine Fault trace and the footwall plain. Perched hydrological heads in the DFDP-1 boreholes (Sutherland et al., 2012), isotopic measurements (Menzies et al., 2016), and very low permeabilities measured for the principal slip zone materials (Boulton et al., 2012; Carpenter et al., 2014) indicate that the Alpine Fault is a barrier throughout the brittle crust to lateral flow from the Southern Alps to the footwall plain. As a result, the down-valley component is driven upward upon reaching the fault at the mouths of the valleys, further contributing to the vertical component of flow due to cross-valley

convergence. Thermal buoyancy-driven flow may also play a role in this system, but will be explored in future contributions.

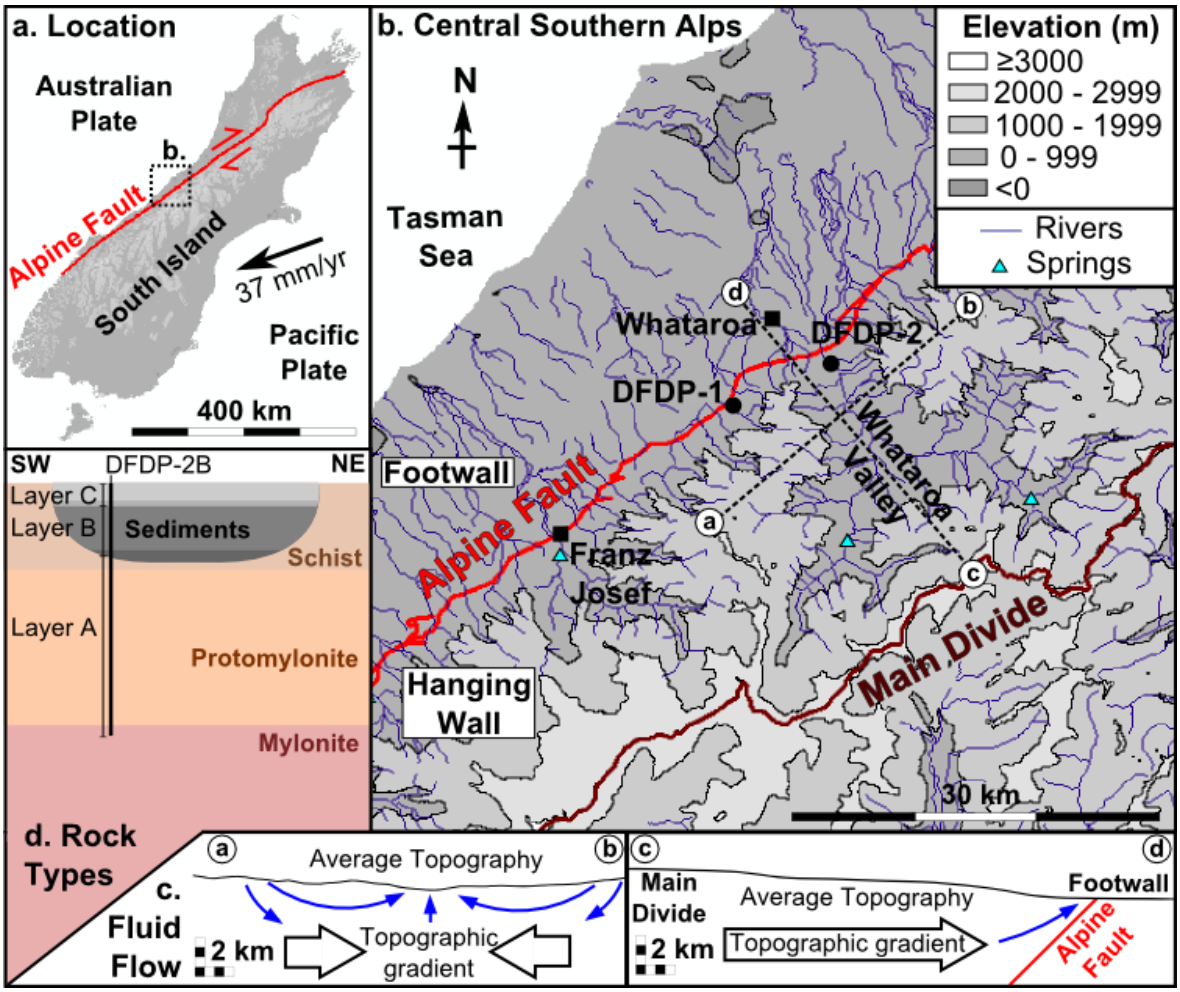

Figure 4.1 a. The Alpine Fault accommodates relative plate motion between the Pacific and Australian plates in South Island, New Zealand (DeMets et al., 1994; Norris and Cooper, 2001, 2007). b. The Whataroa valley is one of a series of valleys that run perpendicular to the Alpine Fault in the central Southern Alps, bounded by the highest topography at the Main Divide. Many contain warm springs (Barnes et al., 1978). The DFDP-2 boreholes are located at the mouth of the Whataroa valley, with boreholes drilled as part of the first phase of the project, DFDP-1, in nearby Gaunt Creek. c. Topographic flow from ridges bounding valleys and from the highest topography at the Main Divide, driven up along the impermeable Alpine Fault contribute to up-flow at valley mouths. d. Illustration of the rock sequence penetrated by the DFDP-2B borehole and the sections into which the drilled interval is split for modelling in this study. Projection of unit boundaries away from the drill site is intended only to illustrate the geological setting. For further detail of unit lithologies, geometries and relationships, please see Toy et al. (2017).

The DFDP-2B borehole is located near the mouth of the Whataroa valley (Fig. 4.1c). The rock sequence penetrated by the borehole from bottom to top, the direction of regional fluid flow, consists of Alpine Schist derived protomylonites and mylonites (Layer A), overlain by riverine and lacustrine sediments (Layer B) and alluvial gravels (Layer C, Fig. 4.1d, 4.2). The borehole has a curvature toward the fault, with most deflection occurring below ~400 m depth and therefore represents a pseudo-vertical profile. A steady state temperature profile of the DFDP-2B borehole, with measurements at 1 m intervals, was obtained using an optical fiber down the length of the borehole, following repeated measurements during relaxation of the drilling induced perturbation (Sutherland et al., 2017). The profile has an average geothermal gradient of 125 ± 55 °C·km^{-1} (Sutherland et al., 2017), with three distinct discontinuities in gradient separating the profile into four sections (Fig. 4.2). The shallower two of these three discontinuities correlate with changes from Alpine Schist rocks to valley-filling sediments and from riverine and lacustrine sediments to alluvial gravels. The third lower discontinuity corresponds to a spike in measured radon gas during drilling but no discernible change in rock type. As the borehole was closed to flow by cemented casing along its entire length and was cement filled below 400 m during collection of this temperature data, it is assumed that observations, following re-equilibration of perturbations from drilling, are representative of undisturbed steady state conditions. In the absence of creep strain on the Alpine Fault (Sutherland et al., 2007), observation points are considered as fixed in space. The conditions proximal to the borehole are of significant vertical fluid flow as result of both components of the regional groundwater flow regime, convergence into the valley and with the fault. This was confirmed by rapid increases in borehole hydraulic head with depth, rising to >60 m head at 818 m (Chapter 3, this thesis; Sutherland et al., 2017).

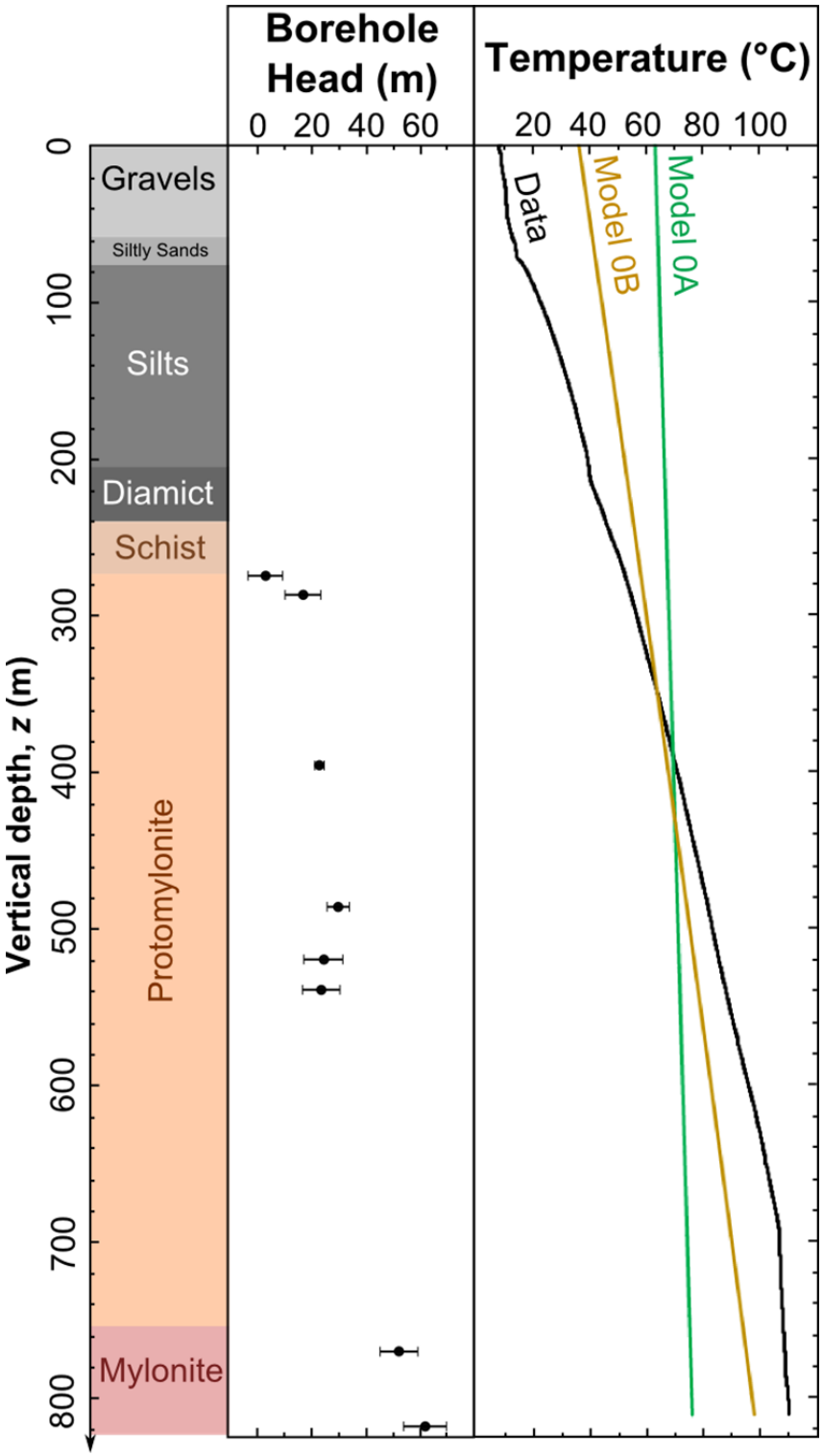

Figure 4.2 DFDP-2B stratigraphy, borehole head and temperature data (Chapter 3, this thesis; Sutherland et al., 2017) with basic model temperature profiles for comparison. Model 0A is a single section model based on typical continental conductive heat flow. Model 0B is a single section model based on heat flow associated with one-dimensional rock advection.

4.2 One-dimensional thermal modelling and analysis

This study builds on the work of earlier thermal models (Allis et al., 1979; Allis and Shi, 1995; Batt and Braun, 1999; Koons, 1987), which considered only the effect of conduction and rock advection, by obtaining estimates for fluid and heat fluxes at depth and quantifying the importance of fluid flow as a means of heat transfer in the shallow Alpine Fault Zone. To obtain insights into the fundamental hydrothermal processes influencing the Alpine Fault, the DFDP-2B temperature profile is fitted using the simplest suitable models. On the basis of a priori knowledge of the system, which indicates regional converging fluid flow beneath DFDP-2B, it is assumed that large-scale fluid and heat flow is on average vertical for the measured profile, with discrete kink points within the data representing locations where lateral flow pathways are significant in modifying the fluid and heat flow up the profile. Implicit in the assumption that heat flow approximates to vertical is that temperature variations associated with borehole curvature are negligible.

On the basis of this conceptual model, one-dimensional models for fluid and associated heat flow are presented, to enable simple assessment of geological scenarios. The approach employed is similar to that used by Bredehoeft and Papadopulos (1965) for estimating fluid flow rates, and that used by Allis et al. (1979)) for modelling the thermal consequences of rapid rock uplift, but incorporates both processes. A two phase rock-fluid system is assumed. The rock phase, with void space equivalent to porosity, φ, is uplifted at a spatially constant vertical rock advection velocity, v_u, relative to a fixed coordinate axis. The fluid phase saturates the void space and is uplifted with the rock, but also flows relative to the rock with vertical Darcy velocity, q. These velocities combine to give an effective vertical advection velocity, v_e. The combined fluid-rock medium has effective volumetric heat capacity, C_e and effective thermal diffusivity, κ_e. Models in this study are based on the equation for steady state heat flux, Q, in one dimension, z, representing depth below the surface:

$$Q = C_e v_e T - C_e \kappa_e \frac{dT}{dz} \tag{4.1}$$

A vertical profile comprising 1 to 4 sections is assumed, with constant v_e and Q within each section. Sections represent intervals over which q and Q are constant, intersected at their boundaries by flow paths that transfer fluid laterally into or out of the model profile. Material properties, including κ_e, are fixed at constant values (Fig. 4.3, see 4.7 Supporting information for further discussion). v_u is assumed constant at 8 mm·yr^{-1} (Little et al., 2005). A best fit solution (minimum root mean square error, RMSE) is calculated with q and Q as fitted parameters for each section. Model errors are 95 % confidence intervals from model regression, and also include the

uncertainties in the fixed parameters κ_e, C_f, C_s, φ and v_u. Heat fluxes are quoted relative to model surface temperature, $T(z = 0)$.

As a starting point for comparison, two baseline models for a single homogeneous layer that simulate conditions of no fluid advection of heat are considered. Model 0A simulates conduction only by setting $v_e \approx 0$, with Q set to a typical continental background value of 70 mW·m^{-2} (Davies and Davies, 2010; Stein, 1995); and Model 0B that simulates rock advection and conductive heat exchange only (q = 0 and Q = 358 mW·m^{-2} based on uplift of rock and water at 500 °C above surface temperature from 15 km depth (Allis et al. 1979). Both models poorly represent the measured data (R^2 = 0.22 and 0.80 respectively) indicating that both fluid flow and rock advection are important and must be included. In comparison, Model 1 of this study, which comprises a single homogeneous section with constant q and Q along the entire profile, gives a good fit to data (R^2 > 0.99), although it diverges at three distinct discontinuities in gradient (Fig. 4.2).

To investigate these divergences the model domain is split into four sections in Models 2 and 3. Section boundaries are positioned at the three major discontinuities in temperature gradient, two of which correspond to changes in rock type. As such model sections (A1, A2, B, C) correspond to Layers A (deformed Alpine Schist), B (riverine and lacustrine sediments) and C (alluvial gravels), with Layer A further split into A1 and A2 sections at 691 m depth, based on the change in geothermal gradient at this depth. Vertical Darcy velocity (q) is allowed to vary between sections in Model 2, with Q in each section dependent on q. Hence, changes in q represent fluid sources or sinks at the same temperature as the profile at the section boundary depth. Model 2 gives a strong fit (R^2 > 0.99) but is also able to reproduce the discontinuities in gradient that Model 1 cannot. In Model 3, steady state vertical heat flux (Q) is allowed to vary between sections, independent of q. This model can therefore represent fluid in and outflow associated with sources and sinks not necessarily at the temperature of the section boundary depth. Model 3, also with R^2 > 0.99, produces a tighter fit to discontinuities than Model 2, but at the expense of increased model complexity with three additional parameters to be fitted.

At the boundary between A1 and A2, Model 2 predicts fluid outflow (Fig. 4.2). Model 3 predicts inflow from a hotter source at this boundary, although confidence intervals for this complex model are large and encompass both inflow and outflow at all boundaries. Both models predict inflow at the boundary between A2 and B, with Model 3 indicating a source cooler than the profile at this depth. At the boundary between B and C both models predict outflow, with Model 3 indicating sink cooler than the profile at this depth.

4.3 Results

First, generalised large-scale insights into heat transport near the Alpine Fault from all models are considered. The poor match of models neglecting fluid flow (Models 0A and 0B) to the thermal profile of the DFDP-2B borehole highlights the importance of fluid heat transport (Fig 2). Although Models 0A and 0B could provide a better fit if Q was set to a much higher value, there is no obvious physical basis for this in the context of only considering conduction and rock advection.

Upward Darcy velocities for Models 1 to 3 range from 5.3×10^{-10} m·s^{-1} to 2.8×10^{-8} m·s^{-1} (Fig. 4.3). Total model heat flux across the observed interval is approximately 720 mW·m^{-2} (Model 1), significantly higher than background continental values of ~70 mW·m^{-2} (Davies and Davies, 2010; Stein, 1995). The value is higher than values for other boreholes in South Island published by Shi et al. (1996), with the closest heat flux a value of 320 mW·m^{-2} measured in the Waiho valley, near Franz Josef. In addition to exceeding the heat flux that can be produced by simplified one-dimensional rock advection (Model 0B), this Model 1 heat flux value is also significantly greater than values predicted by more sophisticated rock advection models, which are <300 mW·m^{-2} (Shi et al., 1996; Upton et al., 2011). The heat flux associated with fluid flow is more than three times larger than that associated with rock advection, for all model best-fit values (Fig. 4.2). Péclet number for the modelled interval, based on heat advection by fluid flow alone is:

$$P_f = \frac{lC_f q}{C_e \kappa_e} \tag{4.2}$$

Where l is the model section length. Model 1 has $P_f \approx 1$, indicating that heat transport by fluid flow is of comparable significance to conduction over the length of the borehole.

The visibly good fit of Model 1 indicates that the assumption of constant q across the drilled interval is suitable for thermal modelling at this scale. Models 2 and 3 improve this fit, by allowing for variations in Darcy velocity, which show no trend with depth and are thus likely to be due to localised features.

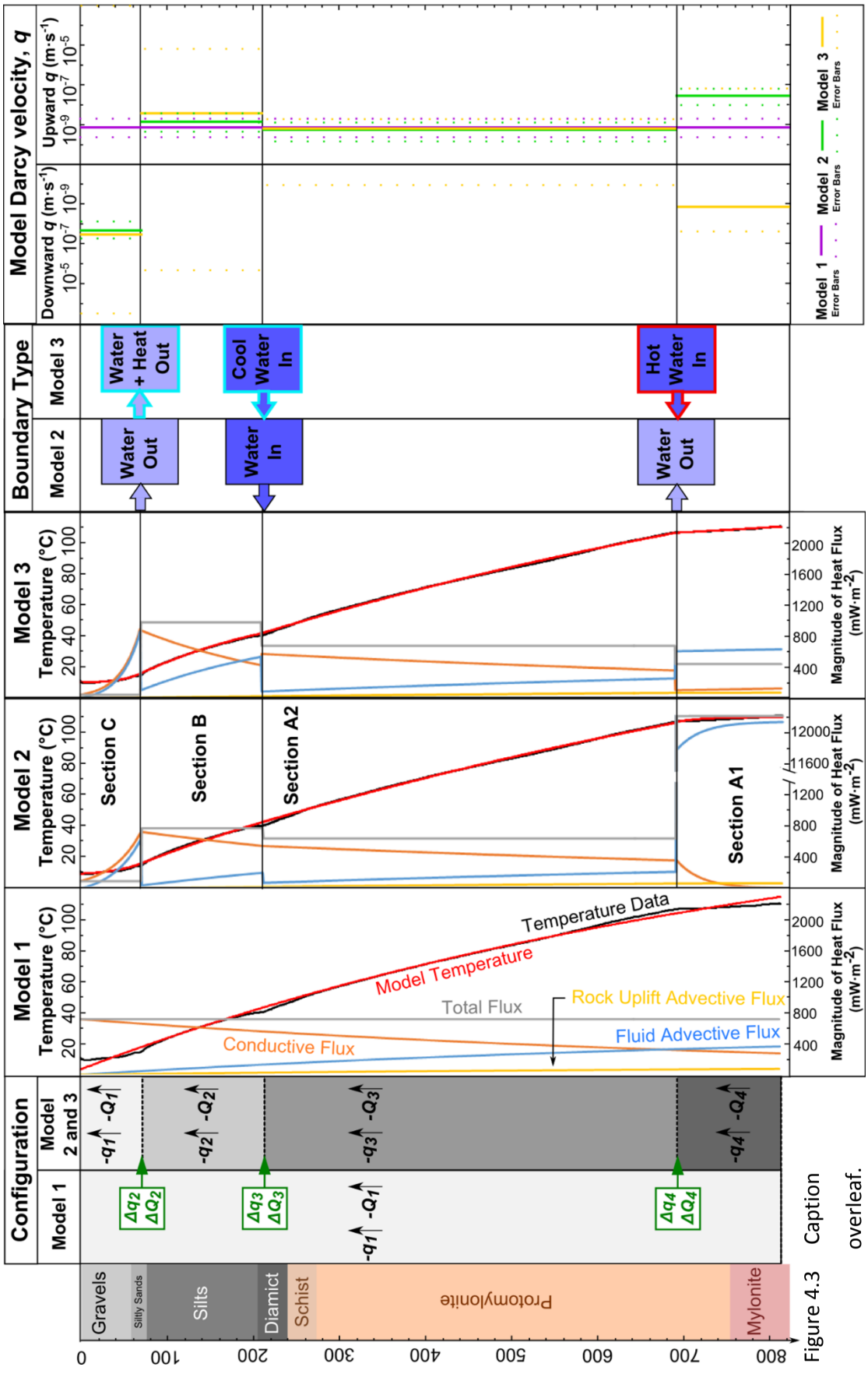

Figure 4.3 Caption overleaf.

Figure 4.3 (Overleaf) Model configurations and results. Models produced as part of this study have a sectionalised configuration- Model 1 has one section, Model 2 and 3 have four sections. As z coordinates represent vertical depth, upward heat and water flow is represented by negative Q and q respectively. For Model 2 heat flux changes as a function of fluid flow such that $\Delta Q_n = C_e(v_{e,n} - v_{e,n-1})T(z_{0,n})$. For Model 3 Darcy velocity and heat flux vary independently from one another, such that $\Delta Q_n = C_e G_n$ where G_n is a fitted constant.

Models 2 and 3 offer insights into how fluid and heat flow is modified by local geological structures. Section A1 corresponds to the deeper part of the metamorphic basement, where thermal gradient is shallowest (~31 °C·km^{-1} between ends of the section). Geothermal gradient increases to ~139 °C·km^{-1} in section A2. The best-fit Model 2 infers a fluid sink between the model sections A1 and A2 to explain the change in gradient. Model 3 indicates that a similar modelled temperature profile can be produced by a heat source at this same depth. A highly fractured zone, intersecting the observed profile at this depth, could laterally remove up-flowing fluids from the observed profile. It could also act as a heat source, transporting hotter fluids to the model profile. Intersection with a barrier to flow, such as the slip plane of a minor fault could also divert up-flowing fluids laterally. Given the sharpness of the gradient discontinuity at this boundary and the orientation of the borehole at this depth, which is approximately normal to mylonitic foliation, any fracture or fault zone is likely to be perpendicular to the borehole and therefore near parallel to foliation and the Alpine Fault.

The geothermal gradient in section B, ~184 °C·km^{-1}, is slightly higher than in section A2. Best fit values from Models 2 and 3 give slightly higher upward q of 1.5 × 10^{-9} m·s^{-1} to 4.0 × 10^{-9} m·s^{-1} in section B compared 5.3 × 10^{-10} m·s^{-1} to 6.2 × 10^{-10} m·s^{-1} in section A2. Applying Darcy's Law to hydraulic gradient data (Fig. 4.2) and Darcy velocities from Models 2 and 3 gives hydraulic conductivity under in situ conditions, $K \geq 10^{-8}$ m·s^{-1} for section B and $K = 10^{-9}$ m·s^{-1} for section A2. A profile elsewhere in valley, where up-flow rates in the basement are higher could act as a source. In this interpretation, fluids reaching the more permeable sediments flow laterally, down a hydraulic gradient to the observed profile. Lateral inflow of fluid on shallow flow paths into the sediments at the flanks of the valley could also act as a source. Model 3 results infer fluids from a source cooler than the model profile, consistent with the latter, hypothesised valley flank source providing the major or only contribution to increased up-flow. However, due to the large confidence interval associated with Model 3, great significance is not attributed to this result in interpreting the source of in-flowing fluids.

Section C has a geothermal gradient of ~73 °C·km^{-1}, significantly lower than section B below. Model 2 and 3 infer downward fluid and associated heat flow in section C to fit this. The alluvial gravels and sands of section C are likely to be have a high K, 10^{-7} m·s^{-1} to 10^{-2} m·s^{-1} (Domenico and Schwartz, 1990) and downward fluid fluxes can be understood as resulting from locally recharged shallow water moving toward the center of the valley. These down-flowing fluids converge with up-flowing fluids from below at this depth meaning that both must travel laterally before reaching the surface.

4.4 Discussion

One-dimensional models of the DFDP-2B equilibrium temperature profile estimate a total heat flux of >700 mW·m^{-2}. This is greatly in excess of that which can be generated by invoking rock advection alone and requires vertical fluid flow with Darcy velocities up to the order of 10^{-8} m·s^{-1}. Previous models for heat flow have discounted the role of groundwater flow in heat transport, on the basis of the small heat contributions associated with the few known warm springs that are only localised features within a regional groundwater circulation (Allis and Shi, 1995). However, most basement fluid upwelling is obscured by thick recent sediment fills of the valley, and inflections in the temperature profile indicate fluid flow and heat advection around the basement-sediment boundary. Model Darcy velocities from this study represent a site away from known warm springs and are greater in magnitude than time-integrated uplift (vertical rock advection) rates ≤2.8 × 10^{-10} ms^{-1} (≤9 mm·yr^{-1}) (Little et al., 2005) across the entire observed interval. This, combined with the higher volumetric heat capacity of water relative to the combined water-rock mass means that for the study interval, fluid flow transports more than three times the heat transported by rock advection. A Péclet number of ~1 for advection by fluid flow indicates it is also of comparable significance to conduction across the observed interval. This indicates that heat advection by fluid flow, rather than being negligible, is likely to act as a major control on temperature distribution in the shallow crust, where high Darcy velocities persist and is key to understanding the elevated heat flux at DFDP-2B.

The Alpine Fault extends to ~35 km (Stern et al., 2007) and rock is being advected from deep in the ductile crust. Reduction in fluid fluxes with depth (Menzies et al., 2016; Sims et al., 2015) means that although heat advected by fluid flow is much greater than that advected by rock advection at DFDP-2B, at some point much shallower than 35 km, heat transfer by fluid flow is likely to become negligible. Thus rock advection supplies heat to the base of a shallow groundwater circulation system, where fluid flow rates are high enough to advect a greater amount of heat than rock advection (Fig. 4.4). In this regional groundwater circulation system, heat is transported from ridges to valleys. Water up-flow increases upward heat flux beneath

valleys, in excess of that supplied by rock advection and water down-flow decreases it beneath ridges. Thus the high heat flux at DFDP-2B indicated by models is dependent on both fluid flow and rock advection.

The depth at which fluid flow ceases to be significant in heat transport will vary spatially. Although there is no evidence of a systematic decrease in Darcy velocity across the observed in Models 2 and 3, extrapolation of high Darcy velocities at DFDP-2B is limited at the deepest to the Alpine Fault, which is ≤1.5 km deep this site. Further south-east, beneath the upstream sections of valleys, where the Alpine Fault is deeper, there is the potential that high upward Darcy velocities could persist deeper than at DFDP-2B. Based on the heat capacities of water and rock, fluid flow will remain the dominant mode of vertical heat transfer where vertical Darcy velocity is $>2 \times 10^{-10}$ m·s^{-1}. Estimated meteoric fluid fluxes at the brittle-ductile transition at ~6 km are of the order 10^{-11} ms^{-1} to 10^{-10} m·s^{-1} (Menzies et al., 2016), indicating that significant heat transport by fluid flow is likely to be restricted to <6 km depth.

4.5 Conclusions

This study has shown that for a single section model (Model 1), an upwards Darcy velocity, $q = 7.8 \times 10^{-10}$ m·s^{-1} provides a good approximation to the measured temperatures at DFDP-2B. Discontinuities in measured temperature gradient can be understood in terms of variable fluid up-flow, resulting from flow into and out of the observed interval at major fracture zones and at the interfaces between sedimentary units. Modelled Darcy velocities, away from known warm springs, have magnitudes $\geq 5.3 \times 10^{-10}$ m·s^{-1}, which are sufficiently high that heat advection by groundwater is of comparable significance to conduction and more than three times greater than heat advection by rock advection across the DFDP-2B interval. The total heat flux at DFDP-2B approximates to ~720 mW·m^{-2}. This is significantly greater than typical continental conductive heat fluxes of ~70 mW·m^{-2} (Davies and Davies, 2010; Stein, 1995) and is also greater than that predicted by models incorporating only conduction and rock advection (<400 mW·m^{-2}). The high heat flux is interpreted as resulting for the regional groundwater flow system that is strongly influenced by the ridge-valley topography developed perpendicular to the Alpine Fault. This enhances the high upward heat flux from rapid rock advection beneath valleys, and reduces heat flux beneath ridges. Thus, it is inferred that groundwater flow is a major control on the temperature field in the shallow (<6 km depth) Southern Alps. Groundwater-driven heat flow will also influence the temperature-dependent mechanical properties of near-surface fault rocks (Kohlstedt et al., 1995), such as in the Alpine Fault of this study.

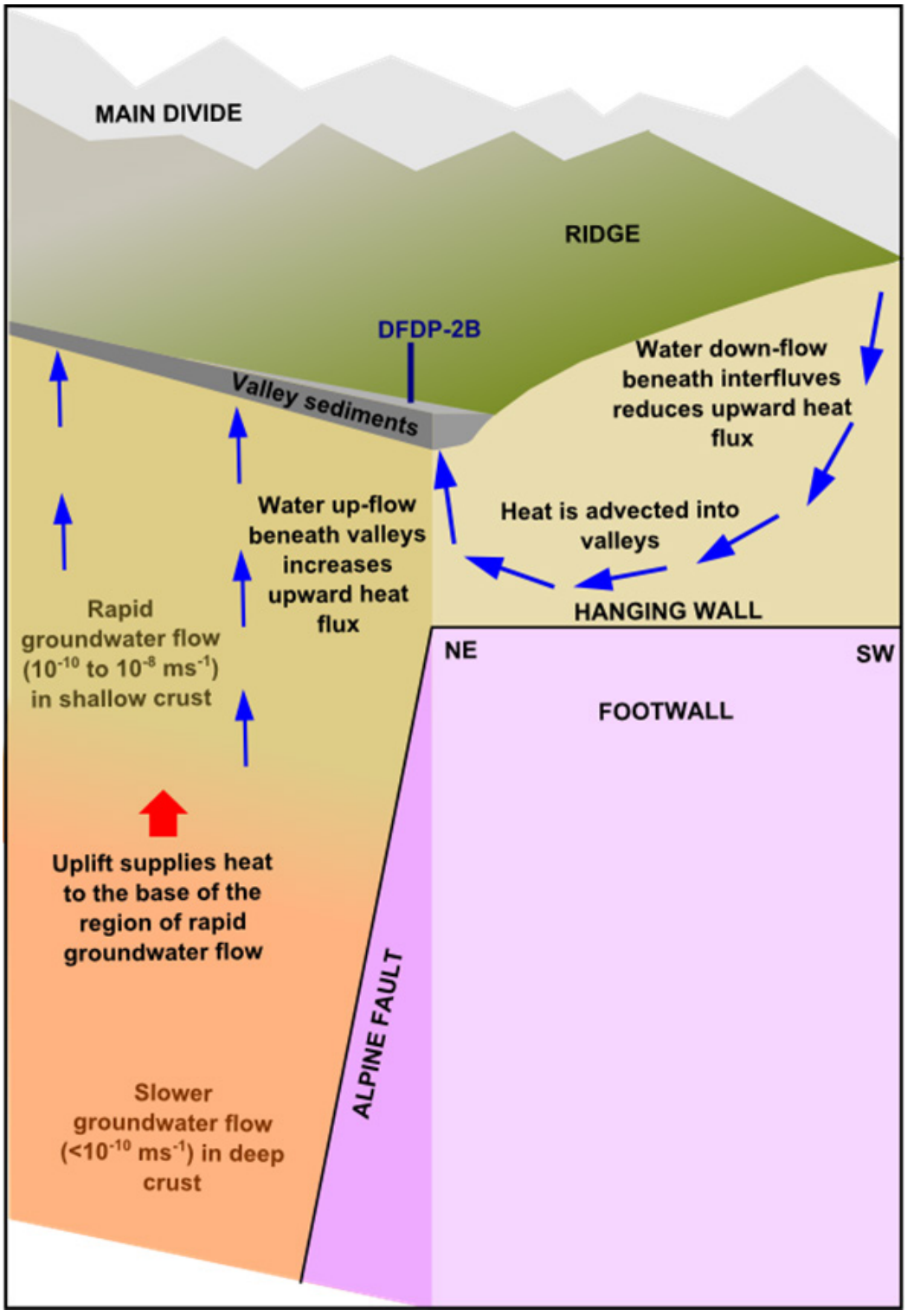

Figure 4.4 Illustration of the role of groundwater flow in heat transport in the Southern Alps. Rock advection results in high heat fluxes to a shallow region, where groundwater flow rates are sufficiently high to advect significant amounts of heat. Water flow from ridges to valleys increases upward heat flux beneath valleys in this shallow region, decreasing it beneath ridges.

4.6 References

Allis, R.G., Henley, R.W., Carman, A.F., 1979. The Thermal Regime Beneath the Southern Alps. Bull. R. Soc. New Zeal. 18, 79–85.

Allis, R.G., Shi, Y., 1995. New insights to temperature and pressure beneath the central Southern Alps, New Zealand. New Zeal. J. Geol. Geophys. 38, 585–592. doi:10.1080/00288306.1995.9514687

Barnes, I., Downes, C.J., Hulston, J.R., 1978. Warm springs, South Island, New Zealand, and their potentials to yield laumontite. Am. J. Sci. doi:10.2475/ajs.278.10.1412

Batt, G.E., Braun, J., 1999. The tectonic evolution of the Southern Alps, New Zealand: insights from fully thermally coupled dynamical modelling. Geophys. J. Int. 136, 403–420.

Berryman, K.R., Cochran, U.A., Clark, K.J., Biasi, G.P., Langridge, R.M., Villamor, P., 2012. Major Earthquakes Occur Regularly on an Isolated Plate Boundary Fault. Science. 336, 1690–1693. doi:10.1126/science.1218959

Boulton, C., Carpenter, B.M., Toy, V., Marone, C., 2012. Physical properties of surface outcrop cataclastic fault rocks, Alpine Fault, New Zealand. Geochemistry, Geophys. Geosystems 13, 1–13. doi:10.1029/2011GC003872

Bredehoeft, J.D., Papadopulos, I.S., 1965. Rates of Vertical Groundwater Movement Estimated from the Earth's Thermal Profile. Water Resour. Res. 1.

Carpenter, B.M., Kitajima, H., Sutherland, R., Townend, J., Toy, V.G., Saffer, D.M., 2014. Hydraulic and acoustic properties of the active Alpine Fault, New Zealand: Laboratory measurements on DFDP-1 drill core. Earth Planet. Sci. Lett. 390, 45–51. doi:10.1016/j.epsl.2013.12.023

Cochran, U.A., Clark, K.J., Howarth, J.D., Biasi, G.P., Langridge, R.M., Villamor, P., Berryman, K.R., Vandergoes, M.J., 2017. A plate boundary earthquake record from a wetland adjacent to the Alpine fault in New Zealand refines hazard estimates. Earth Planet. Sci. Lett. 464, 175–188. doi:10.1016/j.epsl.2017.02.026

Cooper, A.F., Norris, R.J., 1994. Antatomy, structural evolution, and slip rate of a plate boundary thrust: The Alpine Fault at Gaunt Creek, Westland, New Zealand. Geol. Soc. Am. Bull. 106, 627–633. doi:10.1130/0016-7606(1994)106<0627:ASEASR>2.3.CO;2

Cox, S.C., Barrell, D.J.A., 2007. Geology of the Aoraki area. Institute of Geological and Nuclear Sciences 1:250,000 geological map 15.

Cox, S.C., Sutherland, R., 2007. Regional Geological Framework of South Island, New Zealand, and its Significance for Understanding the Active Plate Boundary, in: Okaya, D., Stern, T., Davey, F. (Eds.), A Continental Plate Boundary: Tectonics at South Island, New Zealand. American Geophysical Union, Washington DC, pp. 19–46. doi:10.1029/175GM03

Davies, J.H., Davies, D.R., 2010. Earth's surface heat flux. Solid Earth 1, 5–24.

DeMets, C., Gordon, R.G., Argus, D.F., Stein, S., 1994. Effects of recent revision to the geomagnetic reversal timescale on estimates of current plate motion. Geophys. Res. Lett. 21, 2191–2194.

Domenico, P.A., Schwartz, F.W., 1990. Physical and Chemical Hydrogeology. John Wiley and Sons, New York.

Howarth, J.D., Fitzsimons, S.J., Norris, R.J., Langridge, R., Vandergoes, M.J., 2016. A 2000 yr rupture history for the Alpine fault derived from Lake Ellery, South Island, New Zealand. Bull. Geol. Soc. Am. 128, 627–643. doi:10.1130/B31300.1

Hubbert, M.K., Rubey, W.W., 1959. Role of fluid pressure in overthrust faulting: I. Mechanics of fluid-filled porous solids and its application to overthrust faulting. Bull. Geol. Soc. Am. 70, 115–166. doi:10.1130/0016-7606(1959)70

Kohlstedt, D.L., Evans, B., Mackwell, S.J., 1995. Strength of the lithosphere: Constraints imposed by laboratory experiments. J. Geophys. Res. doi:10.1029/95JB01460

Koons, P.O., 1990. Two-sided orogen: Collision and erosion from the sandbox to the Southern Alps, New Zealand. Geology 18, 679–682. doi:10.1130/0091-7613(1990)018<0679

Koons, P.O., 1989. The topographic evolution of collisional mountain belts: a numerical look at the Southern Alps, New Zealand. Am. J. Sci. doi:10.2475/ajs.289.9.1041

Koons, P.O., 1987. Some thermal and mechanical consequences of rapid uplift: an example from the Southern Alps, New Zealand. Earth Planet. Sci. Lett. 86, 307–319. doi:10.1016/0012-821X(87)90228-7

Leitner, B., Eberhart-Phillips, D., Anderson, H., Nabelek, J.L., 2001. A focused look at the Alpine Fault, New Zealand: Seismicity, focal mechanisms, and stress observations. J. Geophys. Res. 106, 2193–2220.

Little, T.A., Cox, S., Vry, J.K., Batt, G., 2005. Variations in exhumation level and uplift rate along the oblique-slip Alpine fault, central Southern Alps, New Zealand. Bull. Geol. Soc. Am. 117, 707–723. doi:10.1130/B25500.1

Menzies, C.D., Teagle, D.A.H., Craw, D., Cox, S.C., Boyce, A.J., Barrie, C.D., Roberts, S., 2014. Incursion of meteoric waters into the ductile regime in an active orogen. Earth Planet. Sci. Lett. 399, 1–13. doi:10.1016/j.epsl.2014.04.046

Menzies, C.D., Teagle, D.A.H., Niedermann, S., Cox, S.C., Craw, D., Zimmer, M., Cooper, M.J., Erzinger, J., 2016. The fluid budget of a continental plate boundary fault: Quantification from the Alpine Fault, New Zealand. Earth Planet. Sci. Lett. 445, 125–135. doi:10.1016/j.epsl.2016.03.046

Norris, R.J., Cooper, A.F., 2007. The Alpine Fault, New Zealand: Surface geology and field relationships, in: Okaya, D., Stern, T., Davey, F. (Eds.), A Continental Plate Boundary: Tectonics at South Island, New Zealand. pp. 157–176. doi:10.1029/175GM09

Norris, R.J., Cooper, A.F., 2001. Late Quaternary slip rates and slip partitioning on the Alpine Fault, New Zealand. J. Struct. Geol. 23, 507–520. doi:10.1016/S0191-8141(00)00122-X

Shi, Y., Allis, R., Davey, F., 1996. Thermal modeling of the Southern Alps, New Zealand. Pure Appl. Geophys. 146, 469–501. doi:10.1007/BF00874730

Sibson, R.H., 1990. Conditions for fault-valve behaviour. Geol. Soc. London, Spec. Publ. 15–28.

Sibson, R.H., 1973. Interactions between Temperature and Pore-Fluid Pressure during Earthquake Faulting and a Mechanism for Partial or Total Stress Relief. Nat. Phys. Sci. 243, 66–68.

Sims, A., Cox, S.C., Fitzsimons, S., Holland, P., 2015. Seasonal infiltration and groundwater movement in schist bedrock, Southern Alps, New Zealand. J. Hydrol. 54, 33–52.

Stein, C.A., 1995. Heat Flow of the Earth, in: Global Earth Physics – A Handbook of Physical Constants, AGU Reference Shelf 1. American Geophysical Union, Washington DC, pp. 144–158. doi:10.1112/S0024609301008396

Stern, T., Okaya, D., Kleffmann, S., Scherwath, M., Henrys, S., Davey, F., 2007. Geophysical Exploration and Dynamics of the Alpine Fault Zone 207–234.

Sutherland, R., Harris, R.A., Stern, T., Beavan, J., Ellis, S., Henrys, S., Cox, S., Norris, R.J., Berryman, K.R., Townend, J., Bannister, S., Pettinga, J., Leitner, B., 2007. Do Great Earthquakes Occur on the Alpine Fault in Central South Island, New Zealand?, in: Okaya, D., Stern, T., Davey, F. (Eds.), A Continental Plate Boundary: Tectonics at South Island, New Zealand. American Geophysical Union, Washington DC, pp. 235–251.

Sutherland, R., Townend, J., Toy, V., Upton, P., Coussens, J., Allen, M., Baratin, L.-M., Barth, N., Becroft, L., Boese, C., Boles, A., Boulton, C., Broderick, N.G.R., Janku-Capova, L., Carpenter, B.M., Célérier, B., Chamberlain, C., Cooper, A., Coutts, A., Cox, S., Craw, L., Doan, M.-L., Eccles, J., Faulkner, D., Grieve, J., Grochowski, J., Gulley, A., Hartog, A., Howarth, J., Jacobs, K., Jeppson, T., Kato, N., Keys, S., Kirilova, M., Kometani, Y., Langridge, R., Lin, W., Little, T., Lukacs, A., Mallyon, D., Mariani, E., Massiot, C., Mathewson, L., Melosh, B., Menzies, C., Moore, J., Morales, L., Morgan, C., Mori, H., Niemeijer, A., Nishikawa, O., Prior, D., Sauer, K., Savage, M., Schleicher, A., Schmitt, D.R., Shigematsu, N., Taylor-Offord, S., Teagle, D., Tobin, H., Valdez, R., Weaver, K., Wiersberg, T., Williams, J., Woodman, N., Zimmer, M., 2017. Extreme hydrothermal conditions at an active plate-bounding fault. Nature 546, 137–140. doi:10.1038/nature22355

Sutherland, R., Toy, V.G., Townend, J., Cox, S.C., Eccles, J.D., Faulkner, D.R., Prior, D.J., Norris, R.J., Mariani, E., Boulton, C., Carpenter, B.M., Menzies, C.D., Little, T.A., Hasting, M., De Pascale, G.P., Langridge, R.M., Scott, H.R., Reid Lindroos, Z., Fleming, B., Kopf, J., 2012. Drilling reveals fluid control on architecture and rupture of the Alpine fault, New Zealand. Geology 40, 1143–1146. doi:10.1130/G33614.1

Townend, J., Sherburn, S., Arnold, R., Boese, C., Woods, L., 2012. Three-dimensional variations in present-day tectonic stress along the Australia-Pacific plate boundary in New Zealand. Earth Planet. Sci. Lett. 353-354, 47–59. doi:10.1016/j.epsl.2012.08.003

Toy, V.G., Sutherland, R., Townend, J., Allen, M.J., Becroft, L., Boles, A., Boulton, C., Carpenter, B., Cooper, A., Cox, S.C., Daube, C., Faulkner, D.R., Halfpenny, A., Kato, N., Keys, S., Kirilova, M., Kometani, Y., Little, T., Mariani, E., Melosh, B., Menzies, C.D., Morales, L., Morgan, C., Mori, H., Niemeijer, A., Norris, R., Prior, D., Sauer, K., Schleicher, A.M., Shigematsu, N., Teagle, D.A.H., Tobin, H., Valdez, R., Williams, J., Yeo, S., Baratin, L.-M., Barth, N., Benson, A., Boese, C., Célérier, B., Chamberlain, C.J., Conze, R., Coussens, J., Craw, L., M.-L. Doan, Eccles, J., Grieve, J., Grochowski, J., Gulley, A., Howarth, J., Jacobs, K., Janku-Capova, L., Jeppson, T., Langridge, R., Mallyon, D., Marx, R., Massiot, C., Mathewson, L., Moore, J., Nishikawa, O., Pooley, B., Pyne, A., Savage M.K., Schmitt, D., Taylor-Offord, S., Upton, P., Weaver, K. C., Wiersberg, T., Zimmer, M., DFDP-2 Science Team, 2017. Bedrock Geology of DFDP-2B, Central Alpine Fault, New Zealand. New Zeal. J. Geol. Geophys. 60, 497-518. doi:10.1080/00288306.2017.1375533

Upton, P., Craw, D., Yu, B., Chen, Y-G., 2011. Controls on fluid flow in transpressive orogens, Taiwan and New Zealand. Geol. Soc. London, Spec. Publ. 359, 249–265. doi:10.1144/SP359.14

Warr, L.N., Cox, S., 2001. Clay mineral transformations and weakening mechanisms along the Alpine Fault, New Zealand. Geol. Soc. London, Spec. Publ. 186, 85–101. doi:10.1144/GSL.SP.2001.186.01.06

Wells, A., Yetton, M.D., Duncan, R.P., Stewart, G.H., 1999. Prehistoric dates of the most recent Alpine fault earthquakes, New Zealand. Geology 27, 995–998. doi:10.1130/0091-7613(1999)027<0995:PDOTMR>2.3.CO;2

4.7 Supporting information

This supporting information outlines the method used for one-dimensional modelling of DFDP-2B temperature profiles in the above article. It is assumed that the measured interval can be treated as consisting of a solid rock phase with total porosity, φ and a fluid phase of liquid water that saturates the pore space. It is also assumed that total and kinematic porosity are equal. Effective volumetric heat capacity, C_e is calculated based on weighted arithmetic mean (Buntebarth and Schopper, 1998; Scharli and Rybach, 2001):

$$C_e = (1-\varphi)C_s + \varphi C_f \tag{4.3}$$

Where C_s and C_f are the volumetric heat capacity of the solid and fluid phases respectively.

The thermal diffusivity of rocks in the measured interval, κ_s, has been calculated based on the geometric mean of the thermal diffusivity for mineral grains in rock cuttings (Sutherland et al., 2017). The effective thermal diffusivity of the medium in the z direction, κ_e is assumed to be the geometric mean of the thermal diffusivity of rock inferred from analysis of rock cuttings, κ_s, and of water, κ_f:

$$\kappa_e = {\kappa_s}^{1-\varphi}{\kappa_f}^{\varphi} \tag{4.4}$$

It is assumed that thermal dispersion due to mechanical mixing is negligible.

The rock and fluid phases are uplifted at a spatially constant vertical velocity, v_u relative to stationary observation points. The fluid phase also moves relative to the rock with vertical average linear velocity, v_f. Here z represents the vertical depth from the surface, meaning that upward heat and mass flow are represented by negative parameter values.

The equation for steady state vertical heat transport in this case, assuming an absence of significant radiogenic heat generation is:

$$Q = (1-\varphi)C_s v_u T + \varphi C_f (v_u + v_f)T - C_e \kappa_e \frac{\partial T}{\partial z} \tag{4.5}$$

Since the vertical Darcy velocity, q, is equal to,

$$q = \varphi v_f \tag{4.6}$$

and an effective velocity can be defined as,

$$v_e = \frac{C_e v_u + C_f q}{C_e} \tag{4.7}$$

then (4.5) can be re-expressed more succinctly, using (4.6, 4.7), as,

$$Q = C_e v_e T - C_e \kappa_e \frac{dT}{dz} \tag{4.8}$$

(4.8) can also be written as,

$$v_e T(\varsigma) - \frac{\kappa_e}{l}\frac{dT(\varsigma)}{d\varsigma} = f \tag{4.9}$$

which has the solution,

$$T(\varsigma) = \frac{f}{v_e} + \frac{F}{v_e} e^{P\varsigma} \tag{4.10}$$

where,

$$P = \frac{l v_e}{\kappa_e} \tag{4.11}$$

$$f = \frac{Q}{C_e} \tag{4.12}$$

$$l = z_l - z_0 \tag{4.13}$$

$$\varsigma = \frac{z - z_0}{l} \tag{4.14}$$

P is the Péclet number, f and F are heat flux parameters, with the latter calculated based on boundary conditions, l is the thickness of the vertical section of interest, z_0 is the depth of the upper boundary of the section, z_l is the depth of the basal boundary of the section and ς is a dimensionless parameter.

For a model with n sections (4.10) applies to each section, as,

$$T_n(\varsigma_n) = \frac{f_n}{v_{e,n}} + \frac{F_n}{v_{e,n}} e^{P_n \varsigma_n} \tag{4.15}$$

Where subscript n denotes properties of the nth section.

F_1 is a function of the upper boundary temperature, $T_1(0)$:

$$F_1 = v_{e,1} T_1(0) - f_1 \tag{4.16}$$

Section boundaries are considered as the locations of hydraulic features, such as fractures, which may act as fluid sources or sinks, allowing for variation in q between sections. Fixed flux changes, Δf, are applied at section boundaries to reflect changes in heat flux due to these fluid sources and sinks:

$$f_n = f_{n-1} + \Delta f_n \tag{4.17}$$

Temperature is kept continuous between sections, such that $T_n(0) = T_{n-1}(1)$. On this basis F_n for $n > 1$ is given by

$$F_n = \frac{v_{e,n}}{v_{e,n-1}} (f_{n-1} + F_{n-1} e^{P_{n-1}}) - f_{n-1} - \Delta f_n \tag{4.18}$$

Three different models are proposed based on this general approach.

- Model 1 is a single-section model ($n = 1$). q, Q and $T(0)$ are independent fitted paramaters, whilst material properties (i.e. κ_e, C_s, C_f, φ) and v_u are fixed.

- Models 2 and 3 both have four sections ($n = 4$). Section C corresponds to $n = 1$, section B to $n = 2$, section A2 to $n = 3$ and section A1 to $n = 4$. q_{1-4}, Q_1 and $T_1(0)$ are independent fitted paramaters, whilst material properties (i.e. κ_e, C_s, C_f, φ) and v_u are each fixed at a constant value across all sections.
- For Models 2 and 3, changes in q across section boundaries are assumed to be due to in- or out- flow of fluid from a source or sink.
    - For Model 2, changes in q across section boundaries are assumed to be due to in- or out- flow of fluid from a source or sink at the same temperature as the profile at the section boundary depth. Thus, the change in heat flux for each section is:

$$\Delta f_n = (v_{e,n} - v_{e,n-1})T_n(0) \tag{4.19}$$

      As a result, Q_{2-4} are not independent.
    - For Model 3, the assumption that fluid sources or sinks are at the same temperature as the profile at the section boundary depth is not made. Thus Δf_n is an independent parameter set equal to a fitted constant, G_n:

$$\Delta f_n = G_n \tag{4.20}$$

      In this case Q_{2-4} are independent fitted parameters.

The model configuration and parameters used in Models 1 to 3 is summarised in Table 4.1. The best fit parameters for each model are shown in Tables 4.2 and 4.3. Uncertainty rages for fixed parameters and 95 % confidence intervals from model regression are used for calculation of model error. Variation in κ_e between sections with constant q was investigated as an alternative modelling approach but requires variation in κ_e in excess of the natural variation of κ_e in silicate rocks in order to fit the data.

For T in Kelvin, $Q = Q_a$, an absolute heat flux. Heat fluxes presented are relative to surface temperature, Q_s:

$$Q_{s,n} = Q_{a,n} - C_e v_{e,n} T_1(0) \tag{4.21}$$

Table 4.1 (Overleaf) Summary of the conditions and parameters used in Model 1 to 3. As z is defined as the depth below the ground surface, upward flow is represented by negative Q and v. Uncertainty ranges for parameters are based on the maximum and minimum plausible values, with κ_s values based on values from Sutherland et al. (2017); κ_f and C_f values based on data presented by Lemmon et al. (2017); C_s values based on data presented by Eppelbaum et al. (2014) and v_u values based on work by Little et al. (2005).

Table 4.1 Caption overleaf.

Model	Number of sections	Section boundaries	Section boundary conditions (*BC*)	Number of *BC*	Independent parameters (*IP*)	Number of *IP*	Fixed parameters	Uncertainty range for fixed parameters	Fitted parameters
1	1	N/A	N/A	0	f, v_e/κ_e, $T(0)$	3	κ_s = 1.6 × 10^{-6} m^2·s^{-1} κ_f = 1.5 × 10^{-7} m·s^{-1} C_s = 2.5 × 10^6 J·m^{-3}·°C^{-1} C_f = 4.2 × 10^6 J·m^{-3}·°C^{-1} φ = 0.1 v_u = 2.5 × 10^{-10} m·s^{-1}	κ_s = 1.3 × 10^{-6} m·s^{-1} to 1.7 × 10^{-6} m·s^{-1} κ_f = 1.5 × 10^{-7} m·s^{-1} to 1.6 × 10^{-7} m·s^{-1} C_s = 1.6 × 10^6 J·m^{-3}·°C^{-1} to 4.4 × 10^6 J·m^{-3}·°C^{-1} C_f = 4.0 × 10^6 J·m^{-3}·°C^{-1} to 4.4 × 10^6 J·m^{-3}·°C^{-1} φ = 0 to 0.2 v_u = 1.9 × 10^{-10} m·s^{-1} (6 mm·yr^{-1}) to 2.9 × 10^{-10} m·s^{-1} (9 mm·yr^{-1})	Q, q, $T_1(0)$
2	4	$z_{l,1}$ = 71 m $z_{l,2}$ = 212 m $z_{l,3}$ = 691 m $z_{l,4}$ = 814 m	$f_2 = f_1 + (v_{e,2} - v_{e,1})T_2(0)$ $f_3 = f_2 + (v_{e,3} - v_{e,2})T_3(0)$ $f_4 = f_3 + (v_{e,4} - v_{e,3})T_4(0)$	3	f_1, $v_{e,1}/\kappa_{e,1}$, $v_{e,2}/\kappa_{e,2}$, $v_{e,3}/\kappa_{e,3}$, $v_{e,4}/\kappa_{e,4}$, $T(0)$	6			Q_1, q_1, q_2, q_3, q_4, $T_1(0)$
3	4		$f_2 = f_1 + G_2$ $f_3 = f_2 + G_3$ $f_4 = f_3 + G_4$	3	f_1, $v_{e,1}/\kappa_{e,1}$, $v_{e,2}/\kappa_{e,2}$, $v_{e,3}/\kappa_{e,3}$, $v_{e,4}/\kappa_{e,4}$ G_2, G_2, G_4, $T(0)$	9			Q_1, Q_2, Q_3, Q_4, q_1, q_2, q_3, q_4, $T_1(0)$

Table 4.2 Best fit parameters and R^2 values for Model 1 to 3. Negative values indicate upward flow, uncertainty interval is given in brackets.

Model	f_1 (× 10^{-7} K·m·s^{-1})	$v_{e,1}$ (× 10^{-9} m·s^{-1})	$v_{e,2}$ (× 10^{-9} m·s^{-1})	$v_{e,3}$ (× 10^{-9} m·s^{-1})	$v_{e,4}$ (× 10^{-9} m·s^{-1})	G_2 (× 10^{-7} K·m·s^{-1})	G_3 (× 10^{-7} K·m·s^{-1})	G_4 (× 10^{-7} K·m·s^{-1})	$T_1(0)$ (K)	R^2
1	-6.78 (-4.45, -9.34)	-1.48 (-0.96, -2.05)	N/A	N/A	N/A	N/A	N/A	N/A	276.1 (276.4, 275.7)	0.9973
2	101 (151, 60.2)	35.9 (53.6, 21.4)	-2.56 (-1.57, -3.75)	-1.09 (-0.703, -1.52)	-44.1 (-27.2, -64.4)	N/A	N/A	N/A	282.5 (282.8, 282.2)	0.9996
3	155 (183, -4.26)	55.0 (8.68 × 10^5, -8.60 × 10^5)	-6.531 (5870, -5870)	-1.23 (0.0290, -2.08)	2.09 (68.7, -62.5)	-177.6 (1.778 × 10^4, -1.77 × 10^4)	16.13 (1.77 × 10^4, -1.844 × 10^4)	13.58 (268.4, -232)	282.9 (287.2, 279.4)	0.9998

Table 4.3 Parameters and R^2 values for Model 0A and 0B. Only $T_1(0)$ is fitted. Negative values indicate upward flow.

Model	f_1 (× 10^{-7} K·m·s^{-1})	$v_{e,1}$ (× 10^{-9} m·s^{-1})	$T_1(0)$ (K)	R^2
0A	-0.262	0	334.9	0.2806
0B	-2.02	-2.54	302	0.8955

4.8 Supporting information references

Buntebarth, G., Schopper, J.R., 1998. Experimental and theoretical investigations on the influence of fluids, solids and interactions between them on thermal properties of porous rocks. Phys. Chem. Earth 23, 1141–1146. doi:10.1016/S0079-1946(98)00142-6

Eppelbaum, L., Kutasov, I., Pilchin, A., 2014. Applied Geothermics, Applied Geothermics. doi:10.1007/978-3-642-34023-9

Lemmon, E.W., McLinden, M.O., Friend, D.G. Thermophysical Properties of Fluid Systems, in: Linstrom, P.J., Mallard, W.G. (Eds.), NIST Chemistry WebBook, NIST Standard Reference Database Number 69. National Institute of Standards and Technology, Gaithersburg MD. doi:10.18434/T4D303 (accessed 30.08.2017).

Little, T.A., Cox, S., Vry, J.K., Batt, G., 2005. Variations in exhumation level and uplift rate along the oblique-slip Alpine fault, central Southern Alps, New Zealand. Bull. Geol. Soc. Am. 117, 707–723. doi:10.1130/B25500.1

Scharli, U., Rybach, L., 2001. Determination of specific heat capacity on rock fragments. Geothermics 30, 93–110. doi:10.1016/S0375-6505(00)00035-3

Sutherland, R., Townend, J., Toy, V., Upton, P., Coussens, J., Allen, M., Baratin, L.-M., Barth, N., Becroft, L., Boese, C., Boles, A., Boulton, C., Broderick, N.G.R., Janku-Capova, L., Carpenter, B.M., Célérier, B., Chamberlain, C., Cooper, A., Coutts, A., Cox, S., Craw, L., Doan, M.-L., Eccles, J., Faulkner, D., Grieve, J., Grochowski, J., Gulley, A., Hartog, A., Howarth, J., Jacobs, K., Jeppson, T., Kato, N., Keys, S., Kirilova, M., Kometani, Y., Langridge, R., Lin, W., Little, T., Lukacs, A., Mallyon, D., Mariani, E., Massiot, C., Mathewson, L., Melosh, B., Menzies, C., Moore, J., Morales, L., Morgan, C., Mori, H., Niemeijer, A., Nishikawa, O., Prior, D., Sauer, K., Savage, M., Schleicher, A., Schmitt, D.R., Shigematsu, N., Taylor-Offord, S., Teagle, D., Tobin,

H., Valdez, R., Weaver, K., Wiersberg, T., Williams, J., Woodman, N., Zimmer, M., 2017. Extreme hydrothermal conditions at an active plate-bounding fault. Nature 546, 137–140. doi:10.1038/nature22355

Chapter 5:

Permeability controls on coupled groundwater and heat flow in an active orogenic mountain belt; the Southern Alps, New Zealand

Abstract

Fluid and heat flow are key controls on deformation, seismicity and geochemical processes within orogenic mountain belts. The Southern Alps mountain belt has been uplifted on the Alpine Fault, an active plate boundary accommodating motion between the Pacific and Australian plates in South Island, New Zealand. Here, hydrogeological models of the Whataroa valley region in the central Southern Alps are used to quantify the effect of permeability structure on fluid and heat flow in the orogen. The Deep Fault Drilling Project (DFDP) 1B and 2B boreholes within the model domain provide data for comparison to model outputs. Temperature and fluid pressure fields prove sensitive to features of permeability structure such as homogeneous permeability value, permeability-depth relationship, permeability anisotropy and near-fault permeability. Other than the presence of valley sediments, which lowers hydraulic heads below DFDP-2B but has limited regional impact, none of the modelled structures represent a clearly improved fit to borehole data compared to a simple homogenous, isotropic permeability of 10^{-16} m^2. However patterns that are common across a range of models emerge. Groundwater convergence into the valley occurs in all models and is sufficient to perturb isotherms upward below the valley relative to the bounding ridges in the majority, including all models with homogeneous permeability $\geq 10^{-16}$ m^2. This isotherm geometry is consistent with higher geothermal gradients measured in boreholes in major valleys in the central Southern Alps, compared to those between these valleys. Where model permeability is increased, or decreased less sharply with depth, temperature contrasts between the base of the groundwater system and the surface decrease and isotherms are perturbed to higher elevations below the valley compared to below ridges. Hydraulic head increases with depth in the near-surface below the valley in models, but thermal reductions in water density result in a transition to falling head with depth deeper below the valley. Thus, steep rises in head observed below DFDP-2B are not predicted to continue to more than ~1 km below sea level. Models predict that thermal buoyancy is an important driver for vertical flow in regions beneath the valley and its margins. High shallow temperatures due to uplift reduce water viscosity, promoting higher Darcy velocities and more significant heat advection by groundwater.

5.1 Introduction

Fluids may impact orogenic processes through their role in mass and heat transfer as well as their influence on deformation. Although in much continental lithosphere heat flow is dominantly conductive (Stein, 1995), a number of studies have indicated significant heat transport by fluids in mountain belts (Sutherland et al., 2017; Upton and Sutherland, 2014; Whipp and Ehlers, 2007). Modelling by Forster and Smith (1989) showed that for two-dimensional topography with 2 km elevation and a basal heat flux of 120 $mW \cdot m^{-2}$, fluid flow begins to perturb isotherm structure for permeability between 10^{-18} m^2 and 10^{-16} m^2. Hydraulic and thermal processes are coupled, as fluid flow transports heat and the temperature field affects fluid density and viscosity, modifying fluid flow. Thermally driven buoyancy has been inferred as one of the major drivers for groundwater flow in mountain belts, along with topography and sediment compaction (Deming, 1994; Koons and Craw, 1991). In addition to transporting heat, fluid flow advects dissolved chemical species within orogenic mountain belts. In some settings this is essential to drive metamorphic reactions (Etheridge et al., 1983; Ferry, 1988). Where flow rates are sufficiently high, the degree of metamorphism and mineralisation experienced by rocks is a function of time-integrated fluid fluxes (Dipple and Ferry, 1992). Fluid flow may act as a major control on mineralogy and consequently, understanding past fluid flow is significant for interpreting metamorphic history in mountain belts (Dipple and Ferry, 1992; Vavra et al., 1996) and the distribution of economically valuable ore deposits (e.g. Pitcairn et al., 2006). The extent to which groundwater flow plays a significant role in heat and mass transport is dependent on groundwater Darcy velocity, although the range of Darcy velocities over which mass advection is significant is greater than the range over which heat advection is significant, due to the lower coefficients of solute diffusion relative to heat diffusion (Bickle and McKenzie, 1987).

The influence of pore fluid pressure on deformation is evident from the Mohr-Coulomb criterion:

$$\tau = C_\tau + \mu_\tau(\sigma_n - p) \tag{5.1}$$

Where τ is the critical shear stress for failure (shear strength), C_τ is cohesion, μ_τ is the coefficient of friction, σ_n is the confining stress and p is the pore fluid pressure. The strength of a fault influences if and when it fails, whereas changes in strength during failure determine whether the fault slips in earthquakes or creeps aseismically. Where fault rocks are velocity weakening, fault slip is unstable, allowing earthquake nucleation and propagation, rather than stable, aseismic displacement (Scholz, 1998). Increasing pore fluid pressure reduces effective confining stress, weakening a fault and increasing its proximity to failure (Hubbert and Rubey, 1959). Thermal pressurisation of pore fluids during failure may contribute to velocity weakening behaviour, promoting seismicity (Segall and Rice, 2006; Sibson, 1973). In influencing the temperature

distribution ('thermal structure') and composition of fault rocks, fluid flow may also modify their static and velocity dependent frictional behaviour, which are dependent on mineralogy and temperature (Kohlstedt et al., 1995; Scholz, 1998). Thus, fluids may act as a control on the timing and nature of fault failure through the influence of pore fluid pressure and the alteration of fault rocks.

Permeability, k, plays a particularly important role in modulating fluid pressures and flow rates, as unlike many geological parameters, it can vary by many orders of magnitude (Clauser, 1992; Manning and Ingebritsen, 1999). On the basis of permeability estimates from time-integrated fluid fluxes in metamorphic systems and modelling of geothermal data, Manning and Ingebritsen (1999) obtained a permeability depth relationship for continental crust of:

$$\log k = -14 - 3.2 \log z_{km} \tag{5.2}$$

Where z_{km} is depth in kilometres. Although this provides a generalised relationship for continental crust, there are significant differences in permeability between rock types (Domenico and Schwartz, 1990), which are greatest in the near-surface (Manning and Ingebritsen, 1999). Topographic variations result in differences in stress field (Savage and Swolfs, 1986). In compressional settings this results in increased proximity to failure and increased permeability beneath ridges, compared to beneath valleys (Koons and Kirby, 2007; Upton and Sutherland, 2014). Permeability may also vary around fault zones as a result of rock damage and cementation. Fault cores typically have low permeability, with higher permeability in a fractured damage zone and as a result faults may act as conduits for flow, barriers to flow, or combined conduit-barrier systems (Caine et al., 1996; Lockner et al., 2009). Mineral precipitation by fluids may act to reduce permeability of fractured fault rocks and the permeability of a fault zone may change with time through seismic cycles as a result (Sibson, 1990).

5.2 Geological setting

The Alpine Fault forms the tectonic plate boundary between the Pacific and Australian plates in South Island, New Zealand (Fig. 5.1). During the last 50 kyr the fault has experienced 23-25 mm·yr^{-1} strike slip motion and dip slip motion varying along strike from ~0 mm·yr^{-1} to >10 mm·yr^{-1} (Norris and Cooper, 2001, 2007; Sutherland et al., 2006). Rapid uplift on the fault has resulted in the formation of the Southern Alps mountain belt and altered the thermal structure in the region, raising the brittle-ductile transition to depth of 8 ± 2 km in the fault hanging wall (Allis et al., 1979; Koons, 1987; Leitner et al., 2001). The Alpine Fault has an estimated dip of 40-60° to the south-east, beneath the Southern Alps (Sibson et al., 1979; Stern et al., 2007) and is locked to a depth of at least 5 km (Leitner et al., 2001; Wallace et al., 2007),

above which displacement is accommodated in large earthquakes (Sutherland et al., 2007). These occur with a recurrence interval of 291 ± 23 years (Cochran et al., 2017), with the most recent occurring in 1717 (Wells et al., 1999). This indicates that currently the Alpine Fault is late in its seismic cycle.

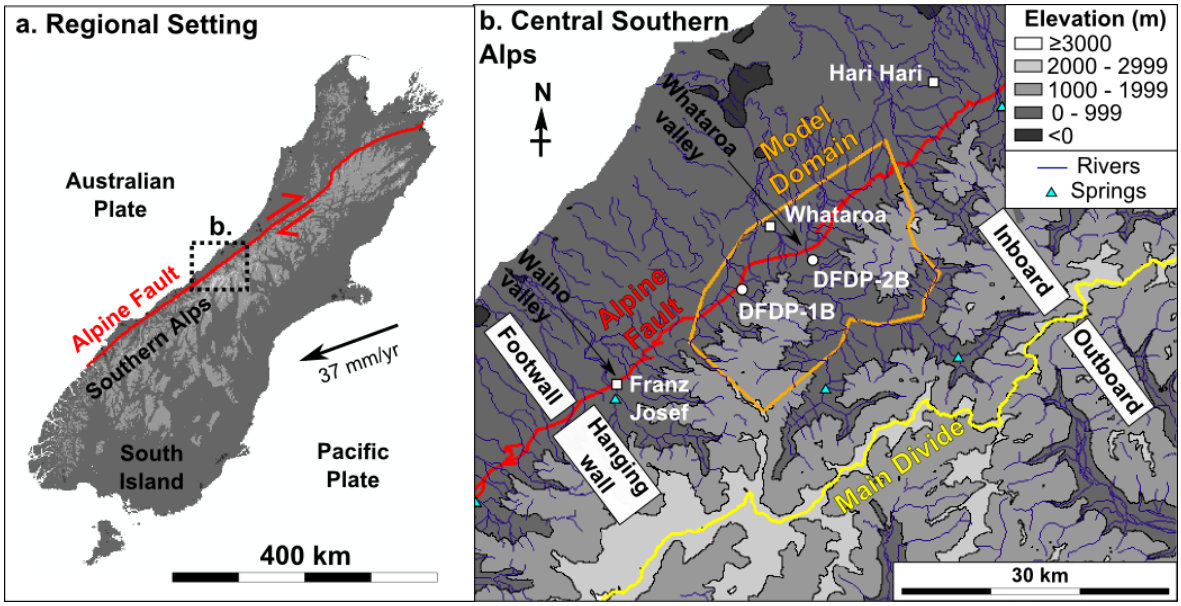

Figure 5.1 a. Regional setting of the Alpine Fault, bounding the Pacific and Australian plates in South Island, New Zealand. b. Setting of the DFDP-1B and DFDP-2B boreholes and the model domain within the Whataroa valley in the central Southern Alps.

As the prevailing winds in the Southern ocean are westerly, orographic precipitation is concentrated on the north-western inboard region of the Southern Alps (Fig. 5.1), forming a rain shadow across the outboard region, to the south-east of the Main Divide (Cox and Sutherland, 2007). Consequently, erosion is concentrated in the inboard region, producing a two-sided wedge geometry to the orogen (Koons, 1990) and a topographic regime in the inboard region of alternating ridges and valleys running between the Alpine Fault and the highest peaks of the Southern Alps at Main Divide (Koons, 1989).

The hanging-wall rocks of the fault are the quartzofeldspathic Alpine Schist and its predominantly greywacke and argillite protoliths (Cox and Barrell, 2007). These are juxtaposed adjacent to Palaeozoic sediments and granitoids, unconformably overlain by Quaternary fluvio-glacial sediments in the footwall of the fault (Cox and Barrell, 2007).

The highest grade Alpine Schist rocks are oligoclase-zone amphibolite facies schists that crop out adjacent the Alpine Fault, with metamorphic grade and total uplift decreasing away from the fault (Cox and Barrell, 2007; Koons, 1989). Foliation in the Alpine Schist dips at ~45 degrees to the south-east near to the fault, steepening to near vertical at the Main Divide (Little et al., 2002).

Adjacent to the fault is a 1-2 km-wide mylonitised zone, with hydrothermally altered cataclasites within 40-50 m of the fault plane (Norris and Cooper, 1995, 2007; Sutherland et al., 2012).

5.3 Groundwater and heat flow in the Southern Alps

The presence of hydrothermal veins within the Alpine Schists (Menzies et al., 2014), the gold mineralisation associated with vein systems near to the Main Divide (Craw et al., 2009) and evidence for alteration by fluid flow from the formation of secondary phyllosilicates, carbonates, quartz and sulphides (Norris and Cooper, 2007; Sutherland et al., 2012; Warr and Cox, 2001), testify to the past fluid activity in the Southern Alps.

Ongoing fluid circulation is evidenced by the presence of warm springs (Barnes et al., 1978). These springs are found in valleys across the Southern Alps and are only known to occur in the hanging wall of the Alpine Fault. Fractures are believed to play an important role in controlling fluid flow in the orogen (Craw et al., 2009), with observed changes in spring temperature at the Copland hot spring following large earthquakes, inferred to reflect changes of fracture apertures resulting from stress changes (Cox et al., 2015). Strontium isotopic ratios for both warm springs and hydrothermal veins fall within the range for hanging wall rocks, showing no evidence for interaction with the highly radiogenic rocks found in the footwall (Menzies et al., 2016).

Magnetotelluric surveys image a zone of low resistivity in the middle to lower crust at ~20-30 km depth, with upward projections at either end, one of which follows the Alpine Fault trace to a depth of ~10 km (Wannamaker et al., 2002). This zone also corresponds to a region of low seismic velocities (Stern et al., 2001) and has been interpreted as a zone of fluid production through metamorphic dehydration reactions (Wannamaker et al., 2002). However, ductilely deformed quartz veins from the Southern Alps have isotopic signatures most simply explained by formation from meteoric fluids, suggesting that meteoric water is the dominant fluid down into the brittle-ductile transition zone (Menzies et al., 2014, 2016; Upton et al., 1995). Although there is evidence for meteoric water penetration as deep as the brittle-ductile transition, much groundwater circulation is likely to be largely restricted to shallower depths, with warm spring geochemistry showing interaction with rocks at <150 °C (Reyes et al., 2010).

The deepest estimates of the thermal regime beneath the Southern Alps are provided by studies of seismicity, thermobarometry of Alpine Schist rocks, and from borehole data. The maximum depth of seismicity represents the approximate depth of the brittle-ductile transition, corresponding to the onset of quartz plasticity, which occurs at ~300 °C (Scholz, 1998). Earthquake depths indicate that the base of the seismogenic crust is at ~8 km beneath the high Southern Alps, 3-4 km shallower than elsewhere in South Island (Leitner et al., 2001), consistent

with the anticipated effects of uplift (Allis et al., 1979; Koons, 1987). Thermobarometric estimates based on fluid inclusion and mineral chemistry are in agreement with seismic data, indicating a significantly steepened geothermal gradient ($\gtrsim$40 °C·km^{-1}) above the brittle-ductile transition compared to below it (~10 °C·km^{-1}), with temperatures exceeding 300 °C by $\lesssim$8 km depth (Toy et al., 2010).

Boreholes drilled as part of the Deep Fault Drilling Project (DFDP) provide direct measurements of temperatures and pressures at depth in the inboard Southern Alps. The DFDP-1A and 1B boreholes are located <200 m from the surface trace of the Alpine Fault (Fig. 5.1) and penetrate through the fault at 91 m and 128 m depth respectively (Sutherland et al., 2011). Measurements in the 150 m-deep DFDP-1B borehole, showed an approximately linear geothermal gradient of 62.6 ± 2.1 °C·km^{-1} (Fig. 5.2) and a fluid pressure drop of 0.53 MPa across the fault (Sutherland et al., 2012). The DFDP-2B borehole was drilled in the Whataroa valley (Fig. 5.1), passing through a 240 m thick sequence of valley sediments before penetrating Alpine Schist basement rocks below and reaching a total depth of 818 m still within the Alpine Fault hanging wall. This borehole showed a geothermal gradient averaging 125 ± 55 °C·km^{-1} and measured borehole hydraulic heads of >60 m above surface elevation (Fig. 5.2), indicating superhydrostatic increases in pore fluid pressure with depth (Chapter 3, this thesis; Sutherland et al., 2017). Much of the increase in hydraulic head down DFDP-2B occurred below 273 m depth, beneath the base of the valley sediments. Like the DFDP-2B borehole in the Whataroa valley, temperature measurements during drilling of an earlier borehole in the Waiho valley, near Franz Josef showed a high geothermal gradient, in this case 95 °C·km^{-1} (Shi et al., 1996). Modelling of temperature data from the DFDP-2B borehole indicates a significant role for fluid advection of heat in the orogen (Chapter 4, this thesis; Sutherland et al., 2017).

Permeability in the Alpine Fault Zone appears to indicate combined conduit-barrier architecture, with a high permeability damage zone adjacent to a low permeability fault core (Caine et al., 1996). Laboratory tests on slip plane gouge from DFDP-1B core and outcrops indicate permeability of the order 10^{-20} m^2, significantly lower than permeabilities measured away from the fault plane (Boulton et al., 2012; Carpenter et al., 2014; Sutherland et al., 2012). On the basis of the observed pressure difference at DFDP-1B, the low measured permeability of fault slip zone gouge and absence of a footwall ^{87}Sr-isotopic signature in hot springs, it has been inferred that the Alpine Fault may be a regional barrier to fluid flow (Carpenter et al., 2014; Sutherland et al., 2012) to significant depth, and possibly throughout the brittle upper crust (Menzies et al., 2016). The fault damage zone, in which macroscopic damage increases toward the fault may act as a channel for focussed fluid flow along the fault plane (Menzies et al., 2016; Sutherland et al., 2012). At the Alpine Fault, the damage zone is 47 m to 154 m wide (Williams, 2017). An increased

abundance of minerals associated with fluid alteration in the hanging wall toward the fault is consistent with this (Norris and Cooper, 2007; Sutherland et al., 2012; Warr and Cox, 2001). However, at this late stage in the seismic cycle of the fault, precipitation of carbonate and phyllosilicate minerals within fractures is inferred to have reduced permeability in heavily altered rocks within ~50 m of the fault (Sutherland et al., 2012).

Permeability estimates from slug tests and modelling of temperature data in the DFDP boreholes, indicate permeabilities in the range 10^{-17} m^2 to 10^{-13} m^2 for Alpine Schist rocks away from the slip plane itself (Chapter 3 and 4, this thesis; Sutherland et al., 2012, 2017). The only other published estimates of in-situ permeability for the inboard Southern Alps are based on data from two boreholes drilled as part of the Amethyst Power project near to the Wanaganui valley. Packer tests in these boreholes showed estimated permeabilities of the order 10^{-13} m^2 to 10^{-12} m^2 (Cox et al., 2015).

Variability in borehole permeability estimates provides some indication of the heterogeneity of permeability in the Southern Alps. However, they only offer a limited insight into the actual permeability structure, given the small number of sites sampled and the limited depth of investigation (<1 km). Conditions at greater depths have been simulated in laboratory tests on specimens (e.g. Boulton et al., 2012; Carpenter et al., 2014). However, studies of veins and alteration indicate that fractures are significant in controlling flow (Craw et al., 2009), and given their small sample volume, laboratory measurements may not be representative of regional-scale permeability. Modelling of the Wanganui valley catchment indicates that regional permeability equivalent to a homogeneous value of $\leq 10^{-13}$ m^2 is required to produce a water table consistent with water levels observed in the Amethyst Power project boreholes (Chapter 2).

Foliated rocks commonly show reduced permeability normal to foliation relative to that parallel to foliation (Singhal and Gupta, 2010). The Alpine Schists show seismic anisotropy associated with their foliation that is not observed in their unfoliated protoliths (Christensen and Okaya, 2007). It is therefore possible that permeability in the Alpine Schists may be anisotropic and that this may have a significant influence on groundwater flow, however control of flow by fractures may mean permeability anisotropy is absent or is not as closely associated with foliation as seismic anisotropy.

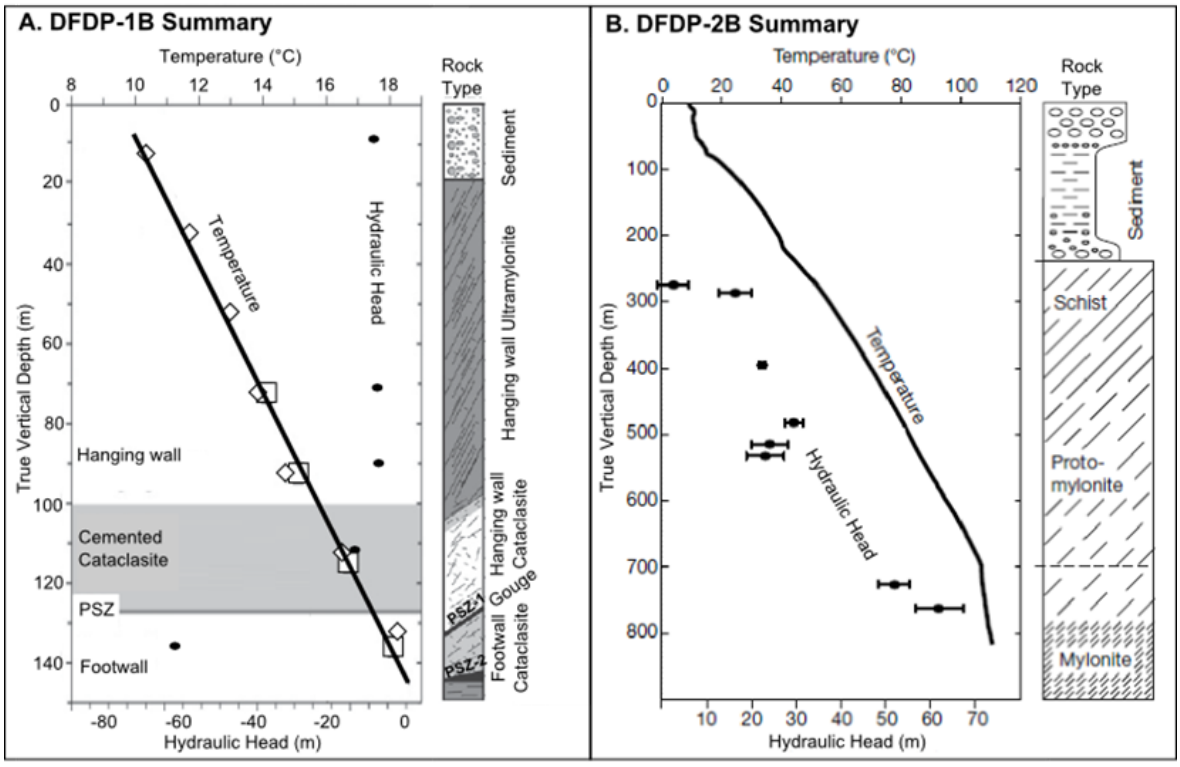

Figure 5.2 Temperature and hydraulic head data, with rock type profiles from the drilled intervals of a. the DFDP-1B borehole (crosses and diamonds represent resistance device and piezometer sensor temperature data respectively), adapted from Sutherland et al. (2012) and b. the DFDP-2B borehole adapted from Sutherland et al. (2017).

5.4 Aims and objectives

The Southern Alps show evidence for past and ongoing fluid circulation, which appears sufficiently vigorous to advect significant heat and to cause widespread hydrothermal alteration. This, coupled with the evidence for repeated failure of the Alpine Fault in large earthquakes and the potential for fluid flow to influence fault behaviour provides clear motivation for modelling the coupled fluid and heat flow at depth in the orogen. This study aims to develop a predictive understanding of temperature and fluid pressure conditions at depth in the orogen, in particular those close to the Alpine Fault and to understand how they may influenced by permeability structure.

Its objectives are:

1. To quantify the effect of permeability structure on groundwater and heat flow in the Southern Alps, in particular focussing on the predicted physical conditions (temperature and hydraulic head) on and near to the Alpine Fault under plausible permeability scenarios.

2. To identify whether there are features of the groundwater and heat flow regimes common across modelled permeability structures.

3. To compare model results for different permeability structures to temperature and fluid pressure measurements taken at DFDP-1B and 2B, also considering the implications of temperatures in the Waiho valley borehole, outside the model domain.

5.5 Governing equations

This study considers steady state single-phase fluid and heat flow in a porous rock medium, with volume fraction porosity (void space), φ saturated with water. Water and rock both move at a constant rock advection velocity relative to a fixed reference frame, described by the vector, $\boldsymbol{v_s}$. Water moves relative to the rock with Darcy velocity vector, $\boldsymbol{q}$. It is assumed that water density varies with temperature, T and pressure, p and that water viscosity varies with temperature, but that variations in density and viscosity due to solute concentrations are negligible, as fluid inclusions from shallow (~500 m depth) veins indicate low concentrations of dissolved species (Craw, 1997).

The study considers fluid flow governed by the mass continuity equation, assuming an absence of internal fluid sources, and Darcy's Law according to:

$$\nabla \cdot (\rho(p,T)\boldsymbol{q}) = 0 \tag{3}$$

$$\boldsymbol{q} = -\frac{\boldsymbol{k}}{\mu(T)}(\nabla p + \rho(T,p)g\hat{\boldsymbol{n}}) \tag{4}$$

Where $\boldsymbol{k}$ is the permeability tensor**,** μ is the dynamic viscosity of the water, ρ is the density of the water, g is the acceleration due to gravity and $\hat{\boldsymbol{n}}$ is a unit vector oriented vertically upward. The role of groundwater flow in heat transport is described by the steady state conservation of energy equation, which in this case, assuming no internal heat sources is:

$$C_f\boldsymbol{q}\cdot\nabla T + C_e\boldsymbol{v_s}\cdot\nabla T - \nabla\cdot(\boldsymbol{\Lambda_e}\cdot\nabla T) = 0 \tag{5}$$

Where C_f is the volumetric heat capacity of the fluid water phase, C_s is the volumetric heat capacity of the solid rock phase, C_e is the effective volumetric heat capacity of the solid and fluid phases, calculated as the porosity weighted arithmetic mean. Volumetric heat capacities are assumed to be homogeneous and independent of p and T. $\boldsymbol{q}$ is the Darcy velocity vector, $\boldsymbol{\Lambda_e}$ is the tensor of effective thermal conductivity for the solid and fluid phases, calculated here as the porosity weighted arithmetic mean, with thermal dispersion assumed to be negligible. Thermal conductivities are assumed to be homogeneous, isotropic and independent of p and T.

5.6 Modelling strategy

A finite-element FEFLOW model (Diersch, 2014) for the Whataroa valley (Fig. 5.3) has been constructed for the central Southern Alps, which solves the equations outlined above (see Supporting Information 5.11.1 for details). The model domain encompasses both the DFDP-2B and DFDP-1A and B boreholes and extends from the topographic surface to 12 km below mean sea level, the approximate position of the base of the brittle crust across much of South Island, where isotherms have not been perturbed by uplift (Leitner et al., 2001). All model elevations given in this study are relative to reference ellipsoid GRS80 (for further information on the NZGD2000 geodetic datum see Land Information New Zealand, 2008). A sub-set of the same models developed here were presented by Sutherland et al. (2017), where viscosity was fixed and the Boussinesq approximation implemented. This approximation assumes that density variations are only significant where multiplied by g (i.e. in the latter, buoyancy related term in Darcy's Law) and is commonly applied to situations where density changes are relatively small (Gray and Giorgini, 1976).

Temperature and pressure data from DFDP-1B and 2B boreholes represent just two threads of observation within a potentially complex three-dimensional system (the Southern Alps), influenced by a range of parameters, including permeability, rock advection velocity and thermal diffusivity, all of which may be temporally and spatially heterogeneous. The sub-set of the models developed here presented by Sutherland et al. (2017) show that the high temperature gradient observed at DFDP-2B can be reproduced in models incorporating both rock advection and groundwater circulation for reasonable permeabilities and rock advection rates. These models also show non-uniqueness in fit of model temperatures to DFDP-1B and 2B data for a range of permeability and rock advection rate combinations. Therefore, this study does not attempt to determine a 'best fit' model. Rather, a set of forward models have been created for plausible permeability structures, representing variations from a fixed baseline model set up, which predict the effects that these structures will have on temperatures and hydraulic heads. All parameters are held constant other than permeability fixed (Table 5.1).

Table 5.1 Thermal parameter values for models presented. Surface (1 atm, 10 °C) water density is based on values from Lemmon et al. (2017).

Parameter	**Value**
Rock advection rate (dip slip)	12 $mm \cdot yr^{-1}$
Isotropic thermal conductivity (water)	0.6 $W \cdot m^{-1} \cdot K^{-1}$
Isotropic thermal conductivity (rock)	2.0 $W \cdot m^{-1} \cdot K^{-1}$
Volumetric heat capacity (water)	4.2 $MJ \cdot m^{-3} \cdot K^{-1}$
Volumetric heat capacity (rock)	2.7 $MJ \cdot m^{-3} \cdot K^{-1}$
Porosity	0.1
Surface water density	999.7 $kg \cdot m^{-3}$

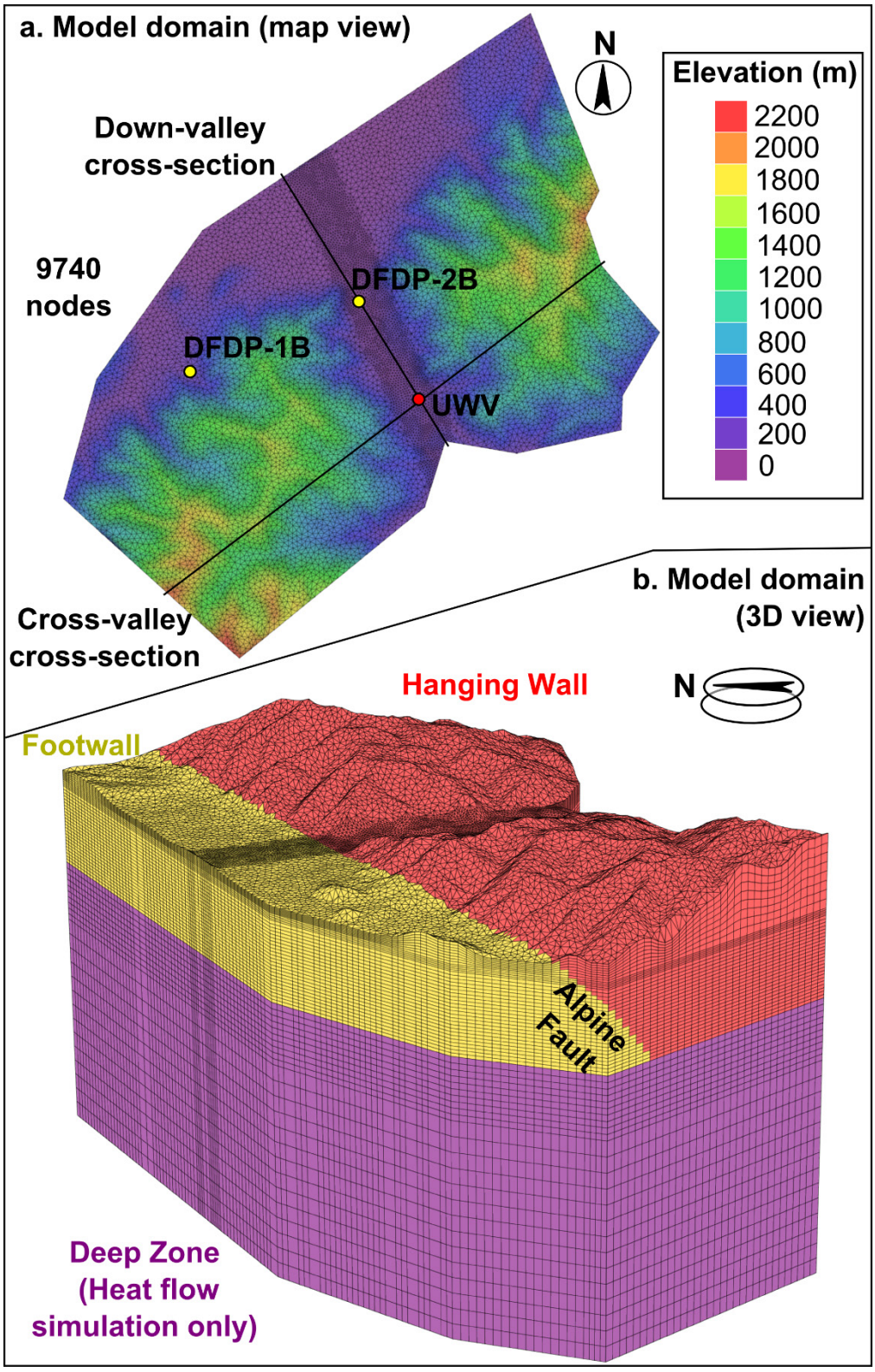

Figure 5.3 Map (a.) and three-dimensional (b.) views of the model domain, which is split into Hanging Wall, Footwall and Deep zones. Results are presented for vertical profiles at the DFDP-1B and 2B borehole sites, a hypothetical observation point (UWV) in the upper Whataroa valley and along cross-valley and down-valley cross-sections.

5.6.1 Baseline model set-up

At the surface of the model domain, hydraulic head is fixed at topographic elevation based on evidence for a high water table in the Southern Alps (Chapter 2) and the upper boundary temperature is fixed at 10 °C, based on the average temperature at 1 m depth in the Whataroa valley, measured at DFDP-2B (Sutherland et al., 2017). Lateral boundaries are located along major ridges in the hanging-wall. No-flow boundary conditions for fluid flow are applied to all lateral boundaries, with the exception of the down-stream footwall boundary, across which hydraulic head is fixed at surface elevation in models where the Alpine Fault is permeable to flow. Transport of heat due to rock advection is simulated by means of a rock advection velocity field applied throughout the model domain, with a conductive heat flux field applied across the base of the model and conditions of no conductive heat flow specified across lateral boundaries. A FLAC geo-mechanical model (Sutherland et al., 2017) is used to generate advection velocity and heat flux values. The flux of water transported by rock advection is dependent on porosity. Rather than attempt to simulate variations in porosity between models of differing permeability or in space, it is assumed that groundwater average linear velocities are sufficiently high in comparison to rocks advection velocities that movement of water by rock advection can be neglected. As such, the rock advection mass flux field is implemented only for the purposes of heat flow simulation. This assumption is consistent with geochemical evidence that meteoric water is the dominant fluid down to the brittle-ductile transition (Menzies et al., 2014), which suggests that average linear velocities remain sufficiently to the base of the brittle crust that the contribution to groundwater movement from uplift must remain minor to negligible. The assumption is further supported by a modelling study of fluid fluxes in the Southern Alps (Chapter 2). This indicates sufficiently high groundwater fluxes persisting to at least -5 km elevation that vertical average linear velocities are at least one and potentially many orders of magnitude larger than uplift velocities for plausible values of porosity in fractured rocks, which are typically low ($<10^{-3}$) and decrease with depth (Freeze and Cherry, 1979; Ingebritsen and Manning, 2003; Snow, 1968). Although a higher porosity than this (0.1) is used in calculation of thermal properties of the bulk water-rock medium (C_e and $\boldsymbol{\Lambda_e}$) for consistency with values used in the FLAC model, the possible range in these properties, based on measured values (Eppelbaum et al., 2014), is large compared to the sensitivity of calculated values to porosity in the range 0.1 to 0.

The Alpine Fault is defined within models as a plane with dip 50° and strike 053. Late Quaternary dip-slip convergence rates in the region lie within the range 6 mm·yr^{-1} to 14 mm·yr^{-1} (Norris and Cooper, 2007). Here a baseline rate of 12 mm·yr^{-1} is adopted for calculation of rock advection velocities, slightly above the midpoint of this interval, as lower rock advection rates give a poor fit to DFDP-2B temperature data across a range of permeabilities (Sutherland et al., 2017). Fluid flow

is simulated within an upper permeable portion of the model. For the baseline model the (horizontal) base of this region is at -3 km elevation (3 km below sea level). An average shallow geothermal gradient of ~50 °C·km^{-1}, based on estimates from borehole measurements (>60 °C·km^{-1}) (Shi et al. 1996; Sutherland et al. 2012, 2017) and geothermometry (≳40 °C·km^{-1}) (Toy et al., 2010) and a maximum temperature of fluid-rock interaction in hot springs of <150 °C (Reyes et al., 2010) indicate a maximum depth for the shallow fluid flow system of <3 km. Thus with topographic elevation >0 km across the model domain, a permeability cut-off at -3 km elevation allows sufficient depth to simulate this shallow flow system. The baseline model assumes homogenous model permeability of 10^{-16} m^2 in the permeable portion of the model. This value of homogeneous permeability was chosen as the baseline as it produces the simulated temperature profile that most closely resembles measured temperatures at DFDP-2B. The 'Deep' portion of the model domain below this, which has its base at -12 km, is used for simulation of heat flow to the base of the permeable region of the model and is assigned a very low permeability (k = 10^{-27} m^2). In models where the Alpine Fault is assumed to be a regional barrier to flow, the model footwall is also assigned this very low permeability. The Boussinesq approximation is implemented for initial simulation, following which temperature at the base of upper permeable portion of the model is fixed and fluid flow simulated with the assumption relaxed. Except where stated otherwise, models calculate variable density and viscosity based on empirically derived relations (Magri et al., 2009; Mercer and Pinder, 1974).

5.6.2 Variations from baseline

Several key aspects of permeability structure are varied in turn (summarised in Table 5.2) in order to test the effect of each on hydraulic head and temperature fields. The significance of changes to a bulk homogeneous permeability is examined by simulating over the range 10^{-14} m^2 to 10^{-17} m^2 (models H-14 to H-17). The study examines the effect of varying the depth of permeability cut-off between -3 km and -5 km elevation (models H-16, CO-4 and CO-5). The effect of systematic reduction in permeability with depth is investigated, based on a log-log relationship (Eq. 5.2) after Manning and Ingebritsen (1999), including models in which the constant coefficients in this function are varied (models MI(-14,-2), MI(-14,-3.2), MI(-14,-4), MI(-16,-2), MI(-16,-3.2) and MI(-16,-4)). The study also examines the effect of regional anisotropy, with permeability normal to foliation 0.1× and 0.01× permeability parallel to foliation, which is assumed to be parallel to the Alpine Fault (models A10 and A100). Next, the importance of more localised features, which may nonetheless have regional significance is investigated. This includes the effect of an Alpine Fault that does not act as barrier to flow on a regional scale (model PF), of a damage zone (model DZ) or cemented zone (model CZ) adjacent to the fault plane, and of higher permeability alluvial

sediments within the valley (models S10 to S100). Although valley sediments contain some fine grained sedimentary units (e.g. lacustrine silts) that could have a relatively low permeability, as well as those expected to have a have high permeability (e.g. clastic fluvial sediments), the minimal head gradient across the upper section of DFDP-2B penetrating through these valley sediments suggests a permeability on the length scale of 100's meters that is higher than in the basement rocks below, potentially due to lack of lateral continuity of low permeability units (Chapter 3).

In addition to the above permeability structures, variants of the baseline model in which density and viscosity are artificially uncoupled are also presented (Table 5.2), in order to investigate the significance of density driven flow and variation of viscosity with temperature for fluid and heat flow in the orogen.

Table 5.2 Outline of models discussed. Continued overleaf.

Model Name	Abbreviation	Hanging wall k (m^2)	Footwall k (m^2)	k cut-off (elevation, km)	Additional features
Homogeneous 10^{-16} m^2 (Baseline)	H-16	10^{-16}	10^{-27}	-3	N/A
Homogeneous 10^{-14} m^2	H-14	10^{-16}	10^{-27}	-3	N/A
Homogeneous 10^{-15} m^2	H-15	10^{-15}	10^{-27}	-3	N/A
Homogeneous 10^{-17} m^2	H-17	10^{-17}	10^{-27}	-3	N/A
Sediments 10× (Hanging wall)	S10	10^{-16}	10^{-27}	-3	Valley sediments (thickness 240 m at DFDP-2B): k = 10^{-15} m^2
Sediments 50×	S50	10^{-16}	10^{-27}	-3	Valley sediments: k = 5×10^{-15} m^2
Sediments 100×	S100	10^{-16}	10^{-27}	-3	Valley sediments: k = 10^{-14} m^2
Permeable Alpine Fault	PF	10^{-16}	10^{-27}	-3	N/A
Damage Zone	DZ	10^{-16}	10^{-27}	-3	Damage zone (≤1 km from Alpine Fault in hanging wall): k = 10^{-15} m^2
Cemented Zone	CZ	10^{-16}	10^{-27}	-3	Cemented zone (≤1 km from Alpine Fault in hanging wall): k = 10^{-17} m^2

Model Name (cont.)	**Abbreviation (cont.)**	**Hanging wall k (m^2) (cont.)**	**Footwall k (m^2) (cont.)**	**k cut-off (elevation, km) (cont.)**	**Additional features (cont.)**
-4 km Cut-off	CO-4	10^{-16}	10^{-27}	-4	N/A
-5 km Cut-off	CO-5	10^{-16}	10^{-27}	-5	N/A
Manning and Ingebritsen (-14, -3.2)	MI(-14,-3.2)	Depth ≥ 1 km: log(k) = -14-3.2log(depth, km); Depth < 1 km: log(k) = -14	10^{-27}	-3	N/A
Manning and Ingebritsen (-14, -2)	MI(-14,-2)	Depth ≥ 1 km: log(k) = -14-2log(depth, km); Depth < 1 km: log(k) = -14	10^{-27}	-3	N/A
Manning and Ingebritsen (-14, -4)	MI(-14,-4)	Depth ≥ 1 km: log(k) = -14-4log(depth, km); Depth < 1 km: log(k) = -14	10^{-27}	-3	N/A
Manning and Ingebritsen (-16, -3.2)	MI(-16,-3.2)	Depth ≥ 1 km: log(k) = -16-3.2log(depth, km); Depth < 1 km: log(k) = -16	10^{-27}	-3	N/A
Manning and Ingebritsen (-16, -2)	MI(-16,-2)	Depth ≥ 1 km: log(k) = -16-2log(depth, km); Depth < 1 km: log(k) = -16	10^{-27}	-3	N/A
Manning and Ingebritsen (-16, -4)	MI(-16,-4)	Depth ≥ 1 km: log(k) = -16-4log(depth, km); Depth < 1 km: log(k) = -16	10^{-27}	-3	N/A

Model Name (cont.)	Abbreviation (cont.)	Hanging wall k (m^2) (cont.)	Footwall k (m^2) (cont.)	k cut-off (elevation, km) (cont.)	Additional features (cont.)
Anisotropic 10×	A10	k_p = 10^{-16}; k_n = 10^{-17}	10^{-27}	-3	N/A
Anisotropic 100×	A100	k_p = 10^{-16}; k_n = 10^{-18}	10^{-27}	-3	N/A
Fully Uncoupled	UF	10^{-16}	10^{-27}	-3	Constant fluid density and viscosity
Density Uncoupled	UD	10^{-16}	10^{-27}	-3	Constant fluid density
Viscosity Uncoupled	UV	10^{-16}	10^{-27}	-3	Constant fluid viscosity

5.6.3 Model outputs

Model pore fluid pressure results are presented in terms of hydraulic head, h:

$$h = \frac{p}{\rho_a g} + z \tag{5.6}$$

Where ρ_a is water density under ambient surface conditions and z is the elevation (Table 5.1). This parameter is used to provide an indication of fluid pressure that is independent of water density variations between models, but is more amenable to graphical analysis than pressure itself, which increases by orders of magnitude with depth within a km scale system. In settings where fluid density variations are not significant, fluid flows down hydraulic head gradients. This is not necessarily the case where variable density is significant, as a result of the dependence of Darcy velocity on both head and density related terms:

$$\boldsymbol{q} = -\frac{\boldsymbol{k}\rho_a g}{\mu}\left[\nabla h + \left(\frac{\rho - \rho_a}{\rho_a}\right)\hat{\boldsymbol{n}}\right] \tag{5.7}$$

Cross-sectional profiles (Fig. 5.4, 5.5) are presented for selected models, with depth profiles available in supplementary information (see Supporting Information 5.11.3). In order to provide insights into the key variations in the three-dimensional temperature and hydraulic head field between all models, outputs are compared in terms of the following summarising metrics, which focus in particular on conditions near to the Alpine Fault and at measured locations:

1. The average down-dip temperature and hydraulic head gradient near to (250 m structurally above) the Alpine Fault, calculated between 0 km and -2 km elevation. Along-strike mean, maximum and minimum values for these gradients are presented (Fig. 5.6). The difference between maximum and minimum values gives an along-strike range.

2. The average vertical temperature and hydraulic head gradient in the hanging-wall (i.e. to 128 m depth) at DFDP-1B (Fig. 5.7). Due to local fault curvature, which is not reproduced by the planar model fault, the base of model hanging-wall is not at 128 m at the DFDP-1B site. Therefore the model borehole site is shifted slightly in the down-dip direction, so as to intersect the fault at 128 m depth.

3. The average vertical temperature and hydraulic head gradient across the full 818 m DFDP-2B drilled interval (Fig. 5.8). Gradients across the upper 128 m are also shown for comparison to DFDP-1B gradients (Fig. 5.7).

4. Temperatures and hydraulic heads at -1 km and -3 km elevation (Fig. 5.9) beneath a hypothetical observation point in the upper Whataroa valley, UWV (Fig. 5.3), where the Alpine Fault is deeper than -3 km elevation.

5. Maximum increase or decrease in elevation of the 100 °C isotherm to a peak or trough (stationary point) beneath the Whataroa valley, relative to a point at the valley margin (Fig. 5.10) along a cross-valley cross-section (Fig. 5.3), to indicate the degree of inflection of isotherms.

For all temperature and head gradients, positive values indicate increases in temperature or head with depth. Changes in all of these metrics are compared to the baseline model in a matrix of results (Fig. 5.11), in order to highlight patterns. Metrics are grouped into ‘shallow’ metrics, representing conditions at or above -1 km elevation (DFDP-1B and DFDP-2B gradients and conditions at -3 km elevation beneath UWV) and ‘deep’ metrics, representing conditions below -1 km elevation (mean, minimum, maximum gradients near to the fault and conditions at -3 km elevation beneath UWV). These different groups show different responses to changes in permeability in models. Metrics that quantify lateral variations between ridges and the valley are termed ‘along-strike variation’ metrics.

Away from the cemented rocks near to the fault the hydraulic head gradient at DFDP-1B is minimal (Fig. 5.2). Under these approximately hydrostatic conditions, the uncased borehole is unlikely to have caused significant hydraulic perturbation. The borehole head gradient (~0 $m \cdot km^{-1}$) is therefore assumed to represent ambient head gradient at DFDP-1 for the purposes of comparison to model outputs. In contrast, DFPD-2B, which was uncased to flow below 263 m depth, shows steep borehole hydraulic head gradients (Fig. 5.2). The borehole is therefore expected to have caused a hydraulic perturbation, meaning that measured borehole hydraulic heads are not equal to ambient hydraulic heads. To allow comparison of model results to borehole data, a radially symmetric nested model for the DFDP-2B borehole is employed to simulate borehole hydraulic heads (see Supporting Information 5.11.2). Ambient hydraulic heads

at the DFDP-2B site from the regional models presented are fixed at the outer boundary of the nested model, 100 m from the centre of the borehole.

5.7 Results

5.7.1 Common patterns

All models share a common pattern of groundwater flow into the valley from the ridges that bound it. Beneath the valley, groundwater flow is upward, whereas beneath the ridges downward flow prevails (Fig. 5.4). Model hydraulic heads initially increase sharply with depth beneath the valley, rising to a maximum, before decreasing with depth, except where water density is held constant (UF and UD) (Fig. 5.5). At the observation point in the Upper Whataroa valley (UWV), this is manifested in higher hydraulic heads at -1 km elevation than at -3 km elevation in all but the most permeable models, H-14 and MI(-14,-2) (Fig. 5.9).

Corresponding hydraulic head metrics and temperature metrics (e.g. mean temperature gradient and mean hydraulic head gradient near to the fault) largely show opposing changes relative to the baseline for a given permeability structure (Fig. 5.11). Where a temperature metric is increased, the corresponding head metric is generally decreased. This is almost always the case for deep (below -1 km elevation) metrics (mean, minimum, maximum gradients near to the fault and conditions at -3 km elevation beneath UWV). This relationship between hydraulic head and temperature variations reflects the influence of temperature dependent density and viscosity on fluid flow.

For homogeneous models where the permeability is $>10^{-17}$ m^2, isotherms are perturbed by the groundwater flow system, deviating upwards beneath the valley to shallower depths than beneath the ridges bounding it (Fig. 5.5, 5.10). In H-17 temperature contours show minimal perturbation by groundwater flow and are approximately parallel to topography in cross-valley cross-sections. The 100 °C isotherm is perturbed to a peak at higher elevation beneath the valley compared to beneath the valley margin in all models other than H-17 and MI(-16,-4) (excluding artificially uncoupled models) (Fig. 5.10). Although MI(-16,-4) does not show a peak in the 100 °C isotherm beneath the valley, the elevation of this isotherm relative to the valley margin is nonetheless perturbed upward in comparison to H-17.

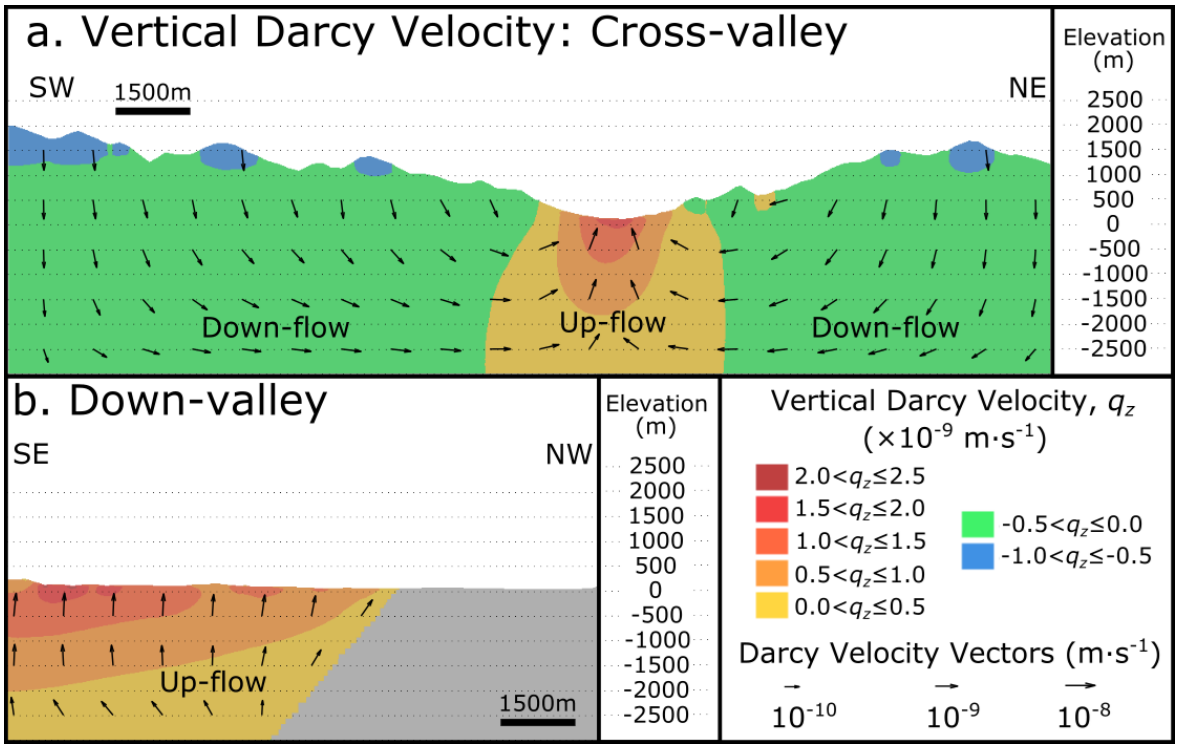

Figure 5.4 Darcy velocity in the baseline model (H-16) along cross-valley (a.) and down-valley cross-sections (b.). Beneath ridges flow is downward, with convergent up-flow in the valley. Darcy velocity vectors are shown at 1 km intervals.

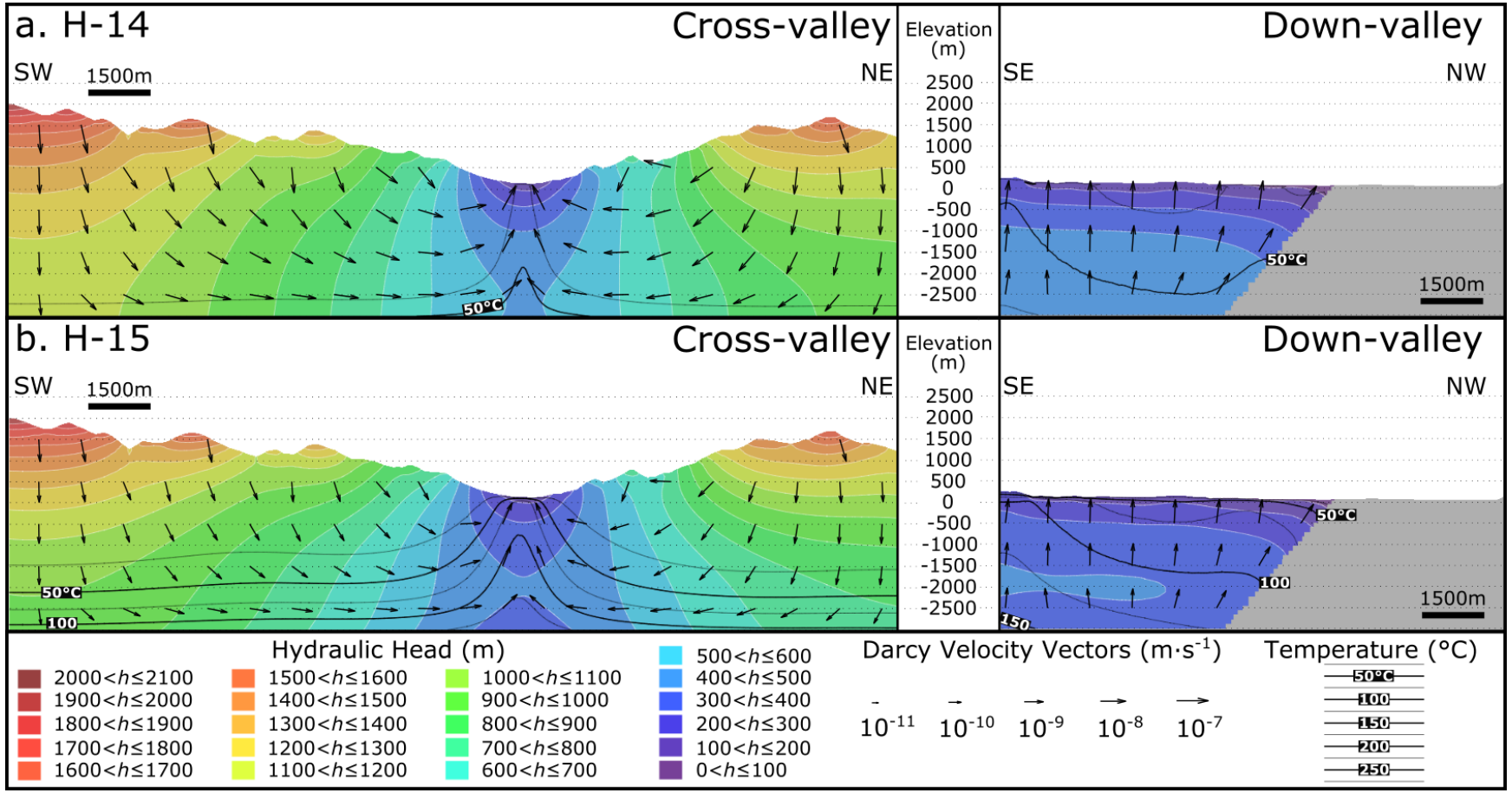

Figure 5.5 Caption and additional panels (5.5c. and 5.5d.) opposite.

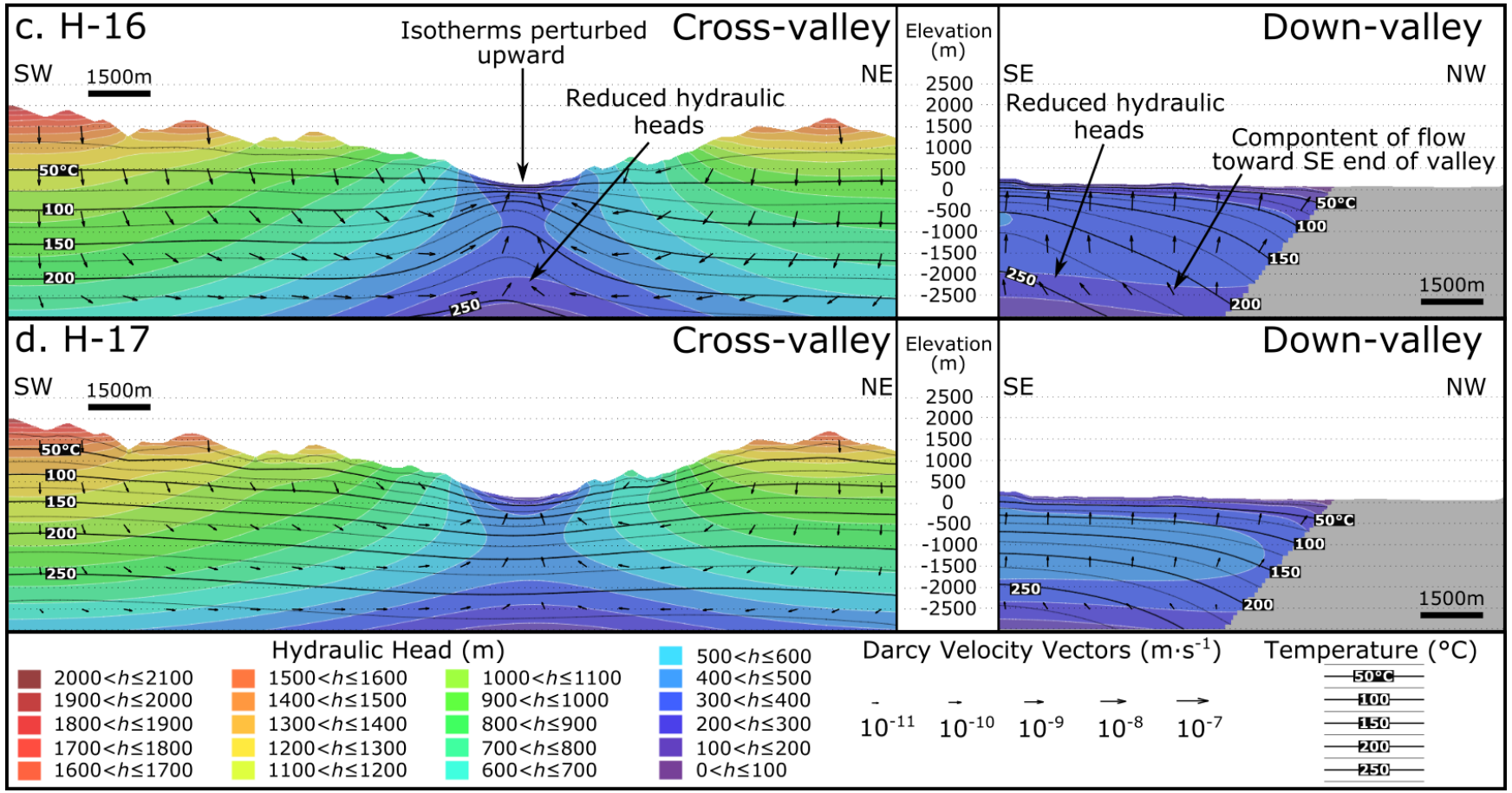

Figure 5.5 Additional panels (5.5a. and 5.5b.) opposite. Temperature isotherms and hydraulic head along cross-valley and down-valley cross-sections for with a range of models with homogeneous permeability above -3 km elevation from 10^{-14} m^2 (a.) to 10^{-17} m^2 (d.). Darcy velocity vectors are shown at 1 km intervals.

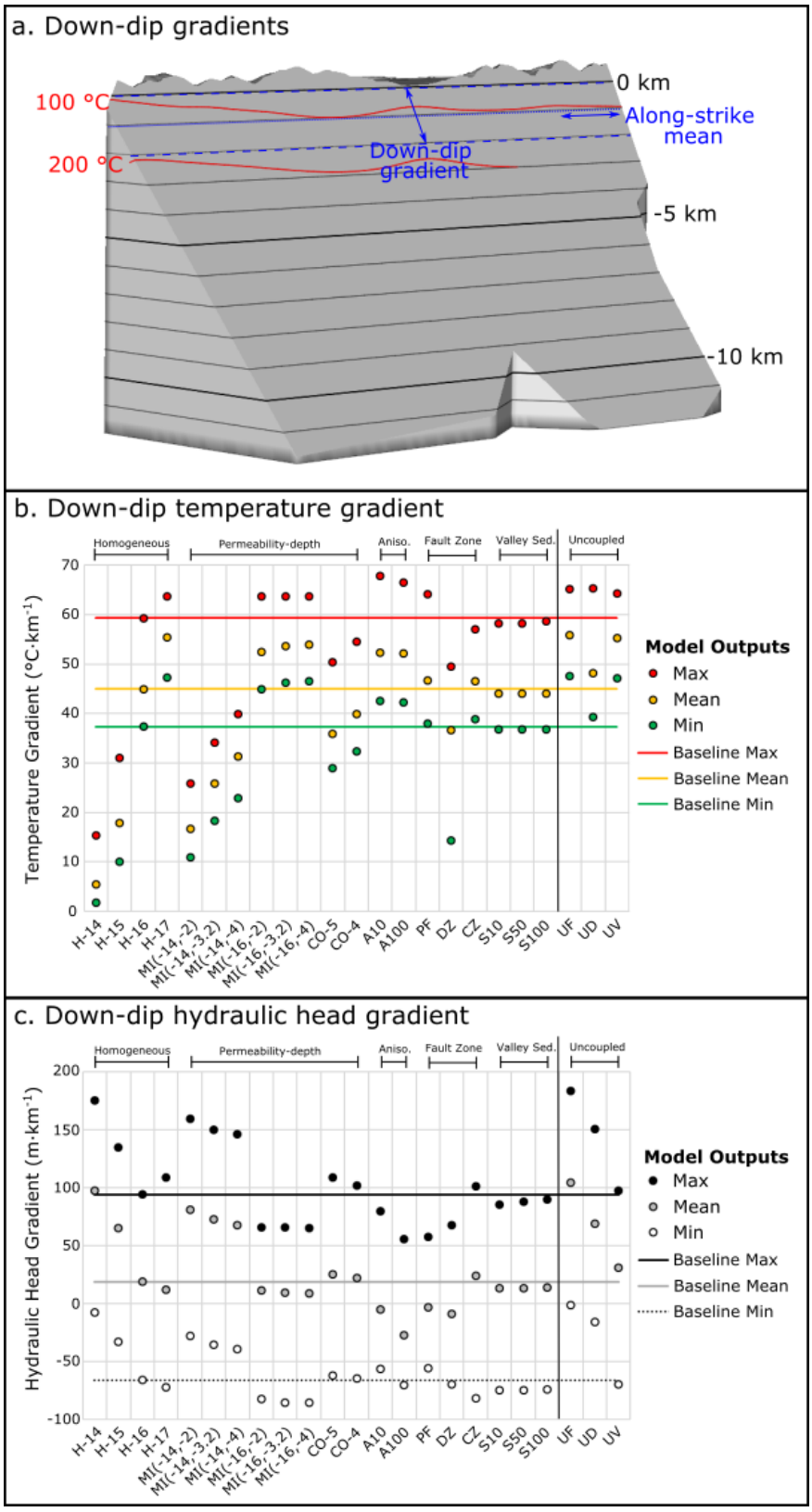

Figure 5.6 Down-dip gradients were calculated between 0 km and -2 km, within 250 m of the Alpine Fault (illustrated for temperature in a.), with along-strike mean, maximum and minimum values found for each model. Results are shown for temperature (b.) and hydraulic head (c.). Positive values for gradients represent down-dip increases.

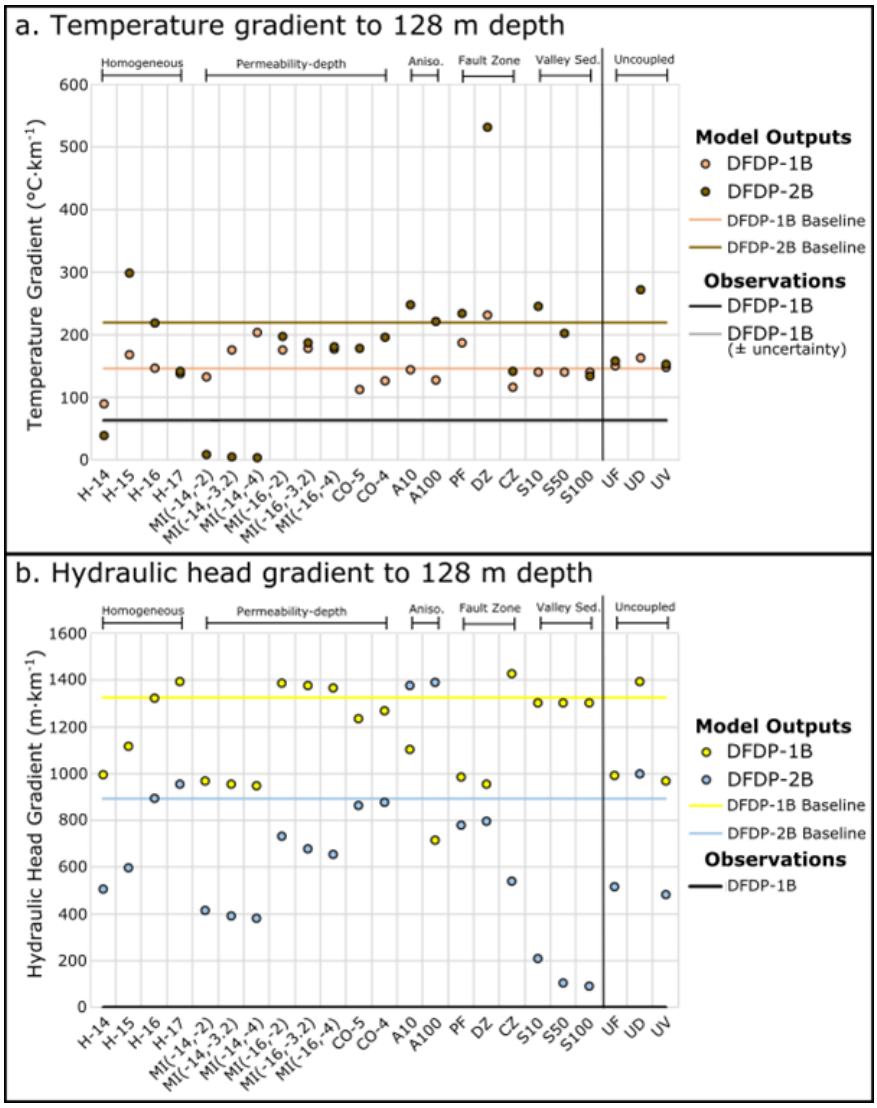

Figure 5.7 The average vertical temperature (a.) and hydraulic head (b.) gradient to the base of the hanging-wall (i.e. the Alpine Fault) at 128 m depth in DFDP-1B and to the same depth at DFDP-2B. Positive values for gradients represent increases with depth.

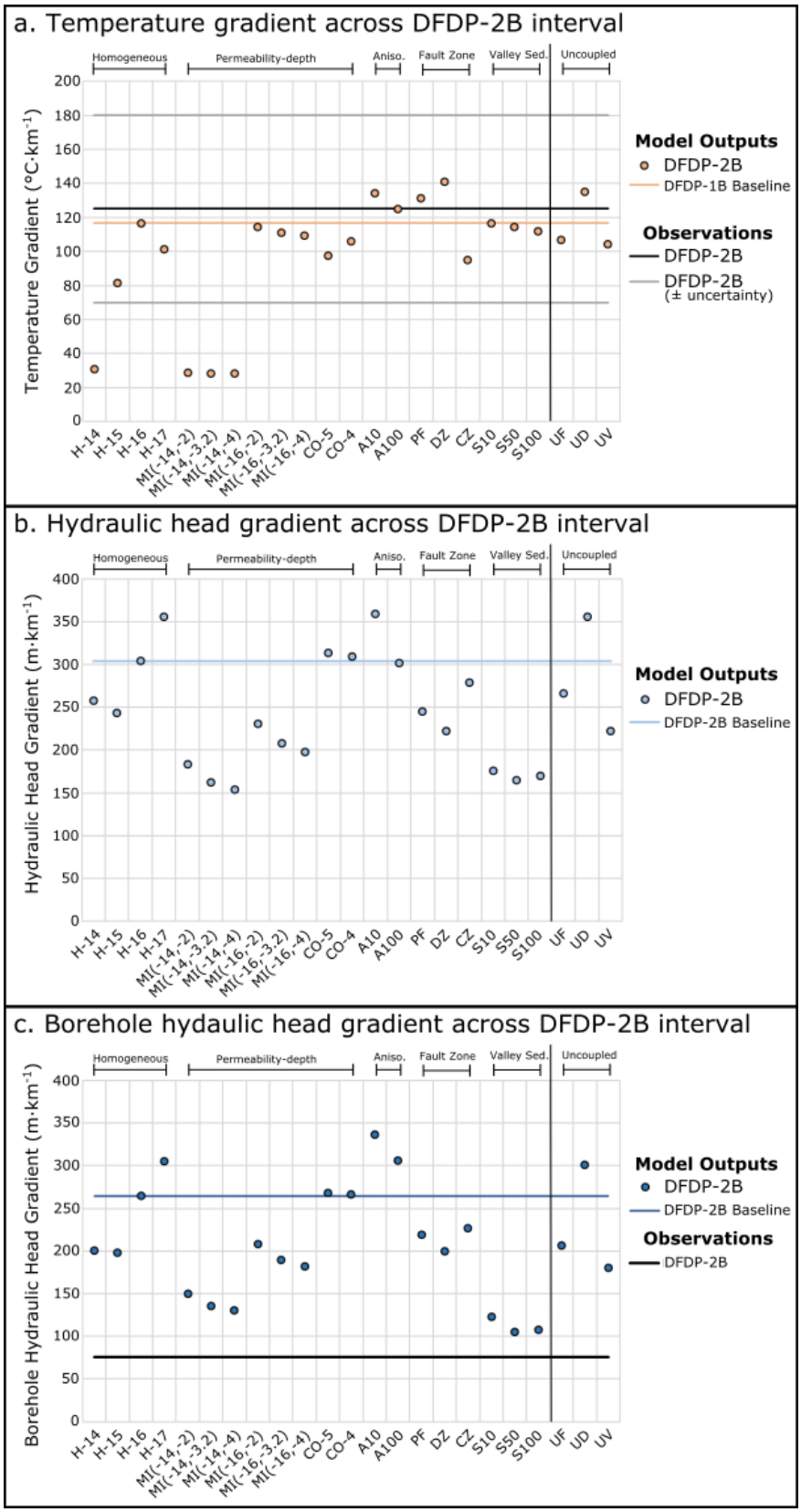

Figure 5.8 The average vertical temperature (a.) and hydraulic head (b.) gradient across the full DFDP-2B drilled interval. The gradient in borehole hydraulic heads (c.) is also simulated for comparison to DFDP-2B data using a nested model, assuming a fixed head at 100 m radius from the borehole, based on values from the regional model. Positive values for gradients represent increases with depth.

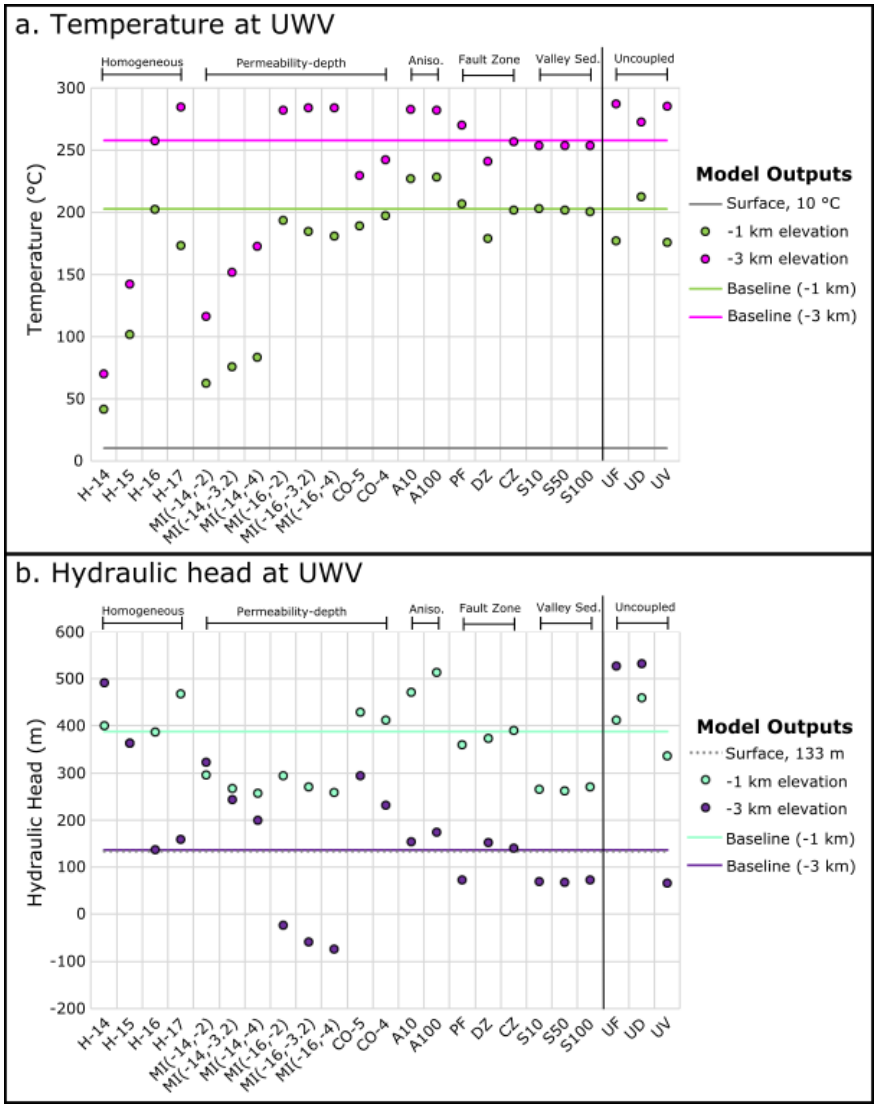

Figure 5.9 Temperatures (a.) and hydraulic heads (b.) at the surface, -1 km and -3 km elevation beneath an observation point (UWV) in the upper Whataroa valley (Fig. 5.3), where the Alpine Fault is deeper than -3 km.

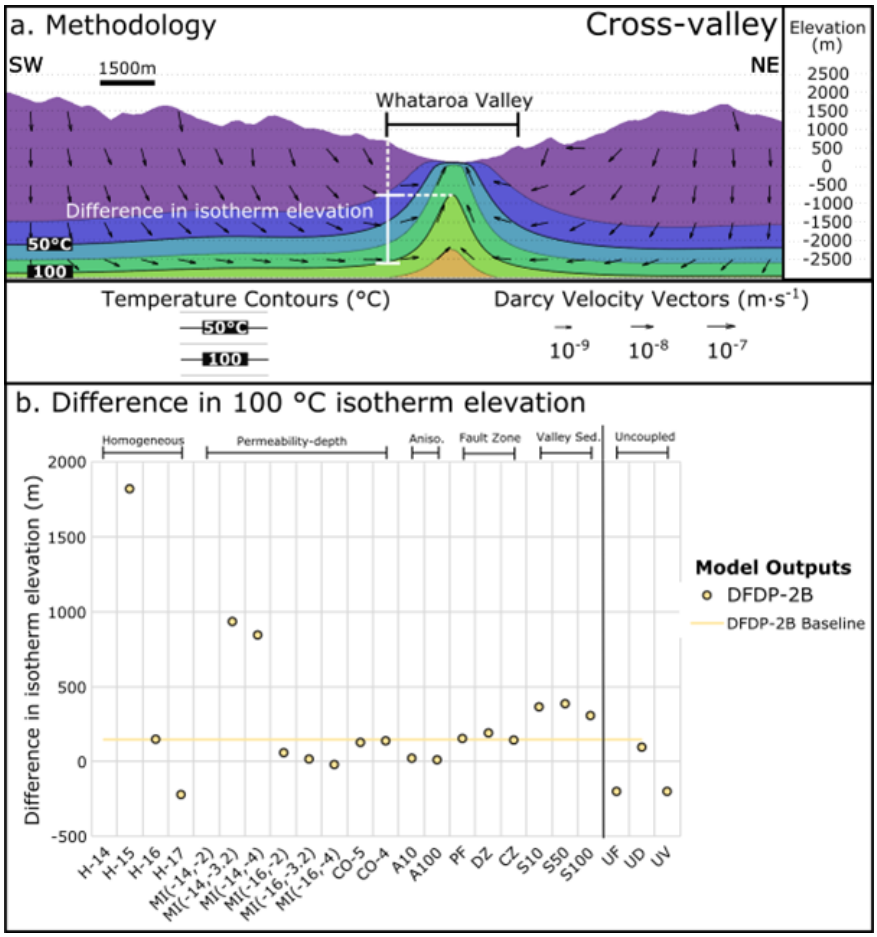

Figure 5.10 a. Differences in 100 °C isotherm elevation beneath the Whataroa valley are calculated relative to a designated point at the valley margin along the cross-valley cross-section (Fig. 5.3). Model H-15 is shown here as an example. b. Increase in isotherm elevation beneath the valley are plotted as positive values, decreases as negative. No values are plotted for H-14 or MI(-14,-2) as the 100 °C isotherm lies below -3 km elevation. Darcy velocity vectors are shown at 1 km intervals.

		Homogeneous				Permeability-depth								Anisotropy		Fault Zone			Valley Sediments			Uncoupled		
	Temperature Metrics	**H-14**	**H-15**	**H-16**	**H-17**	**MI (-14,-2)**	**MI (-14,-3.2)**	**MI (-14,-4)**	**MI (-16,-2)**	**MI (-16,-3.2)**	**MI (-16,-4)**	**CO-5**	**CO-4**	**A10**	**A100**	**PF**	**DZ**	**CZ**	**S10**	**S50**	**S100**	**UF**	**UD**	**UV**
'Deep' metrics (below -1 km elevation) Show clear systematic change with systematic changes in permeability	Mean Fault Gradient	-88	-60	0	23	-63	-43	-30	17	19	20	-20	-11	17	16	4	-19	3	-2	-2	-2	24	7	23
	Maximum Fault Gradient	-74	-48	0	7	-56	-42	-33	7	8	7	-15	-8	14	12	8	-17	-4	-2	-2	-1	10	10	8
	Minimum Fault Gradient	-95	-73	0	27	-71	-51	-39	20	24	25	-22	-13	14	13	2	-62	4	-2	-2	-1	28	5	27
	UWV (-3 km)	-73	-45	0	11	-55	-41	-33	10	10	10	-11	-6	10	10	5	-6	0	-1	-2	-1	11	6	11
'Shallow' metrics Show more complex changes with systematic changes in permeability	UWV (-1 km)	-79	-50	0	-14	-69	-63	-59	-4	-9	-11	-7	-2	12	13	2	-11	0	0	0	-1	-12	5	-13
	DFDP-1B Gradient (to 128m depth)	-38	15	0	-6	-9	21	39	21	22	21	-23	-14	-1	-12	28	59	-21	-4	-4	-4	3	12	1
	DFDP-2B Gradient (to 128m depth)	-82	37	0	-35	-96	-98	-98	-10	-15	-17	-19	-11	13	1	7	143	-35	12	-7	-39	-28	24	-30
	DFDP-2B Gradient (to 818m depth)	-74	-30	0	-13	-75	-76	-76	-2	-5	-6	-16	-9	15	7	13	21	-18	0	-2	-4	-8	16	-10
Along-strike variation metrics	Fault Gradient Range (Maximum-Minimum)	-38	-5	0	-25	-32	-28	-23	-15	-20	-22	-2	1	15	10	20	60	-17	-2	-2	0	-20	18	-23
	Isotherm Elevation Difference	N/A	1126	0	-248	N/A	529	468	-59	-86	-114	-12	-5	-83	-91	4	31	-1	145	159	106	-233	-33	-233
	Hydraulic Head Metrics	**H-14**	**H-15**	**H-16**	**H-17**	**MI (-14,-2)**	**MI (-14,-3.2)**	**MI (-14,-4)**	**MI (-16,-2)**	**MI (-16,-3.2)**	**MI (-16,-4)**	**CO-5**	**CO-4**	**A10**	**A100**	**PF**	**DZ**	**CZ**	**S10**	**S50**	**S100**	**UF**	**UD**	**UV**
'Deep' metrics (below -1 km elevation) Show clear systematic change with systematic changes in permeability	Mean Fault Gradient	419	247	0	-38	332	286	260	-40	-48	-53	35	18	-129	-244	-116	-148	29	-31	-31	-28	457	267	64
	Maximum Fault Gradient	87	43	0	15	70	59	56	-30	-30	-31	16	8	-15	-41	-39	-28	8	-9	-7	-4	95	60	4
	Minimum Fault Gradient	88	50	0	-10	57	46	41	-25	-29	-30	6	2	15	-7	15	-6	-23	-13	-13	-12	98	76	-5
	UWV (-3 km)	260	167	0	17	136	79	46	-117	-143	-154	115	70	13	28	-47	11	3	-49	-50	-46	286	290	-52
'Shallow' metrics Show more complex changes with systematic changes in permeability	UWV (-1 km)	3	-6	0	21	-23	-31	-34	-24	-30	-33	11	6	22	33	-7	-3	1	-31	-32	-30	6	19	-13
	DFDP-1B Gradient (to 128m depth)	-25	-16	0	5	-27	-28	-28	5	4	3	-7	-4	-17	-46	-26	-28	8	-2	-2	-2	-25	5	-27
	DFDP-2B Gradient (to 128m depth)	-43	-33	0	7	-53	-56	-57	-18	-24	-27	-3	-2	54	56	-13	-11	-39	-76	-88	-90	-42	12	-46
	DFDP-2B Gradient (to 818m depth)	-15	-20	0	17	-40	-46	-49	-24	-32	-35	3	2	18	-1	-20	-27	-8	-42	-46	-44	-13	17	-27
	DFDP-2B Borehole Head	-24	-25	0	15	-43	-49	-51	-21	-28	-31	1	1	27	16	-17	-25	-14	-54	-60	-59	-22	14	-32
Along-strike variation metrics	Fault Gradient Range (Maximum-Minimum)	14	4	0	13	17	16	16	-7	-6	-6	7	4	-15	-21	-29	-14	14	0	2	3	15	4	4

Row Minimum — Row Maximum

Figure 5.11 Caption overleaf.

Figure 5.11 (Overleaf) Compilation of metric values, presented in terms of percentage variation from the baseline model (H-16). Each row corresponds to a different metric and cells within each row are coloured according to value relative to the rest of the row. Cells for models with the largest positive variation from the baseline coloured red and those with the largest negative variation are coloured green.

Thus convergent flow into the valley occurs robustly over the range of modelled permeability structures and the advective upwelling of heat associated with this convergence is sufficient to perturb the temperature field across the majority of these structures. Therefore for the majority of models, the artesian, elevated temperature conditions encountered by DFDP-2B and evident at warm springs are a regional feature, and are predicted to occur along the length of the valley.

Although the broad patterns of groundwater and heat flow are consistent across a majority of models, absolute values of temperature and hydraulic head are sensitive to permeability structure. Mean down-dip temperature gradient near the fault (between 0 km and -2 km elevation) varies between 5 °C·km^{-1} and 55 °C·km^{-1} across the model permeability suite, with along-strike variability between maximum and minimum gradients ranging between 14 °C·km^{-1} and 35 °C·km^{-1}. Mean hydraulic head gradients vary even more significantly for different permeability structures, with some showing an overall increase in hydraulic head between the 0 km and -2 km elevation, whereas others show a decrease (Fig. 5.6). As gradients are averaged across this depth interval, values may approach nil where increases in hydraulic head with depth in the near-surface are cancelled out by decreases in head at greater depth.

Conditions at the location of the DFDP boreholes are also sensitive to permeability structure (Fig. 5.7, 5.8). Consequently, although fluid and heat flow patterns can be interpreted with relative confidence, uncertainty in permeability structure leads to considerable uncertainty in the absolute temperatures and pressures estimated.

5.7.2 Homogeneous regional permeability

Increases in homogeneous permeability values correspond to decreases in the deep (below -1 km elevation) temperature metrics (mean, minimum, maximum gradients near to the fault and conditions at -3 km elevation beneath UWV) (Fig. 5.11). The corresponding deep head metrics show increases as permeability is increased between H-16 and H-14. The change in these head metrics between H-17 and H-16 is mixed, with some metrics showing increases and others decreases.

The responses of shallow (at or above -1 km elevation) temperature and head metrics (borehole gradients and conditions at -1 km elevation beneath UWV) are more complex, showing neither systemic increases nor decreases across the modelled permeability range (Fig. 5.11). For example, temperature at -1 km elevation beneath UWV decreases relative to the baseline in both H-15 and H-17. Along-strike changes in temperature near the fault, indicated by the range between maximum and minimum gradients, shows a similar response, increasing with decreasing permeability up to H-16, before decreasing between H-16 and H-17 (Fig. 5.6).

Across all models the deep temperature metrics show more straightforward responses than the shallow metrics (Fig. 5.11). Where permeability is changed systematically across a sub-set of models, such as between homogeneous models, these deep metrics show systematic increases or decreases, which is often not the case for the shallow ones.

Of the homogeneous models, H-16 (the baseline) simulates the average temperature gradient across the DFDP-2B drilled interval closest to that observed along the borehole, with other homogeneous models producing lower gradients. Simulated borehole hydraulic head gradients for DFDP-2B are significantly higher than the observed gradient across all homogeneous models. Each homogeneous model, as well as all other models presented in this study, overestimates temperature and head gradients at DFDP-1B.

5.7.3 Permeability-depth relationship

Where the depth of permeability cut-off is shallower, (e.g. CO-4 compared to CO-5) deep temperature metrics are higher and corresponding head metrics lower, although changes from the baseline are relatively small compared to those for other permeability variations from the baseline (Fig. 5.11). Deep temperature metrics also increase and head metrics decrease where permeability is reduced more sharply with depth from MI(-14,-2) to MI(-14,-4) (Fig. 5.11). Although decreased permeability at depth within MI(-16) models results in increased deep temperature metrics and decreased head metrics relative to the baseline, increasingly rapid permeability reduction across the MI(-16) sub-set results in relatively minor further changes in these metrics between MI(-16,-2) and MI(-16,-4) compared to within the MI(-14) subset (Fig. 5.11). Some deep temperature metrics still show a clear systematic increase from MI(-16,-2) to MI(-16,-4), however others (e.g. maximum down-dip temperature gradient) show minimal change (change equivalent to ≤1 % of the baseline value). The along-strike range in temperature gradient near to the fault is decreased relative to the baseline in both MI(-14) and MI(-16) models. Increasingly rapid permeability reduction with depth causes the along-strike range in near-fault temperature gradient to increase in MI(-14) models, but decreases this range in MI(-16) models.

MI(-14) and MI(-16) models predict a decreased temperature gradient and borehole hydraulic head gradient at DFDP-2B relative to the baseline. As a result, these models' predictions are further from the observed temperature gradient but closer to the observed borehole hydraulic head gradient. CO-4 and CO-5 simulate gradients that are further from observed values for both borehole hydraulic head and temperature at DFDP-2B.

5.7.4 Regional anisotropy

Where permeability is decreased normal to foliation in anisotropic models, deep temperature metrics are increased and corresponding head metrics predominantly decreased, similar to the response of isotropic models to permeability decreases (Fig. 5.11). Notable differences between anisotropic models and H-17, which has isotropic permeability lower than the baseline model, are increased temperatures at -1 km elevation beneath UWV, an increased range in the near-fault temperature gradient and a decreased range in the near-fault hydraulic head gradient.

A10 simulates a temperature gradient at DFDP-2B that does not agree as well with the observed borehole value as that simulated by the baseline model, whereas A100 simulates a gradient that is in slightly better agreement with the observed value than the baseline model. Both predict higher borehole head gradients than the baseline and are there therefore further from the observed value. Although anisotropic models overestimate hydraulic heads and temperatures at DFDP-1B like other models, they are the only models that simulate a lower head gradient at DFDP-1B than across a similar depth interval at DFDP-2B.

5.7.5 Near-fault permeability

A permeable Alpine Fault (PF) has the effect of slightly increasing the mean value of the temperature gradient near to the fault as well as increasing its along-strike variation (Fig. 5.11). Head gradient near to the fault is reduced in terms of mean value and along-strike variation. Increased permeability near to the fault in the form of a damage zone (DZ) results in decreased temperature and head gradients near to the fault, with increased along-strike variation in temperature gradient and decreased variation in head gradient. This is in contrast to the pattern seen if homogeneous permeability is increased regionally from the baseline (e.g. H-15), which reduces along-strike variation in temperature gradient and increases along-strike variation in head gradient (Fig. 5.11). A cemented zone (CZ) has predominantly the opposite effect to a damage zone, slightly increasing mean temperature and head gradients near to the fault, reducing along-strike variation in temperature gradient and increasing along-strike variation in head gradient (Fig. 5.11).

The simulated temperature gradient across the DFDP-2B drilled interval is similar to the baseline in the PF model. It is increased relative to the baseline and the observed value in DZ and decreased in CF. In PF, DZ and CZ the predicted borehole hydraulic head gradient at DFDP-2B is lower than the baseline, but remains higher than the observed gradient.

5.7.6 Valley sediments

The presence of valley sediments in S10, S50 and S100 has the most localised influence of all permeability features investigated. These models show some of the strongest changes to hydraulic heads in the near-surface at DFDP-2B, greatly reducing hydraulic head gradients across the drilled interval (Fig. 5.11). However, the change in hydraulic head metrics away from the valley (e.g. at DFDP-1B) and at depth are much less significant. Thermal metrics show minimal deviation from the baseline model.

In models with valley sediments, the temperature gradient across the DFDP-2B intervals is similar to that predicted by the baseline model and to the observed value. These models also give a significantly reduced hydraulic head gradient across the DFDP-2B interval, closer to the observed value, indicating the importance of valley sediments in locally altering hydraulic head in the Whataroa valley.

5.7.7 Uncoupled models

Models in which viscosity is not thermally coupled (UF and UV) result in thermal structures significantly different from the baseline model, with isotherms approximately parallel to topography, rather than perturbed upwards beneath the valley (Fig. 5.10). In the model with only density uncoupled (UD), isotherms are perturbed to shallower depths beneath the valley relative to the ridges. All uncoupled models show increases in deep temperature metrics (Fig. 5.11).

5.8 Discussion

5.8.1 Regional fluid flow

The regional groundwater circulation regime provides the starting point for interpreting hydraulic head and temperature fields. The pattern of circulation with down-flow beneath ridges and convergent up-flow beneath the valley (Fig. 5.4), is consistent with that expected in a topographically driven flow regime. However, this does not preclude a role for buoyancy driven flow. The influence of density variations on flow vectors is evident in the presence of a component of flow toward the south-eastern end of the valley near the base of the groundwater

system in some models (e.g. Fig. 5.5c-d), which is absent in models where density is held constant (UF and UD). The significance of thermal buoyancy is discussed further subsequently. Convergent fluid flow is responsible for upward perturbation of isotherms to shallower depths beneath the valley across the majority of modelled permeability structures (Fig. 5.5). It also results in strongly artesian hydraulic heads along the length of the valley across all permeability structures. However, an understanding of the regional fluid flow regime alone is not sufficient for interpretation of the hydraulic head field where density contrasts are significant, as fluid pressures and hydraulic heads are influenced by temperature-dependent density. The study therefore begins with discussion of the temperature field prior to discussion of the hydraulic head field.

5.8.2 Temperature field

Differences in the temperature field between models reflect differing Darcy velocities. The consequences of increasing Darcy velocities can be considered in terms of a regional effect on vertical temperature contrasts across the groundwater system and a more local effect on temperature differences between ridges and valleys.

Regionally, groundwater circulation transfers heat from the base of the groundwater flow system to the surface. Increasing Darcy velocities in this circulation system therefore act to minimise the temperature contrasts between its base (-3 km elevation in the baseline model) and the ground surface, where temperature is fixed at 10 °C in all models. These decreased temperature contrasts associated with higher Darcy velocities are indicated by changes in deep temperature metrics- decreased temperatures at -3 km elevation at UWV (Fig. 5.9) and reduced mean down-dip temperature gradient near to the Alpine Fault (Fig. 5.8).

Increasing Darcy velocities also result in greater redistribution of the heat flowing into the groundwater system, locally increasing the total upward heat flux beneath valleys, where fluid flows upwards, relative to ridges, where fluid flows downwards. This produces the most significant contrast in lateral temperature distribution between models- the transition from a scenario in which isotherms approximately follow topography, to one in which isotherms are perturbed upwards beneath the valley, relative to the neighbouring ridges (Fig. 5.10). Only models with the latter isotherm structure produce significantly different near-surface (<128 m depth) temperature gradients beneath DFDP-2B in the Whataroa valley compared to DFDP-1B, which is at higher elevation on the valley flanks (Fig. 5.7). Because of the potential that this isotherm structure offers for variations in temperature gradient between ridges and valleys, it appears more consistent with the significantly higher temperature gradients measured in major

valleys (DFDP-2B, the Waiho valley borehole near Franz Josef) relative to those away from them (DFDP-1B). Upward perturbation of isotherms by groundwater near to the fault also becomes progressively more significant as permeability is increased (Fig. 5.5), producing higher simulated temperature gradients beneath DFDP-1B (closer to the fault) compared to DFDP-2B (more distal from the fault) where permeability is very high (H-14 and the MI(-14) model set, Fig. 5.10). However, the low geothermal gradient observed at DFDP-1B compared to DFDP-2B and the Waiho valley borehole and the absence of known warm springs that are not located within valleys suggest that any such perturbation of isotherms by groundwater up-flow near to the fault is much less significant than the perturbation beneath valleys.

For a temperature field with upward perturbed isotherms beneath major valleys in the Southern Alps, such as the Whataroa valley, hot springs represent a manifestation of significant widespread heat advection by groundwater. In this case, high heat fluxes associated with groundwater flow are not necessary limited to discrete locations, such as those above highly fractured zones with particularly high Darcy velocities, although such heterogeneities will tend to concentrate actual flow at particular points within this generalised up-flow. The existence of high temperature waters in the near-surface is likely to be masked by the large volumes of surface water flowing in rivers along major valleys in many localities.

The transition from isotherms that run approximately parallel with topography to those that are perturbed upward beneath the valley occurs between permeabilities of 10^{-17} m^2 and 10^{-16} m^2 in homogeneous models (Fig. 5.5). It is shown below that this is consistent with the conclusion that may be drawn from calculations based on a simplified version of the system. For the purposes of these calculations Darcy velocities are calculated based on a lateral hydraulic head gradient, which is assumed to approximate to the topographic gradient in the orogen. Buoyancy is neglected, and water viscosity and heat fluxes are based on the average temperature within homogeneous models from this study.

In this simplified case (Fig. 5.12), between permeability values of 10^{-17} m^2 and 10^{-16} m^2, the interval over which isotherm structure changes in models, the heat flux associated with groundwater flow becomes of comparable magnitude to that associated with simplified one dimensional uplift equivalent to 12 $mm \cdot yr^{-1}$ dip slip, from 12 km depth at 400-600 °C, based on the models of Allis et al. (1979) for the Southern Alps.

Changes in advective heat transport between models also result in differences in the along-strike temperature variation near the Alpine Fault, indicated by the changing range between maximum and minimum down-dip temperature gradients (Fig. 5.6a). Decreasing average temperature in the model domain acts to reduce the magnitude of along-strike variation, while increasing advection

of heat from ridges to valleys increases the potential for variation. The degree of along-strike variation in temperature at the Alpine Fault is significant as it may result in lateral variation in the frictional properties of fault rocks and therefore produce different deformational behaviour on ridge and valley sections of the fault (Sutherland et al., 2017).

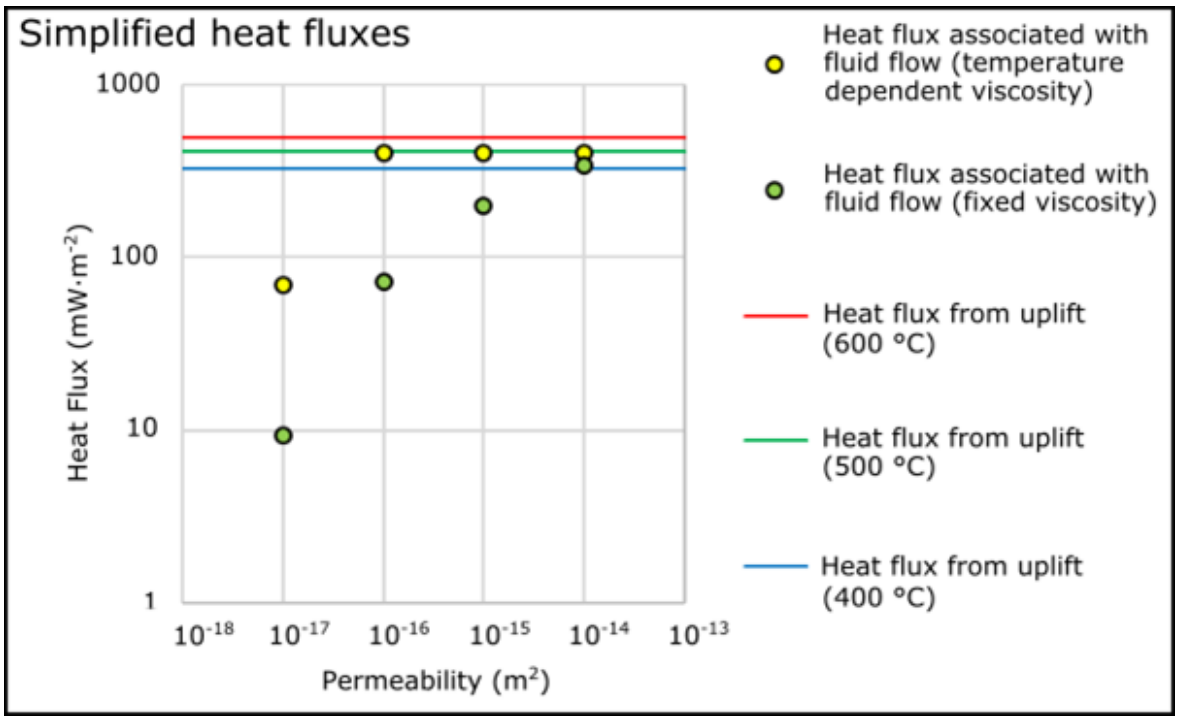

Figure 5.12 Comparison of heat fluxes associated with fluid flow and uplift based on scaling calculations. Heat fluxes associated with fluid flow are calculated based on flow driven by a hydraulic head gradient equal to approximate topographic gradient, 0.2, at an average temperature in the corresponding homogeneous FEFLOW model, neglecting buoyancy. Values for constant viscosity at 10 °C and for temperature dependent viscosity are shown. Heat fluxes from uplift are calculated based on one-dimensional uplift of rocks at 400-600 °C from 12 km to the surface at 10 °C after Allis et al. (1979).

5.8.3 Hydraulic head (fluid pressure) field

In shallow aquifers with minimal density contrasts, fluid flow occurs down hydraulic head gradients. For topographically driven flow in such a system, hydraulic head will decrease with depth beneath ridges and increase with depth beneath valleys (Tóth, 1962, 1963). For models in this study, in which density contrasts are simulated, hydraulic heads increase with depth to a peak value beneath valleys, before decreasing with depth. The transition from increasing hydraulic head to decreasing hydraulic head with depth is a reflection of density reduction with increasing temperature. Plots of hydraulic head, based on a one-dimensional analytical solution for a vertical

profile with a linear geothermal gradient, indicate how such decreases in hydraulic head occur with depth, as a result of decreasing density (Fig. 5.13).

The broad inverse correlation between values for corresponding temperature and head gradients across the models of the study indicates the importance of temperature in modifying hydraulic head via changes in density throughout the model domain, including near to the fault.

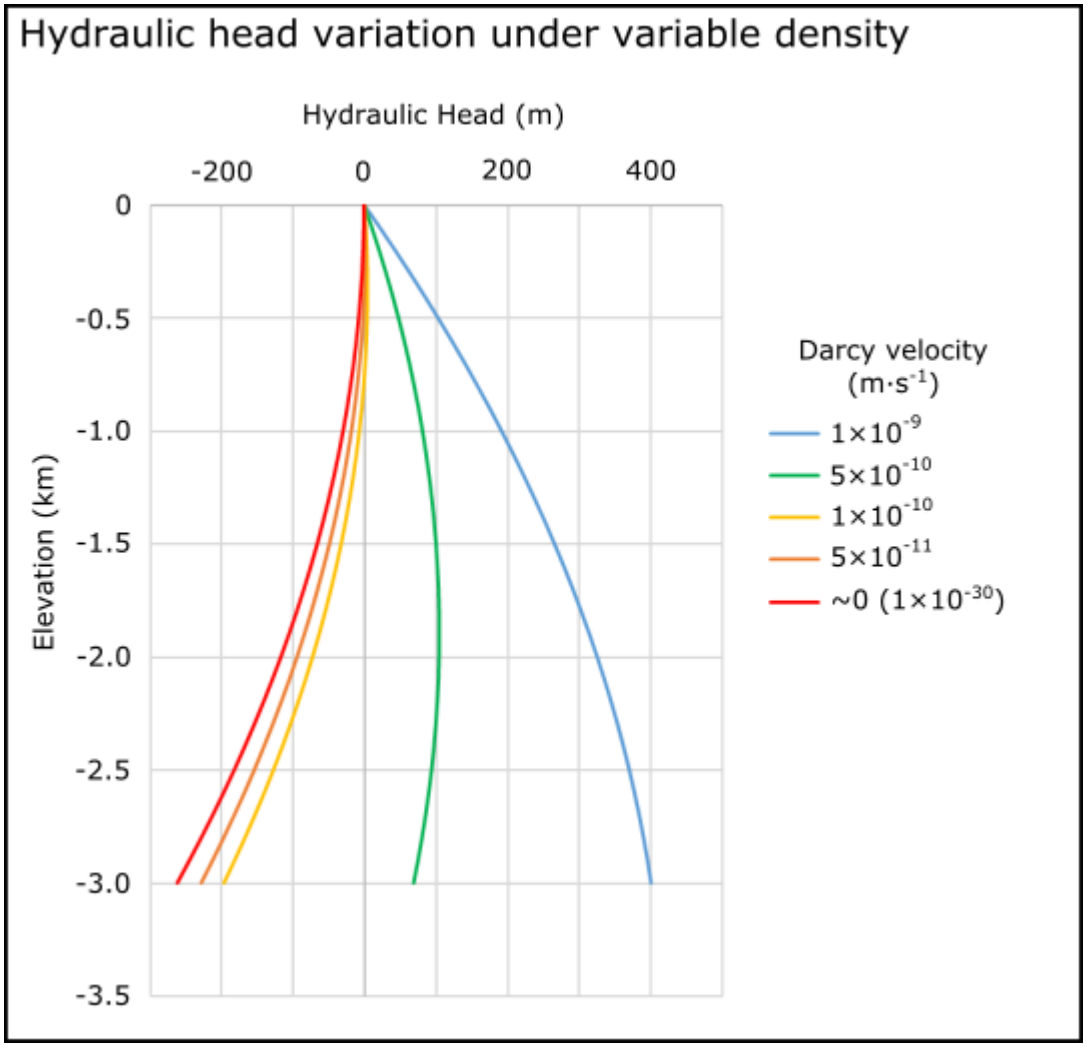

Figure 5.13 Results for an analytical solution for variation of hydraulic head with depth along a profile along which Darcy velocity is constant, temperature varies linearly with depth with a gradient of 80 °C·km^{-1} and viscosity and thermal expansion coefficient are assumed constant at 2.16 × 10^{-4} Pa·s and 7 × 10^{-4} °C^{-1} respectively (see Supporting Information 5.11.4 for details).

Hydraulic heads near to the fault reflect the variations in flow between ridges and valleys. They are also influenced by the extent to which the fluid flow regime varies with distance from the fault and to which it modifies the temperature field near to the fault. For all models the groundwater flow system produces increases in near-fault head between 0 km and -2 km on some sections of

the fault and decreases on others, reflected in positive maximum and negative minimum hydraulic head gradients.

Pore fluid factor, the ratio of fluid and lithostatic pressures, provides a quantification of the potential of fluid pressures to reduce effective confining stress. Under a hydrostatic gradient, assuming constant densities of approximately 1000 $kg \cdot m^{-3}$ for water (Lemmon et al., 2017) and 2700 $kg \cdot m^{-3}$ for rock (Tenzer et al., 2011), the pore fluid factor is 0.37. Beneath ridges hydraulic head decreases with depth in models, indicating increases in pore fluid pressure below the surface density hydrostat and lower pore fluid factors. In the shallow subsurface beneath valleys, increasing heads with depth indicate increases in fluid pressure above the surface density hydrostat, resulting in pore fluid factors >0.37, and consequently weaker fault rocks than under a hydrostatic gradient.

Borehole hydraulic heads in DFDP-2B, representing a lower bound for ambient hydraulic heads due to the perturbation associated with the borehole, indicate pore fluid factors of >0.39. However as models predict that hydraulic head is likely to peak and then decrease with depth beneath valleys, great caution should be taken in extrapolating any super-hydrostatic pore fluid factors indicated by borehole hydraulic head gradients, such as those at DFDP-2B, beyond the interval of measurement. It is possible that significantly higher pore fluid pressures than those indicated by this study, which considers the shallow steady state flow regime, may occur as a result of temporal changes such as porosity reduction through the seismic cycle of the Alpine Fault. Significantly elevated pore fluid pressures are also to be anticipated in the ductile crust, below the shallow flow regime modelled in this study. Near lithostatic fluid pressures are typical in crustal rocks below the brittle-ductile transition (Coombs, 1993; Etheridge et al., 1983; Fyfe et al., 1978; Norris and Henley, 1976), as a result of the collapse of porosity in ductile rocks (Ague, 2003). However in the brittle crust, under a steady state flow regime, ratio of fluid pressure to lithostatic pressure is expected to be highest in the region of shallow crust where hydraulic head increases with depth (above approximately -1 km elevation in the baseline model). Below this region reductions in fluid density with depth will decrease pore fluid factors and reduce the effect of fluid pressure on effective confining stress.

5.8.4 Drivers for groundwater flow

In considering the drivers for groundwater flow, it is useful to consider Darcy's Law in terms of reduced pressure, p_r, which represents the difference between hydrostatic pressure, p_h, (based on mean groundwater density in the domain of fluid flow, ρ_m) and total pressure, p (Phillips, 2009). In this case:

$$p_r = p - p_h \tag{5.8}$$

$$\boldsymbol{q} = -\frac{\boldsymbol{k}\rho_m}{\mu}\left(\frac{\nabla p_r}{\rho_m} + b\hat{\boldsymbol{n}}\right) \tag{5.9}$$

$$b = \left(\frac{\rho - \rho_m}{\rho_m}\right) g \tag{5.10}$$

Where b is buoyancy, a body force per unit mass. Both $\nabla p_r/\rho_m$ and b have units of acceleration ($m \cdot s^{-2}$). Thus the vertical component of Darcy velocity, q_z is:

$$q_z = -\frac{k_z \rho_m}{\mu}(r + b) \tag{5.11}$$

$$r = \frac{\partial p_r/\partial z}{\rho_m} \tag{5.12}$$

Where k_z is the permeability in the vertical axis and r is the reduced pressure driven component of vertical flow.

The UD model with no density coupling shows upward perturbation of isotherms beneath the valley, similar to its coupled equivalent (Fig. 5.10), indicating that the existence of groundwater flow rates sufficiently high to perturb the temperature field is not dependent on density driven flow. The effects of density driven flow are however not negligible. All deep and shallow temperature gradient metrics are increased in UD relative to the baseline, indicating reduced advective heat transport. Comparison of the magnitudes of the buoyancy term and reduced pressure terms in Eq. 5.11, reveals that not only is the buoyancy term of comparable magnitude to the reduced pressure term across much of the orogen, but is also the larger driver for flow across regions beneath the Whataroa valley and its margins (Fig. 5.14).

The subsurface may be split into regions in which vertical reduced pressure driven (r) and buoyancy driven (b) components to flow act in the same direction, constructively reinforcing one another and regions in which they have opposing direction (Fig. 5.15). Beneath ridges both buoyancy and reduced pressure driven components to flow are downward. At intermediate depth beneath the valley both are upward. However, above and below this zone these components have opposing orientations, with upward buoyant flow at depth and retardation of up-flow by this density driven component in the shallowest portion of the valley.

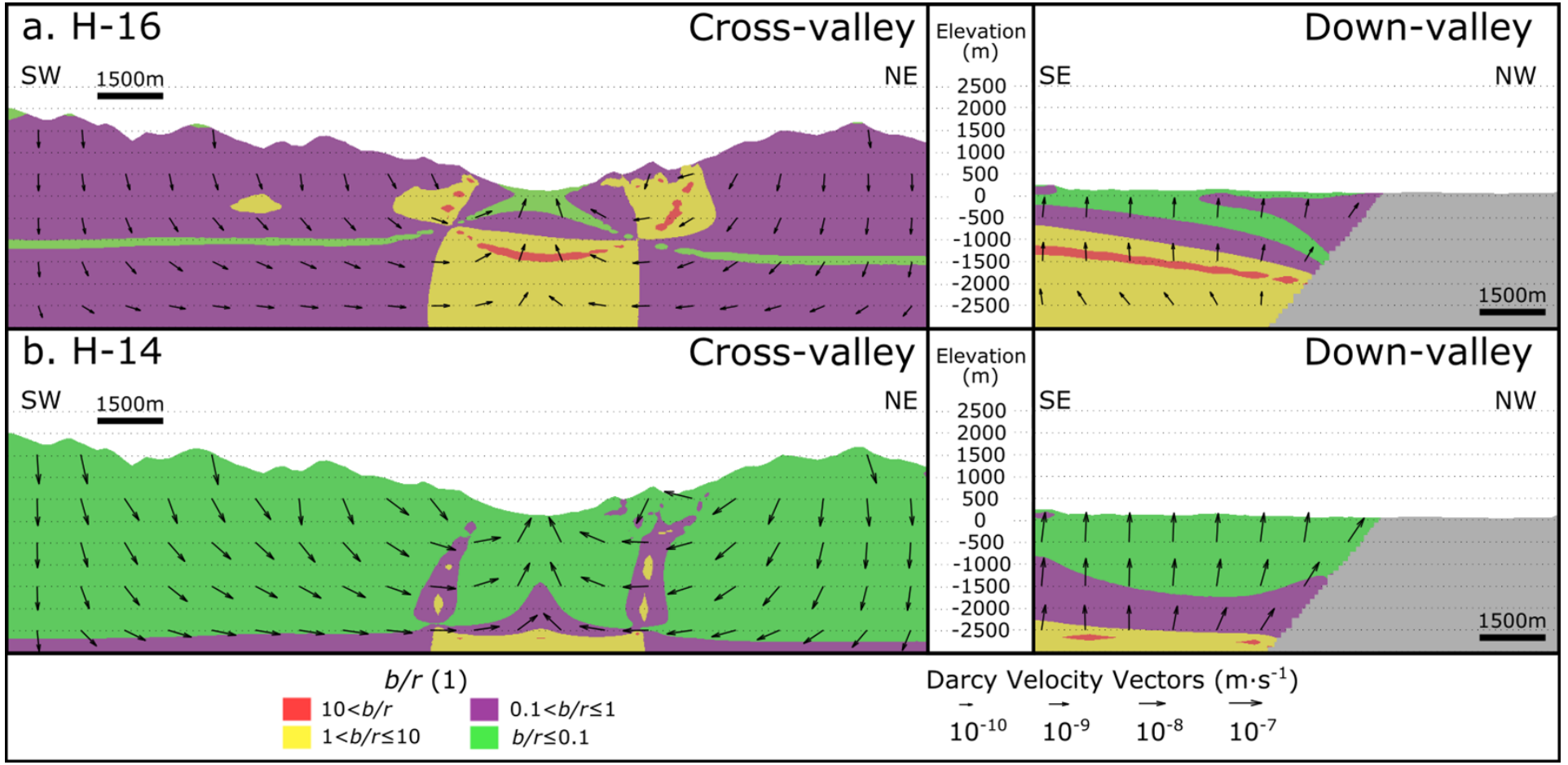

Figure 5.14 Ratio of the buoyancy driven component of vertical Darcy velocity to the reduced pressure driven component, for the baseline (H-16) model (a.) and H-14 model (b.). Darcy velocity vectors are shown at 1 km intervals.

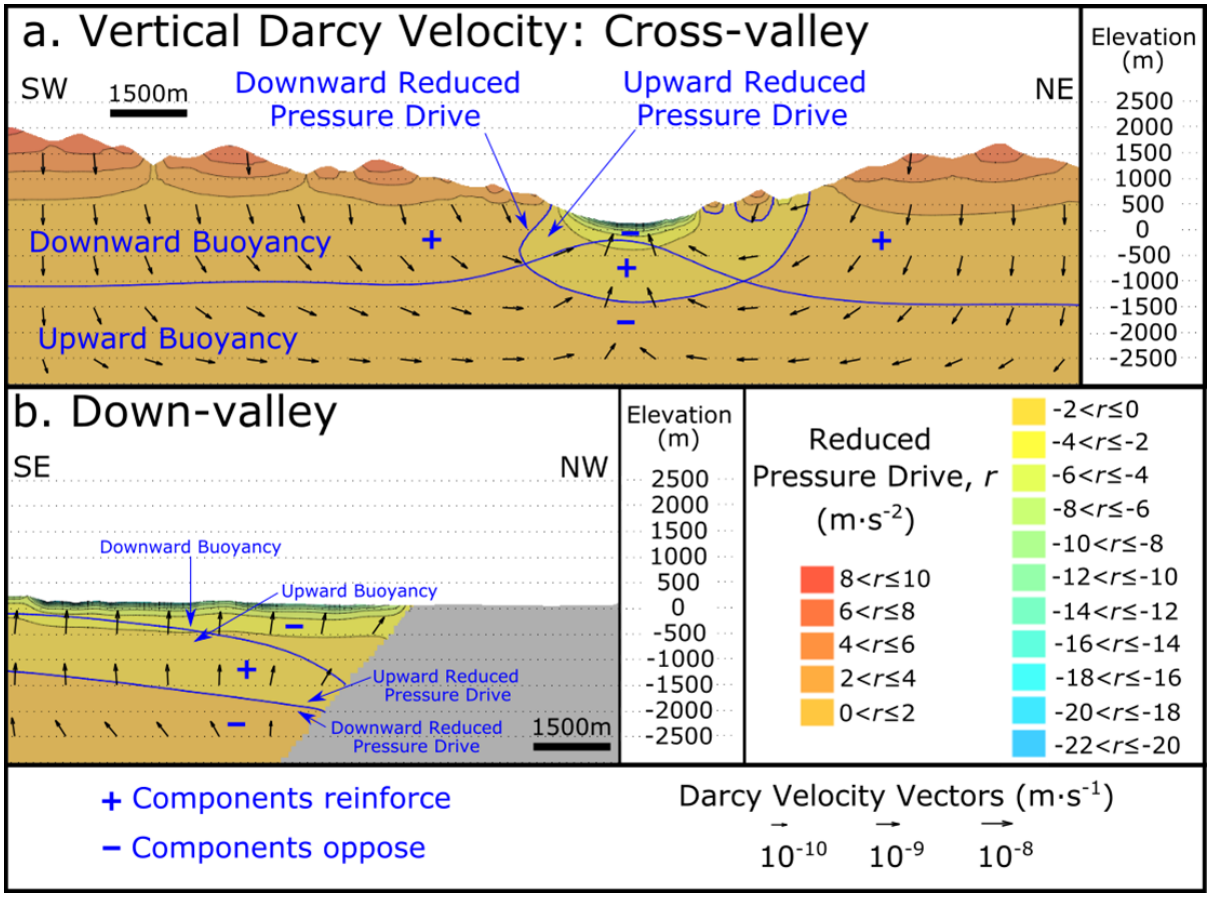

Figure 5.15 Comparison of the directions of reduced pressure and buoyancy driven components of flow in the baseline model (H-16) for cross-valley (a.) and down-valley (b.) sections. The subsurface is split into regions in which the components driving vertical flow, reduced pressure, r, and buoyancy, b, act in the same direction and in opposing directions. Darcy velocity vectors are shown at 1 km intervals.

5.8.5 Role of viscosity

The significantly different results produced by models with uncoupled viscosity, UV and UF, indicate that the temperature dependence of viscosity is significant for modelling of fluid and heat flow in the Southern Alps. These models have a different thermal structure to the baseline model, in which isotherms are not raised to higher elevations beneath the Whataroa valley (Fig. 5.10b). In contrast, isotherms are approximately parallel to topography, similar to lower permeability models (eg. H-17 shown in Fig. 5.5d). Greater vertical temperature contrasts across the permeable region of the UV model, indicated by an increase in deep temperature metrics, reflects reduced advective heat transport in this model.

In keeping with the result of the UV model, a basic fluid and heat flux calculation (Fig. 5.12), based on the assumptions outlined in section 5.8.2, but with fixed rather than temperature dependent

viscosity, indicates heat flux associated with groundwater flow of the order of 10 $mW \cdot m^{-2}$ for permeability of 10^{-16} m^2. This is significantly lower than that associated with uplift, which is of the order of 100 $mW \cdot m^{-2}$. A model that does not include the temperature dependence of water viscosity can therefore result in an underestimate of Darcy velocities and heat transport by groundwater flow. This is because Darcy velocity is inversely proportional to water viscosity (Eq. 5.9), which decreases sharply with temperature. Viscosity is about 5 times lower at 110 °C than at 10 °C. This decrease in viscosity, which is much greater than the decrease in density (~1.05 times) over this temperature interval, results in flow rates are nearly five times higher for a fixed permeability system at 110 °C compared to 10 °C, in this simplified calculation.

Thus, fluid and heat flow are strongly coupled because of the temperature dependence of viscosity, in addition to the influence of buoyancy on groundwater flow. Rock advection not only transports heat into the shallow system, where Darcy velocities are high enough to transport significant heat, but also increases Darcy velocities by raising average temperatures there. This promotes perturbation of the temperature field by fluid flow. The increase in Darcy velocities for meteoric water circulation also means that fluxes of these fluids will remain significant to greater depths (Chapter 2) and will aid penetration of discernible quantities of these fluids to the brittle-ductile transition in the orogen (Menzies et al., 2014). Were uplift rates to decrease over geological time with permeability remaining unchanged (for example following a transition to purely strike-slip displacement), not only would the total heat flux in the orogen be expected to drop, but also the proportion of this flux transported by groundwater flow. The depth of penetration of the shallow flow system and the amount of meteoric fluid reaching the brittle-ductile transition would also be likely to decrease as a result. Reduced topographic elevations might also be expected to contribute to this decrease.

5.8.6 Homogeneous regional permeability

Because differences in hydraulic head between models largely correlate with changes in temperature, reflecting changes in density, discussion is restricted to the effects of different permeability structures on temperature, except where additional discussion of hydraulic head response is merited. As hydraulic head is fixed at the model surface, decreasing homogeneous permeability has the effect of reducing average Darcy velocities. The changing temperature field across the homogeneous model set reflects the two large scale changes as permeability and Darcy velocities increase; 1) the reduction in temperature contrast between at the base of the shallow flow system and the surface, and 2) the increase in shallow temperatures beneath ridges relative to valleys. Deep temperature metrics decrease with permeability reflecting the first of these changes. Shallow temperature metrics reflect an interplay between the overall temperature

decrease and relative temperature increase in valleys associated with higher permeability. For example temperature at -1 km elevation beneath UWV decreases in both H-15 and H-17 relative to the baseline. In the case of the H-15, this decrease can be understood in terms of cooling of the system as a whole by more vigorous fluid flow. In the case of H-17, it can be understood in terms of decreased upward perturbation of isotherms beneath the valley by fluid flow. The changes in along-strike variation in temperature near the fault also show a similar response, decreasing in H-15 as a result of a decrease in the average temperature of the model and decreasing in H-17 as a result of decreased along-strike variation in heat flux.

Across much of the homogeneous model set (H-16 to H-14), falls in the values of all deep temperature metrics are accompanied by rises in the values of all deep head metrics as model permeability is increased. These opposing responses of deep temperature and head metrics can be understood as being concomitant with increases in water density resulting from widespread decreases in temperature. Although all deep temperature metrics also decrease between H-17 and H-16, the response of deep head metrics is mixed, with some showing increases and others decreases. The reason for this can be understood by considering the contrast in isotherm structure between H-17, which shows no significant perturbation of isotherms by groundwater and the higher permeability homogeneous models, in which isotherms are perturbed to shallower elevations beneath the valley compared to beneath the bounding ridges. Although deep temperature metrics are highest in H-17, temperatures beneath the valley in some shallower parts of the model (e.g. -1 km below UWV) are lower than in H-16. These lower shallow temperatures and associated higher water densities contribute to higher heads in some deeper parts of the H-17 model compared to H-16.

5.8.7 Permeability-depth relationship

Where permeability is decreased systematically with depth, average permeability and therefore Darcy velocities are reduced, resulting in a similar response to decreasing the homogeneous permeability, namely increased vertical temperature gradients across the shallow portion of the model where fluid flow takes place and decreases in isotherm elevations beneath valleys relative to ridges. However, as permeability is reduced, heat advection by groundwater becomes less significant and further decreases in permeability begin to have little effect. This is evident in MI(-16) models, in which some deep temperature metrics show little change with increasingly rapid permeability reduction with depth from MI(-16,-2) to MI(-16,-4).

With respect to the full model domain to -12 km elevation, models with a shallower permeability cut-off also have reduced average Darcy velocities compared to those with a deeper permeability

cut-off. The permeability cut-off, in effect, produces a transition to Darcy velocities of 0 $m \cdot s^{-1}$ below it. As a result, decreasing depth of permeability cut-off also results in higher values for deep temperature metrics.

5.8.8 Regional anisotropy

In anisotropic models, reduction in foliation-normal permeability results in increases in the deeper temperature metrics relative to the isotropic baseline. These models show higher temperatures at -1 km elevation at UWV than any other models. This is consistent with decreased down-valley heat transport by fluid flow as a result of the foliation-parallel anisotropy, which trends approximately perpendicular to the valley.

5.8.9 Near-fault permeability

The PF model, in which there is no permeability change associated with the model Alpine Fault, shows an increase in along-strike variation of the near-fault temperature gradient and a slight increase in the mean value of this gradient, relative to the baseline model. The increase in along-strike variation can be attributed to increased Darcy velocities and associated advective heat transport in the footwall in the PF model, as a result of the absence of an impermeable Alpine Fault. The slight increase in the mean value of the near-fault temperature gradient reflects that vertical Darcy velocities are not increased throughout the model, but rather are reduced in parts of the hanging wall. This occurs because water entering the model in the hanging wall may flow laterally and leave the model from the footwall, rather than flowing back to the surface elsewhere within the hanging wall in this model.

In the DZ model, the reduced near-fault temperature gradient can be understood in terms of increased Darcy velocity in the damage zone, reducing temperature contrasts between the surface and the base of the groundwater flow system along the fault zone. Increased Darcy velocities in the damage zone also result in increased variation in heat flow between ridges and valleys, resulting in increased along-strike temperature variation. In this model, the increase in along-strike variation is more significant than the overall decrease in shallow temperatures, which reduces along-strike variability where permeability is increased above the baseline in homogeneous models (e.g. H-15). The CZ model shows the opposite to DZ, with decreased Darcy velocities in the cemented zone resulting in a slight increase in mean temperature gradient and decreased along-strike variation. A lower mean near-fault hydraulic head gradient in the DZ model and a higher mean gradient in the CZ model do not reflect the changes in temperature dependent density associated with these models, indicating that in this case, changes in density

are less significant in controlling hydraulic head than other terms in the fluid flow equations, such as permeability.

5.8.10 Valley sediments

Valley sediments, which are assumed to have relatively high permeability, reduce absolute hydraulic head values at depth. This results in a reduced hydraulic head gradient across the DFDP-2B drilled interval and reduced hydraulic heads at -1 km elevation beneath UWV. However, their influence on hydraulic head is localised to the valley and their influence on temperature is also minimal. As a result they have a much smaller influence on near-fault conditions that other permeability features modelled. The relative insensitivity of local temperature to the presence of valley sediments relative to hydraulic head, reflects the different relationships of hydraulic head and temperature to permeability. For example, considering, for simplicity, a scenario where Darcy velocity is constant, hydraulic head gradient will increase in proportion to permeability, neglecting changes in density and viscosity, whereas temperature will remain unchanged. This is because it is Darcy velocity, not permeability that features in the conservation of energy equation.

5.8.11 Determining permeability structure

The low borehole hydraulic head gradient in the upper portion (≤273 m depth) of DFDP-2B indicates the potential significance of high permeabilities in this section of the drilled interval. This is supported by the reduction in borehole hydraulic head gradient across the DFDP-2B drilled interval, toward observed values, which occurs where low permeability sediments are introduced into models (Fig. 5.8). Given the persistence of a low hydraulic head gradient to 273 m depth, below the base of the sedimentary succession (240 m depth) at DFDP-2B, high permeabilities appear likely to extend into the uppermost basement rocks, potentially reflecting a heavily weathered or fractured zone near to the topographic surface at the time of basal sediment deposition. As is shown in section 5.7.10, although valley sediments may have a strong influence on conditions at DFDP-2B, their regional influence is relatively minor compared to other permeability features. Features such as systematic decreases in permeability with depth, the presence of a damage zone or cemented zone and a fault plane that is permeable to flow also have some potential to lower the modelled borehole head gradient at DFDP-2B. In addition to high permeability sediments, these permeability features may also be important in simulating borehole heads closer to observed values and therefore more accurately simulating coupled fluid and heat flow in the region. Although some of these features produce a better fit to the observed DFDP-2B temperature gradient than others, it is possible that two or more permeability features with contrasting effects on the modelled gradient would produce a better fit when superposed

than they do individually. As such, it is not possible to identify any particular one of these different permeability features as being key for incorporation in future modelling on the basis of DFDP-2B data.

The near-hydrostatic hydraulic heads measured in DFDP-1B are lower than predicted by models. In anisotropic models hydraulic head gradient at DFDP-1B is significantly reduced, suggesting that anisotropy may be a regionally significant permeability feature. Alternatively, as this borehole samples only a short, shallow interval, data may reflect a highly localised hydraulic regime (e.g. it could be dominated by a single well-connected fracture).

On the basis of comparison of model isotherm structure with the temperature data from the DFDP-1B, DFDP-2B and the Waiho valley borehole (Allis and Shi, 1995), which indicate steepened geothermal gradients in valleys, permeability $\geq 10^{-16}$ m^2 appears most appropriate for the region if permeability is treated as homogeneous and isotropic. However, this study has also shown a range of possible features of the permeability structure in the Southern Alps, such as fault zone permeability and decreasing permeability with depth, which deviate from a simple homogeneous, isotropic structure to which temperature and hydraulic head are sensitive. Although some of these modelled permeability features, such as the presence of high permeability sediments, are relatively localised effects, others, such as such as permeability-depth relationships, anisotropy and the permeability of the Alpine Fault Zone have regional influences. The actual permeability field in the Southern Alps is likely to be a highly heterogeneous superposition of features such as sediments, fault damage and cementation and variations in fracture apertures with stress field. Furthermore the temperature field and the hydraulic head field, which is coupled to it, are also influenced by other parameters, such as rock advection rate, which have not been varied between models in this study. Therefore, none of the permeability structures modelled are definitively ruled out on the basis of fit to the currently available data, from just two localities within the model domain.

Other than the presence of permeable valley sediments, which has a significant effect on head locally beneath DFDP-2B, none of the modelled permeability structures offers a clear improved fit to DFDP-1B and 2B observations compared to the baseline model, such that it is unambiguously the most suitable structure for any subsequent modelling. Therefore, although the true permeability structure is certainly more complex, a simplified isotropic homogeneous permeability of 10^{-16} m^2 for rocks above -3 km elevation and an impermeable Alpine Fault appears a suitable starting point for future investigations of groundwater flow in the Southern Alps.

Given the inaccessibility of much of the Southern Alps, and the high temperatures and fluid pressures at depth, the drilling of a large number of additional boreholes would be costly and

challenging. As such, it is likely to prove difficult to accurately resolve three-dimensional permeability structure on the basis of future borehole data. It is therefore important that in any further modelling of hydraulic heads and temperatures in the orogen, models continue to represent the conceptual uncertainty regarding permeability structure.

5.9 Conclusions

This study has analysed the role of permeability on regional groundwater flow and thermal structure in a 296 km^2 region of the Southern Alps, centred on the DFDP-2 drill site (Sutherland et al., 2017). Temperature and pressure data from the borehole are compared to simulations. Models are also used to examine hydrogeothermal conditions along the Alpine Fault plane. The regional predictions have significance for geothermal heat, fluxes of fluid for geochemical processes and deformation on the Alpine Fault.

Across the modelled permeability structures, fluid flow driven by topographic gradients in the orogen produces steep upward hydraulic head gradients, similar to those encountered in DFDP-2B, in the near-surface along the Whataroa valley. For models with homogeneous shallow (above -3 km elevation) permeability $\geq 10^{-16}$ m^2, fluid flow rates are sufficiently high that isotherms are perturbed upwards beneath the Whataroa valley relative to the ridges bounding it, rather than approximately parallel to topography as would be expected under pure conduction. A thermal structure with isotherms perturbed by groundwater flow is consistent with the much higher temperature gradients measured in DFDP-2B in the Whataroa valley and the Waiho valley borehole (Allis and Shi, 1995), compared to at DFDP-1B, located between these valleys, suggesting that if treated as homogeneous and isotropic, regional permeability is $\geq 10^{-16}$ m^2. Hot springs in Southern Alps valleys can be interpreted as a manifestation of this regionally significant advection of heat by fluid flow and upward perturbation of isotherms beneath valleys.

Temperature-determined fluid density and viscosity changes have a significant influence on groundwater flow in the Southern Alps. Although topographic gradients alone are able to induce sufficiently rapid fluid circulation to perturb isotherms upwards beneath the Whataroa valley, buoyancy provides a significant contribution to vertical Darcy velocities and is predicted to be the largest driver of vertical flow in regions beneath and at the margins of the valley. Because of the strong temperature dependence of water viscosity, Darcy velocities are increased as a result of the persistence of high temperatures to shallower depths resulting from uplift. As well as promoting perturbation of isotherms by fluid flow, this may also facilitate flow of geochemically significant fluxes of meteoric water to greater depths (e.g. Menzies et al., 2014) in actively

uplifting mountain belts than in a cooler more stable geological settings with similar permeabilities.

The steep hydraulic head gradients observed in DFDP-2B are not predicted to persist to great depth due to decreases in fluid density with depth. These temperature dependent reductions in density produce a transition to decreasing head with depth, which occurs at approximately -1 km elevation for a homogeneous permeability of 10^{-16} m^2. In a steady state brittle crustal flow regime, the ratio of fluid pressure to lithostatic pressure will be highest and the influence of fluid pressure on effective confining stress greatest in the near-surface, above this transition.

Variations in heat flow between ridges and valleys resulting from the groundwater circulation contribute to along-strike changes in temperature gradient (of the order 10 °C·km^{-1}) near the Alpine Fault, which may contribute to variations in frictional behaviour along the fault (Sutherland et al., 2017).

Lower permeability, or permeability that decreases more sharply with depth results in reduced advective heat transport in models, producing greater vertical temperature contrasts between the base of the shallow fluid flow regime and the surface of the orogen and more subdued variation in isotherm structure between ridges and valleys. Permeability anisotropy may act to reduce fluid and heat flow parallel to the valley. Enhanced permeability near to the fault in the form of a high permeability damage zone acts to reduce the mean down-dip temperature gradient near the fault and to increase its along-strike variation. A fault plane which does not act as a barrier to flow also has the effect of increasing the along-strike variation in temperature gradient near the fault, but has relatively little effect on its mean value. Valley sediments cause significant local decreases in hydraulic head, but have the least significant regional impact of the permeability features investigated. The temperature dependence of fluid density results in a broad correlation between increased temperatures and decreased hydraulic heads.

Modelling results indicate that fluid and heat flow are heavily coupled with one another in the Southern Alps. Groundwater circulation acts to cool the shallow orogen regionally and to locally increase heat flow and elevate isotherms beneath valleys relative to ridges, while thermal buoyancy has a significant influence on fluid flow, particularly beneath valleys and their margins. Thermally decreased water viscosity acts to increase Darcy velocities and therefore to increase the significance heat transport by groundwater circulation, as well promoting penetration of discernible quantities of meteoric groundwater to deeper levels within the orogen.

With the exception of the presence of high permeability valley sediments, which has a significant, but localised effect on hydraulic head, none of the modelled permeability structures produces a

clear improvement on the fit to temperature and hydraulic head observations from DFDP-1B and 2B provided by the simple baseline model, with isotropic homogeneous permeability of 10^{-16} m^2 for rocks above -3 km elevation. Therefore although future work should continue to reflect the uncertainty regarding permeability structure, this simple permeability configuration appears a reasonable starting point for models investigating groundwater and heat flow in the Southern Alps.

5.10 References

Ague, J.J., 2003. Fluid Flow in the Deep Crust, in: Treatise on Geochemistry. pp. 195–228.

Allis, R.G., Henley, R.W., Carman, A.F., 1979. The Thermal Regime Beneath the Southern Alps. Bull. R. Soc. New Zeal. 18, 79–85.

Allis, R.G., Shi, Y., 1995. New insights to temperature and pressure beneath the central Southern Alps, New Zealand. New Zeal. J. Geol. Geophys. 38, 585–592. doi:10.1080/00288306.1995.9514687

Barnes, I., Downes, C.J., Hulston, J.R., 1978. Warm springs, South Island, New Zealand, and their potentials to yield laumontite. Am. J. Sci. doi:10.2475/ajs.278.10.1412

Bickle, M.J., McKenzie, D., 1987. The transport of heat and matter by fluids during metamorphism. Contrib. to Mineral. Petrol. 95, 384–392. doi:10.1007/BF00371852

Boulton, C., Carpenter, B.M., Toy, V., Marone, C., 2012. Physical properties of surface outcrop cataclastic fault rocks, Alpine Fault, New Zealand. Geochemistry, Geophys. Geosystems 13, 1–13. doi:10.1029/2011GC003872

Caine, J.S., Evans, J.P., Forster, C.B., 1996. Fault zone architechture and permeability structure. Geology 24, 1025–1028. doi:10.1130/0091-7613(1996)024<1025

Carpenter, B.M., Kitajima, H., Sutherland, R., Townend, J., Toy, V.G., Saffer, D.M., 2014. Hydraulic and acoustic properties of the active Alpine Fault, New Zealand: Laboratory measurements on DFDP-1 drill core. Earth Planet. Sci. Lett. 390, 45–51. doi:10.1016/j.epsl.2013.12.023

Christensen, N.I., Okaya, D.A., 2007. Compressional and Shear Wave Velocities in South Island, New Zealand Rocks and Their Application to the Interpretation of Seismological Models of the New Zealand Crust, in: Continental Plate Boundary: Tectonics At South Island, New Zealand. pp. 123–155. doi:10.1029/175GM08

Clauser, C., 1992. Permeability of crystalline rocks. Eos, Trans. Am. Geophys. Union 73, 233–238. doi:10.1029/91EO00190

Cochran, U.A., Clark, K.J., Howarth, J.D., Biasi, G.P., Langridge, R.M., Villamor, P., Berryman, K.R., Vandergoes, M.J., 2017. A plate boundary earthquake record from a wetland adjacent to the Alpine fault in New Zealand refines hazard estimates. Earth Planet. Sci. Lett. 464, 175–188. doi:10.1016/j.epsl.2017.02.026

Coombs, D.S., 1993. Dehydration veins in diagenetic and very-low-grade metamorphic rocks: features of the crustal seismogenic zone and their significance to mineral facies. J. Metamorph. Geol. 11, 389–399. doi:10.1111/j.1525-1314.1993.tb00156.x

Cox, S.C., Barrell, D.J.A., 2007. Geology of the Aoraki area. Institute of Geological and Nuclear Sciences 1:250,000 geological map 15.

Cox, S.C., Menzies, C.D., Sutherland, R., Denys, P.H., Chamberlain, C., Teagle, D.A.H., 2015. Changes in hot spring temperature and hydrogeology of the Alpine Fault hanging wall, New Zealand, induced by distal South Island earthquakes. Geofluids 15, 216–239. doi:10.1111/gfl.12093

Cox, S.C., Sutherland, R., 2007. Regional Geological Framework of South Island, New Zealand, and its Significance for Understanding the Active Plate Boundary, in: Okaya, D., Stern, T., Davey, F. (Eds.), A Continental Plate Boundary: Tectonics at South Island, New Zealand. American Geophysical Union, Washington DC, pp. 19–46. doi:10.1029/175GM03

Craw, D., 1997. Fluid inclusion evidence for geothermal structure beneath the Southern Alps, New Zealand. New Zeal. J. Geol. Geophys. 40, 43–52. doi:10.1080/00288306.1997.9514739

Craw, D., Upton, P., Mackenzie, D.J., 2009. Hydrothermal alteration styles in ancient and modern orogenic gold deposits, New Zealand. New Zeal. J. Geol. Geophys. 52, 11–26. doi:10.1080/00288300909509874

Deming, D., 1994. Fluid flow and heat transport in the upper continental crust. Geol. Soc. London, Spec. Publ. 78, 27–42. doi:10.1144/GSL.SP.1994.078.01.04

Diersch, H.-J.G., 2014. FEFLOW: Finite Element Modeling of Flow, Mass and Heat Transport in Porous and Fractured Media. Springer-Verlag, Berlin, Heidelberg.

Dipple, G.M., Ferry, J.M., 1992. Metasomatism and fluid flow in ductile fault zones. Contrib. to Mineral. Petrol. 112, 149–164. doi:10.1007/BF00310451

Domenico, P.A., Schwartz, F.W., 1990. Physical and Chemical Hydrogeology. John Wiley and Sons, New York.

Eppelbaum, L., Kutasov, I., Pilchin, A., 2014. Applied Geothermics, Applied Geothermics. doi:10.1007/978-3-642-34023-9

Etheridge, M.A., Wall, V.J., Vernon, R.H., 1983. The role of the fluid phase during regional metamorphism and deformation. J. Metamorph. Geol. 1, 205–226. doi:10.1111/j.1525-1314.1983.tb00272.x

Ferry, J.M., 1988. Infiltration-driven metamorphism in northern New England, USA. J. Petrol. 29, 1121–1159.

Forster, C., Smith, L., 1989. The influence of groundwater flow on thermal regimes in mountainous terrain: A model study. J. Geophys. Res. Solid … 94, 9439–9451. doi:10.1029/JB094iB07p09439

Freeze, R.A., Cherry, J.A., 1979. Groundwater. Prentice-Hall, Englewood Cliffs, NJ.

Fyfe, W.S., Price, N.J., Thompson, A.B., 1978. Fluids In The Earth's Crust. Elsevier, New York.

Gray, D.D., Giorgini, A., 1976. The validity of the Boussinesq approximation for liquids and gases. Int. J. Heat Mass Transf. 19, 545–551.

Hubbert, M.K., Rubey, W.W., 1959. Role of fluid pressure in overthrust faulting: I. Mechanics of fluid-filled porous solids and its application to overthrust faulting. Bull. Geol. Soc. Am. 70, 115–166. doi:10.1130/0016-7606(1959)70

Ingebritsen, S.E., Manning, C.E., 2003. Implications of crustal permeability for fluid movement between terrestrial fluid reservoirs. J. Geo 79, 1–6. doi:10.1016/S0375-6742(03)00037-2

Kohlstedt, D.L., Evans, B., Mackwell, S.J., 1995. Strength of the lithosphere: Constraints imposed by laboratory experiments. J. Geophys. Res. doi:10.1029/95JB01460

Koons, P.O., 1990. Two-sided orogen: Collision and erosion from the sandbox to the Southern Alps, New Zealand. Geology 18, 679–682. doi:10.1130/0091-7613(1990)018<0679

Koons, P.O., 1989. The topographic evolution of collisional mountain belts: a numerical look at the Southern Alps, New Zealand. Am. J. Sci. doi:10.2475/ajs.289.9.1041

Koons, P.O., 1987. Some thermal and mechanical consequences of rapid uplift: an example from the Southern Alps, New Zealand. Earth Planet. Sci. Lett. 86, 307–319. doi:10.1016/0012-821X(87)90228-7

Koons, P.O., Craw, D., 1991. Evolution of fluid driving forces and composition within collisional orogens. Geophys. Res. Lett. 18, 935–938. doi:10.1029/91GL00910

Koons, P.O., Kirby, E., 2007. Topography, denudation, and deformation: the role of surface processes on fault evolution, in: Handy, M.R., Hirth, G., Hovius, N. (Eds.), Tectonic Faults: Agents of Change on A Dynamic Earth. MIT Press, Cambridge, Massachusetts, pp. 205–230.

Land Information New Zealand, 2008. Land Information Fact Sheet: New Zealand Geodetic Datum 2000 Projections [WWW Document]. URL http://www.linz.govt.nz/system/files_force/media/regulatory-documents/25702-LINZG25702 Fact sheet - New Zealand Geodetic Datum 2000 Projections_4.pdf?download=1&download=1 (accessed 23.02.2015).

Leitner, B., Eberhart-Phillips, D., Anderson, H., Nabelek, J.L., 2001. A focused look at the Alpine Fault, New Zealand: Seismicity, focal mechanisms, and stress observations. J. Geophys. Res. 106, 2193–2220.

Lemmon, E.W., McLinden, M.O., Friend, D.G. Thermophysical Properties of Fluid Systems, in: Linstrom, P.J., Mallard, W.G. (Eds.), NIST Chemistry WebBook, NIST Standard Reference Database Number 69. National Institute of Standards and Technology, Gaithersburg MD. doi:10.18434/T4D303 (accessed 30.08.2017).

Lever, D.A., Jackson, C.P., 1985. On the equations for the flow of concentrated salt solution through a porous medium. UK DOE Report No DOE/RW/85.100.

Little, T.A., Holcombe, R.J., Ilg, B.R., 2002. Ductile fabrics in the zone of active oblique convergence near the Alpine Fault, New Zealand: Identifying the neotectonic overprint. J. Struct. Geol. 24, 193–217. doi:10.1016/S0191-8141(01)00059-1

Lockner, D.A., Tanaka, H., Ito, H., Ikeda, R., Omura, K., Naka, H., 2009. Geometry of the Nojima fault at Nojima-Hirabayashi, Japan - I. A simple damage structure inferred from borehole core permeability. Pure Appl. Geophys. 166, 1649–1667. doi:10.1007/s00024-009-0515-0

Magri, F., Bayer, U., Maiwald, U., Otto, R., Thomsen, C., 2009. Impact of transition zones, variable fluid viscosity and anthropogenic activities on coupled fluid-transport processes in a shallow salt-dome environment. Geofluids 9, 182–194. doi:10.1111/j.1468-8123.2009.00242.x

Manning, C.E., Ingebritsen, S.E., 1999. Permeability Implications of the Continental of Geothermal Data and Metamorphic Systems. Rev. Geophys. 37, 127–150.

Menzies, C.D., Teagle, D.A.H., Craw, D., Cox, S.C., Boyce, A.J., Barrie, C.D., Roberts, S., 2014. Incursion of meteoric waters into the ductile regime in an active orogen. Earth Planet. Sci. Lett. 399, 1–13. doi:10.1016/j.epsl.2014.04.046

Menzies, C.D., Teagle, D.A.H., Niedermann, S., Cox, S.C., Craw, D., Zimmer, M., Cooper, M.J., Erzinger, J., 2016. The fluid budget of a continental plate boundary fault: Quantification from the Alpine Fault, New Zealand. Earth Planet. Sci. Lett. 445, 125–135. doi:10.1016/j.epsl.2016.03.046

Mercer, J., Pinder, G., 1974. Finite element analysis of hydrothermal systems, in: Oden, J.T., Zienkiewicz, O.C., Gallagher, R.., Taylor, C. (Eds.), Finite Element Methods in Flow Problems: Proceedings of the International Symposium on Finite Element Methods in Flow Problems, Swansea, January 1974. University of Alabama Press, Huntsville, pp. 401–414.

Norris, R.J., Cooper, A.F., 1995. Origin of small-scale segmentation and transpressional thrusting along the Alpine Fault, New Zealand. Geol. Soc. Am. Bull. 107, 231–240. doi:10.1130/0016-7606(1995)107<0231:OOSSSA>2.3.CO;2

Norris, R.J., Cooper, A.F., 2001. Late Quaternary slip rates and slip partitioning on the Alpine Fault, New Zealand. J. Struct. Geol. 23, 507–520. doi:10.1016/S0191-8141(00)00122-X

Norris, R.J., Cooper, A.F., 2007. The Alpine Fault, New Zealand: Surface geology and field relationships, in: Okaya, D., Stern, T., Davey, F. (Eds.), A Continental Plate Boundary: Tectonics at South Island, New Zealand. pp. 157–176. doi:10.1029/175GM09

Norris, R.J., Henley, R.W., 1976. Dewatering of a metamorphic pile. Geology 4, 333–336. doi:10.1130/0091-7613(1976)4<333:DOAMP>2.0.CO;2

Phillips, O.M., 2009. Geological Fluid Dynamics. Cambridge University Press, Cambridge.

Pitcairn, I.K., Teagle, D.A.H., Craw, D., Olivo, G.R., Kerrich, R., Brewer, T.S., 2006. Sources of metals and fluids in orogenic gold deposits: Insights from the Otago and Alpine schists, New Zealand. Econ. Geol. 101, 1525–1546. doi:10.2113/gsecongeo.101.8.1525

Reyes, A.G., Christenson, B.W., Faure, K., 2010. Sources of solutes and heat in low-enthalpy mineral waters and their relation to tectonic setting, New Zealand. J. Volcanol. Geotherm. Res. 192, 117–141. doi:10.1016/j.jvolgeores.2010.02.015

Savage, W.Z., Swolfs, H.S., 1986. Tectonic and Gravitational Stress in Long Symmetric Ridges and Valleys. J. Geophys. Res. 91, 3677–3685.

Scholz, C.H., 1998. Earthquakes and friction laws. Nature 391, 37–42. doi:10.1038/34097

Segall, P., Rice, J.R., 2006. Does shear heating of pore fluid contribute to earthquake nucleation? J. Geophys. Res. Solid Earth 111, 1–17. doi:10.1029/2005JB004129

Shi, Y., Allis, R., Davey, F., 1996. Thermal modeling of the Southern Alps, New Zealand. Pure Appl. Geophys. 146, 469–501. doi:10.1007/BF00874730

Sibson, R.H., 1990. Conditions for fault-valve behaviour. Geol. Soc. London, Spec. Publ. 15–28.

Sibson, R.H., 1973. Interactions between Temperature and Pore-Fluid Pressure during Earthquake Faulting and a Mechanism for Partial or Total Stress Relief. Nat. Phys. Sci. 243, 66–68.

Sibson, R.H., White, S.H., Atkinson, B.K., 1979. Fault rock distribution and structure within the Alpine Fault Zone: A preliminary account. Bull. R. Soc. New Zeal. 18, 55–66.

Singhal, B.B.S., Gupta, R.P., 2010. Applied Hydrogeology of Fractured Rocks, 2nd Editio. ed. Springer, New York.

Snow, D.T., 1968. Rock fracture spacings, openings, and porosities. J. Soil Mech. Found. Div. Proc. Am. Soc. Civ. Eng. 94, 73–62.

Stein, C.A., 1995. Heat Flow of the Earth, in: Global Earth Physics – A Handbook of Physical Constants, AGU Reference Shelf 1. American Geophysical Union, Washington DC, pp. 144–158. doi:10.1112/S0024609301008396

Stern, T., Kleffmann, S., Okaya, D., Scherwath, M., Bannister, S., 2001. Low seismic wave-speeds and enhanced fluid pressure beneath the Southern Alps of. New Zealand, Geol. 29, 679–682.

Stern, T., Okaya, D., Kleffmann, S., Scherwath, M., Henrys, S., Davey, F., 2007. Geophysical Exploration and Dynamics of the Alpine Fault Zone 207–234.

Sutherland, R., Berryman, K., Norris, R., 2006. Quaternary slip rate and geomorphology of the Alpine fault: Implications for kinematics and seismic hazard in southwest New Zealand. Bull. Geol. Soc. Am. 118, 464–474. doi:10.1130/B25627.1

Sutherland, R., Harris, R.A., Stern, T., Beavan, J., Ellis, S., Henrys, S., Cox, S., Norris, R.J., Berryman, K.R., Townend, J., Bannister, S., Pettinga, J., Leitner, B., 2007. Do Great Earthquakes Occur on the Alpine Fault in Central South Island, New Zealand?, in: Okaya, D., Stern, T., Davey, F.

(Eds.), A Continental Plate Boundary: Tectonics at South Island, New Zealand. American Geophysical Union, Washington DC, pp. 235–251.

Sutherland, R., Townend, J., Toy, V., Upton, P., Coussens, J., Allen, M., Baratin, L.-M., Barth, N., Becroft, L., Boese, C., Boles, A., Boulton, C., Broderick, N.G.R., Janku-Capova, L., Carpenter, B.M., Célérier, B., Chamberlain, C., Cooper, A., Coutts, A., Cox, S., Craw, L., Doan, M.-L., Eccles, J., Faulkner, D., Grieve, J., Grochowski, J., Gulley, A., Hartog, A., Howarth, J., Jacobs, K., Jeppson, T., Kato, N., Keys, S., Kirilova, M., Kometani, Y., Langridge, R., Lin, W., Little, T., Lukacs, A., Mallyon, D., Mariani, E., Massiot, C., Mathewson, L., Melosh, B., Menzies, C., Moore, J., Morales, L., Morgan, C., Mori, H., Niemeijer, A., Nishikawa, O., Prior, D., Sauer, K., Savage, M., Schleicher, A., Schmitt, D.R., Shigematsu, N., Taylor-Offord, S., Teagle, D., Tobin, H., Valdez, R., Weaver, K., Wiersberg, T., Williams, J., Woodman, N., Zimmer, M., 2017. Extreme hydrothermal conditions at an active plate-bounding fault. Nature 546, 137–140. doi:10.1038/nature22355

Sutherland, R., Toy, V., Townend, J., Eccles, J., Prior, D.J., Norris, R.J., Mariani, E., Faulkner, D.R., Pascale, G. de, Carpenter, B.M., Boulton, C., Menzies, C.D., Cox, S., Little., T.A., Hasting, M., Cole-Baker, J., Langridge, R., Scott, H.R., Lindroos, Z.R., Fleming, B., Wing, R., 2011. Operations and well completion report for boreholes DFDP-1A and DFDP-1B, Deep Fault Drilling Project, Alpine Fault, Gaunt Creek, New Zealand.

Sutherland, R., Toy, V.G., Townend, J., Cox, S.C., Eccles, J.D., Faulkner, D.R., Prior, D.J., Norris, R.J., Mariani, E., Boulton, C., Carpenter, B.M., Menzies, C.D., Little, T.A., Hasting, M., De Pascale, G.P., Langridge, R.M., Scott, H.R., Reid Lindroos, Z., Fleming, B., Kopf, J., 2012. Drilling reveals fluid control on architecture and rupture of the Alpine fault, New Zealand. Geology 40, 1143–1146. doi:10.1130/G33614.1

Tenzer, R., Sirguey, P., Rattenbury, M., Nicolson, J., 2011. Computers and Geosciences A digital rock density map of New Zealand. Comput. Geosci. 37, 1181–1191. doi:10.1016/j.cageo.2010.07.010

Tóth, J., 1963. A theoretical analysis of groundwater flow in small drainage basins. J. Geophys. Res. 68, 4795–4812. doi:10.1029/JZ068i016p04795

Tóth, J., 1962. A Theory of Groundwater Motion in Small Drainage Basins Hydrology in Central Alberta, Canada. J. Geophys. Res. 67, 4375–4387. doi:10.1029/JZ067i011p04375

Toy, V.G., Craw, D., Cooper, A.F., Norris, R.J., 2010. Thermal regime in the central Alpine Fault zone, New Zealand: Constraints from microstructures, biotite chemistry and fluid inclusion data. Tectonophysics 485, 178–192. doi:10.1016/j.tecto.2009.12.013

Upton, P., Koons, P.O., Chamberlain, C.P., 1995. Penetration of deformation driven meteoric water into ductile rocks: Isotopic and model observations from the Southern Alps, New Zealand. New Zeal. J. Geol. Geophys. 38, 535–543. doi:10.1080/00288306.1995.9514680

Upton, P., Sutherland, R., 2014. High permeability and low temperature correlates with proximity to brittle failure within mountains at an active tectonic boundary, Manapouri tunnel, Fiordland, New Zealand. Earth Planet. Sci. Lett. 389, 176–187. doi:10.1016/j.epsl.2013.12.032

Vavra, G., Gebauer, D., Schmid, R., Compston, W., 1996. Multiple zircon growth and recrystallization during polyphase Late Carboniferous to Triassic metamorphism in granulites of the Ivrea Zone (Southern Alps): an ion microprobe (SHRIMP) study. Contrib. to Mineral. Petrol. 122, 337–358. doi:10.1007/s004100050132

Wallace, L.M., Beavan, J., McCaffrey, R., Berryman, K., Denys, P., 2007. Balancing the plate motion budget in the South Island, New Zealand using GPS, geological and seismological datas. Geophys. J. Int. 168, 332–352. doi:10.1111/j.1365-246X.2006.03183.x

Wannamaker, P.E., Jiracek, G.R., Stodt, J.A., Caldwell, T.G., Gonzalez, V.M., McKnight, D.J., Porter, A.D., 2002. Fluid generation and pathways beneath an active compressional orogen, the New Zealand Southern Alps, inferred from magnetotelluric data. J. Geophys. Res. 107, 1–21. doi:10.1029/2001JB000186

Warr, L.N., Cox, S., 2001. Clay mineral transformations and weakening mechanisms along the Alpine Fault, New Zealand. Geol. Soc. London, Spec. Publ. 186, 85–101. doi:10.1144/GSL.SP.2001.186.01.06

Wells, A., Yetton, M.D., Duncan, R.P., Stewart, G.H., 1999. Prehistoric dates of the most recent Alpine fault earthquakes, New Zealand. Geology 27, 995–998. doi:10.1130/0091-7613(1999)027<0995:PDOTMR>2.3.CO;2

Whipp, D.M., Ehlers, T.A., 2007. Influence of groundwater flow on thermochronometer-derived exhumation rates in the central Nepalese Himalaya. Geology 35, 851–854. doi:10.1130/G23788A.1

Williams, J.N., 2017. The damage zone of New Zealand's Alpine Fault. PhD thesis, University of Otago.

5.11 Supporting information

5.11.1 Simulation of rock advection

In basic FEFLOW models, rock advection is not modelled explicitly. Here the additional advective heat transport due to rock advection is simulated by adding an additional water flow during heat transport simulation, to give the equivalent contribution. This method utilises the time dependent code of FEFLOW for both fluid and heat flow simulation and as such time dependent terms are shown. Although models in this study are run to steady state, the method could also be applied to modelling of temporally variable fluid and heat flow.

This study considers a medium consisting of a porous solid rock phase and a fluid phase. Both are uplifted at a rock advection velocity $\boldsymbol{v_u}$ relative to a fixed coordinate system, with erosion of uplifting material assumed to maintain a constant topographic surface at the top of the model domain. The fluid phase may also move relative to the rock at Darcy velocity $\boldsymbol{q}$. In a basic FEFLOW model, $\boldsymbol{v_u}$= 0 is assumed. For saturated flow with no internal heat sources and negligible thermal dispersion, the 'convective form' (Diersch, 1998; Galeati and Gambolati, 1989) of the energy conservation equation normally implemented in FEFLOW is (Diersch, 2014):

$$C_e \frac{\partial T}{\partial t} + \varphi C_f \boldsymbol{q} \cdot \nabla T - \nabla \cdot (\boldsymbol{\Lambda_e} \cdot \nabla T) = 0 \tag{5.13}$$

where,

$$\boldsymbol{\Lambda_e} = \varphi \boldsymbol{\Lambda_f} + (1-\varphi)\boldsymbol{\Lambda_s} \tag{5.14}$$

$$C_e = \varphi C_f + (1-\varphi) C_s \tag{5.15}$$

and φ is the volume fraction porosity (void space) in the solid phase, C_e is an effective volumetric heat capacity for the combined fluid-rock medium, C_f is the volumetric heat capacity of the fluid phase, C_s is the effective volumetric heat capacity of the solid phase and $\boldsymbol{\Lambda_e}$ is the thermal conductivity tensor for the bulk fluid-rock medium, $\boldsymbol{\Lambda_f}$ is the thermal conductivity tensor for the fluid phase and $\boldsymbol{\Lambda_s}$ is the thermal conductivity tensor for the solid phase.

However, for a more general case, with $\boldsymbol{v_s} \neq 0$:

$$C_e \frac{\partial T}{\partial t} + C_f \boldsymbol{q} \cdot \nabla T + C_e \boldsymbol{v_s} \cdot \nabla T - \nabla \cdot (\boldsymbol{\Lambda_e} \cdot \nabla T) = 0 \tag{5.16}$$

The advective heat flux, $\boldsymbol{Q_{adv}}$, in (Eq. 5.16) is given by the terms:

$$\boldsymbol{Q_{adv}} = C_f \boldsymbol{q} \cdot \nabla T + \left(\varphi C_f + (1-\varphi) C_s\right) \boldsymbol{v_u} \cdot \nabla T \tag{5.17}$$

An equivalent heat flux to $\boldsymbol{Q_{adv}}$ can also be achieved by advection of fluid alone, by increasing $\boldsymbol{q}$ by a value, $\boldsymbol{q}^*$:

$$\boldsymbol{Q}^*_{\boldsymbol{adv}} = C_f (\boldsymbol{q} + \boldsymbol{q}^*) \cdot \nabla T \tag{5.18}$$

Equating (Eq. 5.17) and (Eq. 5.18) this gives:

$$\boldsymbol{q}^* = \frac{C_e}{C_f}\boldsymbol{v_u} \tag{5.19}$$

Thus the energy conservation equation (Eq. 5.16) can be re-written:

$$C_e\frac{\partial T}{\partial t} + C_f(\boldsymbol{q} + \boldsymbol{q}^*)\cdot\nabla T - \nabla\cdot(\boldsymbol{\Lambda_e}\cdot\nabla T) = 0 \tag{5.20}$$

For this modification to be implemented successfully, incorporating heat flow due to advection of the solid phase, while leaving the fluid flow simulation unaffected, addition of $\boldsymbol{q}^*$ must take place after fluid flow simulation, but prior to heat flow simulation in a model. $\boldsymbol{q}^*$ must then be returned to its original value, $\boldsymbol{q}_0$, prior to fluid flow simulation in the next time step.

The python script feflow_rock_advection.py calculates $\boldsymbol{q}^*$ and adds it to the existing Darcy velocities at every node within the model prior to heat flow simulation (Fig. 5.16).

$$\boldsymbol{q}_1 = \boldsymbol{q}_0 + \boldsymbol{q}^* \tag{5.21}$$

Where $\boldsymbol{q}_0$ is the nodal Darcy velocity imported from the FEFLOW simulation and $\boldsymbol{q}_1$ is the modified nodal Darcy velocity exported to the FEFLOW simulation.

The script then obtains the Darcy velocity, $\boldsymbol{q}_2$for each node at the post heat flow simulation step. These are equal to the modified velocity, $\boldsymbol{q}_1$, input at the pre heat flow simulation step.

$$\boldsymbol{q}_2 = \boldsymbol{q}_1 \tag{5.22}$$

The script subtracts $\boldsymbol{q}^*$ from $\boldsymbol{q}_2$, to give a new Darcy velocity, $\boldsymbol{q}_3$, which it exports to the model. By doing this, all nodal Darcy fluxes are returned to their pre-modification values prior to fluid flow simulation in the next time step (Fig. 5.16).

$$\boldsymbol{q}_3 = \boldsymbol{q}_2 - \boldsymbol{q}^* \tag{5.23}$$

$$\boldsymbol{q}_3 = \boldsymbol{q}_0 \tag{5.24}$$

In the python script, the above $\boldsymbol{q}$ vectors are imported, modified and exported in their separate Cartesian components. Similarly $\boldsymbol{q}^*$ is calculated in terms of its Cartesian components for addition to and subtraction from imported $\boldsymbol{q}$ vector components.

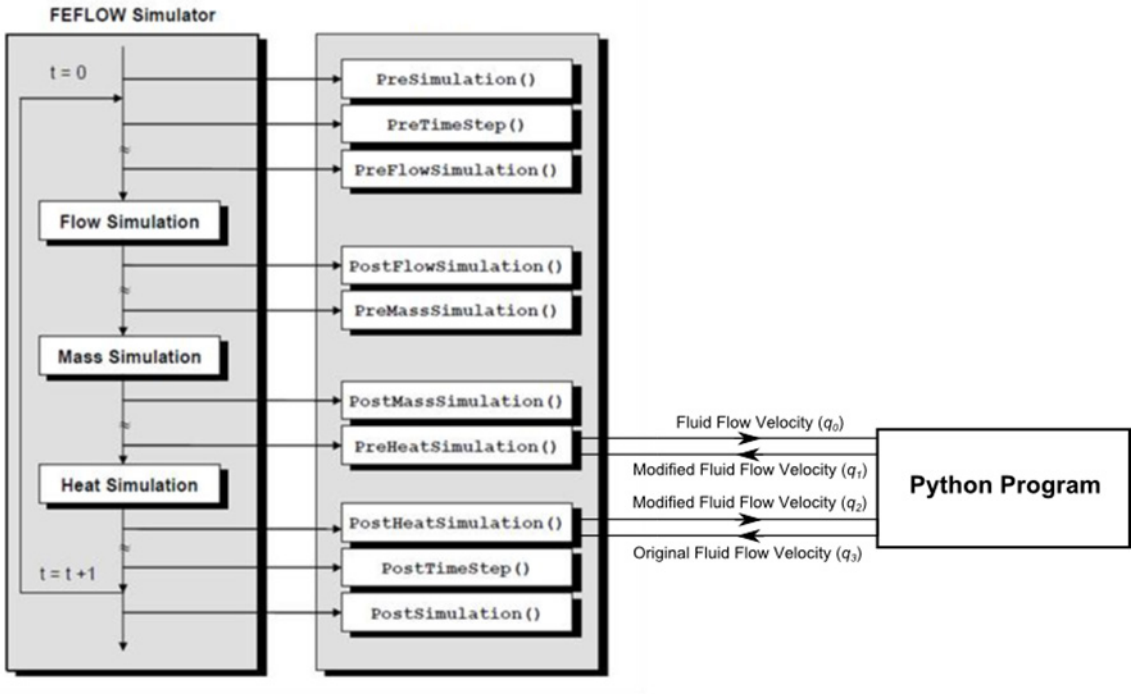

Figure 5.16 The python script modifies fluid flow velocities at the pre-heat simulation stage and returns them to their original values at the post-heat simulation stage of the FEFLOW simulation. Modified from FEFLOW training material (unpublished).

A FEFLOW model for validation (V1) was set up to simulate one-dimensional rock advection between two fixed temperature boundaries, with no fluid flow and was tested against the analytical solution for this scenario presented by Allis et al. (1979).

This FEFLOW model has an upper boundary, z_a, at 0 km elevation and a basal boundary, z_b, at -12 km, with 60 layers. The model domain has an arbitrary width of 25 km wide by 25 km long. Temperature at the model surface, T_a, is fixed at 10 °C and temperature at the model base, T_b, is fixed at 550 °C. Vertical rock advection rate, v_u, is set at test values between 0 mm·yr^{-1} and 14 mm·yr^{-1}. The isotropic thermal conductivities for fluid and rock in this FEFLOW model (Λ_f and Λ_s respectively) were used to calculate a value for effective isotropic thermal diffusivity, κ_e, for use in the analytical solution (Table 5.3). For the modelled v_u values the FEFLOW model V1 gives a good fit to the analytical solution (Fig. 5.17) with errors <0.1 °C for all elevations.

Table 5.3 Parameters used for the FEFLOW validation model V1.

Parameter	Value
z_a (m)	0
z_b (m)	-12000
T_a (°C)	10
T_b (°C)	550
v_u (mm·yr^{-1})	0.0001, 2, 6, 10, 14
C_s (MJ·m^{-3}·K^{-1})	2.7
C_f (MJ·m^{-3}· K^{-1})	4.185
Λ_s (W·m^{-1}· K^{-1})	2
Λ_f(W·m^{-1}· K^{-1})	0.6
φ (-)	0.1
κ_e (m^2·s^{-1}) †	6.53 x 10^{-7}

†Parameter values not specified within FEFLOW, but calculated for use in the analytical solution of Allis et al. (1979).

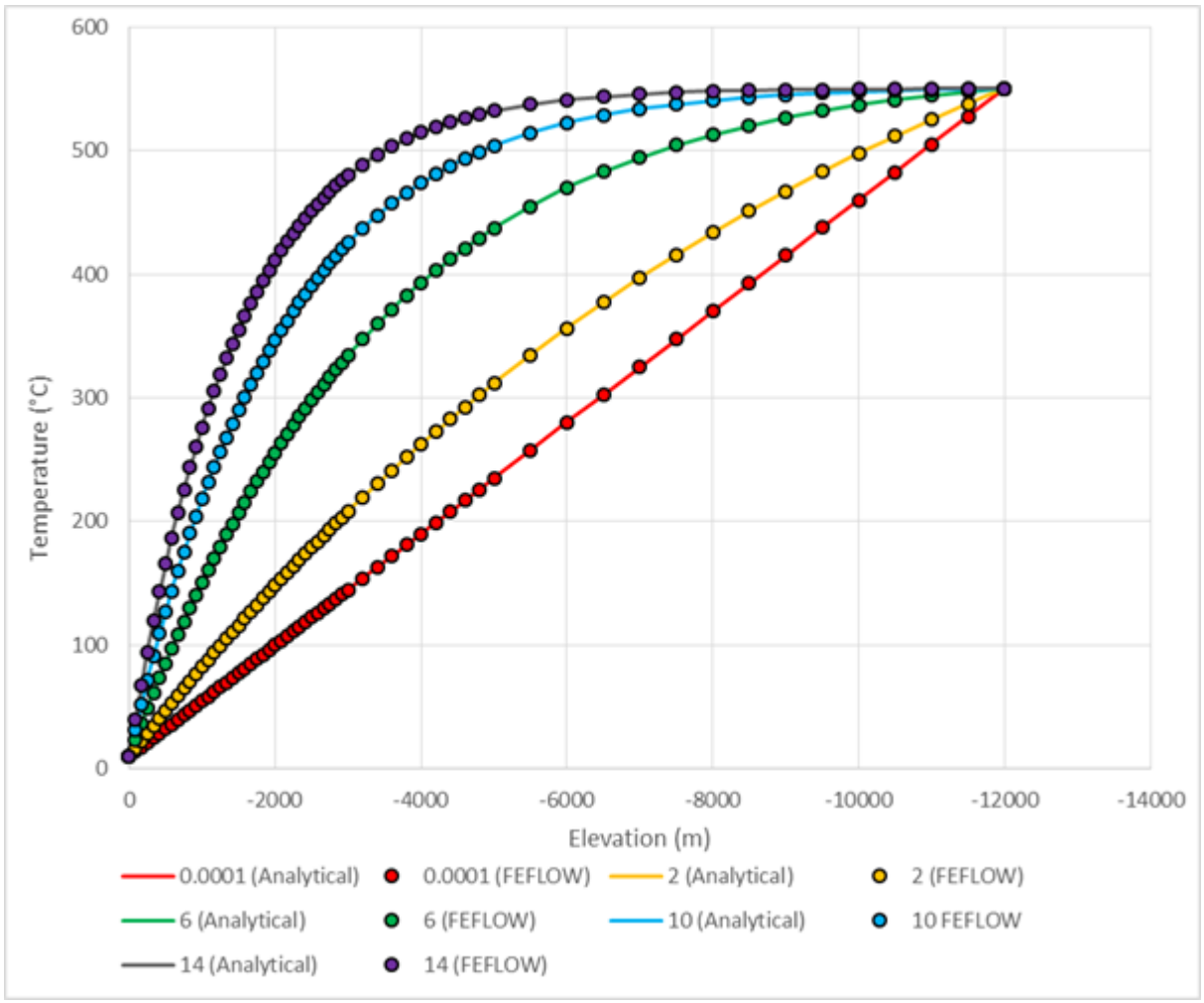

Figure 5.17 Results for a range of uplift rates, v_u (mm·yr^{-1}) for the analytical solution of Allis et al. (1979) (solid lines) and the V1 FEFLOW model with the python program applied (dots).

5.11.2 Nested borehole model

A radial nested model (Fig. 5.18) was used to simulate borehole hydraulic head gradients from regional model hydraulic head data. Regional heads were applied to a fixed outer head boundary at 100 m radius from the borehole, with all other boundaries set as no-flow. The base of the nested model corresponds to the position of the Alpine Fault beneath DFDP-2B in regional models. Permeability is set based on the corresponding regional model. Due to the constraints of radial geometry on anisotropy, for anisotropic models the nested model was isotropic, but run for both maximum and minimum permeabilities. The difference in hydraulic head results between the maximum and minimum permeability models is <0.01 m.

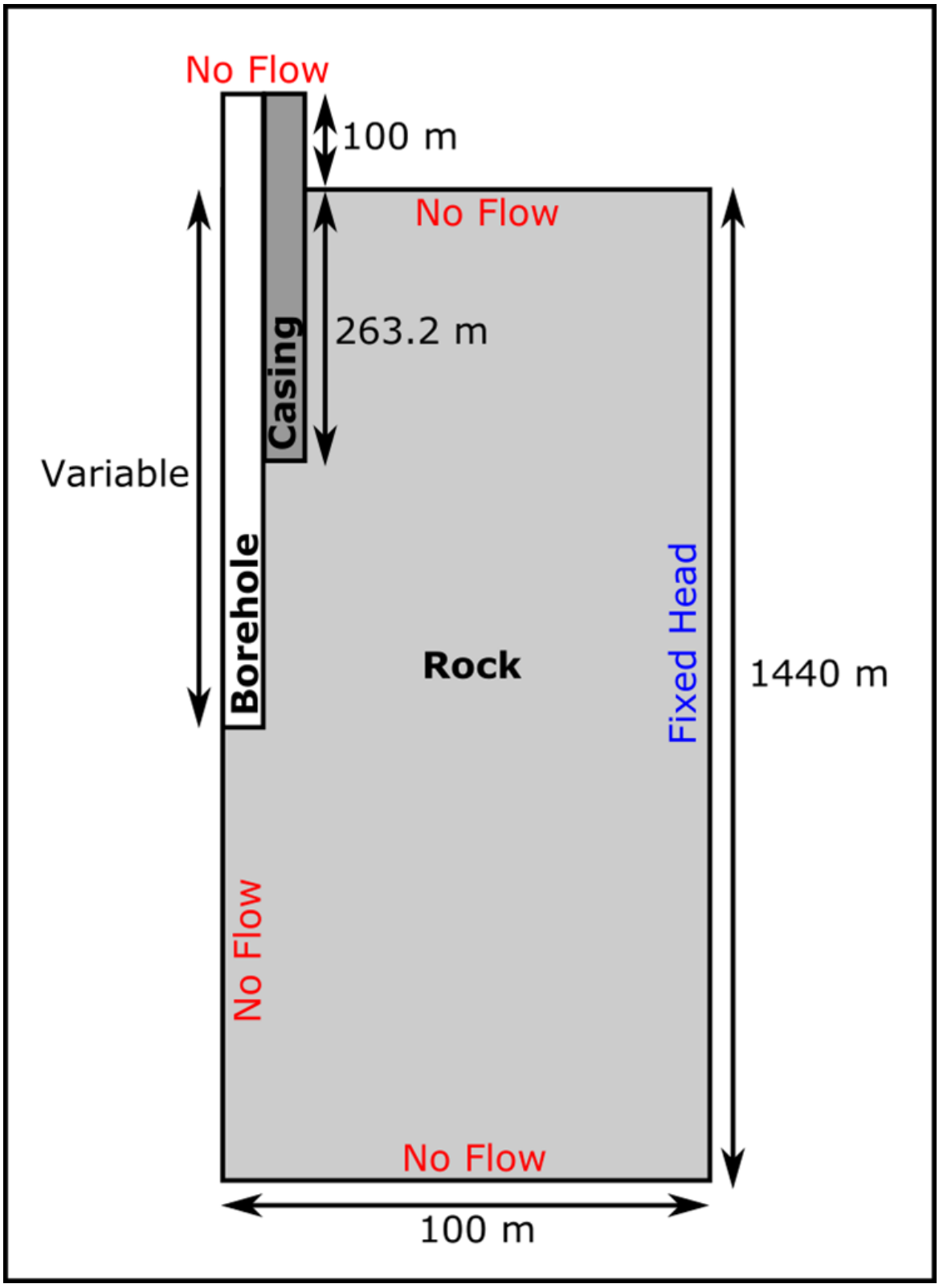

Figure 5.18 Geometry and boundary conditions of the nested borehole model (not to scale), which was built using COMSOL.

5.11.3 Additional profiles

Additional vertical profiles of temperature (Fig. 5.19), hydraulic head (Fig. 5.20) and borehole hydraulic head (Fig. 5.21) beneath the DFDP-2B site are shown. Model results are presented and discussed in terms of gradients and values at selected depths, as this allows for more straightforward comparison than presentation of depth profiles for a large range of models.

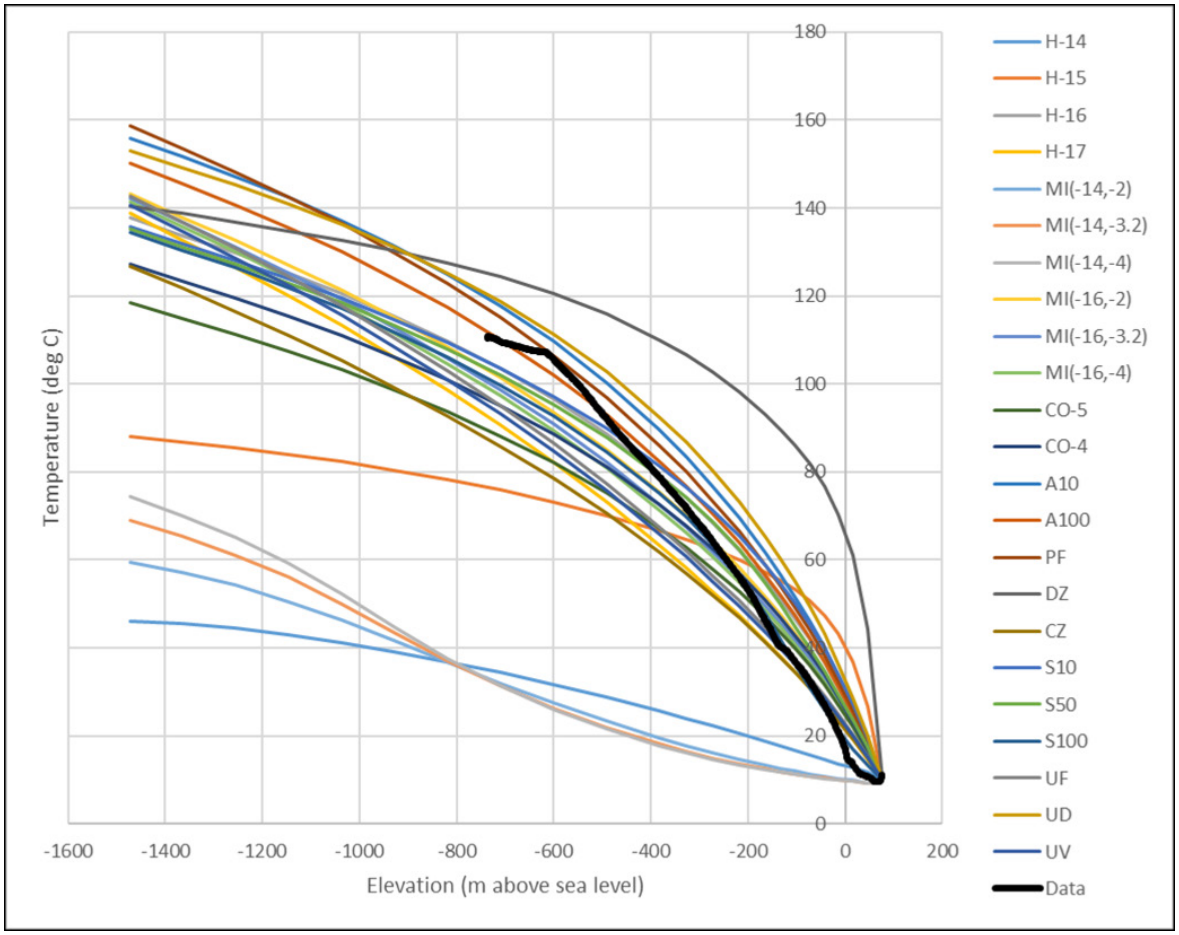

Figure 5.19 Vertical profiles of temperature beneath the DFDP-2B drill site with temperature data from the DFDP-2B borehole for comparison.

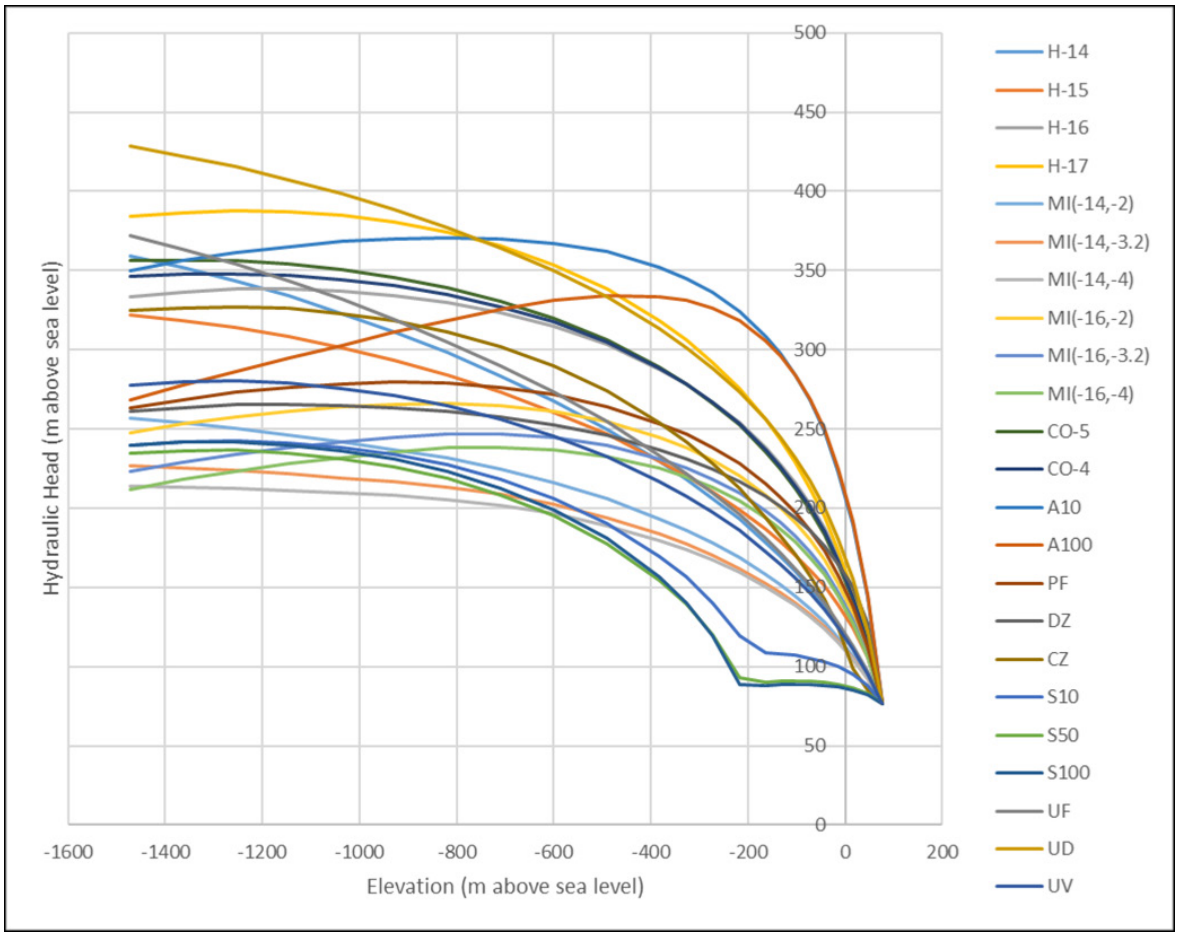

Figure 5.20 Vertical profiles of hydraulic head beneath the DFDP-2B drill site.

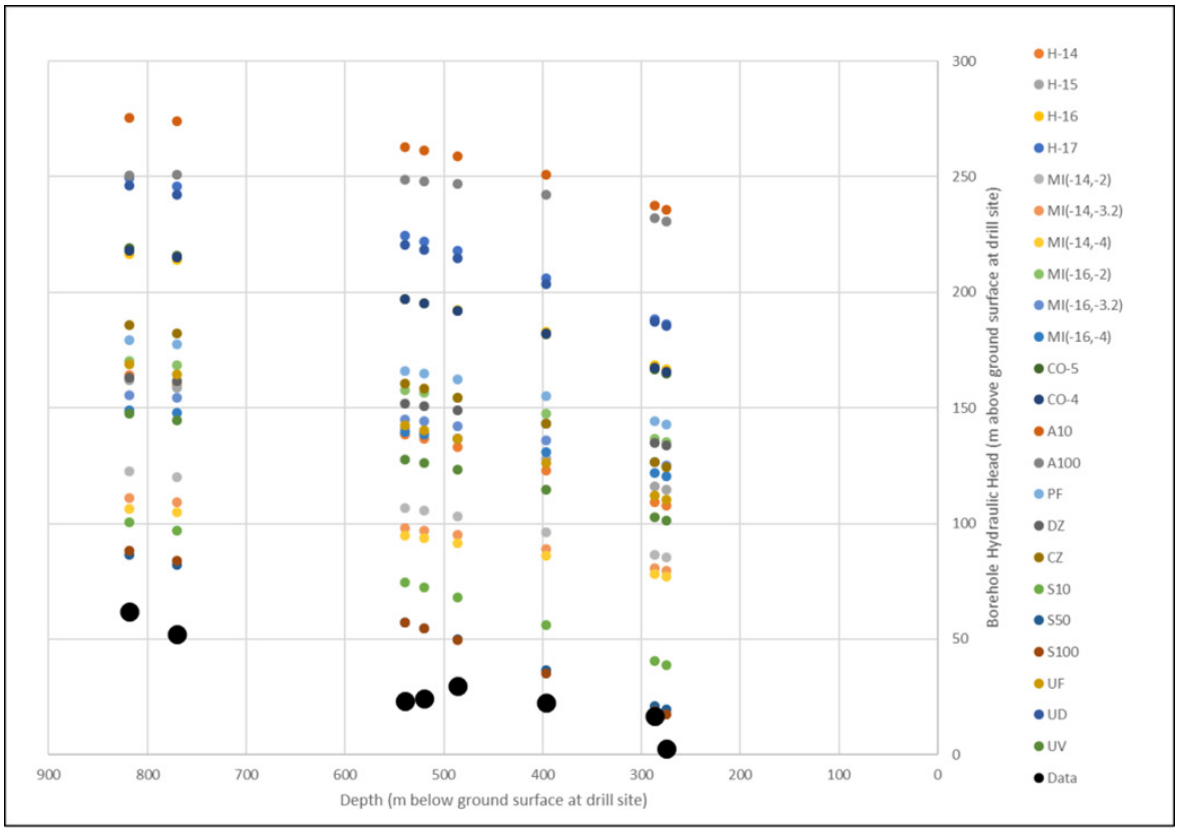

Figure 5.21 Borehole hydraulic heads at DFDP-2B with data from the DFDP-2B borehole for comparison.

5.11.4 Analytical solution for hydraulic head

For saturated flow in one dimension, z, equation (Eq. 5.7) becomes:

$$q_z = -\frac{k_z \rho_a g}{\mu}\left(\frac{dh}{dz} - \left(\frac{\rho_a - \rho}{\rho_a}\right)\right) \tag{5.25}$$

To illustrate the effect of changing density with temperature, it is assumed that q_z, k_z, μ and coefficient of thermal expansion for water, β are constant and that density is only a function of temperature, which varies linearly with depth, with gradient a:

$$\rho = \rho_a\big(1 - \beta(T - T_a)\big) \tag{5.26}$$

$$T = T_a + az \tag{5.27}$$

$$\rho = \rho_a(1 - \beta a z) \tag{5.28}$$

$$q = -\frac{k \rho_a g}{\mu}\left(\frac{dh}{dz} - \beta a z\right) \tag{5.29}$$

Where T_a is ambient surface temperature. Integrating (Eq. 5.29) to solve for h, assuming a fixed head, h_0 at z = 0:

$$h = \frac{\beta a}{2} z^2 - \frac{q_z \mu}{k_z \rho_a g} z + h_0 \tag{5.30}$$

The parameters shown in Table 5.4 are assumed for a range of q values.

Table 5.4 Parameters used in Eq. 5.30 to produce Fig. 5.14. β is calculated based on the difference between a density of ρ_0 = 999.7 kg·m^{-3} at z = 0, which is assumed to be at 10 °C and atmospheric pressure, and the density at z = -3000 m depth, 825.0 kg·m^{-3}, assuming hydrostatic pressure and a temperature gradient of 80 °C·km^{-1}. The viscosity value used is based on the temperature mid-way between these two points, 130 °C.

Parameter	Value
k	1 × 10^{-16} m^2
μ	2.16 × 10^{-4} Pa·s
β	7.00 × 10^{-4} °C^{-1}
a	-80 °C·km^{-1}
h_0	0 m

5.12 Supporting information references

Allis, R.G., Henley, R.W., Carman, A.F., 1979. The Thermal Regime Beneath the Southern Alps. Bull. R. Soc. New Zeal. 18, 79–85.

Diersch, H.-J.G., 2014. FEFLOW: Finite Element Modeling of Flow, Mass and Heat Transport in Porous and Fractured Media. Springer-Verlag, Berlin, Heidelberg.

Diersch, H.-J.G., 1998. About the Difference Between the Convective and the Divergence Form of the Transport Equation. WASY Inst. for Water Resour. And Syst. Res., Berlin.

Galeati, G., Gambolati, G., 1989. On boundary conditions and point sources in the finite element integration of the transport equation. Water Resour. Res. 25, 847. doi:10.1029/WR025i005p00847

Chapter 6:

Conclusions

6.1 Overview

Groundwater has the potential to influence a range of geological processes as an agent of heat and mass transfer and through the effect of pore fluid pressure on rock strength. It may therefore act as a control on the structure of mountain belts and the behaviour of fault zones, which accommodate deformation within these regions. The aim of this thesis is to better understand the fluid flow system within the Southern Alps and its potential to influence other orogenic processes by answering the following questions:

1. What is the permeability structure of the Southern Alps?

2. What are the regional infiltration rates at the surface?

3. What are the fluid fluxes to depth?

4. What are the fluid pressure conditions in the Alpine Fault Zone?

5. What are the fluid flow rates (Darcy velocities) in the Alpine Fault Zone?

6. How significant is the influence of fluid flow on subsurface heat flow and temperature field?

7. How does permeability structure influence the temperature and fluid pressure fields at depth in the Southern Alps and in particular, near to the Alpine Fault?

8. What role does thermal buoyancy play in driving groundwater circulation and how significant is the temperature dependence of water viscosity?

The answers to each of these questions, provided by work in this thesis, are outlined below. This is followed by a summary of the conclusions of the thesis regarding fluid flow in the Southern Alps. Potential avenues for future investigation are then considered in the form of a set of further questions, each with an associated proposal for future work.

6.2 Questions addressed

1. What is the permeability structure of the Southern Alps?

The intrinsic permeability of a porous medium, k, is often measured and expressed in terms of hydraulic conductivity, K, which is proportional to k, but also to fluid density and viscosity. Since conversion between these two parameters is common, the term 'permeability' is used here to encompass expressions and estimates of k in terms of K, with specific values for each parameter given where appropriate. Here, estimates of K are related to k based on water properties at appropriate Southern Alps surface conditions of 0.01 - 10 °C, 1 atm, except where otherwise stated. Permeability is a key control on fluid flow rates and estimates for permeability or for Darcy velocity, are commonly required for interpreting geochemical data related to fluid transport (e.g. Menzies et al., 2016). Despite its importance, information on in situ permeability was sparse prior to the work in this thesis (Cox et al., 2015). Existing permeability estimates came from hydraulic tests and flow measurements carried out during engineering assessments at a small number of relatively shallow boreholes and tunnels, only one of which was in the inboard Southern Alps and from the DFDP-1B borehole (Cox et al., 2015; Sutherland et al., 2012). These estimates span a wide range of values (K = 10^{-10} m·s^{-1} to 10^{-4} m·s^{-1}; k = 10^{-17} m·s^{-1} to 10^{-11} m·s^{-1}) and include permeabilities sampled at a relatively small scale (≥10 m). In contrast, in this thesis, permeability estimates have been obtained from a range of scales (~10 m to ~10^5 m) (Fig. 6.1; Table 6.1).

An estimate for regional-scale permeability has been obtained based on modelling of the water table at the Amethyst Ravine (Chapter 2). In order to maintain a water table consistent with observed borehole water levels, both analytical models for local region containing the boreholes and finite element models for the Wanganui valley region, incorporating the Amethyst Ravine, indicate that regional K to infiltration ratio must be greater than ~0.3. As sources of infiltrating water other than precipitation are likely to be minor, this requires regional $K \leq 5 \times 10^{-7}$ m·s^{-2}. The upper limit for k is 9×10^{-14} m^2 ≈ 10^{-13} m^2 and is established by assuming uniform low temperature conditions, as higher temperatures in models simulating the thermal structure of the Southern Alps increase the infiltration rate required to sustain a given water table elevation. Packer test measurements at the Amethyst boreholes indicate values in excess of these limits ($K \geq 10^{-6}$ m·s^{-1}; $k \geq 10^{-13}$). These high measured permeabilites are inferred to be restricted to the shallowest rocks in the orogen and to those where permeability is locally enhanced as a result of fault damage, as unrealistically high infiltration rates (>100 % precipitation) are required if this permeability is applied as a homogeneous value for the shallow crust (above -6 km elevation) in models.

Further information on regional-scale permeability is provided by models for coupled groundwater and heat flow in the Whataroa valley region (Chapter 5). These indicate that the

upward perturbation of shallow isotherms beneath valleys relative to ridges requires regional $k \geq 10^{-16}$ m^{-2}. Temperature data from the DFDP-2B borehole in the Whataroa valley and from a borehole in the Waiho valley indicate steeper temperature gradients than the shallow DFDP-1B borehole, which is not located within a major valley. These observations allow further refinement of estimates of regional-scale permeability, and therefore 10^{-16} m$^{-2} \leq k \leq 10^{-13}$ m^{-2} is the preferred range of bulk permeability in the shallow (above -3 km to -6 km elevation) Southern Alps. This range is consistent with the permeability-depth relationship of Manning and Ingebritsen (1999), which predicts $k \geq 10^{-16}$ m^{-2} for ≥ 6 km depth, although this does not necessarily imply that that the Manning and Ingebritsen (1999) permeability model is the most suitable for simulating flow in the Southern Alps.

Local permeability estimates have also been obtained for rocks to 818 m depth in the Alpine Fault Zone using DFDP-2B data (Table 6.1). Modelling of slug test (Chapter 3) using the methods of Bouwer and Rice (1976) and Hvorslev (1951) indicates bulk K at DFDP-2B in the range 10^{-9} m·s^{-1} to 10^{-7} m·s^{-1} (k = 10^{-17} - 10^{-13} m^2, see Table 6.1 for water properties assumed). Application of Darcy's Law to model Darcy velocity and hydraulic head gradient estimates suggests K = 10^{-9} m·s^{-2} (k = 10^{-16} m^2, see Table 6.1 for water properties assumed) for basement rocks at DFDP-2B and $K \geq 10^{-8}$ m·s^{-2} ($k \geq 10^{-15}$ m^2, see Table 6.1 for water properties assumed) for valley sediments in the upper part of the drilled interval. A value of $k \sim 10^{-16}$ m^2 for basement rocks at DFDP-2B is consistent with estimates from both of these complementary approaches (slug test modelling and Darcy velocity modelling). This value falls within the range indicated for bulk regional permeability but is lower than estimates for shallower depths obtained from DFDP-1B and the Amethyst Ravine boreholes (Table 6.1). The permeability estimates from DFDP-2B in this thesis and those obtained from the DFDP-1 boreholes are significantly lower than those estimated based on packer tests near the Amethyst Ravine (Cox et al., 2015). With only three sites to compare, it is unclear whether this reflects local conditions at these sites or a regional trend. However, the higher permeability estimates obtained from the Amethyst Ravine boreholes relative to DFDP-1B and DFDP-2B, which are at lower elevation, appear consistent with the pattern of increased permeability beneath ridges relative to valleys predicted by the stress dependent permeability models (e.g., Upton and Sutherland, 2014).

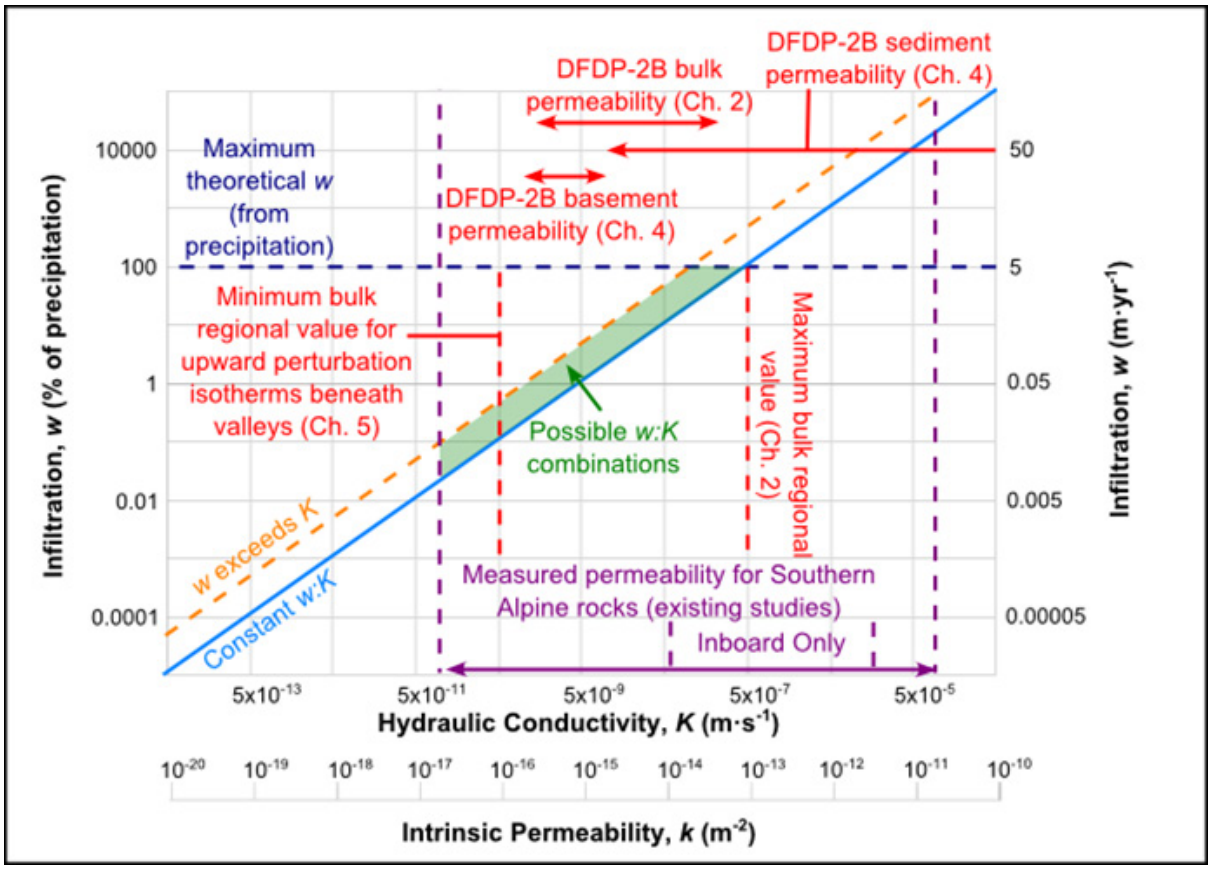

Figure 6.1 Hydraulic conductivity, intrinsic permeability and infiltration constraints for the Southern Alps from work in this thesis, with existing estimates in purple. Adapted from Chapter 2. Permeability estimates from hydraulic tests are plotted based on hydraulic conductivity value.

Table 6.1 Permeability estimates from borehole tests in the inboard Southern Alps.

Borehole	Borehole depth (m)	Testing method	K (m·s^{-1})	k (m^2)	Source
Amethyst borehole BH2	180	Packer test	10^{-6}	10^{-13}	Cox et al., 2015 (also see Chapter 2)
Amethyst borehole BH2	309	Packer test	10^{-5}	10^{-12}	Cox et al., 2015 (also see Chapter 2)
DFDP-1B	150	Slug test	10^{-8} - 10^{-7}	10^{-14}	Sutherland et al., 2012
DFDP-2B	818	Slug test	10^{-9} - 10^{-7}	10^{-17} - 10^{-13}	Chapter 2
		Darcy velocity estimation from temperature data, head estimation from slug test data	10^{-9} (basement) ≥ 10^{-8} (sediments)	10^{-16} (basement) ≥ 10^{-15} (sediments)	Chapter 3

Notes: Due to high temperatures and pressures and the presence of drilling mud in the DFDP-2B borehole during slug tests, k values for these tests also account for fluid properties based on measured values for drilling mud and for water up to 100 °C, in the pressure range 1 to 10 MPa. k values based on DFDP-2B model Darcy velocities are based on mean temperature in the basement and sediment layers for which K was calculated, 78 °C and 30 °C respectively, in the pressure range 1 to 10 MPa.

2. What are the regional infiltration rates at the surface?

Prior to the work in this thesis the only estimate of the rate of water infiltration into the groundwater system of the Southern Alps was provided by the comparison of rainfall data with tunnel flow measurements at the Tatare Tunnel near Franz Josef. These indicated infiltration of 0.3 % to 20 % of precipitation, assuming a 0.54 km^2 catchment area for the tunnel (Sims et al., 2015). Models of the Amethyst Ravine region in this thesis (Chapter 2) provide new regional-scale estimates for water infiltration rates into the Southern Alps. These scale with permeability and indicate that infiltration must be ≥ 0.02 % of rainfall based on the minimum measured permeability in Haast Schist Group rocks of K = 10^{-10} m·s^{-1} to 10^{-4} m·s^{-1}; k = 10^{-17} m·s^{-1} to 10^{-11} m·s^{-1}

(Cox et al., 2015). However, models indicate that if high permeabilities measured in the Amethyst Ravine boreholes (K = 10^{-6} m·s^{-1} to 10^{-5} m·s^{-1}; k = 10^{-13} m^2 to 10^{-12} m^2) are representative of rocks at similar depths across the orogen, regional infiltration must be >20 % precipitation. Widespread high permeabilities in the near-surface, similar to those estimated at the Amethyst Ravine are not precluded by much lower permeability estimates for basement rocks at DFDP-2B (K = 10^{-6} m·s^{-1}; k = 10^{-16} m^2) as these rocks are overlain by >200 m of sediments with potentially much higher permeability ($K \geq 10^{-8}$ m·s^{-1}; $k \geq 10^{-15}$ m^2) than the basement below.

3. What are the fluid fluxes to depth?

Although the fluxes of meteoric water into the brittle-ductile transition zone (BDTZ) have been estimated (Menzies et al., 2016), the knowledge of how fluid fluxes change between the surface and the BDTZ is poor. Models of the Amethyst Ravine region in the thesis (Chapter 2) indicate that the majority of infiltrating precipitation (>70 % for modelled permeability structures) leaves the groundwater system at seeps without reaching 500 m depth, meaning that the fluid flux penetrating beyond 500 m is predicted to be <30 % of the average infiltration flux. Seepage in models is widespread and many rivers are in continuity with groundwater, including some at >1750 m elevation.

Regional models with reasonable permeability structures estimate that there are further significant reductions in fluid infiltration with depth, with a fluid flux equivalent to ≤8 % of the average infiltration flux reaching -3 km elevation and a flux equivalent to ≤4 % of the average infiltration flux reaching -5 km elevation. The latter estimate is consistent with geochemical estimates for fluxes to brittle-ductile transition, for surface infiltration rates of the order 1 % precipitation of greater.

If present, foliation-parallel permeability anisotropy is predicted to reduce the extent of seepage and to reduce the fall in fluid flux with depth, compared to isotropic permeability situations. High temperature gradients result in less significant reductions in fluid flux with depth, allowing a greater percentage of infiltrating water to reach deeper levels within the models. Therefore, steepened temperature gradients in the brittle crust resulting from rapid uplift in the Southern Alps may facilitate penetration of greater volumes meteoric water to the brittle-ductile transition than in similar settings with lower temperature gradients.

4. What are the fluid pressure conditions in the Alpine Fault Zone?

The only existing estimates of fluid pressure conditions in the Alpine Fault Zone prior to the work in this thesis were from the DFDP-1B borehole and were limited to 150 m depth. These showed near hydrostatic fluid pressures in the Alpine Fault hanging wall and a pressure drop of 0.53 MPa

across the fault principal slip zone (PSZ) (Sutherland et al., 2012). Here modelling of mud levels from the DFDP-2B borehole has been used to estimate fluid pressure conditions to 818 m depth in the fault zone hanging wall (Chapter 3). Results indicate borehole hydraulic heads that increase rapidly below the base of valley sediments at DFDP-2B, reaching >60 m at the base of the borehole. The increasing heads with depth are consistent with significant upward flow, which implies that undisturbed ambient heads are likely to be even higher. Borehole models show that ambient head could be >120 m at the base of the borehole. These conditions mean that, in order to obtain the best estimates for ambient fluid pressure conditions and fault rock permeability in future drilling at the DFDP-2B site or within another Southern Alps valley, attempts must be made to hydraulically isolate sections of the borehole for testing, for example through use of packers or through insertion of isolating casing at more regular intervals.

Regional models (Chapter 5) indicate that steep increases in heads with depth, similar to those observed at DFDP-2B occur along the length of Southern Alps valleys in the near-surface, but a transition to decreasing head with depth occurs deeper in the orogen (approximately -1 km elevation for homogeneous k = 10^{-16} m^{-2}), as a result of decreasing water density.

5. What are the fluid flow rates (Darcy velocities) in the Alpine Fault Zone?

Fluid flow rates in the hanging wall of the Alpine Fault have the potential to control rates of mass and heat transfer within the fault zone. The only existing estimates of flow rates in the Southern Alps prior to the work in this thesis are drawn from basic scaling calculations (Menzies et al., 2016). Here more precise estimates have been obtained based on measurements within the fault zone from the DFDP-2B borehole (Chapter 4). One dimensional heat flow models have shown that across the 818 m section of the fault zone penetrated by DFDP-2B, an upwards Darcy velocity, q = 7.8×10^{-10} $m \cdot s^{-1}$ ≈ 10^{-9} $m \cdot s^{-1}$ approximates measured steady state temperatures well. Models with multiple layers indicate that Darcy velocity may vary in the range 5.3×10^{-10} $m \cdot s^{-1}$ to 2.8×10^{-8} $m \cdot s^{-1}$ across this interval, producing discontinuities in temperature gradient. These changes in Darcy velocity result from the occurrence of fracture zones and the boundaries of sedimentary units, which act as sources and sinks for upward fluid flow in a vertical profile. The volume flux of meteoric fluid estimated to reach the brittle-ductile transition zone by Menzies et al. (2016) is equivalent to a spatially averaged Darcy velocity ~10^{-10} $m \cdot s^{-1}$. This is approximately an order of magnitude lower than approximate Darcy velocity across DFDP-2B estimated here of ~10^{-9} $m \cdot s^{-1}$. This is consistent with the ~10 × drop in fluid flux that occurs in thermally coupled regional models (Chapter 2) between 500 m depth and -5 km elevation.

6. How significant is the influence of fluid flow on subsurface heat flow and temperature field?

On the basis of the small cumulative heat flux associated with known warm springs in the Southern Alps, which are only localised features of the groundwater system, past thermal models for the orogen have considered heat advection by fluid flow negligible (Allis and Shi, 1995). However, one dimensional modelling of temperature data from the DFDP-2B borehole indicates that the profile cannot be explained in terms of rock advection and conduction alone (Chapter 4). Models incorporating fluid flow better fit the temperature profile. These indicate a heat flux of ~720 $mW \cdot m^{-2}$ in the drilled interval, significantly higher than estimated heat fluxes in models incorporating rock advection alone (Shi et al., 1996; Upton et al., 2011). The elevated total heat flux at DFDP-2B can be understood in terms of the redistribution of heat by regional groundwater circulation, which transports heat from ridges to valleys. For the range of estimated Darcy velocities at DFDP-2B, the vertical heat flux associated with groundwater flow is more than three times greater than that associated with rock advection. A Péclet number of ~1 for heat advection by groundwater flow relative to conduction across the drilled interval shows that, at the length scale of the borehole, both transport mechanisms are of similar significance. Groundwater circulation is therefore a major heat transport mechanism in the shallow crust and likely to be an important control on temperature field. As fluid fluxes decrease with depth (Chapter 2), heat advection by groundwater will only be significant across a finite vertical interval and is likely to be insignificant by <6 km depth. Rock advection supplies heat to the base of this interval, above which groundwater flow significantly redistributes heat, concentrating upward heat flow into valleys.

7. How does permeability structure influence the temperature and fluid pressure fields at depth in the Southern Alps and in particular, near to the Alpine Fault?

Thermal models for the central Southern Alps and Alpine Fault Zone developed prior to those outlined in this thesis had previously not included the effects of groundwater flow on temperature field. Furthermore fluid pressure conditions at depth in the orogen had not been quantified. In this thesis models that simulate coupled groundwater and heat flow in the Southern Alps illustrate the strong influence of permeability structure on modelled conditions at depth in the orogen, however common features to the fluid and heat flow regimes, which are robust across a range of permeability structures emerge (Chapter 5). Models for the Whataroa valley region include both DFDP-1B and DFDP-2B boreholes, allowing temperature and fluid pressure data from these boreholes to be compared to model results.

Regional topographic flow into the valley from the ridges that bound it occurs across all modelled permeability structures and results in steep increases in hydraulic head with depth beneath the

valley, as observed at DFDP-2B. Although flow is upward beneath valleys, a transition to decreasing heads at depth is predicted in models, a result of reduced groundwater density. This occurs at around -1 km elevation for the baseline permeability structure of homogeneous $k = 10^{-16}$ m^{-2}. Modelled isotherms are perturbed upwards beneath the valley relative to the bounding ridges, rather than having a geometry approximately parallel to topography for homogeneous permeabilities ≥ 10^{-16} m^2. This isotherm structure is consistent with high temperature gradients observed at DFDP-2B within the Whataroa valley and a borehole in the neighbouring major valley (the Waiho valley), relative to DFDP-1B, which located between these valleys. In this context, warm springs represent a local manifestation of regional up-flow and associated isotherm perturbation along Southern Alps valleys.

Near the fault plane, along-strike variations in temperature occur between ridges and valleys, which may cause in differences in fault frictional behaviour between ridge and valley sections (Sutherland et al., 2017). Rapidly increasing heads with depth beneath valleys will decrease fault strength relative to hydrostatic conditions and compared to fault sections that terminate the ridges, where heads decrease with depth. However, the transition to decreasing heads with depth beneath valleys, which occurs due to reduced water density, means that fluid pressures arising from the steady state topography and buoyancy driven flow regime will have the greatest influence on effective confining stress in the near-surface of valleys (above approximately -1 km elevation).

The groundwater circulation system in the Southern Alps regionally transports heat from its base to the ground surface and locally increases total upward heat flux beneath valleys, where water flows upwards, relative to the ridges, where water flows downwards. Decreased Darcy velocities in this circulation system resulting from reduced homogeneous permeability or increasingly rapid permeability reduction with depth have the effect of increasing the temperature contrast between the base of the groundwater flow system and the surface and lowering isotherms beneath valleys relative to ridges. At the Alpine Fault, these permeability reductions have the effect of increasing the down-dip temperature gradient and altering the along-strike range in this gradient, although the magnitude of this range may be increased or decreased depending on the exact permeability structures being compared. Where temperature increases between models of differing permeability structure, hydraulic heads and head gradients generally decrease, as a result of temperature dependent density, reflecting a highly coupled fluid and heat flow system.

Models indicate that permeability anisotropy, with decreased permeability normal to foliation, may reduce fluid and heat flow parallel to the valley. Increased permeability in the fault zone in the form of a high permeability hanging wall damage zone acts to reduce the mean down-dip

temperature gradient near the fault and to increase its along-strike variation. Increased permeability in the form of a fault plane that is not a barrier to flow has relatively little impact on the mean down-dip temperature gradient, but increases the along strike variation in this gradient. High permeability valley sediments play an important role in reducing hydraulic heads at depth along the valley, but their influence is localised to the valley floors and has less influence on conditions near to the Alpine Fault plane than other modelled permeability structures.

8. What role does thermal buoyancy play in driving groundwater circulation and how significant is the temperature dependence of water viscosity?

Although topography and thermal buoyancy have been inferred to be major drivers for fluid circulation in the Southern Alps (Koons and Craw, 1991), their relative significance had not been investigated prior to this thesis. The importance of the temperature dependence of viscosity has also not been previously assessed. Models of fluid and heat flow in the Whataroa valley region were used to investigate the influence of changes in both density and viscosity on groundwater flow in the Southern Alps (Chapter 5). Upward perturbation of isotherms beneath the Whataroa valley occurs in models in which density is held constant and those in which water density is coupled to temperature and pressure, suggesting that the topographic drivers for flow in the Southern Alps alone are able to generate sufficiently high flow rates to produce the proposed groundwater-influenced thermal regime. However, analysis of the driving forces for vertical flow in models suggests that buoyancy is significant in the orogen and provides the dominant driving contribution to vertical fluid flow in regions beneath and at the margins of the Whataroa valley. Whataroa valley models also show that the temperature dependence of viscosity is important in determining the threshold permeability for the transition in thermal structure from isotherms that are approximately parallel to topography to isotherms perturbed upwards beneath major valleys. The reduction in water viscosity that occurs with increasing temperature acts to increase Darcy velocities and the relative significance of groundwater flow in heat transport if other factors are held constant. Additionally, thermal decreases in viscosity and associated increases in fluid flow rate have the potential to influence fluid fluxes reaching deeper levels of the brittle crust. This is illustrated by the smaller reduction in fluid fluxes with depth that occurs in models for the Wanganui valley under higher temperature gradients (Chapter 2).

6.3 Summary

Research in this thesis has shown that at least 0.02 % of the ~10 $m \cdot yr^{-1}$ precipitation in the inboard Southern Alps infiltrates into the groundwater system and that if high shallow permeabililities measured in boreholes are widespread, infiltration must be more than 20 % of precipitation (Fig.

6.2). The Southern Alps have highly elevated water tables and groundwater seeps out at the surface and into rivers across large areas of the orogen. The majority of infiltrating water (>70 % for modelled permeability structures) travels on shallow flow paths, less than 500 m below the ground surface. Bulk regional-scale permeability in this shallow (above -3 km to -6 km elevation) groundwater system must be in the range 10^{-16} m^{-2} ≤ k ≤ 10^{-13} m^{-2}. The permeability of basement rocks at DFDP-2B is estimated to be ~10^{-16} m^{-2} based on complementary modelling of both mud level and temperature data and lies within this range of bulk regional values, albeit at the lowermost end. Groundwater plays a major role in heat transport within the orogen, with Darcy velocities in the range 10^{-10} m·s^{-1} to 10^{-8} m·s^{-1} beneath the Whataroa valley sufficiently high that groundwater advects more than three times the heat than transported by rock advection for the 818 m interval penetrated by DFDP-2B. High heat fluxes across this drilled interval of ~720 mW·m^{-2} are the result of the redistribution of heat into valleys by circulating groundwater, which both increases heat fluxes and perturbs isotherms upwards beneath valleys relative to ridges. Models indicate that higher regional permeability and the less significant reductions in permeability with depth promote this upward perturbation of isotherms beneath valleys but reduce the temperature contrast between the base of the groundwater flow system and the surface. In addition to transporting heat, convergent groundwater flow beneath valleys results in steep increases hydraulic head with depth in the near-surface. Heads reach >60 m at 818 m depth beneath the Whataroa valley at DFDP-2B. However, these increases in hydraulic head are not predicted to persist to depth, due to reductions in fluid pressure associated with the reduction of water density with increasing temperature. Although the geometry of the thermal structure of the orogen is not dependent on the contribution to Darcy velocities from thermal buoyancy, in regions of the subsurface beneath and at the margins of the Southern Alps valleys, buoyancy provides an important contribution to driving vertical groundwater flow. Decreasing water viscosity with temperature acts to increase Darcy velocities and may allow greater fluxes of meteoric water to reach the base of the brittle crust in the Southern Alps than in regions of elevated topography but without high rates of tectonic uplift. Although important advances in understanding of the Southern Alps can be made on the basis of simplifying assumptions, the temperature field and the fluid pressure fields in the orogen cannot be fully understood independently of one another, because of the important couplings between groundwater circulation and heat flow evident from these findings.

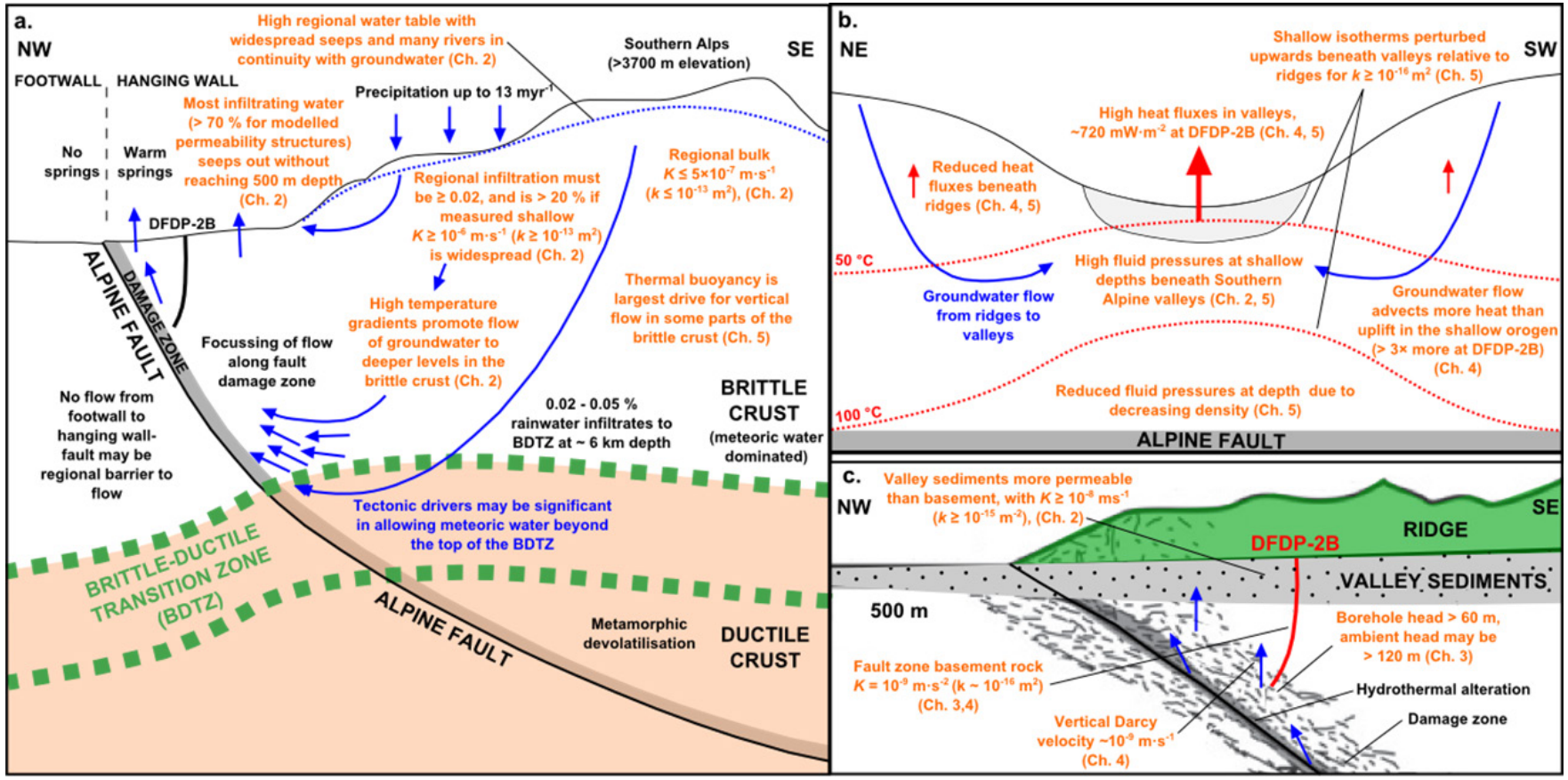

Figure 6.2 Overview of the Southern Alps groundwater system, with new insights provided by work in this thesis in orange, illustrated using cross sections perpendicular to the fault (a.) and parallel to the fault (b.) and a smaller scale section perpendicular to the fault, focussing on flow in the Alpine Fault Zone (c.). (a) is adapted from Menzies et al. (2016) and (c.) from Sutherland et al. (2012).

6.4 Future work

This thesis has contributed to knowledge of the groundwater flow systems in the Southern Alps, but a number of important questions remain to be addressed and some aspects of future research are detailed below:

1. How do temporal changes through the seismic cycle of the Alpine Fault influence temperature and fluid pressure conditions at depth?

Having investigated the subsurface temperature and fluid pressure fields in the Southern Alps assuming steady state conditions, a logical next step is to consider temporally variable models that simulate the effects of changing permeability through the seismic cycle of the fault on the fluid and heat flow regimes. These changes may include damage to low permeability fault zone material, allowing temporary cross-fault fluid flow and decreasing permeability in the fault damage zone through seismic cycles associated with cementation of void space created during rupture. Variations in temperature and pressure field during the interseismic period may affect the frictional properties of the fault and could play a role in influencing the apparent periodicity of Alpine Fault rupture of 291 ± 23 years (Cochran et al., 2017). Finite element models outlined in this thesis have the capability of simulating these temporal variations and preliminary investigations have already been conducted. The change in effective confining stress through a seismic cycle based on simulated fluid pressure changes can be calculated and used to estimate the impact of these pressure changes on the length of the seismic cycle of the fault.

2. What are the permeability architecture, flow rates and fluid pressures within 10s of meters of the fault plane at >1 km depth and how do they change through a seismic cycle?

The DFDP-2B borehole provides important observations of deeper conditions in the Alpine Fault Zone than previously available. The data collected provide valuable insights into the flow regime of the Southern Alps, although the borehole did not reach the fault itself. Significant further insights could be obtained through a further phase of DFDP drilling to intersect the fault at >1 km depth.

Although fluid pressure measurements at DFDP-1B indicate that the fault acts as a local barrier to flow (Sutherland et al., 2012), they do not confirm that it is a barrier on a regional scale. Cross-fault flow from the hanging wall to the footwall is not precluded by geochemical evidence (Menzies et al., 2016) showing that warm spring waters have not interacted with footwall rocks. If fluid pressure measurements spanning the fault plane at >1 km depth were obtained, the hypothesis that the fault acts a regional barrier to flow could be further tested. Estimates of flow

rates and permeability at this depth would indicate whether flow is focused into particular zones at this late stage in the fault seismic cycle, allow the delineation of the extent of a high permeability damage zone, and highlight the regions where permeability has been significantly reduced by mineral precipitation or recrystallisation. As the estimated probability of a surface rupturing earthquake on the fault in the next 50 years is 29 % (Cochran et al., 2017), the opportunity to investigate post-rupture conditions could arise within decades, years or less. In order to be able to contrast these conditions with those prior to rupture, it would be prudent to characterise the pre-rupture state of the fault zone while the opportunity exists.

A future phase of DFDP drilling could continue toward the Alpine Fault at the DFDP-2B site, where conditions to 818 m depth are now relatively well understood. Hydraulic testing could be carried out, in line with the suggestions outlined in this thesis (Chapter 3) to obtain estimates for permeability and fluid pressure conditions. It may also be possible to obtain temperature profiles, from which Darcy velocities can be estimated through the methods employed in this thesis (Chapter 4).

3. What are the typical residence times for fluids within the Southern Alps?

The residence times for groundwater in the Southern Alps are not well constrained and anticipated to vary spatially. As a result the timescales over which different styles of fluid-rock interactions take place, key for interpretation of geochemical processes, remain uncertain. Having narrowed the range of possible values for regional-scale permeability, existing models could be adapted to simulate the residence times for flow through the Southern Alps. Model ages could then be compared to geochemically estimated residence times for water flowing from water springs and in tunnels, such as the Tatare Tunnels and the Amethyst hydroelectric tunnel (Chapter 2), or tested using groundwater dating techniques (e.g., ^{14}C, Noble gas ages). Disparities between the observed spatial distribution of ages and those predicted by models could provide further insights into differences in permeability structure between different parts of the Southern Alps, for example between the Alpine Fault Zone and parts of the orogen more distal from the fault.

4. How does water volume change during uplift in the Southern Alps and could this facilitate permeability generation through hydrofracture?

This thesis has largely focussed on the shallow flow regime in the brittle crust of the Southern Alps. In future work, investigations can be extended to greater depth, considering flow in the ductile crust and how it may be controlled. In a classic paper, Norris and Henley (1976) proposed a mechanism for the release of lithostatically pressured fluids from uplifting rocks through hydrofracture resulting from expansion of water. In their original study, model temperature

profiles representing uplift of Haast Schists rocks in the Southern Alps were presented, but the uplift rates considered (≤1 mm·yr^{-1}) are significantly lower than recent estimates for the central southern Alps of 6 - 9 mm·yr^{-1} (Little et al., 2005). Furthermore these models considered unsteady state thermal conditions during uplift whereas the Southern Alps are now thought to have reached thermal steady state (Fig. 6.3) (Koons, 1987; Little et al., 2005). Temperature profiles based on models developed for this thesis (Chapter 2, 5), from other existing models and updated versions of classic analytical models for the Southern Alps (Allis et al., 1979), and from thermobarometry (Toy et al., 2010) can be used to indicate whether water in Southern Alpine rocks experiences increases in volume during uplift and if so, over what depth range (Fig. 6.4). In doing so, the significance of thermal expansion of water for facilitating fluid flow in the ductile crust can be assessed.

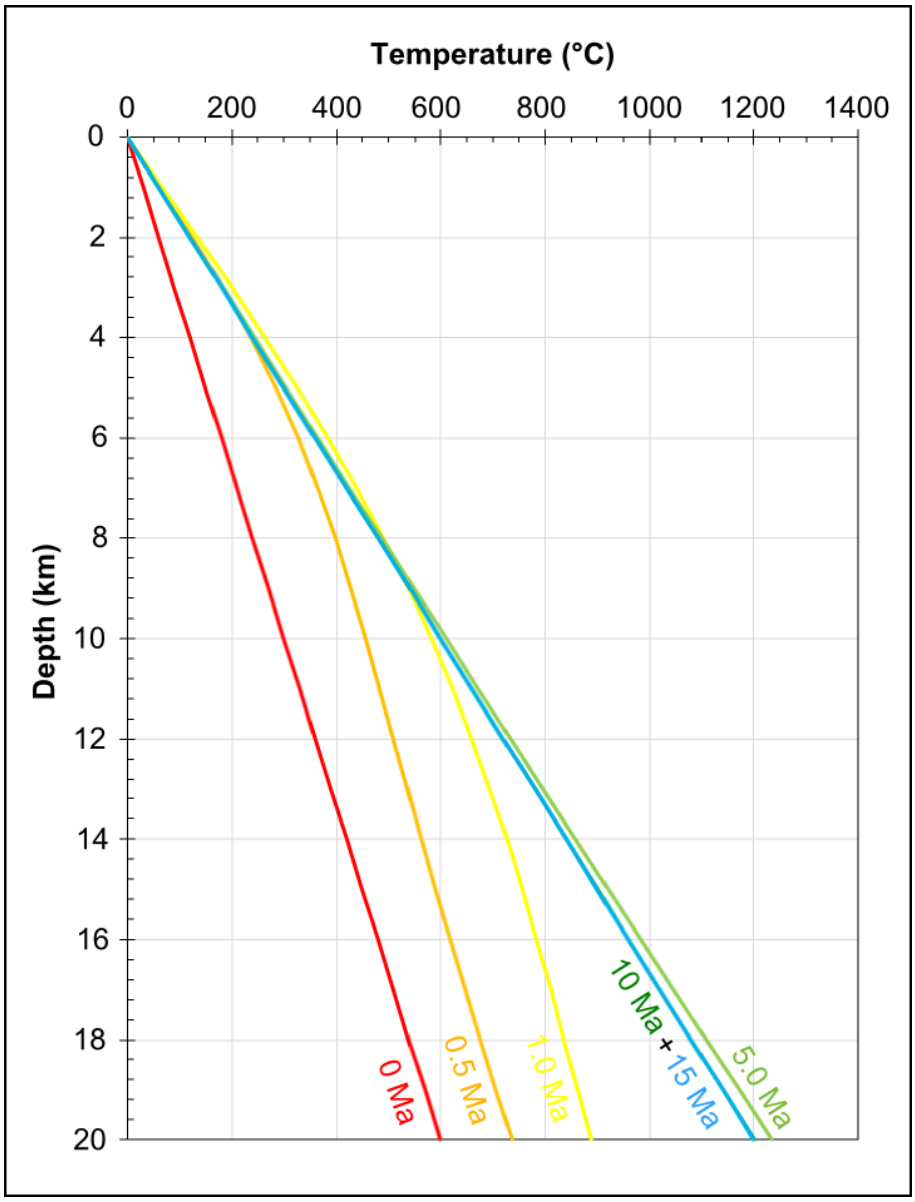

Figure 6.3 Plot of changing temperature with time along a vertical profile calculated using the solution of Clark and Jaeger (1969), as employed by Norris and Henley (1976). Uplift rate is increased to 9 mm·yr^{-1} based on recent estimates (Little et al., 2005) and all other parameters the same as in the original study. Consistent with thermochronometric studies, this suggests that the Southern Alps have reached an approximate thermal steady state, with uplift potentially having taken place for >10 Ma (Adams and Gabites, 1985; Batt et al., 2004, 1999; Herman et al., 2009; Kamp et al., 1992; Tippett and Kamp, 1993). Thus rocks being uplifted today are not predicted to experience the temporal increases in temperature during uplift indicated by the profiles presented by Norris and Henley (1976) (for the temperature of an uplifting volume of rock), based on the same solution.

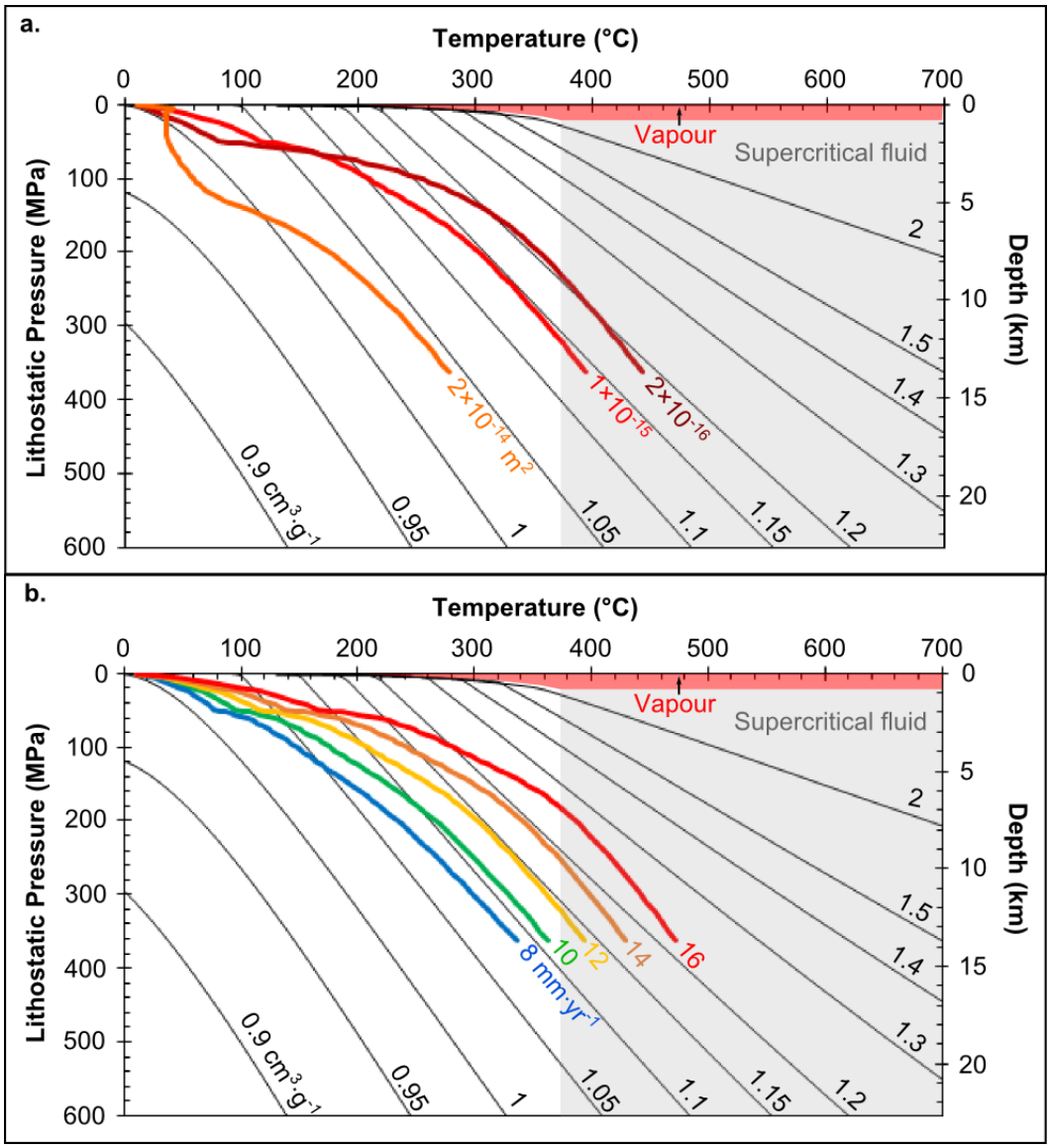

Figure 6.4 Example plot of changes in water specific volume (contoured) for temperature profiles from models contributed by the author to Sutherland et al. (2017) (see Chapter 5 for modelling details). Depths and lithostatic pressures are related assuming a density of 2700 kg·m^{-3}. Results are shown for a range of permeability values (a.) with convergence rate constant at 12 mm·yr^{-1} and a range of convergence rates (b.) with permeability constant at 1 × 10^{-15} m^{-2}. Profiles shown here are vertical but future work should also consider the impact of movement toward the Australian plate during uplift.

5. How are fluid and heat flow influenced by the geometry, tectonics, climate and rock properties of mountain belts?

The investigation of fluid and heat flow in this thesis has considered the specific example of the Southern Alps. Models considering more generalised orogenic geometries would allow the extent to which the fluid and heat flow within a mountain belt is influenced by a range of different parameters to be investigated. In this way conditions within the Southern Alps could be related to other mountain belts (e.g. Taiwan or the Himalayas). By obtaining an understanding of how conditions within a mountain belt vary with a range of parameters, insights from one mountain belt could be used to make predictions about the conditions within others. They could also provide insights into the changes that might occur within a mountain belt through its history as a result of changes in climate and tectonics.

Geometric parameters that could be varied include the dip of the plate bounding fault, the distance between the plate bounding fault and the highest topography, the elevation of the highest topography and the spacing of ridges and valleys draining the orogen. Models should include the thermal effects of rock advection and could consider a range of convergence rates. Infiltration rates should be varied to represent a range of climatic conditions, which may vary both between mountain belts and through the history of a single mountain belt, for example as a result of periods of extensive of glaciation. Additional parameters that should be varied include the thermal properties and permeability of the rocks making up the model mountain belts. Parameters values based on the Southern Alps would provide a suitable baseline scenario for these generalised mountain belt models, from which conditions could be varied. Model outputs that could be compared include the minimum depth of brittle-ductile transition, the fluid flux at the base of the brittle crust, the maximum heat flux and the maximum ratio of fluid to lithostatic pressure (pore fluid factor). Aspects of fluid and heat flow can often be described by non-dimensional numbers, for which a particular dependent variable remains unchanged while the non-dimensional number is held constant. The dependence of water table elevation on the ratio of hydraulic conductivity and infiltration rate (Chapter 2) and the dependence one-dimensional temperature profiles on the Péclet number (Chapter 3) provide examples of this behaviour within this thesis. Models can be used to investigate the extent to which subsurface conditions within a mountain belt can be described using a small number of non-dimensional numbers.

6.5 References

Adams, C.J., Gabites, J.E., 1985. Age of metamorphism and uplift in the Haast Schist Group at Haast Pass, Lake Wanaka and Lake Hawea, South Island, New Zealand. New Zeal. J. Geol. Geophys. 28, 85–96. doi:10.1080/00288306.1985.10422278

Allis, R.G., Henley, R.W., Carman, A.F., 1979. The Thermal Regime Beneath the Southern Alps. Bull. R. Soc. New Zeal. 18, 79–85.

Allis, R.G., Shi, Y., 1995. New insights to temperature and pressure beneath the central Southern Alps, New Zealand. New Zeal. J. Geol. Geophys. 38, 585–592. doi:10.1080/00288306.1995.9514687

Batt, G.E., Baldwin, S.L., Cottam, M.A., Fitzgerald, P.G., Brandon, M.T., Spell, T.L., 2004. Cenozoic plate boundary evolution in the South Island of New Zealand: New thermochronological constraints. Tectonics 23, 1–17. doi:10.1029/2003TC001527

Batt, G.E., Kohn, B.P., Braun, J., McDougall, I., Ireland, T.R., 1999. New insight into the dynamic development of the Southern Alps, New Zealand, from detailed thermochronological investigation of the Mataketake Range pegmatites. Geol. Soc. London, Spec. Publ. 154, 261–282. doi:10.1144/GSL.SP.1999.154.01.12

Bouwer, H., Rice, R.C., 1976. A slug test for determining hydraulic conductivity of unconfined aquifers with completely or partially penetrating wells. Water Resour. Res. 12, 423. doi:10.1029/WR012i003p00423

Clark, S.P.J., Jaeger, E., 1969. Denudation rate in the Alps from geochronologic and heat flow data. Am. J. Sci. 267, 1143–1160.

Cochran, U.A., Clark, K.J., Howarth, J.D., Biasi, G.P., Langridge, R.M., Villamor, P., Berryman, K.R., Vandergoes, M.J., 2017. A plate boundary earthquake record from a wetland adjacent to the Alpine fault in New Zealand refines hazard estimates. Earth Planet. Sci. Lett. 464, 175–188. doi:10.1016/j.epsl.2017.02.026

Cox, S.C., Menzies, C.D., Sutherland, R., Denys, P.H., Chamberlain, C., Teagle, D.A.H., 2015. Changes in hot spring temperature and hydrogeology of the Alpine Fault hanging wall, New Zealand, induced by distal South Island earthquakes. Geofluids 15, 216–239. doi:10.1111/gfl.12093

Herman, F., Cox, S.C., Kamp, P.J.J., 2009. Low-temperature thermochronology and thermokinematic modeling of deformation, exhumation, and development of topography in the central Southern Alps, New Zealand. Tectonics 28. doi:10.1029/2008TC002367

Hvorslev, M.J., 1951. Time Lag and Soil Permeability in Ground-Water Observations. Bull. (Waterways Exp. Stn. Corps Eng. U.S. Army, Vicksburg, Mississippi) 36, 53. doi:Bulletin no. 36

Kamp, P.J.J., Green, P.F., Tippett, J.M., 1992. Tectonic Architecture of the Mountain-Foreland Basin Transition, South Island, New Zealand, Assessed by Fission Track Analysis. Tectonics 11, 98–113.

Koons, P.O., 1987. Some thermal and mechanical consequences of rapid uplift: an example from the Southern Alps, New Zealand. Earth Planet. Sci. Lett. 86, 307–319. doi:10.1016/0012-821X(87)90228-7

Koons, P.O., Craw, D., 1991. Evolution of fluid driving forces and composition within collisional orogens. Geophys. Res. Lett. 18, 935–938. doi:10.1029/91GL00910

Little, T.A., Cox, S., Vry, J.K., Batt, G., 2005. Variations in exhumation level and uplift rate along the oblique-slip Alpine fault, central Southern Alps, New Zealand. Bull. Geol. Soc. Am. 117, 707–723. doi:10.1130/B25500.1

Manning, C.E., Ingebritsen, S.E., 1999. Permeability Implications of the Continental of Geothermal Data and Metamorphic Systems. Rev. Geophys. 37, 127–150.

Menzies, C.D., Teagle, D.A.H., Niedermann, S., Cox, S.C., Craw, D., Zimmer, M., Cooper, M.J., Erzinger, J., 2016. The fluid budget of a continental plate boundary fault: Quantification from the Alpine Fault, New Zealand. Earth Planet. Sci. Lett. 445, 125–135. doi:10.1016/j.epsl.2016.03.046

Norris, R.J., Henley, R.W., 1976. Dewatering of a metamorphic pile. Geology 4, 333–336. doi:10.1130/0091-7613(1976)4<333:DOAMP>2.0.CO;2

Shi, Y., Allis, R., Davey, F., 1996. Thermal modeling of the Southern Alps, New Zealand. Pure Appl. Geophys. 146, 469–501. doi:10.1007/BF00874730

Sims, A., Cox, S.C., Fitzsimons, S., Holland, P., 2015. Seasonal infiltration and groundwater movement in schist bedrock, Southern Alps, New Zealand. J. Hydrol. 54, 33–52.

Sutherland, R., Townend, J., Toy, V., Upton, P., Coussens, J., Allen, M., Baratin, L.-M., Barth, N., Becroft, L., Boese, C., Boles, A., Boulton, C., Broderick, N.G.R., Janku-Capova, L., Carpenter,

B.M., Célérier, B., Chamberlain, C., Cooper, A., Coutts, A., Cox, S., Craw, L., Doan, M.-L., Eccles, J., Faulkner, D., Grieve, J., Grochowski, J., Gulley, A., Hartog, A., Howarth, J., Jacobs, K., Jeppson, T., Kato, N., Keys, S., Kirilova, M., Kometani, Y., Langridge, R., Lin, W., Little, T., Lukacs, A., Mallyon, D., Mariani, E., Massiot, C., Mathewson, L., Melosh, B., Menzies, C., Moore, J., Morales, L., Morgan, C., Mori, H., Niemeijer, A., Nishikawa, O., Prior, D., Sauer, K., Savage, M., Schleicher, A., Schmitt, D.R., Shigematsu, N., Taylor-Offord, S., Teagle, D., Tobin, H., Valdez, R., Weaver, K., Wiersberg, T., Williams, J., Woodman, N., Zimmer, M., 2017. Extreme hydrothermal conditions at an active plate-bounding fault. Nature 546, 137–140. doi:10.1038/nature22355

Sutherland, R., Toy, V.G., Townend, J., Cox, S.C., Eccles, J.D., Faulkner, D.R., Prior, D.J., Norris, R.J., Mariani, E., Boulton, C., Carpenter, B.M., Menzies, C.D., Little, T.A., Hasting, M., De Pascale, G.P., Langridge, R.M., Scott, H.R., Reid Lindroos, Z., Fleming, B., Kopf, J., 2012. Drilling reveals fluid control on architecture and rupture of the Alpine fault, New Zealand. Geology 40, 1143–1146. doi:10.1130/G33614.1

Tippett, J.M., Kamp, P.J.J., 1993. Fission Track Analysis of the Late Cenozoic Veritical Kinematics of Continental Crust, South Island, New Zealand. J. Geophys. Res. 98, 16119–16148.

Toy, V.G., Craw, D., Cooper, A.F., Norris, R.J., 2010. Thermal regime in the central Alpine Fault zone, New Zealand: Constraints from microstructures, biotite chemistry and fluid inclusion data. Tectonophysics 485, 178–192. doi:10.1016/j.tecto.2009.12.013

Upton, P., Craw, D., Yu, B., Chen, Y.-G., 2011. Controls on fluid flow in transpressive orogens, Taiwan and New Zealand. Geol. Soc. London, Spec. Publ. 359, 249–265. doi:10.1144/SP359.14

Upton, P., Sutherland, R., 2014. High permeability and low temperature correlates with proximity to brittle failure within mountains at an active tectonic boundary, Manapouri tunnel, Fiordland, New Zealand. Earth Planet. Sci. Lett. 389, 176–187. doi:10.1016/j.epsl.2013.12.032

Appendices

Appendix A